ANALYSIS AND MODELING OF NONINVASIVE MEASUREMENT OF TISSUE CHROMOPHORES BY THE OPTICAL PHARMACOKINETIC SYSTEM

by

Stephen Chad Kanick

B.S., West Virginia University, 2002

M.S., University of Pittsburgh, 2004

Submitted to the Graduate Faculty of

the Swanson School of Engineering in partial fulfillment

of the requirements for the degree of

Doctor of Philosophy

University of Pittsburgh

2008

UNIVERSITY OF PITTSBURGH

SWANSON SCHOOL OF ENGINEERING

This dissertation was presented

by

Stephen Chad Kanick

It was defended on

February 19th 2008

and approved by

Dr. Robert S. Parker, Associate Professor, Department of Chemical and Petroleum

Engineering

Dr. J. Karl Johnson, W. K. Whiteford Professor, Department of Chemical and Petroleum

Engineering

Dr. Sachin Velankar, Assistant Professor, Department of Chemical and Petroleum

Engineering

Dr. Julie Eiseman, Research Associate Professor, Deptartment of Pharmacology

Dissertation Director: Dr. Robert S. Parker, Associate Professor, Department of Chemical

and Petroleum Engineering

ANALYSIS AND MODELING OF NONINVASIVE MEASUREMENT OF TISSUE CHROMOPHORES BY THE OPTICAL PHARMACOKINETIC SYSTEM

Stephen Chad Kanick, PhD

University of Pittsburgh, 2008

Efficient design of anti-cancer treatments involving radiation- and photo-sensitizing therapeutics requires knowledge of tissue-specific drug concentrations. This dissertation investigates the utility of the Optical Pharmacokinetic System (OPS), a fiber-optic based elastic-scattering spectroscopy device, to noninvasively quantitate concentrations of sensitizing compounds and hemoglobin within tissue *in vivo*.

The OPS was used to quantitate concentrations of motexafin gadolinium (MGd), in mouse tissues *in vivo* and *in situ*. An algorithm was developed to quantify MGd absorbance by integration of the MGd peak absorbance area, thereby relaxing the requirement that the extinction coefficient be known *a priori*. Concentrations measured by OPS were well-correlated with measurements by high-performance liquid chromatography (HPLC).

Compartmental pharmacokinetic models were developed from tissue-specific MGd concentrations measured by OPS and HPLC. Models predicted both rapid initial distribution and slow elimination of MGd in plasma, fast transport of MGd out of the skin, and MGd retention at long times in the tumor. *In vivo* tumor MGd concentrations measured by the OPS were estimated by a linear combination of the plasma, tumor, and skin PK profiles.

A theoretical analysis of the OPS measurement of tissue was conducted using a Monte Carlo (MC) model of light transport through tissue that included discrete blood vessels. Simulation results motivated extensions to a previous analysis algorithm, including: (1) a novel analytic functionality between mean photon path length and total absorption coeffi-

cient; and (2) incorporation of a vessel correction factor to account for the pigment packaging effect of discrete vessels on the OPS-estimated absorption coefficient. These extensions improved OPS-estimates of both silicon phthalocyanine (Pc4) and hemoglobin concentration in a mouse xenograft *in vivo* following photodynamic therapy (PDT).

Mathematical models were utilized to investigate *in silico* the sensitivity of the OPS to chronically and acutely hypoxic regions within tumor tissue. PDT-induced acute hypoxia occured via simulation of the photodynamic reaction. Subsequent simulation of the OPS measurement suggested that the OPS may be sensitive to the presence of chronically hypoxic vessels (an OPS-estimated hemoglobin saturation of $\geq 57\%$ indicated $< 6\%$ of vessels hypoxic), but may have limited application to detection of acute hypoxia following PDT.

TABLE OF CONTENTS

LIST OF TABLES

LIST OF FIGURES

PREFACE

The work presented within this document represents the combined efforts of many people. I will start by thanking my Mom, Dad, and, my sister, Meagan. I owe them many thanks for their support and patience (which was tested many times) over the years. My parents could tell that I would be an engineer at a young age. It might have been because of the overly complicated LEGO constructions that I built, or because the response 'just because' was never a valid answer when I would ask 'why?' (oh, my poor parents). I am proud, and lucky, to have them as my family.

Next on the list is Suzanne, who has been my best friend for years, and now I am lucky enough to now call her my wife. When things didn't work well in lab, as was often the case, she was the person who would hear about it, dissolve the anxiety, give me confidence, and help me get back to figuring out how to make it work. Dissertations show the names of the author and of the committee, but I would find it just as fitting to have her name listed under 'person who without which this would not have been done'.

Continuing on the family theme, I did not have brothers growing up, but I found quite a few during college. Specifically, I would like to mention Chris, Jarod, Kyle, Matt, Ray, and Scotty. The majority of what I retained from college, I learned from them. For better or for worse, I would not be the person that I am today without their influences.

The time that I have spent at the University of Pittsburgh has been a great experience. Bob Parker was my primary advisor during my PhD work, and he did an excellent job of advising me along my way. Of all of the things that Bob taught me, the most important was showing me the importance of finishing the last (and most tedious bit) of a project. Perhaps most importantly, he has been an excellent mentor and became a good friend.

Another major influence on my graduate career was Julie Eiseman, who was our main collaborator at the Hillman Cancer Center, and was effectively my co-advisor during my Ph.D. work. Her tenacity forced me to mature professionally and to take pride in my work. All of the experimental work presented within this dissertation was generated by Julie and her co-workers: Jainxia Guo, Erin Joseph, and Li Bai. Additionally, other collaborators who provided much needed insight along the way, including: Merril Egorin, Jan Beumer, Erin Joseph, Robert Bies, and Jeff Florian. These people have made me a much better researcher, worker and leader than I was when I began.

Lastly, having been born and raised in West Virginia, and having graduated with a B.S. from West Virginia University, it was sometimes difficult to consider myself a Pitt student (this is quite an understatement for anyone who knows me). So, fittingly, I would like this to be the only time my favorite quote is included in a University of Pittsburgh dissertation: 'Let's Go Mountaineers!'

1.0   INTRODUCTION

Noninvasive quantitation of optically-active chromophores in tissue *in vivo* has extensive utility in clinical applications. Specifically, the noninvasive measurement of tissue drug concentration has potential to improve anti-cancer treatment utilizing radiation-sensitizing or photo-sensitizing therapeutics [4, 5]. Ideally, tissue-sensitizing compounds have the specialized properties to selectively localize within malignant tissue following administration and to generate reactive oxygen species in response to radiation or light exposure [6, 7]. The protocols outlining the administration of these treatments generally involve systemic drug administration followed by tumor irradiation at a later time, ideally when the concentration of the sensitizing agent is higher in the targeted tumor than in the surrounding normal tissues [4, 5]. It is well-known that the rates of distribution of the sensitizing agent into targeted malignant tissue may vary between individuals [8, 9]. However, current standard clinical protocols do not measure tissue sensitizer concentrations following administration, and therefore, cannot account for interpatient variability. For those compounds that selectively localize in malignant tissue, there are few options for the clinical measurement of tissue sensitizer concentrations. Standard plasma sampling is of limited use, because the plasma concentration may not be representative of tissue concentrations [10]. Direct measurement of tissue-localized sensitizer concentrations is usually not conducted because conventional tissue assay techniques require invasive biopsies [11] and time consuming destructive tissue analysis *ex vivo*.

Moreover, the capability to noninvasively measure hemoglobin saturation in tissue has the potential to improve photo-sensitizing treatments. During treatment, such a measurement may provide information about the amount of oxygen available for use in generating reactive oxygen species (ROS), potentially providing information about the status of the reaction.

1

Following treatment, the measurement of photosensitizer concentrations remaining within the tissue, or oxygen concentrations within the local vasculature, may indicate the amount of damage induced to the targeted tissue during treatment, potentially providing an indicator of treatment outcome.

The Optical Pharmacokinetic System (OPS) is an optical spectroscopic device that is capable of measuring concentrations of optically active compounds noninvasively *in vivo*. Examples include its use in measuring the concentrations of sensitizing compounds and the saturation of hemoglobin [3, 12, 13]. This dissertation develops analysis methods that improve the accuracy of concentration estimates from the elastic-scattering measurements made by the OPS. The dissertation also develops mathematical models that simulate OPS measurement of tissue *in silico*, with simulations investigating the physiological relevance and clinical utility of OPS estimated tissue concentrations.

1.1 *IN VIVO OPTICAL SPECTROSCOPY*

Over the past 40 years, optical spectroscopy has been investigated as a method to measure concentrations of optically-active compounds noninvasively in tissues *in vivo* [14, 15, 16, 17]. The visible (vis) - near-infrared (NIR) wavelength spectrum ($400 - 900$ nm) is the major focus of *in vivo* optical spectroscopy [15, 16]. In this region, tissue absorbance is at a relative minimum compared with shorter (≤ 400) or longer (≥ 900 nm) wavelengths. Here, vis-NIR light can transmit deeply through tissue, which allows optical devices to sample macroscopic tissue volumes (in the range of mm^3-cm^3) during measurement [15]. While many endogenous compounds absorb light in this region, hemoglobin is the dominant absorber, with absorption that is an order of magnitude larger than any other endogenous compound, such as cytochrome oxidase. [17]. The absorption bands of hemoglobin are oxygenation-state dependent, as shown in Figure 1.1. This plot contains the extinction coefficients of oxygenated (HbO$_2$) and deoxygenated (Hb) hemoglobin. Investigators have often utilized the distinct absorption bands of HbO$_2$ and Hb to quantify hemoglobin saturation noninvasively in tissue *in vivo* [18, 19, 20]. Between the major absorption bands of hemoglobin ($500 - 600$ nm)

and the absorption of water at ≥ 800 nm, a region of low tissue absorption exists. It is in this region where many chemo-, radio-, and photodynamic therapeutic compounds display strong absorption bands. Therefore, exogenously delivered compounds can be detected noninvasively in this region; leading this region to be termed the 'therapeutic window' [21].

In order to understand *in vivo* optical spectroscopy, it is important to begin with a brief description of light propagation through tissue. Light transport through tissue can be described by interactions between photons and the subcomponents of the tissue [15]. These interactions can be simplistically categorized into two types of events: absorption and scattering. Absorption events involve the transfer of the energy within a photon to an accepting substance within the tissue. The absorption coefficient $\mu_a(\lambda)$ represents the average distance that photons travel within a medium before absorption occurs [15]. This property is wavelength (λ) dependent, such that compounds posses characteristic $\mu_a(\lambda)$ profiles [17]. As light passes through a medium, the intensity is reduced due to interactions with the tissue, and this reduction is termed attenuation [15]. Beer and Lambert identified the analytical relationship between the attenuation of light that passes through a medium and the concentration of absorbing compounds within that medium [17]. This relationship is known as the Beer-Lambert law, and is given as:

$$I_{atten}(\lambda) = I_{incident}(\lambda)\, e^{(-\epsilon_i(\lambda)C_i L(\lambda))} \tag{1.1}$$

Here, $I_{incident}(\lambda)$ is the intensity of light incident on the sample, $I_{atten}(\lambda)$ is the intensity of attenuated light collected by the detector, $L(\lambda)$ is the path length of light within the sample, and $\epsilon_i(\lambda)$ and C_i are the extinction coefficient and concentration of compound i within the sample, respectively. This relation is classically applied to *in vitro* optical spectroscopy devices, which measure a clear (non-scattering) solution that contains a small amount of a known compound. In this situation, the distance traveled by the light within the sample ($L(\lambda)$) is simply the geometrical distance between the source and detector. Therefore, $I_{incident}(\lambda)$, $L(\lambda)$, and $\epsilon_i(\lambda)$ are known parameters, and measurements of $I_{atten}(\lambda)$ are used to calculate changes in C_i. Moreover, the concentration of multiple compounds could be estimated by detecting multiple wavelengths of light (with at least one wavelength per component) [22] and solving Equation (1.1) in matrix form.
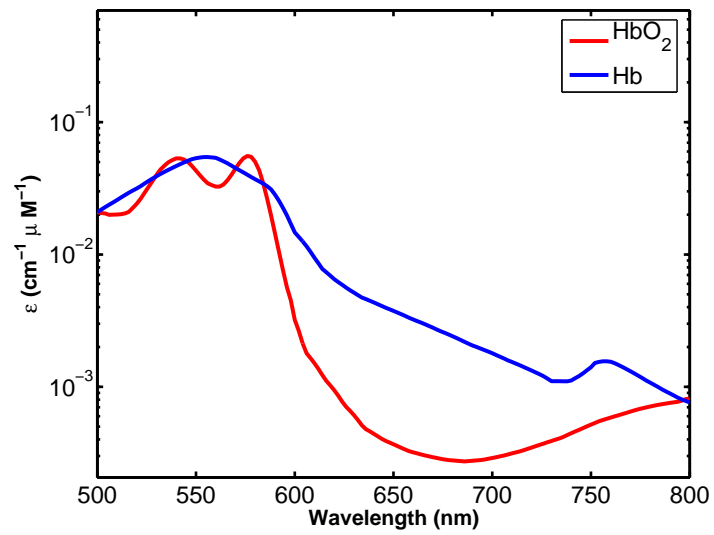
Figure 1.1: Molar extinction coefficients of oxygenated and deoxygenated hemoglobin [2].

In tissues, the process is more complicated due to scattering. Scattering events change the direction of photon propagation and are caused by differences in the speed that photons travel through subcomponents of the tissue [15]. Scattering events are assumed to be elastic [23], however they do attenuate light intensity due to the diffuse 'spreading' of photons as light propagates through tissue. Photon scattering within tissue is wavelength-dependent and can be quantified by the scattering coefficient $\mu_s(\lambda)$, which describes the average number of scattering events that a photon experiences per distance [15]. During a scattering event, the path of the photon is altered by an angle ($\theta_{scatter}$). This angle is dependent upon the anisotropy (g) of the medium. The anisotropy factor provides the mean $\cos(\theta_{scatter})$ value for photons within the medium. A value near 1 would indicate to an average deviation from the initial path that is negligible, and this is considered forward-scattering. A value near 0 would indicate to a near-reversal of the photon path, and this is considered backward-scattering. Tissue is classified as a strong forward-scattering medium, with g values in the range of $0.70 - 0.95$. The scattering properties determine the amount of light that remits from the tissue surface, and the amount that is 'lost' by propagation deep into tissue. From this description of light propagation, it is clear that attenuation of the light collected from the tissue is dependent on both scattering and absorption properties.

Within tissue, scattering dominates photon propagation, with $\mu_s(\lambda) >> \mu_a(\lambda)$ [24]. Therefore, during spectroscopic measurement of tissue, the photons may be scattered many times during propagation from source to detector. This may result in photon path lengths that can be many times greater than the geometrical separation between the source and detector [16, 17]. Moreover, the detector collects a range of photon paths, and this range is affected by the total $\mu_a(\lambda)$ value within tissue. Measurements of tissue with large absorption coefficients collect fewer photons that have traveled long paths because these photons are more likely to be absorbed. Therefore, during optical measurement of tissue *in vivo*, the photon path length is dependent on both the total values of $\mu_s(\lambda)$ and $\mu_a(\lambda)$; this information is not known *a priori* [16]. This complication makes optical measurements of tissue difficult to interpret.

Many *in vivo* optical spectroscopic devices have been developed that measure the intensity of light remitted from tissue [13, 18, 20, 25, 26]. Here, 'remittance' may refer to light

exiting either an opposite face of the tissue (termed transmittance), or light that scatters, reverses direction, and exits the original surface (termed diffuse reflectance) [15]. Due to the high scattering coefficient of tissue, most *in vivo* optical spectroscopy devices measure diffuse reflectance.

Early *in vivo* optical spectroscopic devices were developed to measure the diffuse reflectance at multiple source-detector separations [18,25]. The detected signal was analyzed using an analytical model of light transport known as diffusion theory [27], which estimated both scattering and absorption properties within the tissue [18,25]. However, these devices contained some inherent limitations. The optical probes usually contained source-detector separations on the order of mm to cm, which resulted in optically sampled tissue volumes that may be larger than clinically desired (≥ 1 cm^3). Another problem faced by these devices was that the high absorption bands of hemoglobin in the $500 - 600$ nm wavelength range prevented adequate detection of light at large source-detector separations. This effectively truncated the range of measured wavelengths to $650 - 800$ nm [18], reducing the amount of information that can be estimated from the data. Moreover, the use of diffusion theory for spectral analysis was problematic. Diffusion theory is unable to describe light transport short distances from the source fiber (~ 1 mm) [27]. Also, diffusion theory requires that the absorption coefficient be much smaller than the scattering coefficient, a requirement that may be violated in the $500 - 600$ nm wavelength range. These complications combine to limit the utility of 'diffusion theory based' *in vivo* optical spectroscopic devices.

Mourant *et al.* presented an alternative approach that utilized a single, short source-detector separation. The hypothesis was that a source-detector separation could be selected that reduced the dependence of photon path length on the scattering properties within the tissue [28]. This hypothesis was based on observations of how changes in scattering coefficient affect the photon path length. Both large source-detector separations and large scattering coefficients would case photons propagating from source to detector to undergo many scattering events. Logically, in this situation, large scattering coefficients result in long photon path lengths. Conversely, for very small source-detector separations, very small scattering coefficients allow photons to penetrate deeply into the tissue before being backscattered to the detector fiber. Therefore, in this situation, small scattering coefficients result in long photon

path lengths. Mourant *et al.* identified a source-detector separation in the 'intermediate' range of these two situations $(1.5 - 1.8$ mm) that made the photon path length insensitive to the scattering properties of the medium [28]. This stipulation simplifies the problem of estimating changes in chromophore concentrations from changes in light attenuation by removing the requirement that the total scattering coefficient be known. This design was incorporated into the device known as the Optical Pharmacokinetic System (OPS), which is described in detail in Section 1.1.1.

Before extensive description of the OPS, it is worth noting some of the more-recent *in vivo* optical spectroscopic devices and technologies that have been developed. Finlay and Foster further developed the use of a fiber optic probe with a single, short source detector separation (1 mm) to measure diffuse reflectance [29]. The data were analyzed using an analytical model of light movement through tissue termed a hybrid P_3-diffusion model [30]. This modeling technique uses a third order approximation of the light transport equation, which overcomes the limitations of diffusion theory at short distances from the source and in mediums with large absorption coefficients. This device is capable of accurately quantitating hemoglobin concentration in tissue *in vivo* and tissue simulating phantoms *in vitro*, and comparatively, it represents a very similar device to the OPS.

Another device was developed by Amelink and Sterenborg [26], who termed the technology differential path-length spectroscopy. This device utilized source and detector fibers nearly adjacent to each other. During measurement, photons exit the source, scatter through the tissue, and are collected by both the source and detector fibers. This geometry utilizes both detected signals to accurately estimate the photon path length, and in turn, accurately estimate $\mu_a(\lambda)$ [26, 31]. However, the sampled tissue volume is limited to a few superficial layers, which may limit the capability this device to quantitate drug concentrations within macroscopic tissues.

The spectroscopic devices considered thus far are termed steady-state devices [15]. Steady-state measurements involve light entering tissue, establishing a stable distribution throughout the sampled tissue, and photons being collected over a 'window' in time, with all collected photons contributing to the detected intensity [32]. Another type of spectroscopic device is termed a time-resolved device [33]. Time-resolved spectroscopy utilizes short light

pulses (on the scale of picoseconds) and time-resolved detectors (with sensitivities on the scale of pico- to nanoseconds) [15]. Using this method, the 'time of flight' of collected photons are recorded and used to estimate the path length traveled by the collected photons [33,34]. Moreover, the distribution of collected photon path lengths can provide information about inhomogeneities within the tissue sampled [32,35]. Time-resolved technologies are more complicated (and expensive) than steady-state devices and this is the trade-off for the increased information obtained from measurement with these devices.

Another alternative technology that is relevant to the complete description of *in vivo* optical spectroscopy is the field of fluorescence spectroscopy. In brief, this technique involves the excitation a compound (termed a fluorophore) with a beam of light (usually a laser), which causes the compound to emit light of a lower energy [36]. The fluorescence spectroscopic devices detect the emitted light and use this to quantitate the concentration of the fluorophore *in vivo*. It has been noted that fluorescence and reflectance spectroscopies are less 'competing' and more 'complimentary' technologies [23]. Specifically, fluorescence spectroscopy offers the ability to quantify the concentrations of compounds that have absorption bands that overlap strong endogenous absorbers, but have a fluorescence emission spectra that is distinct from endogenous compounds. This may allow fluorescence techniques to probe a deeper volume of tissue during measurement. Conversely, it is possible that reflectance may be more well-suited to quantitate compounds if the fluorescence emission signal is convoluted with other endogenous fluorophores, but the absorption bands are distinct from other endogenous chromophores. The field of fluorescence spectroscopy has been extensively reviewed and discussed by Wagnieres *et al.* [36].

1.1.1 Optical Pharmacokinetic System (OPS)

The OPS is a portable, hand-held, fiber-optic based spectroscopy device that measures the intensity of elastically-scattered light at an accessible tissue site [3,12,37]. Figure 1.2 shows a schematic of the tip of the hand-held probe, containing two optical fibers; one leads from a light source with the second returning to a spectrophotometer. The light source is broadband, with light in the vis-NIR wavelength range ($450 - 900$ nm). During OPS measurement of

tissue, the tip is placed in contact with the surface of the tissue and photons exiting the source fiber are elastically-scattered throughout. Photons that are back-scattered and collected by the detection fiber are sent to the spectrophotometer.

Bigio *et al.* uses the term 'elastically-scattered' to make a distinction between the OPS and more 'general' reflectance spectroscopy devices [23]. Specifically, elastically-scattered light does not contain specular reflectance, which is defined as light that did not scatter through tissue, instead reflecting off of the tissue/air interface and being collected by the detector. For clarification, the elastic-scattering measurement is essentially a reflectance measurement made with the detector fiber in contact with the surface of a tissue.

As described previously, the source-detector fiber separation distance in the range of $1.5-1.8$ mm makes the effective photon path length insensitive to changes in tissue scattering [28]. Using a modification to the Beer-Lambert law, changes in collected light intensity are related to changes in the concentration of absorbing compounds within the medium (this methodology is explained in detail in Chapters 2 and 4). Recent studies have utilized the Optical Pharmacokinetic System to accurately quantitate optically active drugs in mouse tissues *in vivo* [3, 12, 13, 37]. These results suggest that the OPS may have direct and potentially significant application to the field of photodynamic therapy (PDT), which is described in the following Section.

1.2   PHOTODYNAMIC THERAPY (PDT)

PDT is a promising treatment option for malignant and nonmalignant pathologies [4, 5, 38]. PDT involves the use of a photo-activated compound, termed a photosensitizer (PS) that becomes excited when exposed to light of a specific wavelength. In the early 1900's, Raab was the first to report the use of a PS to destroy biological organisms [39]. He discovered, by chance, that cells exposed to both the compound acridine and light died, while cells exposed to either acridine or light were preserved [39]. In the 1970's this fundamental concept was applied to the modern clinical treatment of cancer by Dougherty and Weishaupt [40, 41]. It
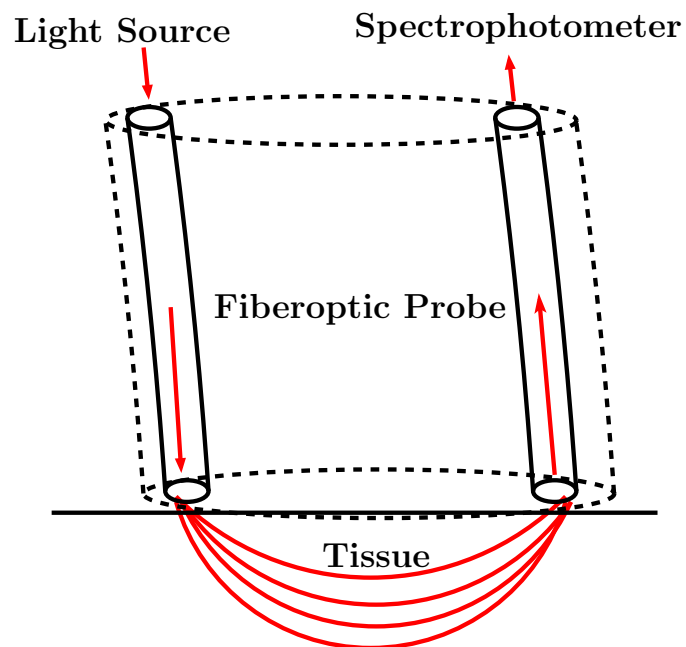
Figure 1.2: Schematic of the OPS probe tip. During measurements, photons exit the source fiber and are elastically-scattered throughout the tissue. Photons that are backscattered and collected by the detector fiber are sent to a spectrophotometer.

was Dougherty who extensively reported the tumor-destructive capabilities of PDT [40, 41], while Weishaupt identified singlet oxygen as the cytotoxic agent of PDT [42].

Figure 1.3 shows the energy transitions between PS and oxygen during the photodynamic reaction of PDT. Singlet state PS molecules can interact to yield a more-stable triplet state PS molecule, which can cause cellular damage via two pathways. The type I pathway involves direct interaction of the triplet state PS with cellular components. The type II pathway involves interaction of the triplet state PS with molecular oxygen, which generates singlet oxygen and other ROS that damage cellular components. ROS compounds are highly reactive due to the presence of unpaired valance shell electrons and are known to damage cellular components (including DNA). The type II pathway is accepted as the dominant cause of PDT-induced tissue damage [42, 43].

In anti-cancer PDT, the PS is usually administered via intravenous (i.v.) injection. However, for superficial malignancies, the PS can be administered locally via topical application [4]. An ideal PS compound preferentially localizes in malignant tissue during drug distribution, such that after some elapsed time, a positive concentration gradient exists between malignant and surrounding non-malignant tissues [6, 38, 44]. At this time, illumination of targeted tumor tissue with a specific wavelength of light inflicts damage to the tumor cells and (ideally) preserves the surrounding healthy tissues. This targeted therapy limits the exposure of healthy tissues to toxic material, thereby reducing the systemic side effects and patient morbidity associated with conventional anti-cancer treatments (e.g., whole body chemo- or radiation-therapies) [38, 44, 45]. The mechanism of PDT does not make it susceptible to drug resistance by tumor lines [5]. It also is possible to repeat PDT treatments at a target site multiple times without additive toxicity, unlike conventional chemo- and radio-therapies [5, 45]. Possible side effects of PDT can include damage to surrounding healthy tissue (including burns, swelling, pain, and scarring), and skin photosensitivity [4], which is the excitation of the PS in skin by ambient light following treatment. The occurrence and severity of these side-effects can be reduced by delivering PS and light doses that do not induce damage to healthy tissues [45], and by using PS compounds that rapidly clear following treatment, reducing the need for prolonged dark periods following treatment to avoid photosensitivity [6].
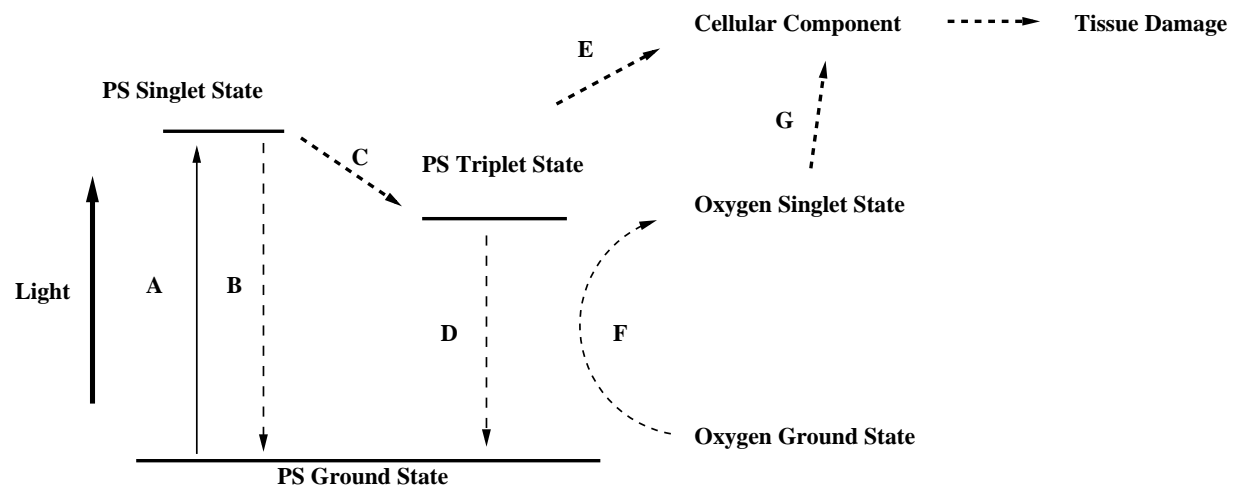
Figure 1.3: Jablonski diagram of the populations and transitions of PS and oxygen during PDT: (A) excitation, (B) fluorescence, (C) inter-system crossing, (D) phosphorescence, (E) interaction of triplet state PS with cellular component, (F) transfer of energy converting ground state to singlet state oxygen, (G) oxidation of cellular component.

1.2.1 Photosensitizing Compounds

Ideally, the PS is nontoxic in the absence of light and becomes excited to a singlet state when exposed to a specific wavelength of light [6, 44], with efficient PS compounds capable of generating large amounts of ROS in response to excitation. Preferably, the excitation wavelength is in the 'therapeutic window' wavelength region, which allows deep penetration of the light into the tumor tissue.

Photofrin® is the most commonly utilized and researched PS compound to date. Photofrin® is manufactured by purification of hematoporphyrin derivative, and was shown to be effective against tumor lines by Dougherty [5]. Medical review boards world wide have approved Photofrin® for treatment of bladder, cervical, esophageal, lung, and head and neck cancers, as well as precancerous lesions in patients with Barrett's esophagus (a possible precursor to esophageal cancer) [4, 46]. However, it is not an ideal PS because it has a relatively low absorption maximum in the red wavelength range (at 632 nm), potentially limiting the delivered ROS yield during laser administration.

Second generation PS compounds have been developed that improve upon the capabilities of Photofrin®. Verteporfin® is a formulation of benzoporphyrin derivative, with an absorption maximum at 690 nm. Studies have shown that Verteporfin® is useful in targeting vasculature during treatment and is approved to treat age-related macular degeneration [47, 48]. Verteporfin® is also being considered as a treatment option for skin cancer [49]. meta-tetrahydroxyphenyl chlorin (m-THPC, or Foscan®) has an absorption maximum at 652 nm, has shown increased efficiency compared with Photofrin, and is capable of achieving equivalent treatment outcome with relatively low drug doses and low light fluence [5]. Foscan® is being investigated for treatment of esophageal, lung, head and neck, thoracic, and skin cancers [50, 51]. 5-aminolevulinic acid (ALA) is a compound that accumulates in malignant cells and is metabolized *in vivo* into the photosensitive compound protoporphyrin-IX [5]. ALA has an absorption maximum at 632 nm, and been investigated to treat actinic keratosis and basal cell carcinoma [52]. Aluminum phthalocyanine sulfonate (AlPcS) has an absorption maximum at 675 nm, shows tumor localization, and is being investigated to treat cutaneous cancers [53]. Motexafin lutetium (MLu, or Lutex®) is a

non-porphyrin PS that has an absorption maximum at 732 nm, allowing deeper penetration of light during treatment compared with Photofrin®, Verteporfin®, or Foscan® [5]. MLu has been investigated to treat breast [54] and prostate [55] cancers. A similar compound, motexafin gadolinium (MGd, or Gadtex®) is being investigated as a radiation-sensitizer and chemo-sensitizer [56,57]; MGd is further discussed in Chapter 2. Silicon phthalocyanine (Pc4) has a strong absorption maximum at 672 nm, and has been shown to be effective preclinically [58], and is being considered to treat cutaneous cancers [59]; Pc4 is further discussed in Chapter 4.

1.2.2   PDT Dosimetry

Despite the numerous advantages of PDT, there has not yet been widespread implementation of this treatment option in the clinic [4, 45]. This is attributed to sub-optimal treatment outcomes that can result from current clinical protocols [60,45]. The photochemical reaction of PDT requires adequate amounts of photosensitizer, oxygen, and light fluence at the site of action in order to generate the ROS yield required to induce tumor cell death [4,5,60,61]. An inadequate supply of any these components can limit the photodynamic reaction [4,5,45,61, 62] and potentially result in non-uniform tumor necrosis, a sub-optimal treatment outcome. Classic clinical protocols include three phases [45,44]: (1) PS administration; (2) elapsed time to allow the PS to distribute into the target tissue; and (3) illumination of the target site with laser light. The PS dose is usually determined by patient body weight [60], while the elapsed time between drug administration and light exposure (known as the drug-light interval) is usually fixed for all patients, as is the laser light intensity and laser exposure time [60]. The *a priori* specification of these treatment parameters does not account for interpatient variability in either the rate and magnitude of the PS distribution into the tumor prior to illumination or the rate of oxygen consumption within the target tissue during illumination. Treatment designs that do not consider interpatient variability of these treatment paramters can result in incomplete tumor cell kill and lead to tumor recurrence [4, 5, 60, 62, 61].

PDT dosimetry aims to design treatments that 'potentiate' the efficacy of the photochemical reaction [61, 63, 64, 65, 66, 67]. Dosimetry studies aim to deliver a sufficient amount

of biological damage that results in the destruction of the targeted tissue. Early studies defined the delivered PDT dose as the product of the delivered fluence and the PS concentration [61]. In the presence of sufficient oxygen, this definition of dose is proportional to the amount of ROS generated during treatment, and therefore is proportional to the amount of necrosis induced within the targeted tissue [68]. However, in the *in vivo* situation, the rapid consumption of oxygen can deplete oxygen concentrations, and limit the photodynamic reaction. Therefore, oxygen concentration, in addition to PS concentration and light fluence, must be considered when estimating the PDT dose delivered during treatment [69, 70, 71].

Multiple approaches to dosimetry have been described by Wilson and coauthors [65, 72]. Direct dosimetry refers to the direct measurement of a known indicator of the treatment outcome, such as measuring singlet oxygen at the target site during treatment [66, 73, 72]. Such measurements are currently limited *in vivo* due to the low fluorescent signal produced by singlet oxygen and the difficulties associated with accurately quantitating the signal over noise [74]. Implicit dosimetry refers to the measurement of a quantity that is an indirect indicator of the ROS yield, such as using the rate of PS photobleaching to estimate the rate of ROS generation during treatment [65]. Photobleaching is the irreversible destruction of the PS molecule caused by interaction with either triplet-state PS molecules or ROS compounds. This process causes PS concentrations to decrease during PDT. Observation of the photobleaching rate *in vivo* has been identified as a dosimetry metric [63, 64], because it is dependent on the rate that ROS and other radical species are generated. Explicit dosimetry refers to the measurement of a physical quantity that is involved in the photodynamic reaction, such as PS concentration, tissue oxygenation (measured as hemoglobin saturation), or delivered light fluence [65]. It should be noted that hemoglobin saturation is an indirect assessment of tissue oxygen concentration and the quality of this relationship may be questionable during PDT; this is discussed in Chapter 5. Hypothetically, measurement of these quantities could determine if adequate amounts of the components of the photodynamic reaction are available during treatment.

As noted, effective PDT treatment requires the presence of sufficient PS concentrations during laser illumination. Studies have reported that in the presence of adequate oxygen and fixed light dose, a positive correlation exists between pre-laser tumor PS concentrations and

the degree of necrosis induced by the PDT treatment [75]. Patient-specific assessment of PS concentrations are fundamental to PDT dosimetry because investigators have reported large inter-patient and intra-tumor variability in PS concentrations following administration for commonly used compounds, such as: Verteporfin® [76], AlPcS [77], and MLu [78, 79]. In a preclinical study, Zhou, *et al.* investigated the effect of tailoring the delivered laser light intensity to the Verteporfin® concentration measured in the tumor. This study sampled many small tumor tissue volumes (on the order of intercapillary distances) to determine the mean Verteporfin® concentration and also the intersubject variability throughout the tumor. It was shown that adjustment of laser dose to either the lower-quartile or mean PS concentration measured within tumors significantly reduced the variability in tumor response following treatment [60]. Currently, it is not known if these results could be obtained using a 'bulk' measurement of PS concentration via a device such as the OPS.

During the photodynamic reaction, the rapid consumption of ground state oxygen molecules by triplet state PS molecules can cause hypoxic regions to develop within the tissue [62, 76, 80, 81, 82]. This can limit the generation of ROS to the rate of oxygen resupply from the vasculature. Henderson, *et al.* showed that the rate of oxygen depletion in tissue is highly dependent on the intensity of the laser light to which the tissue is exposed during Photofrin®-mediated PDT [62, 82]. A low intensity light dose consumes oxygen at a lesser rate than high intensity light, thereby preserving the oxygen supply and making the treatment more effective for the same total delivered light dose [62, 81]. However, this low intensity scheme can require long treatment times, which are not embraced clinically, so a method to monitor oxygen concentrations within the tissue could allow a more efficient treatment to be designed. Another technique used to maintain tissue oxygenation is the fractionation of light dose during treatment. Here, the laser is administered in cyclic 'light' and 'dark' periods, with laser illumination periodically halted to allow resupply of oxygen from local blood vessels, which results in increased treatment efficacy for a fixed total light dose [83, 84]. Curnow *et al.* reported temporal changes in oxygen concentration during ALA-mediated PDT, with depletion during light cycles, and subsequent replenishment during dark cycles [85]. However, this study determined the temporal sequence of the light and dark periods *a priori* and did not use measurements of oxygen concentration to adjust

16

the light/dark cycles. The on-line determination of dark periods may be important because tissue oxygen supply can change temporally during PDT treatment, which means that the optimal length of dark periods may change during treatment.

It is well-known that PDT can induce changes to both blood flow and hemoglobin saturation. This has been observed for many commonly used PS compounds, including: Photofrin® [86, 87, 88, 67], AlPcS [84], ALA [89, 85], and Verteporfin® [89, 90]. Wang *et al.* observed that hypoxia in tumor tissue following PDT treatment resulted from vascular occlusion [87]. Chen *et al.* observed PDT-induced changes to relative blood flow [90] and vascular permeability [91], both of which affect the rates of oxygen resupply to the tissue during PDT treatment. The rates of tissue re-oxygenation during PDT are specific to the patient, and may or may not be consistent between treatments on individual patients. Therefore, clinical assessment of patient-specific changes in blood flow and hemoglobin saturation within tissue could allow clinicians to adjust the light dose and/or fractionation periods to preserve tissue oxygen and possibly achieve more uniform tumor necrosis. Moreover, some studies have reported that the degree of hypoxia induced by PDT in the targeted tissue following treatment is a marker of tissue necrosis [87, 88]. Therefore, spectroscopic measurement of tissue following treatment may provide valuable information about the long term outcome of the delivered treatment.

The time interval between drug and light administration has been shown to be another important parameter in PDT optimization. Researchers have shown that the drug-light interval can be used to select the treatment target as either the tumor cells or the local vasculature [92, 93, 94]. For treatments with short drug-light intervals, the PS is primarily localized within the vasculature during laser administration. Laser administration at this time damages blood vessels, resulting in decreases in oxygen concentration within the tumor tissue during and following treatment. For treatments with longer drug-light intervals, the PS is localized in the tumor tissue during laser administration. Laser administration at this time directly damages tumor cellular components. Pogue *et al.* has shown that the drug-light interval effects on treatment are dependent on the specific PS compound [89].

Recent studies have considered targeting both the vasculature and the tumor cellular components by administering two drug doses: one dose at a long time prior to treatment

(on the order of hours/days), and one dose just prior to light exposure (on the order of minutes/hours) [92,93]. These results showed that this dosing regime is more effective than individual targeting of either the vasculature or the tissue [92,93]. Such a treatment protocol may benefit from noninvasive measurement of PS concentrations by the OPS. The OPS measurement of tissue *in vivo* detects the PS localized in both tissue and blood perfusing the tissue. Hypothetically, the OPS could be used to mathematically estimate the optimal time interval between the second (vascular targeted) PS dose and the administration of laser for individual patients. This concept is further discussed as a future direction in Chapter 6.

1.3 MATHEMATICAL MODELING OF THE PDT PROCESS

This Section outlines theoretical models that are used to study the complex interaction among the of reactive components of the photodynamic reaction of PDT. The following sections outline pharmacokinetic models of the PS (Section 1.3.1), models of the photodynamic reaction (Section 1.3.2), and mathematical models of light propagation through tissue (Section 1.3.3)

1.3.1 Mathematical Modeling of Photosensitizer Pharmacokinetics

Pharmacokineitc (PK) theory, introduced by Teorell [95, 96], is the kinetic description of drug absorption, disposition, metabolism, and excretion of compounds within the body. Mathematical models are used to describe time-dependent changes in the drug concentrations within different regions of the body. Compartmental modeling treats the body as a group of 'compartments', which may not be reflective of physiology, but is capable of predicting the dynamics of drug concentrations that occur within the biologic system following administration.

PK analysis of classical chemotherapeutics is often concerned with predicting the overall exposure of the tumor to the drug, which is often correlated with the effect of the drug on the tumor. PK analysis of PS compounds is slightly different, since the PS is (ideally)

only active in the presence of light [6], such that PDT-induced tissue damage is dependent on the PS concentration during illumination. This makes the drug-light interval a critical variable in PDT treatment design, yet current clinical protocols do not determine the interval for individual patients because tissue PS concentrations are not monitored following administration. Hypothetically, the OPS could be used to monitor PS concentrations in the tumor and surrounding tissues following administration, providing information useful to the 'optimal' selection of the drug-light interval.

Knowledge of the PK of the PS may allow the clinician to selectively target either tumor tissue or the tumor vasculature during treatment [89, 94, 97]. Pogue and coauthors [77, 98], as well as Triesscheijn *et al.* [94] suggested the importance of the temporal shifting of the PS from vasculature to tissue during distribution. This was modeled by Jones *et al.* [97], who developed a compartmental PK model of Foscan® distribution in a rat tumor model. Here, multiple drug-light intervals were investigated, and increased effective response was noted for laser administration both at 2 hr and 24 hr following Foscan® dose. These times correlated with the maximum Foscan® concentrations estimated by the PK model in plasma and tumor, respectively.

1.3.2 Mathematical Modeling of the Photodynamic PDT Reaction

Mathematical models of the photochemical reaction allowed researchers to identify oxygen consumption as a limiting factor for PDT in tissue *in vivo* [69, 70]. Foster and coauthors developed a one-dimensional model of oxygen consumption and diffusion within tissue during PDT [69, 70]. These studies concluded that oxygen consumption could potentially limit ROS generation [69, 70]. The distance between capillaries defined the potential of treatment being limited by oxygen deficit [70]. The studies concluded that laser administration in a fractionated schedule (30 sec laser on / 30 sec laser off) could relax the oxygen limitation and improve ROS generation [69, 70]. Model results adequately explained oxygen measurements within tissue-spheroids during PDT [99]. The model was extended by Henning *et al.* [100] to incorporate temporal changes in oxygen and ROS, concluding that optimal laser fractionation periods should be asymmetric, with longer time allowed for oxygen resupply than

for reaction. Yuan *et al.* further extended the theory to consider the development of axial gradients of reactive components during PDT, which can cause nonuniform photodynamic dose deposition [101].

Pogue *et al.* [102] modeled the effect of light/dark cycle length on the rate of singlet oxygen generation. The study concluded that the optimal light fractionation schemes found empirically (on the order of $30 - 60$ sec reoxygenation time) are much longer than would be required for average intercapillary spacing if oxygen supply was constant during treatment (on the order of $5-10$ sec). These results suggest that vascular occlusion, vascular damage, or chronic/acute hypoxic regions within the tissue may cause the optimal fractionation schedule found *in vivo* to be longer than the time required for oxygen resupply during normal blood flow.

Wang *et al.* further developed this type of model by incorporating a time-dependent oxygen source within blood vessels and linking hemoglobin saturation to the oxygen concentrations in the intercapillary space [74]. Moreover, Wang concludes that volume-averaged hemoglobin saturation is not sensitive to 'microregional' heterogeneities, but the signals are dependent on the intercapillary spacing. The conclusion of PDT dependence on capillary density (spacing) is one potential explanation for the high variability observed between patients. This is because tumor vasculature can be distributed irregularly throughout the tissue, with intra- and inter-tumor variability in capillary density. Moreover, this value cannot be determined noninvasively prior to clinical treatment. Therefore, these findings support the need for patient-specific therapeutic monitoring.

The irregular arrangement of blood vessels within tumors compounds the complexity of a mathematical description of the PDT process *in vivo*. Pogue *et al.* presented a numerical method to simulate the spatial distribution of oxygen within tumors by applying a finite element technique within geometries obtained from histological cross sections of tumors [103]. This model predicted large regions of hypoxia within the tumor tissue at steady state, and the results are consistent with other empirical [104] and theoretical [105] descriptions of tumor hypoxia. These predictions suggest that PDT-targeted tumor tissue may be hypoxic at steady state, a condition which could limit the PDT reaction.

The variability in tumor blood vessel arrangement and blood flow rates limits the ability of mathematical models to predict individual PDT treatment outcome *in vivo*. Nonetheless, mathematical models of PDT provide insight into the interaction among the reaction components and provide a means to interpret measurements of the system made during treatment. Hypothetically, these models could be informed with measurements of PS concentrations, blood flow rates, and hemoglobin saturation during PDT treatment, providing feedback regarding the clinical administration of laser during the treatment.

1.3.3 Mathematical Modeling of Light Propagation through Tissue

Mathematical models that describe the propagation of light through tissue are capable of simulating spectroscopic measurement of tissue by optical devices such as the OPS. This Section provides a brief outline of the light propagation models, and describes the development and utility of these models to emulate spectroscopic measurement of tissue *in silico*.

An analytical description of light transport through tissue is possible using diffusion theory [27]. This technique describes the movement of light through tissue in the direction of a decreasing 'photon concentration' gradient [27]. Diffusion theory is capable of accurately describing the spatial steady state fluence profile within a model geometry. Solutions can be achieved quickly, making this model useful in calculating the light fluence delivered during laser administration and for estimating the optical properties from measurements of some diffuse reflectance devices [18,25]. However, model predictions are not valid at short distances (~ 1 mm) from the light source and are not well-suited to describe complex geometries [106]. Therefore, diffusion theory is not applicable to the mathematical description of the OPS measurement of tissue.

Monte Carlo (MC) modeling of light transport is a commonly used technique, where the optical properties of the tissue are specified by the user and photon movements are stochastically simulated [29, 106, 107, 108, 109]. MC models originally described the movement of light throughout a homogeneous medium [106]. This structure was extended by Wang and coauthors, to describe light propagating through multilayered structures, termed MCML [107]. The MCML code was applied to the more complicated situation of tissues that

contain heterogeneous chromophore distributions [110], with highly absorbing blood localized within discrete blood vessels. Simulation of large numbers of photons provide estimates of reflectance and transmittance that approach true (empirical) photon distributions [106]. MC models can require significant computational time, but allow users to specify complicated geometries, including the incorporation of discrete objects and the specification of heterogeneous optical properties. Therefore, MC models are appropriate for simulation of the OPS measurement of tissue. Mathematical models of light transport contributed to the understanding of how discrete vessels affect the reflectance signal measured *in vivo* by optical spectroscopic devices. Discrete vessels affect the distribution of light propagation because blood (which is the dominant endogenous absorbing compound within the tissue) is localized into small volumes within the tissue. As light enters a vessel, the blood located around the vessel edge absorbs a large amount of light, effectively shielding the blood at the vessel center from light. This is shown schematically in Figure 1.4. This effect is more pronounced in the wavelength region where hemoglobin has strong absorption bands. Therefore, the light that is remitted from the tissue may have only sampled a subset of the total amount of blood within the tissue (due to the shielding effect shown in Figure 1.4). This phenomena causes the absorption coefficient estimated optically to be less than the 'true' absorption coefficient within the tissue. This phenomena was reported empirically, and termed 'pigment packaging' [20]. Theoretical analysis of this phenomena reported how the degree of pigment packaging is related to the average size of the vessels and the absorption coefficient within the vessels [110, 111, 112]. These studies suggested that a 'vessel correction factor' could be incorporated into model-based analysis of spectra to estimate the wavelength-dependent effect of pigment packaging on the absorption detected optically. Incorporation of this vessel correction factor improved the ability of the model estimates to capture features of the measured data [113]. Application of the vessel correction factor to the OPS measurement is discussed in Chapter 4.
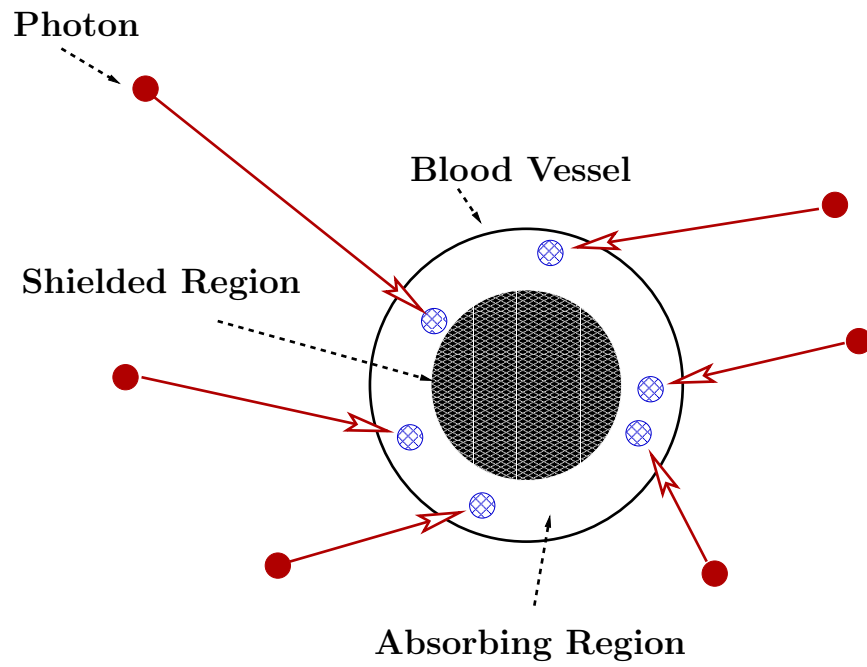
Figure 1.4: Schematic of the 'pigment packaging' effect of discrete blood vessels on diffuse light. See Section 1.3.3 for details.

1.4 DISSERTATION OVERVIEW

Chapter 2 develops an analysis method that is capable of estimating chromophore concentrations in the presence of matrix-induced wavelength-shifts in the extinction coefficient of the compound. This method is applied to OPS measurement of MGd in tissue-simulating phantoms *in vitro* and in mouse tissues *in vivo* and *in situ*.

Chapter 3 utilizes the plasma, tumor, and skin MGd concentrations measured in Chapter 2 to develop compartmental PK models that describe the dynamics of MGd disposition following intravenous administration. Models are fitted to data measured by both OPS *in vivo* and *in situ* and HPLC *ex vivo*. The temporal contribution of MGd localized in plasma, skin, and tumor to the 'total' MGd concentration measured in tumor tissue *in vivo* by the OPS is also considered.

Chapter 4 investigates necessary extensions to a previous OPS data analysis algorithm to account for effects of discrete vessels and high total absorption coefficients on absorption measured in a murine xenograft model following PDT treatment. This study utilizes an MC model of the OPS measurement of tissue *in silico* to investigate: (1) the analytical relationship between total absorption coefficient and mean photon path length; and (2) the utility of the vessel correction factor in estimating the true tissue absorption coefficient.

Chapter 5 utilizes a sequence of mathematical models to investigate the ability of the OPS to detect both chronic and acute hypoxia within tumor tissue. The model geometry mimics the tumor microvascular environment, with irregular vessel patterns and hemoglobin saturations estimated from empirically reported frequency distributions. The photodynamic reaction of PDT is simulated in tissue, and spatial changes in oxygen, hemoglobin saturation, and ROS yield are calculated. Simulations investigate how changes in oxygen supply within the vasculature and acute damage induced by PDT may affect both the progression of PDT treatment and the signal detected by the OPS.

Chapter 6 presents an overview of the contributions this dissertation makes to the fields of optical spectroscopy and photodynamic therapy. The Chapter also outlines possible extensions of the work within this dissertation to further the understanding and application of the OPS as a PDT dosimetric tool.

2.0 NONINVASIVE MEASUREMENT OF MGD BY OPS

2.1 BACKGROUND

Motexafin gadolinium (MGd) is a texaphyrin compound that has an expanded porphyrin structure containing a central Gd ion [114,115], as shown in Figure 2.1. MGd has shown the ability to localize in tumor tissue and is currently being considered as both a radiation and chemotherapy sensitizing agent [56,57,116,117,118,119,120]. A method to determine MGd concentrations in tissue noninvasively *in vivo* could allow clinicians to administer radiation treatment at a time when a positive MGd concentration gradient exists between malignant and surrounding non-malignant tissues, resulting in the destruction of the tumor and possible preservation of surrounding healthy tissues.

Mourant *et al.* [3] presented a mathematical method to calculate drug concentrations from intensity spectra collected by the OPS. The study reported a linear correlation between doxirubicin concentrations measured *in vivo* by OPS and *ex vivo* by high performance liquid chromatography (HPLC). Over an 8-fold concentration range, the slope of a line fit to the data (and forced through the origin) was 0.65 ± 0.08. The study showed promising results; however, the algorithm required *a priori* knowledge of the exact extinction coefficients for all dominant chromophores, including the drug, ϵ_{drug}. This assumption may be problematic because ϵ_{drug} is dependent upon the surrounding environment [121] and, for novel compounds, may not be well-characterized *in vivo*. A mismatch between the ϵ_{drug} specified and the ϵ_{drug} that is expressed in the *in vivo* environment can result in the introduction of bias into estimated concentrations.

The work presented in this Chapter extends the previous data-analysis algorithm to calculate changes in MGd absorbance from measured light intensity spectra, while allow-

ing empirical determination of ϵ_{drug}. The magnitude of MGd absorbance is quantitated by integration of the MGd peak absorbance area, and MGd concentrations are estimated by comparison with standard curves generated using HPLC, an independent measure of concentration. The work presented in this Chapter has been published in the Journal of Photochemistry and Photobiology B: Biology [122].

2.2 MATERIALS AND EXPERIMENTAL METHODS

All of the experimental work presented in this Chapter was conducted by Julie Eiseman, Jainxia Guo, and Erin Joseph at the University of Pittsburgh Cancer Institute.

2.2.1 Drugs and Reagents

Motexafin gadolinium (MGd, XCYTRIN®, NSC 695238) and motexafin lutetium, HPLC internal standard, (MLu, NSC 695239) were provided by Pharmacyclics (Sunnyvale, CA) through the NCI CTEP (Rockville, MD). Intralipid® 10% was purchased from Fresenius Kabi Clayton, L.P. (Clayton, NC). Sterile water and heparin were purchased from Baxter Healthcare Corp. (Deerfield, IL). RPMI-1640 Medium with L-glutamine was purchased from Combrex Bio Science Walkersville (Walkersville, MD). Gentamicin and trypsin 10X were purchased from Invitrogen, Gibco (Grand Island, NY). Fetal bovine serum (heat inactivated) and phosphate buffered saline (pH 7.4, without calcium or magnesium) were purchased from Invitrogen, Biosource (Camarillo, CA). Methoxyflurane was purchased from Medical Developments (Springvale, Australia). Ammonium acetate was purchased from EM Science (Cherry Hill, NJ). Acetonitrile was purchased from Alfa Aesar (Ward Hill, MD). Methanol was purchased from EMD Chemicals (Gibbstown, NJ). Nitrogen and carbon dioxide were purchased from Valley National Gases Inc. (West Mifflin, PA).
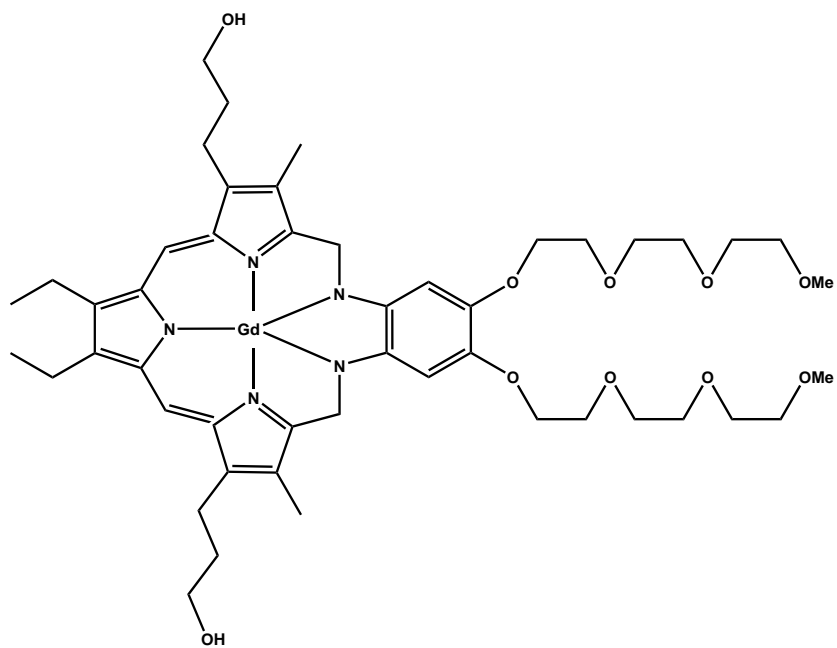
Figure 2.1: Chemical structure of MGd.

2.2.2   Experimental Methods

2.2.3   *In vitro* Tissue-Phantom Preparation

MGd was added to 1% Intralipid® in sterile water to attain concentrations of 0.03, 0.1, 0.3, 1, 3, 10, 30, and 100 μM; a blank (0 μM) was represented by 1% Intralipid®. These samples were prepared in duplicate and 200 μL of each solution were pipetted into separate wells of 96-well culture plates. Prior to OPS readings, the plate was placed on a black background to prevent light reflection from the bottom of the wells. During sample preparation and subsequent measurement, overhead fluorescent lights were turned off to prevent activation of MGd.

2.2.4   OPS Instrumentation

The illumination light source was a pulsed xenon short-arc lamp (model FX-1160 with driver model LS-1130, Perkin Elmer, Wellesley, MA), driven as a pulse burst (ranging, typically, from $2-20$ pulses) during the correlated integration time ($10-100$ msec) of the linear-array CCD detector, which is built into the spectrometer (model S2000, Ocean Optics, Dunedin, FL). The total optical energy incident on the tissue is less than 1 mJ. Light is delivered to the tissue and collected from the tissue using silica optical fibers. The source and detector fiber-core diameters are 400 and 200 μM, respectively. The center-to-center separation of the fibers was 1.5 mm.

2.2.5   Measurement Method

The OPS was initialized with the following values: number of pulses $= 4$; and integration time $= 20$ msec. To account for the total system response (*i.e.*, the wavelength dependence of the light source, fibers, grating and detector array, couplers, etc.), a reference measurement of reflectance from a spectrally-flat diffuse reflector (Spectralon, Labsphere Inc., North Sutton, NH) was made once at the beginning of a procedure prior to all other measurements. OPS measurements *in vitro* were recorded in triplicate and made by placing the probe in the center of each well, with the tip just breaking the fluid meniscus. The probe tip was cleaned with

ethanol:water (70 : 30, v/v) between measurements of each well to prevent sample mixing. OPS measurement sites *in vivo* and *in situ* were located by finding areas not directly adjacent to visible blood vessels, and gently placing the probe into contact with the tissue surface. Triplicate collected light spectra were recorded on all measured sites.

2.2.6 HPLC Sample Preparation

The methods used were a modification of those published by Parise *et al.* [123]. Tissues were homogenized in 3-to-5 volumes of phosphate-buffered saline. To plasma or tissue homogenates (250 μL), 10 μL of MLu (25 μM) was added. After vortexing for approximately 10 sec, 1 mL of acetonitrile:methanol (1:1, v/v) was added to precipitate proteins. Following protein precipitation, the sample was vortexed again and centrifuged (10 min, 12,000 $\times$ g, room temperature). The resulting supernatant was decanted into glass tubes and evaporated to dryness under a gentle stream of nitrogen at 40°C. The dried residue was reconstituted in 300 μL of mobile phase of 100 mM ammonium acetate (adjusted to pH 4.3 with glacial acetic acid):acetonitrile:methanol (59 : 21 : 20, v/v/v). The clear supernatant was transferred to an autosampler vial, and 100 μL was injected onto the HPLC system. All standards for HPLC analysis were prepared in the appropriate biological matrix and processed in the same way as the plasma and tissue samples before being injected onto the HPLC system. For preparation of standards, 20 μL of MGd and 10 μL MLu was added to each tube containing 250 μL of matrix such that the final MGd concentrations were 0.03, 0.1, 0.3, 1, 3, 10, 30, and 100 μM.

2.2.7 HPLC Instrumentation

The Beckman HPLC (Beckman Coulter, Fullerton, CA) Programmable Gradient System consisted of a model 508 Autosampler, model 128 gradient solvent delivery module, and a model 166 UV detector module. MGd and MLu were separated on a Zorbax Eclipse XDB-C 18 (3.5 μm, 3.0 x 150 mm) column (Agilent Technologies, Palo Alto, CA) fitted with a Brownlee C18 guard column (PerkinElmer, Boston, MA). A model LC-22A temperature controller column heater (Bioanalytical Systems Inc., W. Lafayette, IN) was used to maintain the column temperature at 55° C. The isocratic mobile phase was pumped at 0.6 ml/min.

Column eluent was monitored at 470 nm. Under these conditions, the retention times of MGd and MLu were approximately 18 and 22 min, respectively. The LLQ was determined as 0.03 μM, and the assay was linear over the range examined, with similar variability ($\leq 15\%$) at low, medium and high concentrations.

2.2.8 Animals

C.B-17 SCID female mice ($4 - 6$ weeks of age and specific pathogen-free) were purchased from Taconic Farms (Germantown, NY) and handled in accordance with the Guide For the Care and Use of Laboratory Animals [124] and on a protocol approved by the Institutional Animal Care and Use Committee of the University of Pittsburgh. Mice were allowed one week for acclimation to the animal facility before studies were initiated. Mice were housed in sterile microisolator caging to minimize exogenous infections. Ventilation and air flow in the animal facility were set to a minimum of 12 changes per hour. Room temperature was regulated at 72 ± 2^oF, humidity was held between 30 and 70%, and the room was kept on a 12 hr light/dark cycle. Mice received Prolab ISOPRO RMH 3000, Irradiated Lab Diet (PMI Nutrition International, Brentwood, MO) and sterile water *ad libitum*. On the day prior to the study, food was removed at approximately 6 PM and withheld until 4 hr after dosing on the next day. Sentinel mice, housed in 20% dirty bedding from study mice, remained murine antibody profile-negative using Assessment + (Charles River Laboratories, Wilmington, MA), indicating that the study mice were pathogen-free.

2.2.9 Tumor Cell Line

MDA-MB-231 human breast cancer cells were obtained from ATCC (Manassas, VA) and expanded in culture in RPMI 1640 medium containing L-glutamine supplemented with 10% heat inactivated fetal bovine serum and 10 μL/mL gentamicin. Cells were maintained at 37°C in an incubator with atmosphere composed of 95% room air and 5% CO_2 at 95% humidity. Cells in log phase growth were harvested using trypsin, washed with media and resuspended at 1×10^8 cells/ml. Then 0.1 mL of the suspension was injected subcutaneously

into the right flanks of passage SCID mice. Tumor volumes were calculated twice weekly using the formula:

$$V_{Tumor} = \frac{lw^2}{2}$$

Where V_{Tumor} is tumor volume (mm^3), l (mm) is the length of the longest diameter of the tumor, and w (mm) is the length of the diameter perpendicular to l. When tumors in the passage mice reached $500 - 1000$ mm^3, the mice were euthanized and tumors were removed using sterile techniques. Tumors were cut into approximately 25 mg fragments, study mice were anesthetized with methoxyflurane in a vented laminar air flow hood, and the fragments subcutaneously implanted using sterile techniques. When tumor volumes in the study mice were greater than 100 mm^3 (range: $0.1 - 0.2$ g), study mice were stratified into groups (n=3) by body weight and tumor volume so that all groups were similar based on ANOVA (Minitab, State College, PA). On the day before the study, mice were anesthetized with methoxyflurane in a vented laminar air flow hood, and the skin over the tumor and on the opposite flank was shaved.

2.2.10 Dosing

MGd was administered to mice at a dose of 23 mg/kg (0.01 ml/g fasted body weight) by bolus lateral tail vein injection. Vehicle-treated mice received 0.9% saline (0.01 ml/g fasted body weight).

2.2.11 Sampling

Two min before the scheduled euthanasia time, the mice were gently restrained by hand and triplicate OPS measurements (termed *in vivo* measurements) were made on the skin over the subcutaneous (s.c.) tumor and on the skin site on the opposite flank. Immediately thereafter, three mice per time point were euthanized with CO_2 and blood was collected by cardiac puncture using heparinized syringes. The time points of euthanasia were: 5, 15, 30, 60, 120, 240, 420, 960, and 1440 min after MGd administration and 5 min after vehicle administration. Blood was transferred to microcentrifuge tubes and placed on ice until it was

centrifuged at $13000 \times$ g for 4 min to separate the plasma from the packed red blood cells. After exsanguination and prior to removal of the tissues, triplicate OPS measurements were made on the ventral surfaces of the following tissues (termed *in situ* measurements): liver (right medial lobe), right kidney, lungs, heart, spleen, brain, fat, skeletal muscle, tumor and opposite flank skin. It should be noted that low scattering prevented OPS measurement of plasma samples. Following the triplicate measurements, the tissues were removed, weighed, and snap frozen in liquid N_2 (approximately 2 min following OPS measurements). All tissues, plasma, and packed blood cells were stored at -70^oC until HPLC analysis (termed *ex vivo* measurements).

2.3 DATA ANALYSIS

2.3.1 OPS Measurement Theory

The OPS records the intensity of collected light that has been elastically-scattered throughout a sample (*e.g.*, Intralipid® solution, or tissue). For a single OPS measurement, the Beer-Lambert law applies as follows:

$$I\left(\lambda\right) = I_{incident}\left(\lambda\right) e^{-\mu_a^{total}(\lambda)\langle L\rangle\left(\mu_a^{total}(\lambda)\right)+G} \tag{2.1}$$

Here, λ is the wavelength, $I\left(\lambda\right)$ is the collected light intensity, $I_{incident}\left(\lambda\right)$ is the intensity of incident light entering the sample, $\mu_a^{total}\left(\lambda\right)$ is the total molar absorption coefficient, $\langle L\rangle\left(\mu_a^{total}\left(\lambda\right)\right)$ is the effective photon path length (which is a function of the total molar absorption coefficient), and G is a geometry-dependent factor that accounts for light lost due to scattering. It should be noted that while the collected light intensity is affected by changes in scattering properties, the path length is insensitive to these changes [28]. Here, $\mu_a^{total}\left(\lambda\right)$ is calculated as the summation of contributions from individual chromophores:

$$\mu_a^{total}\left(\lambda\right) = \sum_{i=1}^{k} \epsilon_i\left(\lambda\right) C_i \tag{2.2}$$

Here, $\epsilon_i(\lambda)$ and C_i are the molar extinction coefficient and concentration of chromophore i, respectively, and k is the total number of chromophores.

Equation (2.1) can be used to represent measurements of a sample before (at time t_o) and after the addition of a chromophore, such as a drug (at t). Changes in the collected light due to the addition of the drug can be evaluated using the ratio of the expressions at t and t_o, as follows:

$$\frac{\frac{I(\lambda,t)}{I_{incident}(\lambda,t)}}{\frac{I(\lambda,t_o)}{I_{incident}(\lambda,t_o)}} = \frac{e^{-\mu_a^{total}(\lambda,t)\langle L\rangle\left(\mu_a^{total}(\lambda,t)\right)+G}}{e^{-\mu_a^{total}(\lambda,t_o)\langle L\rangle\left(\mu_a^{total}(\lambda,t_o)\right)+G}} \tag{2.3}$$

Assuming that there are no changes in the incident intensity and that scattering properties do not change significantly between animals, Equation (2.3) reduces to:

$$\frac{I(\lambda,t)}{I(\lambda,t_o)} = e^{-\mu_a^{total}(\lambda,t)\langle L\rangle\left(\mu_a^{total}(\lambda,t)\right)+\mu_a^{total}(\lambda,t_o)\langle L\rangle\left(\mu_a^{total}(\lambda,t_o)\right)} \tag{2.4}$$

It is important to note that $\langle L\rangle\left(\mu_a^{total}(\lambda,t)\right)$ decreases as the total absorption coefficient increases [125]. This phenomenon is a result of photons with long path lengths having a higher probability of undergoing absorption events than those with short path lengths. Accordingly, photons with long path lengths are collected less often than photons with short path lengths, resulting in the reduction of the effective mean path length of collected photons. Therefore, the addition of a chromophore, yielding $\mu_a^{total}(\lambda,t_o) < \mu_a^{total}(\lambda,t)$, decreases the effective path length, with $\langle L\rangle\left(\mu_a^{total}(\lambda,t_o)\right)$ greater than $\langle L\rangle\left(\mu_a^{total}(\lambda,t)\right)$. This relationship can be described by the introduction of a scaling factor, $0 < \delta_L\left(\mu_a^{total}(\lambda,t)\right) \leq 1$, which relates the difference between the path lengths as follows:

$$\langle L\rangle\left(\mu_a^{total}(\lambda,t)\right) = \delta_L\left(\mu_a^{total}(\lambda,t)\right)\langle L\rangle\left(\mu_a^{total}(\lambda,t_o)\right) \tag{2.5}$$

Here, $\delta_L\left(\mu_a^{total}(\lambda,t)\right)$ decreases as $\mu_a^{total}(\lambda,t)$ increases. Substitution of Equation (2.5) into Equation (2.4) yields:

$$\frac{I(\lambda,t)}{I(\lambda,t_o)} = e^{-\mu_a^{total}(\lambda,t)\delta_L\left(\mu_a^{total}(\lambda,t)\right)\langle L\rangle\left(\mu_a^{total}(\lambda,t_o)\right)+\mu_a^{total}(\lambda,t_o)\langle L\rangle\left(\mu_a^{total}(\lambda,t_o)\right)} \tag{2.6}$$

Next, an effective change in absorption is introduced as:

$$\Delta\mu_a'(\lambda,t) = \mu_a^{total}(\lambda,t)\,\delta_L\left(\mu_a^{total}(\lambda,t)\right) - \mu_a^{total}(\lambda,t_o) \tag{2.7}$$

33

Note that $\Delta\mu'_a(\lambda, t)$ is not linearly related to changes in $\mu_a^{total}(\lambda, t)$ because $\langle L \rangle \left(\mu_a^{total}(\lambda, t) \right)$ is not constant between t_o and t. Substitution of $\Delta\mu'_a(\lambda, t)$ into Equation (2.6) yields:

$$\frac{I(\lambda, t)}{I(\lambda, t_o)} = e^{-\Delta\mu'_a(\lambda, t)\langle L \rangle \left(\mu_a^{total}(\lambda, t_o) \right)} \tag{2.8}$$

Solving Equation (2.8) for $\Delta\mu'_a(\lambda, t)$ yields:

$$\Delta\mu'_a(\lambda, t) = -\ln\left(\frac{I(\lambda, t)}{I(\lambda, t_o)} \right) \left[\langle L \rangle \left(\mu_a^{total}(\lambda, t_o) \right) \right]^{-1} \tag{2.9}$$

Here, $\langle L \rangle \left(\mu_a^{total}(\lambda, t_o) \right)$ is a constant, but it is not known *a priori*, preventing explicit calculation of $\Delta\mu'_a(\lambda, t)$. However, $\Delta\mu'_a(\lambda, t)$ is linearly related to absorbance, $A(\lambda, t)$, which is:

$$A(\lambda, t) = -\ln\left(\frac{I(\lambda, t)}{I(\lambda, t_o)} \right) \tag{2.10}$$

Changes in MGd absorbance can be quantitated by integrating the peak area of the MGd absorbance band within $A(\lambda, t)$, and standard curves are constructed to relate MGd peak absorbance area to MGd concentration, C_{MGd} (see Section 2.3.5).

2.3.2 Deconvolution of MGd and Hemoglobin Absorbance

In tissues, $\mu_a^{total}(\lambda, t)$ is composed of contributions from exogenous MGd and endogenous compounds such as hemoglobin, which exists in both the oxygenated (HbO_2) and the deoxygenated (Hb) state. Changes in the total absorption between t_o and t can be given as:

$$\Delta\mu_a^{total}(\lambda, t) = \epsilon_{MGd}(\lambda)\, \Delta C_{MGd}(t) + \epsilon_{Hb}(\lambda)\, \Delta C_{Hb}(t) + \epsilon_{HbO_2}(\lambda)\, \Delta C_{HbO_2}(t) \tag{2.11}$$

Here, $\Delta C_i(t) = C_i(t) - C_i(t_o)$ are the changes in the concentrations of $i = \{MGd, Hb, HbO_2\}$, respectively. This assumes that the contribution of other endogenous chromophores do not contribute significantly to $\Delta\mu_a^{total}(\lambda, t)$ (*i.e.*, their concentrations do not change significantly over the course of the study) [126]. Figure 1.1 shows $\epsilon_{Hb}(\lambda)$ and $\epsilon_{HbO_2}(\lambda)$ in stroma-free hemoglobin solutions prepared from erythrocyte suspensions in saline solution, as reported by Zijlstra *et al.* [2]. These profiles are representative of absorbance bands *in vivo* in the

range of wavelengths we have considered [127]. Inspection of these curves shows absorption maxima between $520 - 630$ nm and a minor peak located near 760 nm. These bands overlap with the MGd absorbance bands, which are dominant between $650 - 790$ nm, as shown in Figure 2.2. Because of this overlap, changes in C_{Hb} and C_{HbO_2} could affect the integrated MGd peak absorbance area

The method developed here requires that MGd be the primary contributor to absorption over the wavelength range of interest. It should be noted that by taking the ratio of collected light intensities at t and t_o, the calculation accounts for the concentrations of hemoglobin and other endogenous absorbers that are present in the pre-drug measurement (at t_o), and therefore, the only contributions of endogenous chromophores to the absorbance are due to changes in their concentrations between t_o and t. It was a concern that $\Delta C_{Hb}(t)$ and $\Delta C_{HbO_2}(t)$ affect to $A(\lambda, t)$ and may affect the calculated MGd peak absorbance, so their contribution was estimated and removed. In order to do this, the method assumes that changes in $C_{Hb}(t)$ and $C_{HbO_2}(t)$ between t_o and t have a negligible effect on the photon path length (the impact of this assumption is addressed in the Section 2.5). Using this assumption, $A(\lambda, t)$ can be represented by a combination of absorbance due to MGd, which is termed $A_{MGd}(\lambda, t)$, and changes in hemoglobin oxygenation states, which is termed $A_{\Delta Hb}(\lambda, t)$. Here, $A(\lambda, t)$ can be represented as,

$$A(\lambda, t) = A_{MGd}(\lambda, t) + A_{\Delta Hb}(\lambda, t) \qquad (2.12)$$

where $A_{\Delta Hb}(\lambda, t)$ is approximated by:

$$A_{\Delta Hb}(\lambda, t) = \epsilon_{Hb}(\lambda)\zeta_1 + \epsilon_{HbO_2}(\lambda)\zeta_2 \qquad (2.13)$$

It is important to note that ζ_1 and ζ_2 do not provide information about the concentrations of total hemoglobin or oxygenation states because these would require knowledge of $C_{Hb}(t_o)$ and $C_{HbO_2}(t_o)$ and the relationship between hemoglobin concentration and $A_{\Delta Hb}(\lambda, t)$. In Equation (2.13), ζ_1 and ζ_2 represent the component of $A(\lambda, t)$ that is attributable to changes in $C_{Hb}(t)$ and $C_{HbO_2}(t)$ between t_o and t. Values for ζ_1 and ζ_2 were estimated over 520-620 nm, a wavelength range containing information about Hb oxygenation without confounding

effects from MGd. The values were calculated using Equation (2.13) within a generalized least-squares problem that is solvable analytically [128].

Next, $A_{\Delta Hb}(\lambda, t)$ was evaluated over $500 - 800$ nm, and its contribution to absorbance was subtracted from $A(\lambda, t)$, such that the remaining absorbance is attributed to MGd, and is calculated as:

$$A_{MGd}(\lambda, t) = A(\lambda, t) - A_{\Delta Hb}(\lambda, t) \tag{2.14}$$

It should be noted that this calculation was performed for spectra measured in tissues. For spectra measured in tissue-simulating phantoms, the absorbance area was entirely attributable to MGd, as:

$$A_{MGd}(\lambda, t) = A(\lambda, t) \tag{2.15}$$

2.3.3 MGd Peak Absorbance Area Calculation

MGd absorbance was calculated by integrating the MGd peak area between $A_{MGd}(\lambda, t)$ and a linear baseline over the wavelength range: $650 - 790$ nm. In order to decrease the sensitivity of the integrated area to the baseline endpoint values, the endpoints were selected as an average of 15 data points (approximately 5.4 nm) on $A_{MGd}(\lambda, t)$ centered about 650 and 790 nm, respectively. The baseline serves two purposes: first, it compensates for underlying trends in $A_{MGd}(\lambda, t)$ attributable to differences in scattering properties between OPS measurements at t_o and t. [3]; second, the baseline is constructed individually for each $A_{MGd}(\lambda, t)$ spectra, thus normalizing for differences in absolute collected intensities. For each type of sample measured (well-plate or tissue), the intensity spectra at t was ratio-ed to a mean intensity spectra calculated at t_o, as in Equation (2.8). MATLAB (V.70.0.19901 R.14 ©2006, The Mathworks, Natick, MA) code was scripted to integrate the MGd peak absorbance area numerically using the modified Simpson's Rule:

$$
\mathcal{A}(t) = \Delta\lambda \left[\frac{5}{12} A_{MGd}(\lambda(1), t) + \frac{13}{12} A_{MGd}(\lambda(2), t) + \left(\sum_{i=3}^{N-2} A_{MGd}(\lambda(i), t) \right) \cdots \right.
$$
$$
\left. \cdots \qquad + \frac{13}{12} A_{MGd}(\lambda(N-1), t) + \frac{5}{12} A_{MGd}(\lambda(N), t) \right] \tag{2.16}
$$

Here, N represents the number of measurement points along the wavelength axis between $650 - 790$ nm.

2.3.4 Noise Reduction Techniques

In order to remove the contribution of random noise in intensity spectra to peak absorbance area, a boxcar filter was applied to $A(\lambda, t)$ (absorbance prior to hemoglobin deconvolution). Each point was evaluated as the average of the surrounding 15 data points (approximately 5.4 nm), a boxcar width that was less than 4% of the MGd peak width. Post-filtering noise in $A(\lambda, t)$ was quantitated by integrating peak absorbance at t_o, $\mathcal{A}_{noise} = \mathcal{A}(t_o)$. The $\mathcal{A}_{noise}$ was calculated for each tissue individually and used to identify the OPS lower limit of detection (LLD), which was set equal to the mean of the noise areas plus one standard deviation ($LLD = \mathcal{A}_{noise} + \sigma_{noise}$). Prior to construction of standard curves, all $\mathcal{A}(t)$ values were decreased by $\mathcal{A}_{noise}$, correcting for the noise contribution to the peak absorbance area.

2.3.5 OPS Standard Curve Construction

Empirically, the relationship between $\mathcal{A}(t)$ and MGd concentration measured by HPLC, $C_{MGd}^{HPLC}(t)$, was determined to be a power law function. This relationship is consistent with Equation (2.6). The functionality represents a decreased differential increase of "effective" absorbance in response to increases in $\mu_a^{total}(\lambda, t)$ due to a decrease in photon path length. In the expression:

$$\mathcal{A}(t) = x\left[C_{MGd}^{HPLC}(t)\right]^y \tag{2.17}$$

the power law coefficients (x and y) were calculated as follows: (1) $\mathcal{A}(t)$ and $C_{MGd}^{HPLC}(t)$ were paired per mouse subject; (2) $\mathcal{A}(t)$ values were weighted; and (3) x and y were calculated by minimizing the sum-squared error between the regressed model and data. The weighting scheme was either $\frac{1}{\sigma^2}$, or for data showing heteroschedastic characteristics, $\frac{\overline{\mathcal{A}}}{\sigma}$ (where $\overline{\mathcal{A}}$ is the mean absorbance area and σ is the standard deviation of the absorbance for each measured concentration). Standard curves were generated individually for each type of

37

sample measured (*e.g.*, tissue-simulating phantoms *in vitro*, and in the tissue-matrix *in vivo* and *in situ*).

The goodness-of-fit of model predictions are quantified by the Pearson correlation coefficient (r). This value shows the strength of the correlation between two variables (*e.g.*, X and Y), and is calculated as follows [129]:

$$r = \frac{n_{meas} \sum X_i X_i - \sum X_i \sum Y_i}{\sqrt{n_{meas} \sum X_i^2 - \left(\sum X_i\right)^2} \sqrt{n_{meas} \sum Y_i^2 - \left(\sum Y_i\right)^2}} \tag{2.18}$$

Here, n_{meas} is the number of measurements. r values range between 0 (no correlation) and 1 (perfect correlation). The square of this value, r^2, is often used to quantitate how the model describes the variability present in the data set. It should be noted that a 'weighted' r is calculated after the parameters X and/or Y are multiplied by a weighting factor, as described above.

2.4 RESULTS

This study evaluated the capability of the OPS to quantitate MGd in Intralipid® tissue-simulating phantoms *in vitro* and in the tissue-matrix both *in vivo* (noninvasively) and *in situ* (nondestructively). Standard curves were generated to relate $\mathcal{A}$ with C_{MGd}^{HPLC}. These standard curves were used to estimate C_{MGd}^{OPS}, which was expected to equal C_{MGd}^{HPLC}, such that a line fit to subject-paired C_{MGd}^{OPS} versus C_{MGd}^{HPLC} data (and forced through zero) would have a slope of unity. The value of this slope was used to assess the accuracy of C_{MGd}^{OPS}, assuming the value of C_{MGd}^{HPLC} to be the accepted 'gold standard' [123].

2.4.1 *In vitro* Studies in Tissue-Simulating Phantoms

Figure 2.2 shows mean $A\left(\lambda\right)$ data from OPS measurements of MGd in 1%Intralipid® tissue-simulating phantoms. The absorbance has been normalized by dividing by the known concentration. No additional peaks emerge in the absorption spectra, confirming that there is no change in the extinction coefficient due to aggregation. No confounding absorbers were

present, such that $A_{MGd}(\lambda) = A(\lambda)$, and the magnitude of absorbance bands between 650 and 790 increase with increased C_{MGd}. Here, the increase in C_{MGd} resulted in a linearly proportional increase in $A(\lambda)$. This agrees with the data in Figure 2.3, which shows a near-linear relationship over the $3 - 30~\mu$M concentration range.

Figure 2.3 shown a representative Intralipid® standard curve. The standard curves were reproducible, with less that 20% area variability observed on repeat measurements performed on separate days for all concentrations examined. Back-calculated C_{MGd}^{OPS} estimates were well-correlated with C_{MGd}^{HPLC}, such that the slope of the C_{MGd}^{OPS} versus C_{MGd}^{HPLC} regression line achieved a slope near unity (slope $= 0.997$, $r^2 = 0.999$). This indicates that the OPS can accurately quantitate MGd in 1% Intralipid® tissue-simulating phantoms.

2.4.2   *In vivo* and *in situ* Studies in Mouse Tissues

Table 2.1 contains $\mathcal{A}(t)$ data per subject for:*in vivo* and *in situ* OPS measurements of tumor and skin, and Table 2.2 contains data from *in situ* measurements of skeletal muscle, fat, kidney, heart, lung, and liver. It should be noted that there was no difference between absorbance areas calculated with and without the deconvolution of hemoglobin absorbance (data not shown), and the values reported here are not corrected for hemoglobin absorbance.

Table 2.3 contains C_{MGd}^{HPLC} data for plasma, tumor, skin, skeletal muscle, fat, kidney, heart, lung, liver, and lung for each mouse at each time point. Table 2.4 contains OPS standard curve coefficients from subject-paired tissue matrix data that show significant variability among tissues. Table 2.5 contains the slopes of a line fit (forced through zero) to subject-paired C_{MGd}^{OPS} versus C_{MGd}^{HPLC} data from both Intralipid® and tissue standard curves.

2.4.2.1   Tumor and Skin   Figure 2.4(Top) shows collected light intensity spectra from OPS measurements on skin of the normal flank *in vivo*, taken before and 15 min after an i.v. MGd dose (curve is the mean of three measurements). Differences between the spectra are due to changes in the absorption of hemoglobin $(500 - 620$ nm) and MGd $(650 - 790$ nm). Figure 2.4(Bottom) shows $A_{MGd}(\lambda)$ and $A(\lambda)$ calculated from one of the intensity measurements at 15 min after dosing. Over the wavelength range $650 - 790$ nm, there
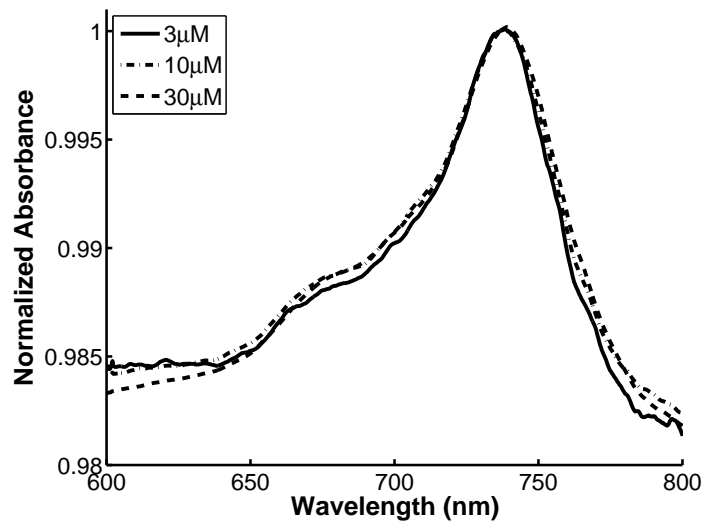
Figure 2.2: Absorbance of MGd, normalized to concentration, detected by the OPS in tissue-simulating phantoms (MGd dilution in 1% Intralipid®, curves are the means of 6 measurements per concentration).
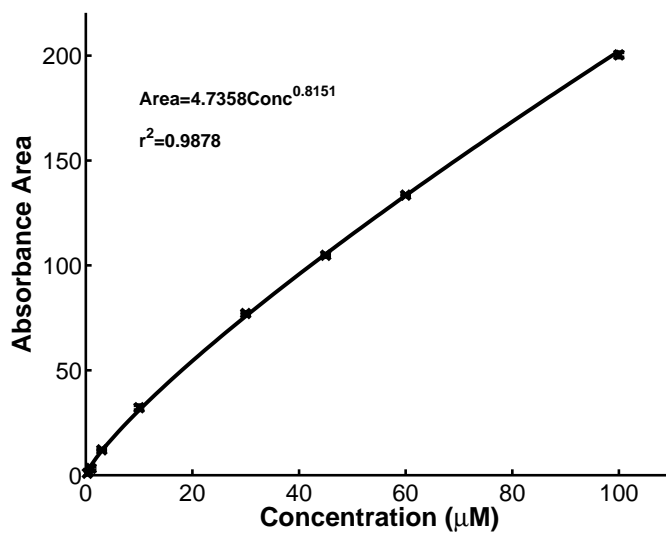
Figure 2.3: Standard curve relating OPS-determined absorbance area to HPLC-measured concentration from tissue-simulating phantom *in vitro* (1%Intralipid®).

is no difference between the corrected and uncorrected absorbance curves. All absorbance attributable to hemoglobin was located $\leq$ 650 nm. This result was similar for all other tissues *in vivo* and *in situ*, and therefore, only the uncorrected absorbance areas are reported in Tables 2.1 and 2.2.

Figure 2.5 shows the mean $\mathcal{A}(t)$ versus time data from s.c. tumor measured both *in vivo* and *in situ*. Between $5 \leq t < 120$ min, $\mathcal{A}(t)$ calculated from the *in vivo* measurements are greater than the corresponding *in situ* measurements. Plasma C_{MGd}^{HPLC} values are elevated over this time range, as shown in the Figure inset. These observations support a hypothesis that OPS measurements of tissues *in vivo* detect MGd present in both the tissue and the blood perfusing the tissue. At the early time points ($5 \leq t < 120$ min) MGd within the blood contributes to the absorbance area, while at later time points ($120 \leq t \leq 1440$ min) the absorbance area is representative of MGd present in the tissue. C_{MGd}^{OPS} values were calculated using the Intralipid® standard curve. Table 2.5 shows the comparison of C_{MGd}^{OPS} with C_{MGd}^{HPLC} between $120 \leq t \leq 1440$ min. For OPS measurements of tumor *in situ*, C_{MGd}^{OPS} values were compared with C_{MGd}^{HPLC} values over $5 \leq t < 1440$ min, because both measurements were made after exsanguination and represented tissue-localized MGd (Table 2.5). Concentration comparisons based on an Intralipid® standard curve yielded slope values below unity, with high error in the regression estimate as shown by the relatively low weighted r^2 values. To address the source of this error, C_{MGd}^{OPS} values were estimated using a standard curve from the subject-paired $\mathcal{A}(t)$ and C_{MGd}^{HPLC} data for measurements in the tissue-specific matrix. Figure 2.6 shows the OPS standard curve for tumor from tissue-matrix measurements *in vivo*, constructed using data over the $120 \leq t \leq 1440$ min time range. Using the this standard curve, the C_{MGd}^{OPS} versus C_{MGd}^{HPLC} slope was closer to unity (slope = 0.900), but outliers affected the overall fit. Appendix B contains the plots of each absorbance spectra (for all sampled times) measured in tumor *in vivo* by the OPS and shows the linear baseline used to integrate the MGd peak absorbance area.

Figure 2.7(Top) shows estimated C_{MGd}^{OPS} from OPS measurements of tumor *in vivo* and C_{MGd}^{HPLC} in tumor tissues over all time points sampled. As expected, C_{MGd}^{OPS} is greater than C_{MGd}^{HPLC} over $5 \leq t < 120$ min, and C_{MGd}^{OPS} is approximately equal to C_{MGd}^{HPLC} over $120 \leq t \leq 1440$ min. For OPS measurements of tumor *in situ*, a standard curve was constructed
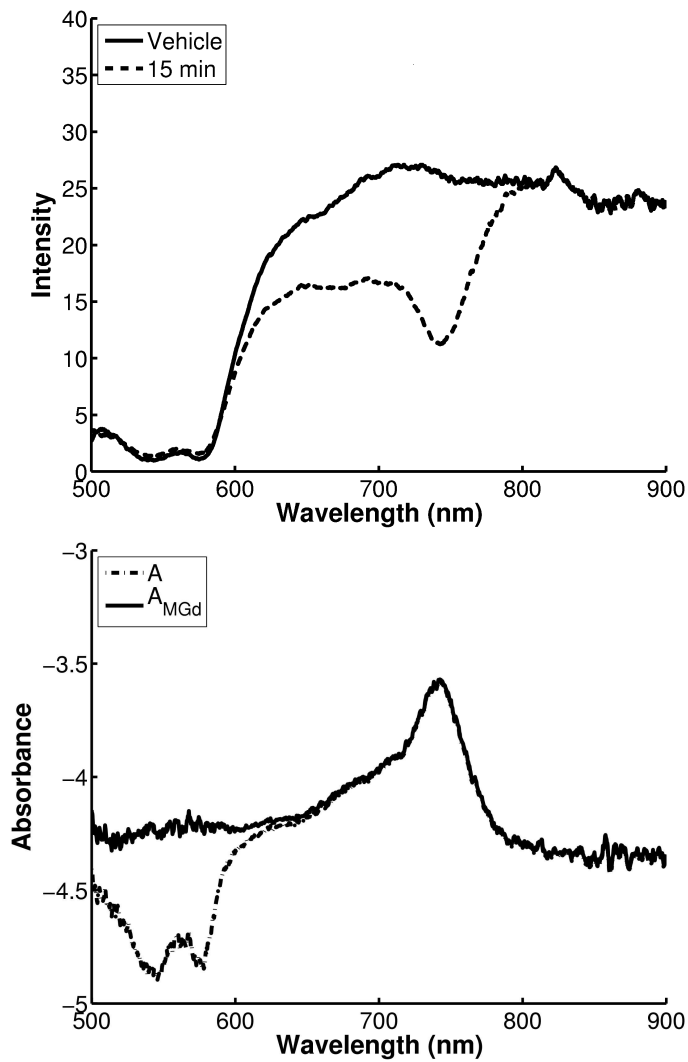
Figure 2.4: (Top) Collected light intensity profiles from OPS measurements of skin *in vivo*. Curves show vehicle (no MGd) and 15-min post MGd i.v. dose, and spectra were normalized in the flat 800-850 nm range for visualization purposes. (Bottom) Absorbance curve before (A) and after (A_{MGd}) deconvolution of hemoglobin absorbance.
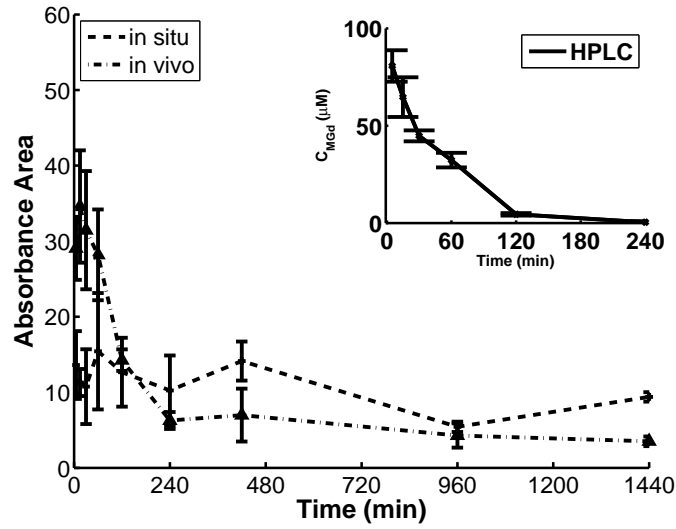
Figure 2.5: Peak absorbance area versus time from OPS measurements of tumor *in vivo* and *in situ*. Inset shows MGd concentrations in plasma measured by HPLC.
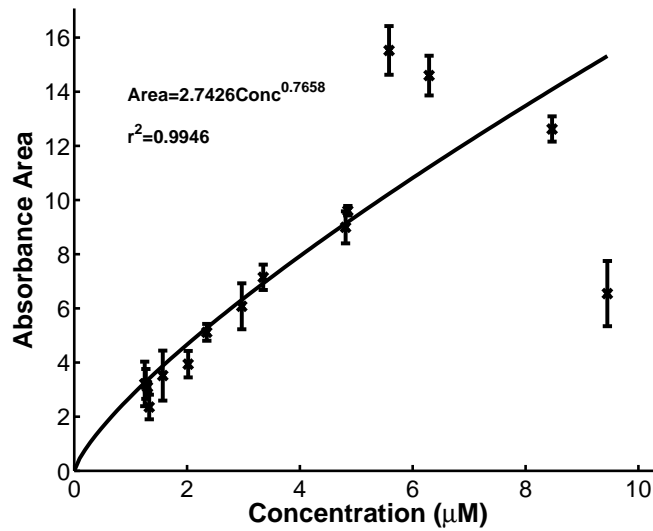
Figure 2.6: Tissue-matrix standard curve from OPS measurements of tumor *in vivo*: subject-paired absorbance area versus concentration measured by HPLC over $120 \leq t \leq 1440$. (Note: reported r^2 value is weighted.)

from tissue data (Table 2.4). Figure 2.7(Bottom) shows agreement between C_{MGd}^{OPS} and C_{MGd}^{HPLC}. These results indicate that the OPS accurately detects temporal changes in MGd concentrations in tumor tissue. In contrast, the use of the Intralipid® standard curve introduces a systematic negative-bias into the estimate of C_{MGd}^{OPS}.

MGd concentrations in the skin of the opposite flank were not detectable by HPLC after 120 min, or by OPS *in vivo* or *in situ* after 420 min. The OPS measurements of skin *in vivo* detected MGd present in multiple sources, including the skin, underlying tissues (skeletal muscle and fat), and blood perfusing those tissues. C_{MGd}^{OPS} values calculated using the Intralipid® standard curve were overestimates of C_{MGd}^{HPLC} (slope = 1.724). This results from the OPS detecting MGd in multiple sources, while the HPLC measured MGd only in skin. For the skin *in vivo* measurements, the absorbance was not attributable to MGd localized in skin, so a tissue matrix standard curve could not be constructed. For OPS measurements on the skin of the opposite flank *in situ*, the skin was removed from underlying tissue such that absorbance was attributable to skin-localized MGd. However, estimates of C_{MGd}^{OPS} in skin from the Intralipid® standard curve did not correlate well with C_{MGd}^{HPLC}, and use of a tissue matrix standard curve was not predictive (see Table 2.5).

2.4.2.2 Internal Tissues In the kidney, inspection of the intensity spectra showed dominant absorbance bands at $t \leq 15$ min, which were not present in measurements of MGd in any other tissues. Figure 2.8(Top) shows intensity spectra in the kidney at 5 and 15 min after MGd dose, with the new absorbance peak located at 775 nm. Hypothetically, these bands could indicate the presence of a metabolite, aggregation of MGd, or altered photochemical properties of MGd. $\mathcal{A}(t)$ was integrated over the expanded absorbance bands (650-810 nm) to evaluate the existence of a proportional relationship between the area of the convoluted peaks and MGd concentration. C_{MGd}^{OPS} was calculated using the Intralipid® and tissue matrix standard curves, with high variability noted between OPS and HPLC estimates (see Table 2.5). Figure 2.8(Bottom) shows qualitative and dynamic agreement between C_{MGd}^{OPS} and C_{MGd}^{HPLC} in the kidney.

In brain, neither OPS nor HPLC showed quantitatable MGd concentrations, with MGd detected by OPS at 5 min attributed to the presence of plasma in the sample; $\mathcal{A}(t)$ was $< 2\times$
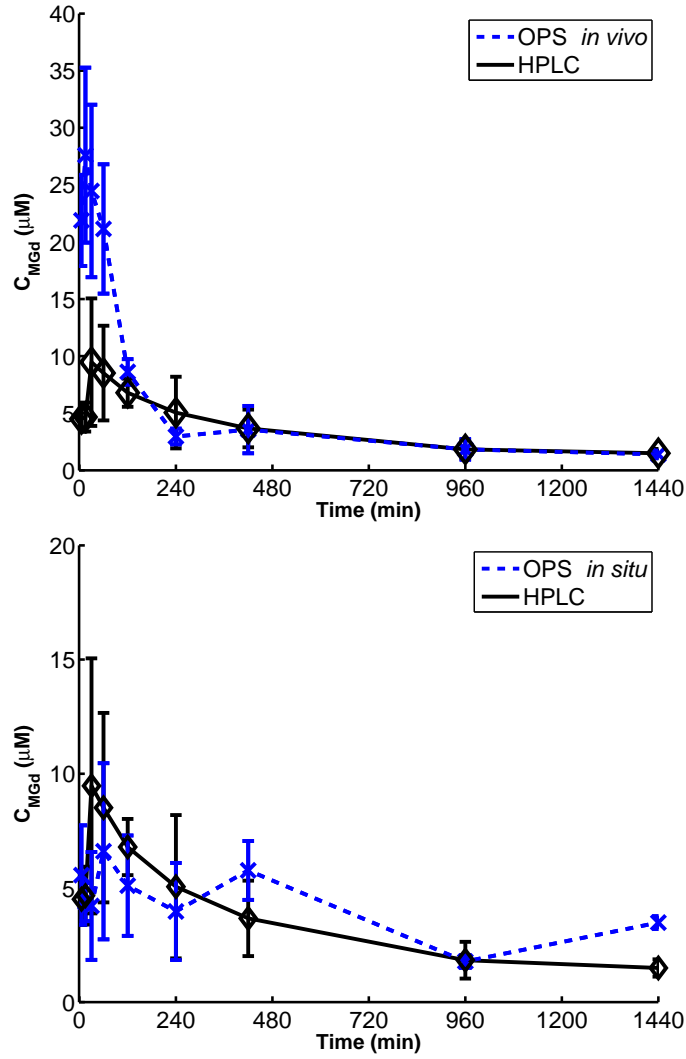
Figure 2.7: OPS estimate of tumor MGd concentration (using the tissue matrix standard curve) and HPLC measured tumor MGd concentration versus time for OPS measurements (Top) *in vivo* and (Bottom) *in situ*.

LLD after 5 min (data not shown). In skeletal muscle, MGd was undetectable after 120 min by both OPS and HPLC. In skeletal muscle and fat, individual estimates of OPS and HPLC concentrations were uncorrelated (Table 2.5), possibly complicated by low concentrations (ranges: $0.98 - 3.5 \ \mu M$ in skeletal muscle, $0.4 - 5.1 \ \mu M$ in fat) that produced low absorbance areas not far above the OPS LLD. In the heart, C_{MGd}^{OPS} estimates obtained from a tissue-matrix standard curve yielded a slope of 0.75, but the regression could not explain substantial variability in the data (Table 2.5). In the lung, there was good dynamic agreement between concentrations measured by OPS and HPLC, and individual estimates were related (Table 2.5). In the liver, $\mathcal{A}(t)$ was not representative of MGd absorbance, with a peak at 240 min, while peak concentration measured by HPLC fell between 5 and 60 min. In the spleen, only two mice (subjects 21 and 22) had repeatable absorbance areas above the LLD. Analysis in spleen was complicated by low concentrations (range: $0.02 - 6.3 \ \mu M$) and low collected light intensities (data not shown).

2.4.2.3   Selective Localization of MGd in Tumor tissues   Both the OPS and the HPLC detected selective localization of MGd in tumor tissue in comparison to local surrounding non-malignant tissues. Both OPS and HPLC detected MGd present in the tumors at 24 hr. The HPLC was unable to detect MGd in skin and skeletal muscle after 120 min, and in fat after 420 min. Ratios of C_{MGd}^{HPLC} were: tumor to skin ratio of 6.2 at 120 min, tumor to skeletal muscle ratio of 6.7 at 120 min, and tumor to fat ratios of 15.06, 12.43, and 8.43 at 120, 240, and 420 min, respectively. The OPS was unable to detect MGd in skin *in vivo* after 420 min, and in skin or skeletal muscle *in situ* (in multiple subjects per time) after 120 min and 240 min, respectively. Ratios of $\mathcal{A}(t)$ in tumor and in surrounding tissues were: tumor to skin *in situ* ratio of 2.07 at 120 min, tumor to skeletal muscle ratio of 6.37 and 6.42 at 120 min and 240 min, and tumor to fat ratios of 3.58 and 2.68 at 120 min and 240 min, respectively.
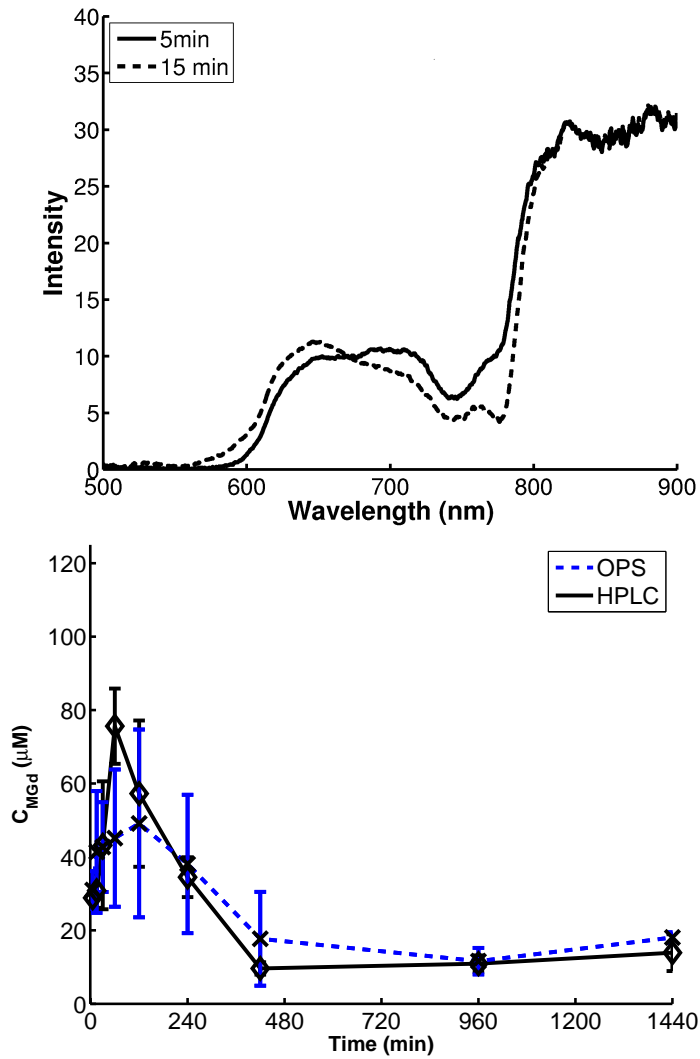
Figure 2.8: (Top) Collected light intensity profile from OPS measurement of kidney *in situ* at 5 and 15 min after MGd dose. (Bottom) OPS estimate of MGd concentration (using the tissue matrix standard curve) and HPLC measured MGd concentration versus time in the kidney.

2.5 DISCUSSION

The effectiveness of tumor treatment involving radiation-sensitizing and photo-sensitizing therapeutics depends on the concentration of the therapeutic compound within tumor and surrounding tissues at the time of irradiation [130, 89]. A method to measure concentrations of the therapeutic agent noninvasively in tissues *in vivo* would provide pharmacokinetic information about tissue-localized drug concentrations not generally available clinically due to the invasiveness of biopsies. Mourant *et al.* previously developed a method to quantitate concentrations of optically-active compounds in mouse tissues *in vivo* [3]. This paper extended the previous work by developing a mathematical method that allows the absorbance bands of an exogenous compound to be determined empirically, facilitating analysis in the presence of possible shifts due to compound-matrix interaction, and provides a means to reduce error in OPS estimates of concentration.

One motivation for the analytical method developed here is to allow the quantitation of a compound that undergoes red- or blue-shifting of the extinction coefficient *in vivo*, without the exact nature of the shift being specified *a priori*. It should be noted that the absorbance area metric makes no distinction between absorbance attributable to free drug, and absorbance attributable to drug that is either protein bound or in an aggregated state. In these scenarios, the shift in absorbance bands may reflect a change in the activity of the drug, and therefore, the absorbance area metric may not quantitate drug that contributes to treatment efficacy. In the present study, the MGd absorption spectra do not appear to undergo shifting due to protein binding or aggregation. Hence, the spectra represent MGd present as parent compound. Protein binding or drug aggregation limitations may be overcome by using the absorption spectrum of the bound or aggregated drug to remove the contributions of these components to the spectra or by selecting a wavelength range for integration that is representative of absorbance bands only attributable to the free drug. Conversely, if the absorbance bands for both free and bound/aggregated drug are well-known, the extinction coefficients could be fit using the method developed by Mourant *et al.* [3].

The algorithm developed in this Chapter required construction of a standard curve with an independent measure of drug concentration. In order for this method to become clinically

useful, absorbance area must be related to concentration by standard curves that are easily generated and validated. Ideally, standard curves would be generated from tissue-simulating phantoms *in vitro*, which do not require destructive tissue analysis. However, the results of this study suggest that $\mathcal{A}(t)$ evaluated in Intralipid® *in vitro* is not representative of the *in vivo* situation, because application of the *in vitro* standard curve biased estimates of C_{MGd}^{OPS}. For tissues that returned appreciable light in the 500-600 nm range, we noted no difference in absorbance areas if the absorbance attributable to changes in hemoglobin was deconvoluted, suggesting this is not a major source of error in this study. Background tissue absorption is one contributor to the mismatch between the *in vitro* and *in vivo* standard curves developed in this study.

The standard curve relates the absorbance area metric to concentration without requiring the calculation of changes in either absorption coefficient or path length individually, because these relationships are implicitly captured by the standard curves. This method assumes that changes in the background absorption between t_o and t due to changes in hemoglobin concentration or oxygenation do not significantly affect the photon path length, which could be a source of error because such changes would alter the relationship between absorbance area and drug concentration. The magnitude of this error was characterized for physiologically relevant ranges of hemoglobin concentration and oxygenation within tumors, as reported by Finlay *et al.* [20], with the photon path length calculated as a function of total absorption coefficient, as reported by Mourant *et al.* [3]. For changes in the total hemoglobin concentration from the mean value of 82 μM to either the lower (13.5 μM) or the upper bound (150.5 μM), the calculated change in path length was less than 10%. Changes in the oxygen saturation from the mean value of 21% to either a low (10%) or high (33%) value changed the calculated path length by approximately 1%. Therefore, if standard curves are constructed with a μ_a^{total} tailored to match the specific tissue being analyzed, changes in hemoglobin concentration or oxygenation between t and t_o are not expected to introduce significant error. It should be noted that, at present, tissue-specific phantoms neither perfectly match tissue optical properties, nor address the issue of dynamically changing background absorbers upon the introduction of exogenous chromophores. This is an area in need of future work before the OPS measurement technique can be utilized in the clinic.

The algorithm outlined in this Chapter also required that changes in absorbance in the wavelength range of interest be attributable to changes in C_{MGd}. In tissues that contained strong endogenous absorbers, identification of MGd absorbance was problematic. In the kidney, new absorption bands were observed (Figure 2.8(Bottom)), however, the total integrated area was proportional to C_{MGd}. In the liver, the absorbance area did not correlate with C_{MGd}. The C_{MGd}^{HPLC} reached a maximum value by 60 min and then began decreasing, while absorbance area gradually increased from 5 min to a maximum at 240 min. In the heart, high levels of hemoglobin absorbance were observed in the spectra, and the algorithm was unable to deconvolute MGd and hemoglobin absorbance because no appreciable light was transmitted between 500 and 600 nm. It is possible that more precise estimates of C_{MGd}^{OPS} could be attained in these tissues with complete knowledge of the convoluted absorbance bands, or with appreciable collected light intensities across the necessary wavelength ranges.

In this study, C_{MGd}^{OPS} estimates were considered accurate if the regressed slope of a line fit to subject paired C_{MGd}^{OPS} versus C_{MGd}^{HPLC} data approached unity. However, the significance of these relations was often low, with low r^2 values often reported (Table 2.5). Previous studies have reported high variability in noninvasive measurements of optically-active compounds, resulting from: (1) high inter-tumor concentration differences between subjects [89, 55]; and (2) high intra-tumor concentration gradients within tumors [131, 78, 55], possibly due to heterogeneous perfusion [132]. Specifically, Du *et al.* reported high degrees of spatial heterogeneity in the distribution of MLu within human prostate tissue, with as much as a five-fold intra-subject variation in drug concentration [55]. Therefore, it is reasonable to expect that MGd would distribute heterogeneously within tissues, which could contribute to the variability present in OPS-based estimates of MGd concentration.

Further complicating the comparison of OPS with HPLC results is the caveat that each method analyzes a different volume of the tissue. The OPS interrogates a small section of the tumor volume, with a mean sampling depth of approximately 1.5 mm in a hemispherical shape [3], while the HPLC analyzes a homogenized sample of the entire tissue. An attempt was made to use the OPS to measure the homogenized tissue samples prepared for HPLC analysis. However, because the tissue samples had been diluted 3-to-5 fold, many samples that previously registered detectable MGd absorbance returned signals below the OPS LLD.

Future studies comparing *in vivo* optical measurements with *ex vivo* analytical techniques should consider correctly matching the tissue volume measured by each technique, possibly by excising the exact tissue volume that was optically interrogated, or optically sampling multiple sites on the tissue to obtain a representation of drug concentration heterogeneity throughout the tissue.

The C_{MGd}^{OPS} values in tissues *in vivo* were representative of the "total" MGd present within the optically interrogated tissue volume, including contributions from plasma, skin, and subcutaneous tissue. At short times after drug administration, estimates of C_{MGd}^{OPS} *in vivo* were influenced by blood-localized drug, while estimates at later times were representative of the tissue-specific MGd concentration. This temporal dependence of *in vivo* measurements was reported in a similar study by Lee *et al.*, who measured concentrations of the photosensitizer AlPcS by fluorescence *in vivo* [98]. Future studies may consider use of the OPS to monitor blood and tissue pharmacokinetics noninvasively after sensitizer administration to determine the most beneficial timing sequence for irradiation.

It should be noted that the results reported here were obtained after an MGd dose of 23 mg/kg in mice. A recent clinical study established the maximum tolerated dose for MGd as 6.3 mg/kg [119]. Based on metabolic rate and surface area, the allometric scaling factor between mice and man, it is expected that a ten-fold lower dose of MGd in human subjects would result in similar tissue concentrations to those observed in mice obtained at a 10-fold higher dose [133]. It also should be noted that the OPS was able to detect MGd in the forearm skin of patients *in vivo*, up to 240 min following a $10 - 15$ min infusion of MGd at 2.9 and 3.6 mg/kg (unpublished results). Therefore, it has yet to be determined if the OPS is capable of quantitating MGd following clinically-relevent doses in human subjects.

2.6   SUMMARY

The results in this study indicate that the OPS can accurately quantitate MGd present in Intralipid® tissue phantoms *in vitro*. The OPS can detect absorbance attributable to MGd in mouse tissues *in vivo* and *in situ*, but comparison of C_{MGd}^{OPS} with C_{MGd}^{HPLC} is complicated

by a mismatch between tissue volumes measured by the OPS and the HPLC, possible heterogeneous spatial distribution of MGd and other absorbers in tissues, and the detection of blood-localized MGd by OPS at early time points. These results indicate that standard curves must be developed in a medium with tissue-specific background absorption properties in order to avoid individual studies for each species/organ/drug of interest. The mathematical method developed in this study is applicable to other optically-active compounds that have detectable absorption in the long visible wavelength spectrum. The MGd concentrations measured in this Chapter are used to develop PK models of MGd distribution into plasma, tumor, and skin in Chapter 3.

Table 2.1: MGd peak absorbance area measured by OPS on tumor and skin. Mean absorbance area for each mouse subject $\overline{\mathcal{A}}$ and standard deviation σ.

Time	Tumor *in vivo*[a]		Tumor *in situ*[a]		Skin *in vivo*[a]		Skin *in situ*[a]		Subject
	$\overline{\mathcal{A}}$	σ	$\overline{\mathcal{A}}$	σ	$\overline{\mathcal{A}}$	σ	$\overline{\mathcal{A}}$	σ	
	25.776	5.345	8.940	3.155	33.353	0.955	12.360	0.755	1
5	32.834	0.685	17.716	2.157	40.142	6.127	9.003	0.614	2
	28.545	1.583	14.159	2.747	44.940	3.675	12.488	0.872	3
	41.443	1.400	9.322	1.551	51.326	4.698	16.769	1.432	4
15	38.088	5.322	12.656	0.692	41.137	2.163	12.399	0.477	5
	26.508	0.894	11.907	0.819	21.821	2.142	4.093	1.149	6
	19.234	1.130	9.952	1.205	34.127	0.976	12.021	2.199	7
30	36.678	1.42	16.498	3.046	31.365	5.188	11.917	1.489	8
	34.370	2.937	5.797	0.153	28.246	2.306	25.443	0.740	9
	31.708	0.355	23.720	2.243	23.667	1.595	10.490	1.158	10
60	32.397	1.331	16.137	2.342	18.632	0.331	4.723	0.348	11
	20.470	2.834	6.431	1.222	31.803	3.280	6.949	0.914	12
	12.624	0.468	11.207	3.790	8.433	1.353	4.493	1.729	13
120	15.525	0.900	17.547	1.925	5.439	0.202	6.463	0.174	14
	14.597	0.7335	9.204	2.846	9.270	0.939	7.340	0.137	15
	6.544	1.204	15.190	1.073	7.034	2.429	3.635	1.283	16
240	5.114	0.310	9.160	1.236	R		−	−	17
	7.146	0.469	4.451	0.651	6.17	1.425	−	−	18
	9.604	0.175	16.417	0.884	3.413	0.015	−	−	19
420	2.356	0.453	−	−	3.187	0.058	2.838	0.413	20
	8.992	0.594	11.850	0.509	3.748	0.018	−	−	21
	6.077	0.849	−	−	−	−	−	−	22
960	3.210	0.551	4.879	0.082	−	−	−	−	23
	3.209	0.823	5.576	0.392	−	−	−	−	24
	3.938	0.489	−	−	−	−	R		25
1440	3.095	0.163	9.072	0.795	−	−	R		26
	3.517	0.923	9.708	0.160	−	−	−	−	27
LLD	1.095		3.57		2.79		1.25		

a: integration bounds 650-790nm

-: measurement ≤ LLD, R: data removed due to poor spectra quality

Table 2.2: MGd peak absorbance area measured by OPS on selected internal tissues. Mean absorbance area for each mouse subject $\overline{\mathcal{A}}$ and standard deviation σ.

Time	SkMuscle *in situ*[a]		Fat *in situ*[a]		Kidney *in situ*[b]		Heart *in situ*[a]		Lung *in situ*[a]		Liver *in situ*[a]		Subject
	$\overline{\mathcal{A}}$	σ	$\overline{\mathcal{A}}$	σ	$\overline{\mathcal{A}}$	σ	$\overline{\mathcal{A}}$	σ	$\overline{\mathcal{A}}$	σ	$\overline{\mathcal{A}}$	σ	
	2.609	0.248	12.109	1.264	91.282	2.073	10.888	1.313	35.231	3.041	5.968	1.108	1
5	5.794	0.475	4.536	0.394	68.471	1.57	10.546	2.065	98.967	5.276	4.820	0.490	2
	6.866	0.462	10.618	0.121	90.717	0.403	13.053	0.906	56.12	6.582	3.423	0.407	3
	5.040	0.266	5.908	0.909	148.720	3.067	13.729	0.061	73.637	3.326	16.294	1.180	4
15	8.208	1.251	11.102	1.425	84.279	1.075	—	—	57.389	6.403	13.879	1.586	5
	3.376	0.592	4.319	0.638	80.198	2.309	9.322	2.07	61.313	7.683	7.132	1.345	6
	1.596	0.392	12.311	1.286	74.892	6.328	—	—	66.380	15.812	22.738	1.000	7
30	2.591	0.697	3.154	0.736	130.710	1.095	—	—	34.020	1.915	20.559	0.859	8
	2.007	0.839	2.265	0.038	117.060	1.352	8.844	0.978	37.694	1.339	16.703	0.237	9
	5.166	0.397	6.772	1.239	141.190	16.407	8.614	1.060	—	—	22.122	0.641	10
60	4.931	0.655	3.434	0.419	132.220	1.153	12.687	3.382	46.729	4.445	16.495	0.090	11
	3.403	0.372	3.566	1.067	61.365	5.881	10.053	1.060	48.262	0.781	21.377	1.221	12
	2.053	0.626	3.338	0.430	147.200	2.861	8.159	0.306	14.458	1.873	25.310	0.567	13
120	1.924	0.655	3.731	0.349	47.477	2.019	—	—	17.840	0.895	35.551	1.004	14
	—	—	—	—	160.090	3.762	—	—	7.210	3.203	27.903	1.854	15
	—	—	3.097	1.096	123.280	7.445	—	—	9.868	2.151	38.958	0.999	16
240	1.730	0.212	4.064	0.355	124.680	3.857	—	—	—	—	22.888	6.263	17
	1.270	0.280	—	—	41.932	1.374	—	—	—	—	25.502	1.346	18
	—	—	2.336	0.089	91.722	1.091	—	—	11.970	3.234	26.692	0.888	19
420	2.425	0.459	—	—	31.297	0.451	—	—	10.273	1.458	35.768	0.428	20
	—	—	—	—	31.692	2.044	—	—	—	—	20.317	0.642	21
	—	—	—	—	34.248	1.821	—	—	24.565	11.460	9.674	1.211	22
960	1.495	0.199	—	—	49.779	2.140	9.289	0.265	6.596	0.023	17.506	0.988	23
	—	—	2.336	0.0886	29.359	1.582	—	—	11.344	9.380	11.686	0.294	24
	—	—	—	—	50.792	2.050	—	—	—	—	15.582	1.051	25
1440	—	—	—	—	53.997	1.926	—	—	26.738	6.398	14.600	1.167	26
	—	—	—	—	57.774	1.728	—	—	9.714	0.224	16.911	1.403	27
LLD	1.11		1.78		4.70		7.32		4.66		2.56		

a: integration bounds 650-790nm, b: integration bounds 650-810nm

-: measurement $\leq$ LLD, R: data removed due to poor spectra quality

Table 2.3: MGd concentrations measured by HPLC: C_{MGd}^{HPLC} (μM)

Time	Plasma	Tumor	Skin	Skeletal Muscle	Fat	Kidney	Heart	Lung	Liver	Subject
	75.209	3.080	7.698	2.020	3.860	33.710	5.170	31.80	11.998	1
5	92.133	3.680	2.972	2.214	2.590	26.930	8.395	28.680	9.460	2
	74.783	3.740	3.320	1.550	5.177	25.880	9.398	30.330	12.150	3
	60.937	4.070	8.345	2.167	4.107	36.840	6.579	33.510	12.380	4
15	54.510	6.420	9.785	2.256	0.766	25.430	6.215	26.690	13.880	5
	78.645	3.490	8.192	1.682	0.597	30.150	4.629	15.920	9.140	6
	44.397	5.360	3.554	2.278	1.553	23.740	5.023	19.150	10.270	7
30	41.564	17.360	3.5710	3.5025	0.715	65.980	4.869	18.440	8.120	8
	48.385	5.670	5.162	2.035	2.047	39.770	3.682	20.490	9.550	9
	27.736	9.611	3.388	1.907	1.839	62.120	3.946	17.650	11.930	10
60	32.371	12.950	3.610	1.646	1.475	77.750	4.293	15.790	13.810	11
	36.937	2.970	7.419	2.043	2.700	86.950	4.081	11.280	9.827	12
	4.836	8.470	1.328	1.038	0.448	85.420	2.024	4.590	8.790	13
120	3.602	5.580	1.072	0.987	0.486	43.970	1.690	5.030	4.550	14
	4.977	6.290	0.880	1.014	0.422	42.340	1.866	4.680	7.830	15
	0.353	9.450	—	—	0.404	41.550	1.455	1.110	6.780	16
240	0.393	2.350	—	—	0.410	28.350	—	1.890	3.730	17
	0.484	3.350	—	—	0.407	33.550	1.595	1.750	5.130	18
	0.347	4.850	—	—	0.385	11.710	—	0.330	1.970	19
420	0.351	1.330	—	—	0.459	7.610	—	1.150	4.180	20
	0.374	4.810	—	—	0.397	9.580	—	0.570	1.170	21
	0.353	2.970	—	—	—	12.070	—	0.300	0.810	22
960	0.349	1.270	—	—	—	12.950	—	0.270	0.850	23
	0.351	1.250	—	—	—	7.810	—	0.920	0.690	24
	0.345	2.020	—	—	—	8.460	—	0.240	1.280	25
1440	0.353	1.299	—	—	—	12.750	—	0.150	0.960	26
	0.350	1.570	—	—	—	20.570	—	0.150	—	27

Table 2.4: OPS standard curve coefficients in Intralipid® and tissue matrix. Follows the function: $\mathcal{A}(t) = x \left[C_{MGd}(t) \right]^y$

Sample	x	y
Intralipid®	4.965	0.803
Tumor *in vivo*	2.743	0.766
Tumor *in situ*	6.374	0.425
Skin *in situ*	7.195	0.393
Kidney *in situ*	21.98	0.424
Heart *in situ*	6.089	0.413
Lung *in situ*	12.607	0.480

Table 2.5: C_{MGd}^{OPS} versus C_{MGd}^{HPLC} comparisons per subject

Sample	Standard Curve	slope	r^2
Intralipid®		0.997	0.999
Tumor *in vivo*[1]	Intralipid®	0.414	0.472
	tissue matrix	0.900	0.477
Tumor *in situ*[2]	Intralipid®	0.687	≈ 0
	tissue matrix	1.185	0.269
Skin *in vivo* [2]	Intralipid®	1.730	0.159
	tissue matrix	N/A	
Skin *in situ*[2]	Intralipid®	0.475	≈ 0
	tissue matrix	1.019	0.011
Kidney *in situ*[2]	Intralipid®	0.820	0.164
	tissue matrix	0.942	0.353
Heart *in situ*[2]	Intralipid®	0.488	≈ 0
	tissue matrix	0.750	0.297
Lung *in situ*[2]	Intralipid®	0.858	0.597
	tissue matrix	1.070	0.513
Liver *in situ*[2]	Intralipid®	0.527	≈ 0
	tissue matrix	NA	

1: comparisons made over $120 \leq t \leq 1440$ min

2: comparisons made over all time points with detectable MGd

3.0 PK MODELING OF MGD IN SCID MICE

3.1 BACKGROUND

An ideal radiation- or photodynamic-sensitizing agent is one that preferentially localizes in malignant tissue during drug distribution, such that after some elapsed time, a positive concentration gradient exists between malignant and surrounding non-malignant tissues [6,44,134]. Irradiation at this time results in damage to tumor and possible preservation of surrounding normal tissues. Current clinical protocols do not quantitate the sensitizer concentration in the target tissues following dosing [45]. Without this measurement, the elapsed time between dose and irradiation is not tailored to individual patients, and treatment fails to account for patient-specific pharmacokinetics (PK) of the sensitizer. A method to determine the sensitizer PK noninvasively at the site of action would allow clinicians to design patient-specific treatment schedules, possibly improving the efficacy of therapy [10].

Chapter 2 reported MGd concentrations measured in female C.B-17 SCID mice bearing human breast cancer xenografts dosed i.v. with 23 mg/kg. MGd concentrations were measured in tissues noninvasively by the OPS *in vivo*, nondestructively by OPS *in situ*, and destructively by HPLC *ex vivo*. This Chapter utilizes those reported concentrations to develop compartmental PK models of MGd disposition in plasma, tumor, and skin. The MGd tumor concentrations measured by OPS *in vivo* are estimated by a combination of PK model predictions of MGd concentrations in plasma, tumor, and skin.

3.2 MATHEMATICAL MODELING

3.2.1 Pharmacokinetic Model

Figure 3.1 shows the compartmental model structure used to model MGd concentrations in plasma, skin, and tumor. Parallels between the mathematical model and physiology may be considered, with compartment 1 representative of plasma, compartment 3 representative of skin, compartments 4 and 5 representative of tumor, and compartment 2 representative of other 'peripheral' tissues. However, it must be noted that this model is not physiologic. In this system, the drug is introduced into the plasma compartment via an i.v. bolus, transport occurs between plasma and tissues, and the drug is ultimately cleared from the plasma. These phenomena are governed by the following ordinary differential equations:

$$\frac{dx_1(t)}{dt} = D(t) + k_{21}x_2(t) + k_{31}x_3(t) + k_{41}x_4(t) - (k_{10} + k_{12} + k_{13} + k_{14})x_1(t) \quad (3.1)$$

$$\frac{dx_2(t)}{dt} = k_{12}x_1(t) - k_{21}x_2(t) \quad (3.2)$$

$$\frac{dx_3(t)}{dt} = k_{13}x_1(t) - k_{31}x_3(t) \quad (3.3)$$

$$\frac{dx_4(t)}{dt} = k_{14}x_1(t) + k_{54}x_5(t) - (k_{41} + k_{45})x_4(t) \quad (3.4)$$

$$\frac{dx_5(t)}{dt} = k_{45}x_4(t) - k_{54}x_5(t) \quad (3.5)$$

$$\hat{C}_1(t) = \frac{x_1(t)}{V_1} \quad (3.6)$$

$$\hat{C}_3(t) = \frac{x_3(t)}{V_3} \quad (3.7)$$

$$\hat{C}_4(t) = \frac{x_4(t)}{V_4} \quad (3.8)$$

Here, $x_q(t)$ is the mass of MGd in compartment q (where $q \in \{1, 2, 3, 4, 5\}$), k_{10} is the mass elimination rate from plasma, and k_{mn} is the mass transport rate from compartment m to n. $D(t)$ is the bolus dose of MGd converted to 546.8 nmoles based on the average mouse weight of 27.3 g. $\hat{C}_i(t)$ and V_i are the estimated MGd concentration and volume of distribution, respectively, in compartment i (where $i \in \{1, 3, 4\}$). For plasma, V_1 is the apparent volume of distribution (mL), a parameter that can exceed the physical volume of plasma [128], and it is a fitted parameter. The skin volume, V_3, is calculated as 16 % of the average volume

of the mice used in this study, assuming the density is equivalent to that of water [135]. The tumor volume, V_4, is calculated from the measured weight of the extracted tumor tissue (average tumor weight = 1.09 g). V_3 and V_4 are not fitted to data.

The model is informed using MGd concentration data from plasma, skin and tumor, which correspond to compartments 1, 3, and 4, respectively. The plasma concentration was measured by HPLC; the tumor and skin concentrations were measured by two methods: OPS *in situ* and HPLC *ex vivo*. The model parameters were estimated independently for the tissue-specific MGd concentrations measured by OPS and HPLC, resulting in OPS-based and HPLC-based PK models. Compartments 2 and 5 are incorporated to allow the model to capture the MGd dynamics observed in plasma and tumor; the mass within these compartments is not used to estimate concentrations. The potential physiological basis for the inclusion of these compartments is discussed in Section 3.4.

In order to determine an appropriate model structure that describes the data, candidate model structures of increasing compartmental complexity were evaluated based on the observed MGd concentrations and compared using Akaike's information criterion (AIC) as a performance metric. AIC is calculated as [136]:

$$AIC = N \ln \left(\frac{SSE}{N} \right) + 2M \tag{3.9}$$

N is the number of data points, SSE is the sum squared error between measured and predicted concentrations, and M is the number of estimated parameters. The AIC metric is used to identify the model that provides the best fit without overparamaterizing the model. The model resulting in the lowest AIC value is the superior model.

3.2.2 Parameter Estimation

The metric used to describe the quality of model fit was the sum squared error (SSE) between the natural log of measured and estimated concentrations. The objective function was formulated as:

$$J_i \left(p \right) = \sum_{q=1}^{N_c} \sum_{j=1}^{N_t} \left(\ln \left(C_i(j) \right) - \ln \left(\hat{C}_i(j, p) \right) \right)^2 = SSE \tag{3.10}$$
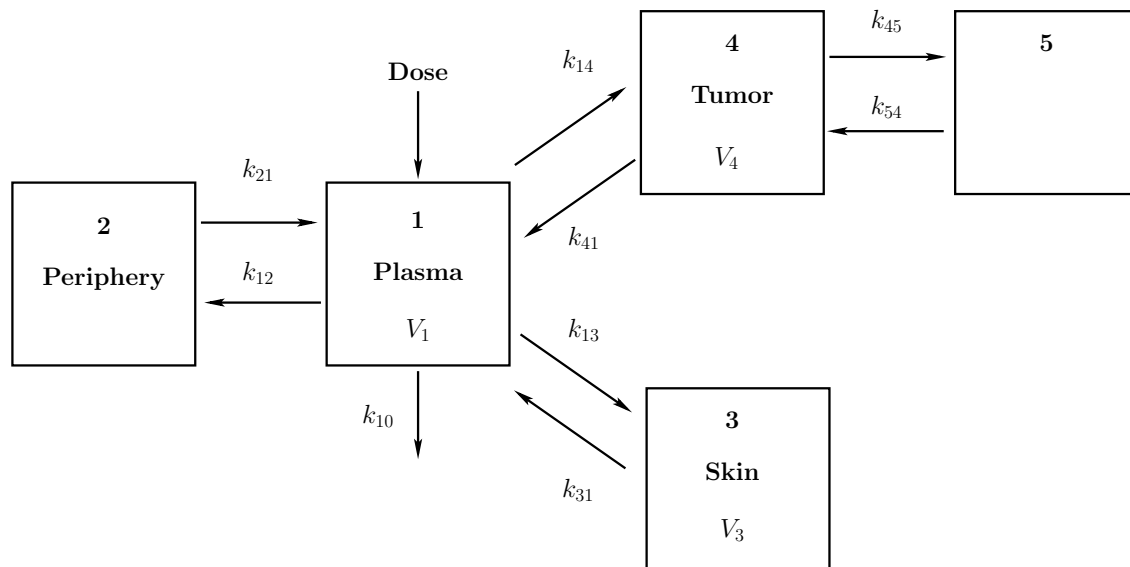
Figure 3.1: Compartmental model of MGd concentrations in plasma, skin, and tumor tissues following i.v. administration.

Here, $C_i(j)$ is the measured concentration and $\hat{C}_i(j, p)$ is the model estimated concentration in compartment i (where $i \in \{1, 3, 4\}$), at time j for the parameter set p (where $p = \{k_{mn}, V_1\}$ and $mn \in \{12, 13, 14, 21, 31, 41, 45, 54\}$). The objective function sums the error over all time-points, N_t, for all compartments corresponding to a measured concentration, N_c The natural logarithm functions were incorporated to equally balance the contribution of error from measurements at all measured time points to the overall error in Equation (3.10). Parameter estimates for all k_{mn} values and V_1 were determined by minimizing Equation (3.10) using the *lsqnonlin* function from the statistics toolbox in MATLAB (Release 14, Ⓡ 2007, The MathWorks, Natick, MA). 95% confidence intervals for the estimated parameters were calculated from the residual error and the Jacobian matrix using the *nlparci* function, also available in the MATLABⓇ statistics toolbox [137].

3.2.3 Estimation of MGd Detected in Tumor *in vivo*

It is hypothesized that the observed concentration *in vivo*, C_{invivo}^{OPS}, may be represented as a linear combination of simulated PK predictions in plasma, tumor, and skin. An expression for the *in vivo* concentration estimate (termed $\hat{C}_{invivo}^{OPS}$) was formulated as follows:

$$\hat{C}_{invivo}^{OPS/OPS}(t) = f_{plasma}\hat{C}_1^{HPLC}(t) + f_{tumor}\hat{C}_4^{OPS}(t) + f_{skin}\hat{C}_3^{OPS}(t) \tag{3.11}$$

$$\hat{C}_{invivo}^{OPS/HPLC}(t) = f_{plasma}\hat{C}_1^{HPLC}(t) + f_{tumor}\hat{C}_4^{HPLC}(t) + f_{skin}\hat{C}_3^{HPLC}(t) \tag{3.12}$$

Here, the *in vivo* concentration may be represented by measurements from OPS, $\hat{C}_{invivo}^{OPS/OPS}(t)$ or HPLC, $\hat{C}_{invivo}^{OPS/HPLC}(t)$. f_{plasma}, f_{tumor}, and f_{skin} represent the respective fractional contribution of the simulated MGd plasma, tumor, and skin concentrations to C_{invivo}^{OPS}. Therefore, each f value lies on the interval $[0, 1]$, while the sum of the values is not required to equal unity. The values of $p = \{f_{plasma}, f_{tumor}, f_{skin}\}$ were obtained by minimizing the difference between estimated and measured *in vivo* tumor concentration (as in Equation (3.10)). f values were estimated for both OPS- and HPLC-based PK models.

3.3 RESULTS

Both one and two compartment structures were considered for modeling the plasma data (*i.e.*, with and without compartment 2). The two compartment model resulted in a better fit (AIC of -28.29 vs. 12.19). Figure 3.2 shows C_{plasma}^{HPLC} data and $\hat{C}_1^{HPLC}$ predictions. Each data point represents the mean concentration measured in three mice per time point, and one standard deviation is shown about each point. The PK model represents only plasma dynamics with both k_{13} and k_{14} equal to zero, thereby eliminating transport from plasma into either skin or tumor compartments. Estimated parameter values are listed in Table 3.1.

Following the i.v. dose, the C_{plasma}^{HPLC} decreases rapidly, with a 99.5% decrease in the concentration between 5 and 240 min. The concentration then remains relatively unchanged, at the observed concentration of 0.349 ± 0.004 μM at 24 hr. The compartmental PK model follows the HPLC observed data, predicting both the fast initial elimination of MGd, with a 99.4% decrease in concentration from 5 to 240 min, and MGd retention at late time points, with a predicted concentration of 0.30 μM at 24 hr.

Figure 3.3 shows the data and predictions from the 5-compartment PK model that includes plasma, skin, and tumor. Figures 3.3(A) and (B) show C_{skin}^{HPLC} and C_{skin}^{OPS} data and the corresponding PK predictions, $\hat{C}_3^{HPLC}$ and $\hat{C}_3^{OPS}$. In the skin, MGd is rapidly cleared following an i.v. dose, resulting in undetectable concentrations at 240 min. Both HPLC- and OPS-based models capture this behavior, with predicted peak MGd concentrations of 8.1 and 5.4 μM occurring at 20 and 23 min, respectively, and predicted decreases of 99.0% and 98.7% between the observed peak and 240 min, respectively. Estimated skin to plasma transport rates (k_{31}) are an order of magnitude larger than the plasma to skin rates (k_{13}), as shown in Table 3.1.

PK models of the tumor data considered one- or two-compartment structures, with and without compartment 5 in Figure 3.1. It was found that the inclusion of compartment 5 allowed the models to capture both the peak and retention, which improved model fit and resulted in a reduced AIC for both HPLC-based (-72.6 vs. -59.1) and OPS-based (-44.5 vs. -37.5) models. Table 3.1 shows the estimated parameter values. There is significant variability in the estimation of the tumor to plasma (k_{41}) and intratumoral (k_{54}) MGd
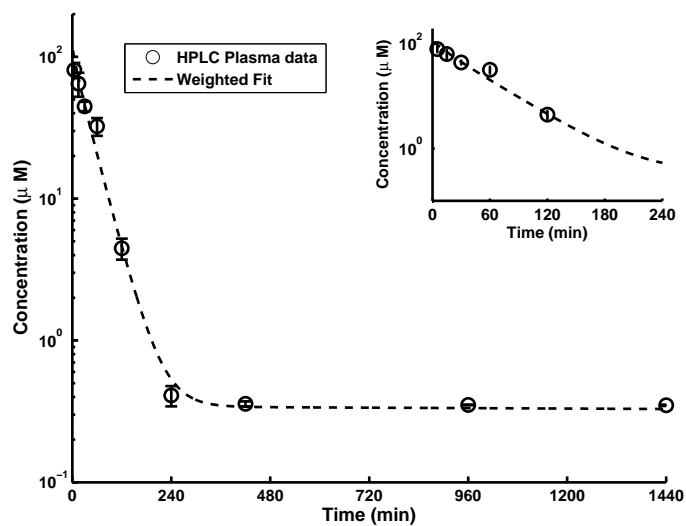
Figure 3.2: MGd concentrations in plasma following i.v. dose as measured by HPLC *ex vivo* and predicted using a two-compartment PK model. Inset shows MGd concentrations at short times following dose.

transport rates. Figures 3.3(C) and (D) show C_{tumor}^{HPLC} and C_{tumor}^{OPS} data and the corresponding PK predictions, $\hat{C}_4^{HPLC}$ and $\hat{C}_4^{OPS}$. The HPLC-based model predicted a peak of 10.9 μM to occur 71 min following i.v. dose, with a decrease of 83% by 960 min, and predicted a near zero slope between 960 and 1440 min. The OPS-based model predicted a peak of 8.8 μM to occur 55 min following i.v. dose, with a decrease of 70% by 960 min, and predicted a near zero slope from 960 to 1440 min.

It should be noted that the addition of compartments 3, 4, and 5 did not significantly change the estimated plasma MGd concentrations in compartment 1. The average percentage deviation between the predicted plasma concentrations from the two-compartment (plasma-only) and the five-compartment (plasma-tissue) models were 1% for the HPLC-, and 7% for the OPS-based models.

The model shown in Figure 3.1 was unable to predict the *in vivo* tumor MGd concentrations measured by OPS, because compartment 4 was not representative of the sampled volume, which included plasma, tumor, and skin. Figure 3.4 shows C_{invivo}^{OPS} data and a linear combination estimate, $\hat{C}_{invivo}^{OPS/HPLC}$, as well as the respective contributions of plasma, $f_{plasma}\hat{C}_1^{HPLC}$, tumor, $f_{tumor}\hat{C}_4^{HPLC}$, and skin, $f_{skin}\hat{C}_3^{HPLC}$, to the estimated *in vivo* PK. The minimization of the SSE between C_{total}^{OPS} and $\hat{C}_{invivo}^{OPS/HPLC}$ was achieved using Equations (3.10) and (3.11) with $f_{plasma} = 0.231$, $f_{tumor} = 0.819$, and $f_{skin} = 0.534$. The estimate of $\hat{C}_{invivo}^{OPS/OPS}$ is show in the bottom plot of Figure 3.4, with similar results. The minimal SSE between C_{invivo}^{OPS} and $\hat{C}_{invivo}^{OPS/OPS}$ was achieved using Equations (3.10) and (3.11) with $f_{plasma} = 0.245$, $f_{tumor} = 0.811$, and $f_{skin} = 0.806$. The estimate of f_{skin} was higher for $\hat{C}_{invivo}^{OPS/OPS}$ than for $\hat{C}_{invivo}^{OPS/HPLC}$ because the MGd skin concentration estimated by the OPS was lower than by HPLC. These results suggest the plasma, tumor, and skin each contribute to the concentration detected *in vivo*.

3.4 DISCUSSION

This Chapter presents compartmental PK models that describe MGd concentrations in plasma, skin, and tumor following an i.v. dose. The models are informed with MGd
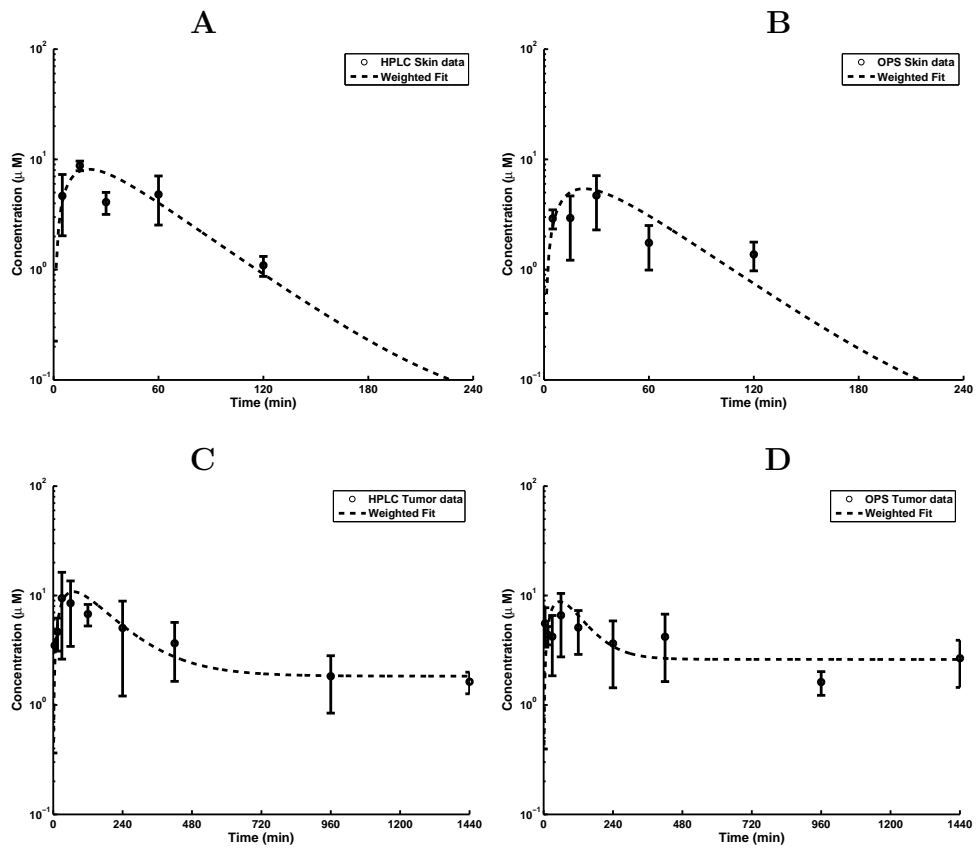
Figure 3.3: Measured concentrations and 5-compartment PK model predictions for MGd disposition. Top: Skin concentrations from 0 to 240 min, as measured by HPLC (A) and OPS *in situ* (B). Bottom: Tumor concentrations from 0 to 1440 min, as measured by HPLC (C) and OPS *in situ* (D).
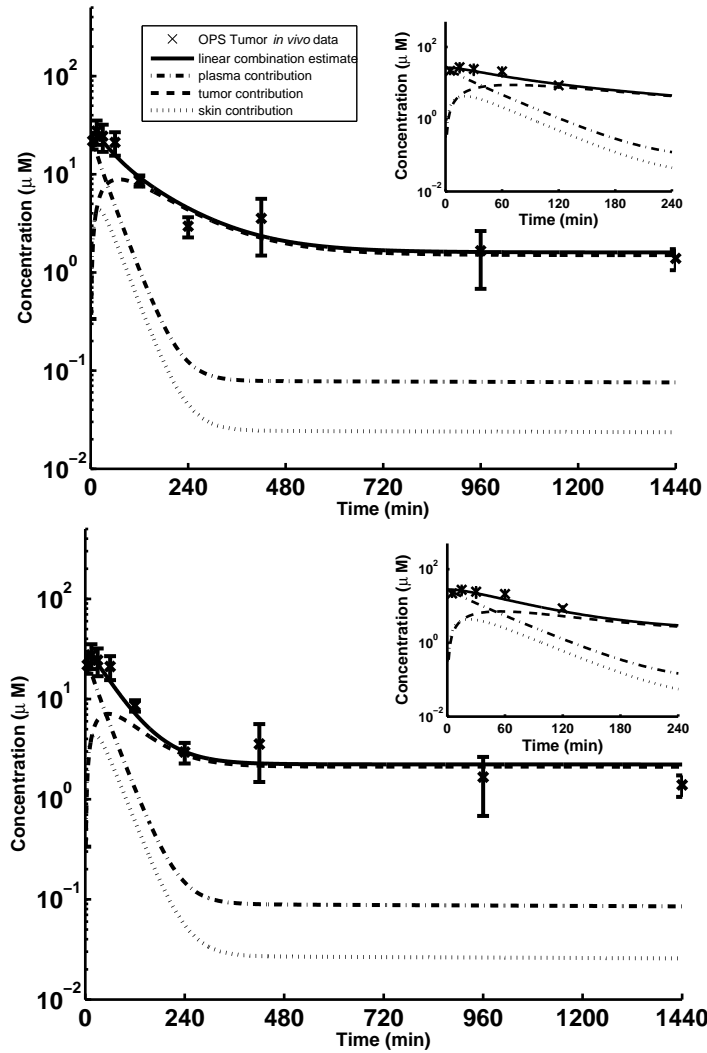
Figure 3.4: MGd tumor concentrations measured by OPS *in vivo* and estimated MGd tumor concentration ($\hat{C}_{invivo}^{OPS/HPLC}$) using a linear combination of PK model estimates of MGd in plasma, tumor, and skin. (Top) estimate from HPLC-based PK models ($\hat{C}_{invivo}^{OPS/HPLC}$); (Bottom) estimate from OPS-based PK models ($\hat{C}_{invivo}^{OPS/OPS}$). The contribution of plasma is given as $f_{plasma}\hat{C}_{plasma}^{HPLC}$ is displayed on both plots. The contribution of tumor is given as $f_{tumor}\hat{C}_{tumor}^{HPLC}$ (Top) and $f_{tumor}\hat{C}_{tumor}^{OPS}$ (Bottom) The contribution of skin is given as $f_{skin}\hat{C}_{skin}^{HPLC}$ (Top) and $f_{skin}\hat{C}_{skin}^{OPS}$ (Bottom). Insets show MGd concentrations at short times following dose.

Table 3.1: Pharmacokinetic Parameters. Apparent plasma volume (V_1) and mass transport rates (k_{mn}) given in the form: mean $\pm$ half width of 95% confidence interval.

Parameter	Units	Plasma model	HPLC-based model	OPS-based model
V_1	mL	5.16 ± 1.23	4.76 ± 1.69	4.81 ± 1.55
k_{10}	(min^{-1})	$(4.07 \pm 1.21) \times 10^{-3}$	$(6.60 \pm 1.35) \times 10^{-3}$	$(7.60 \pm 5.31) \times 10^{-3}$
k_{12}	(min^{-1})	$(2.22 \pm 0.05) \times 10^{-4}$	$(2.19 \pm 0.188) \times 10^{-2}$	$(1.90 \pm 0.54) \times 10^{-2}$
k_{21}	(min^{-1})	$(1.06 \pm 0.43) \times 10^{-5}$	$(1.19 \pm 0.48) \times 10^{-4}$	$(1.20 \pm 0.80) \times 10^{-4}$
k_{13}	(min^{-1})	-	$(7.43 \pm 2.34) \times 10^{-3}$	$(4.56 \pm 1.86) \times 10^{-3}$
k_{31}	(min^{-1})	-	$(7.71 \pm 0.23) \times 10^{-2}$	$(6.65 \pm 3.49) \times 10^{-2}$
k_{14}	(min^{-1})	-	$(9.87 \pm 2.25) \times 10^{-4}$	$(9.03 \pm 4.33) \times 10^{-4}$
k_{41}	(min^{-1})	-	$2.34 \times 10^{-10} \pm 0.002$	$5.813 \times 10^{-5} \pm 0.010$
k_{45}	(min^{-1})	-	$(7.51 \pm 1.49) \times 10^{-3}$	$(1.74 \pm 1.11) \times 10^{-2}$
k_{54}	(min^{-1})	-	$(2.46 \pm 0.96) \times 10^{-5}$	$(8.90 \pm 7.28) \times 10^{-5}$

concentrations measured noninvasively *in vivo* and nondestructively *in situ* by OPS and destructively *ex vivo* by HPLC. Both OPS- and HPLC-based models described MGd concentrations in plasma, tumor, and skin. PK model predictions in plasma, tumor, and skin were utilized to describe the MGd detected by the OPS in tumor *in vivo*.

A previous study analyzed the MGd PK following 40 mg/kg i.v. dose in non-tumor-bearing CD1 mice [138]. A two-compartment model best predicted the MGd concentrations in plasma in both the previous and current studies. Both PK analyses predicted the rapid initial elimination of MGd from plasma, followed by a slow terminal phase. Direct comparison of model parameters is not possible because the previous study utilized the NONMEM software package to fit a different set of parameters from those used in the current study [138].

During the selection of the model structure used, candidate model structures were chosen based on the observed MGd concentration vs. time profiles. The most appropriate structure was identified by calculating AIC. MGd concentrations in plasma and tumor show two distinct phases, which were best predicted by two-compartment models. Therefore, description of the concentrations within these tissues required the addition of Compartments 2 and 5 to capture both phases in plasma and tumor, respectively. During the 'initial' phase in plasma, MGd distributes into peripheral tissues and is cleared by the liver and kidneys. The 'slow' phase is attributable to release of MGd from the peripheral tissues back into the vasculature. In tumor tissue, the 'initial' phase represents influx of MGd from the vasculature, while the 'slow' phase is attributable to an inability of the tumor to efficiently clear the drug. The physiological basis of MGd retention is hypothesized to may be a less well-developed lymphatic and blood vessel network that impedes the effective clearance of the MGd from the tumor tissue. However, it should be noted that the inclusion of Compartment 5 was instituted by the dynamics of the data, and is not directly linked to a physiological effect within the tumor tissue.

The addition of Compartment 5 reduced the AIC, supporting the use of the 5-compartment model to describe the data. However, it is a concern that the selected model structure for tumor resulted in some estimated parameters having very large 95% confidence intervals (CIs), and that these CIs overlap or nearly overlap the parameter value of zero. This indicates that the available data are insufficient to accurately characterize the trans-

port of MGd from tumor to plasma (k_{41}) and within the tumor (k_{54}), and furthermore, this indicates that the amount of drug in the tumor does not significantly impact plasma MGd dynamics (small k_{41} values). The inclusion of sampled MGd tumor concentrations at later time points (*e.g.*, 72 hr following i.v. dose) could allow estimation of these parameters with higher confidence.

The predicted peak MGd concentration in the tumor *in situ* and *ex vivo* occurs approximately 1 hr following i.v. dose, at a time when significant MGd is present in the skin and vasculature surrounding the tumor. However, at 4 hr following i.v. dose, the MGd concentration in the tumor tissue is an order of magnitude higher than the concentration in either the skin or plasma. The OPS-based PK models were able to capture the development of the MGd gradient between tumor and skin. These results suggest that OPS measurements may be used to inform patient-specific PK models that can be used to calculate the optimal time to administer irradiation.

Figure 3.3 clearly shows two-phase behavior in tumor MGd concentration vs. time profiles as measured by OPS *in situ* and HPLC *ex vivo*. In order to verify that the early phase was not attributable to blood remaining in the tissue after exsanguination, we compared the observed peaks in plasma and tumor. These occurred at 5 min and approximately 1 hr following i.v. dose, respectively. This 55 min interval between plasma and tumor peaks strongly suggests the early phase in tumor is MGd distribution into tumor, rather than residual blood that would have been present in the tumor at earlier times following dose.

In contrast to the OPS *in situ* and HPLC *ex vivo* tumor MGd data, the OPS *in vivo* MGd profile presented in Figure 3.4 clearly shows an early peak related to plasma MGd concentrations. This occurs because the tissue volume sampled optically during the OPS measurement of tumor *in vivo* included contributions from plasma, tumor, and skin. The estimated f values in Equations (3.11) and (3.12) represent the respective fractions of the MGd concentration in plasma, tumor, and skin that are detected during measurement of the tumor by the OPS *in vivo*. In order to determine the percentage of the *in vivo* concentration that is attributable to the each tissue, the contributions of each are calculated as: plasma, $f_{plamsa}\hat{C}_{plasma}$, tumor, $f_{tumor}\hat{C}_{tumor}$, and skin, $f_{skin}\hat{C}_{skin}$, with each concentration measured either by the OPS or HPLC. Based on the estimated concentrations, as shown in Figure 3.4,

plasma and skin PK have a near zero contribution to the *in vivo* tumor concentration estimate after 240 min. Figure 3.5 shows changes in the percentage contribution of various tissues to the total *in vivo* concentration at times between 5 and 240 min after dose. At 5 min after dose, the estimated *in vivo* concentration was predominately due to plasma localized MGd (87%). From 240 to 1440 min, the *in vivo* MGd concentration was dominated by the tumor tissue concentration ($> 93\%$). These results indicate that Equations (3.11) and (3.12) allow estimation of the tumor-localized MGd concentration from the *in vivo* tumor concentration measured by the OPS. Hypothetically, this information could be used to make decisions about the timing of radiation or concurrent chemotherapy administration following MGd administration based on the degree of MGd localization or on the concentration gradient between tumor and surrounding tissues.

Comparison of the estimated f values for both HPLC- and OPS-based models shows similar f_{plasma} and f_{tumor} values, but a difference between f_{skin} estimates (0.534 and 0.806, respectively). This difference may be a result of the lower predicted peak concentration in the skin from the OPS measurement (8.1 μM vs. 5.4 μM as measured by HPLC and OPS, respectively). The tissue volume sampled by the OPS included contributions from underlying tissues, such as skeletal muscle. The skeletal muscle contained lower MGd concentrations than skin at all measured time points [122], and hypothetically, could also contribute to difference in estimated f_{skin} values.

The HPLC- and OPS-based PK models predicted differences in the time and magnitude of the peak MGd tumor concentrations. As reported in Section 2.5, these differences may be due to the mismatch in the volume of tissue sampled by each technique, as well as heterogeneous distribution of the drug within the tissue. These results suggest that in order to characterize the PK of MGd in tumor tissue using the OPS, it may be necessary to sample multiple sites on the tissue to estimate a tissue-average concentration. It should be noted that the error associated with the peak MGd prediction would not affect the use of the OPS measurement to detect the large tumor/skin gradients at the 4 hr time point. It is at these times when OPS measurements may provide clinically relevant information to inform radiation planning.
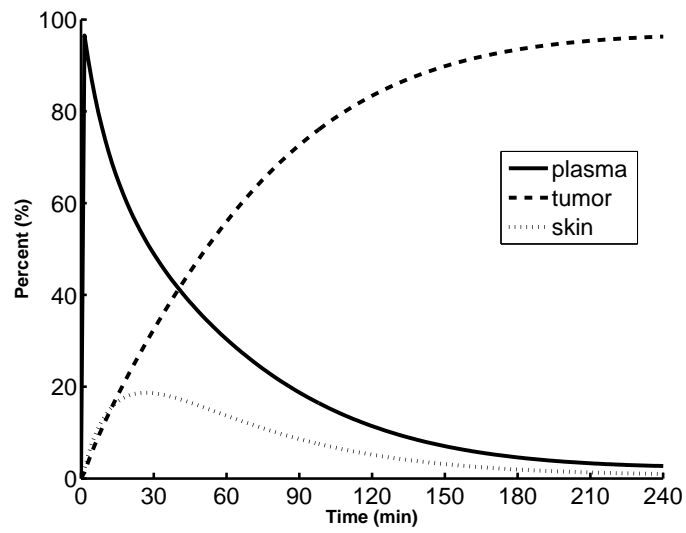
Figure 3.5: Model-simulated percentage contribution of plasma, tumor, and skin to the *in vivo* MGd tumor concentration detected in blood-perfused tumor during measurement by OPS.

3.5 SUMMARY

This Chapter presents PK models developed using tissue-localized MGd concentrations measured by OPS and HPLC in plasma, tumor, and skin. A linear combination of PK model estimates of MGd in plasma, skin, and tumor was used to describe the "total" MGd concentration measured in tumor *in vivo* by the OPS. Hypothetically, the modeling structure presented here is extendable to other sensitizing compounds detectable by the OPS. The potential application of this type of model to determine patient-specific irradiation schemes for PS compounds during PDT treatment is presented in Chapter 6.

4.0 OPS MEASUREMENTS OF PC4-MEDIATED PDT IN MURINE TUMORS

4.1 BACKGROUND

Silicon phthalocyanine (Pc4) is a photosensitizing compound that is being investigated for use in anti-cancer PDT both preclinically [58] and clinically [59]. Pc4 has a strong absorption band at 672 nm, as shown in Figure 4.1. The strength and location of this band make Pc4 a well-suited candidate for measurement by the OPS.

As explained in Chapter 2, the modified Beer-Lambert law is used to relate the changes in light intensities measured by the OPS with changes in chromophore concentrations within the measured medium. A previous study by Mourant *et al.* presented a mathematical algorithm that estimates changes in the concentration of chromophores, the effect of changes in scattering on the collected light intensity, and the effect of the total absorption coefficient on the mean photon path length [3]. The study reported a linear correlation between doxirubicin concentrations measured *in vivo* by OPS and *ex vivo* by high performance liquid chromatography (HPLC). The algorithm presented by Mourant *et al.* [3] defines a functional relationship between the mean photon path length and the total absorption coefficient. This function was selected empirically, by linearizing the estimated and true absorber concentrations from *in vitro* data. This functional relationship was valid for a total absorption coefficient (μ_a^{total}) less than 1 cm^{-1}, however, for $\mu_a^{total} > 1$ cm^{-1}, the function predicts a constant path length of 0.6 cm. The absorption coefficient within tissue can exceed this value [78,139], especially in the $500 - 600$ nm wavelength range where hemoglobin has strong absorption bands. Therefore, the previous function for estimating photon path length may
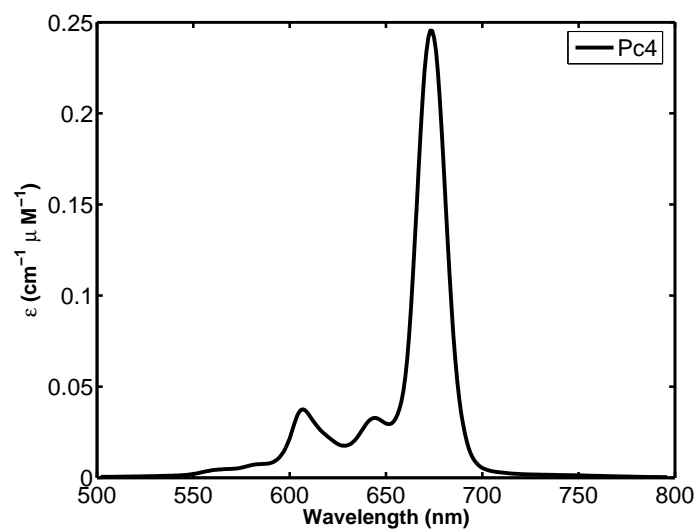
Figure 4.1: Molar extinction coefficients of Pc4 as measured in a clear solution by spectrophotometer.

introduce error into the calculation by estimating an unrealistic 'saturation' of the path length for measurements of mediums containing large absorption coefficients.

Moreover, the algorithm presented by Mourant *et al.* [3] assumes that chromophores are distributed homogeneously throughout the medium. It is well known that tissues contain heterogeneous chromophore distributions [110, 111, 112], with whole blood localized in discrete vessels. Whole blood contains strong absorption bands in the vis-NIR wavelength range [16]. This spatial distribution of μ_a^{total} affects the propagation of light through tissue. As light traverses a vessel, the blood located around the vessel edge strongly attenuates the light, effectively shielding the blood at the vessel center from light. Due to this, the light that is collected by the OPS may have only sampled a subset of the total amount of blood within the tissue. In this situation, the 'apparent' absorption coefficient estimated from the modified Beer-Lambert law is less than the 'true' absorption coefficient (due to the shielding effect of blood) within the measured tissue volume [110, 111, 112]. This phenomenon is termed 'pigment packaging' [29]. Previous studies accounted for this by incorporating a correction factor that estimates the effect of pigment packaging on the model-estimated absorption coefficient [113, 140]. In these studies, the correction factor improved the ability to mathematically capture features of the measured data, especially at wavelengths where hemoglobin compounds have strong absorption bands, thereby causing packaging to have a significant effect. The current study incorporates a vessel correction factor into the analysis of elastically-scattered spectra measured by the OPS.

This Chapter presents a theoretical analysis of the measurement of tissue by the OPS *in silico*. A Monte Carlo (MC) model of light propagation through tissue [107] is used to emulate OPS measurement of a medium containing discrete vessels. Simulations are used to investigate the functional relationship between photon path length and μ_a^{total}, as well as the incorporation of a vessel correction factor into the data analysis algorithm. These extensions are incorporated into the data analysis algorithm presented by Mourant *et al.* [3]. This resultant algorithm is utilized to analyze OPS measurements for a mouse xenograft before and after Pc4-mediated PDT. Estimates of Pc4 and total hemoglobin concentrations, as well as hemoglobin saturation, are calculated using the previous and the extended algorithms.

4.2 EXPERIMENTAL METHODS

All of the experimental work presented in this Chapter was conducted by Julie Eiseman and Li Bai at the University of Pittsburgh Cancer Institute.

4.2.1 Drugs and Reagents

Pc4 (NSC 676418) was obtained from the NCI (Bethesda, MD). Sterile water and 0.9 % Sodium Chloride Injection Solution (Saline) were purchased from Baxter Healthcare Corp. (Deerfield, IL). RPMI medium, fetal bovine serum (heat inactivated), Trypsin-EDTA (10 x), and phosphate-buffered saline (PBS, pH 7.4, without calcium or magnesium) were purchased from Invitrogen (Carlsbad, CA). Penicillin-Streptomycin were purchased from Biofluids Division (Rockville, MD). Nembutal sodium solution (Covation Pharmaceutical, Inc. Deerfield, IL), isoflurane (Hospira Inc., Lake Forest, IL) and heparin sodium for injection (10000 Units/ml, American Pharmaceutical Partners, Inc. Schaumburg, IL) were obtained through UPCI pharmacy.

4.2.2 Animals and Tumor Model

Female C.B-17 SCID mice (specific pathogen free, $4 - 6$ weeks of age) were purchased from Charles River Laboratories (Wilmington, MA) and allowed one week to acclimate to the animal facilities at the University of Pittsburgh. Mice were handled in accordance with the Guide For the Care and Use of Laboratory Animals [124] and on a protocol approved by the Institutional Animal Care and Use Committee of the University of Pittsburgh. MDA-MB-231 cells were obtained from ATCC (Manassas, VA) and grown in RPMI 1640 medium containing 10% heat inactivated fetal bovine serum, penicillin, and streptomycin in a humidified incubator at 37 ^oC and 5% CO_2. When cells were 70% confluent, they were trypsinized and resuspended at a final concentration of 5×10^7 cells/ml in medium. 5×10^6 cells were implanted subcutaneously to the right flank of each passage mouse. MDA-MB-231 tumor fragments (approximately 25 mg) from passage mice were implanted subcutaneously on the right flank of mice.

4.2.3 OPS Sampling

For *in vivo* measurements, mice were gently restrained by hand and triplicate OPS measurements were made on the skin over the subcutaneous tumor. Before Pc4 administration, and at 5, 15, 30, 60, 120, 360, 1440 min after Pc4 administration, tumor Pc4 concentrations were measured *in vivo* in triplicate.

4.2.4 Pc4-PDT

40 C.B-17 SCID female mice bearing MDA-MB-231 xenografts were stratified into 5 groups with 8 mice in each group so that the mean tumor volumes and mean body weights of these groups are similar. These five groups were Laser only (150 J/cm^2); Pc4 (2 mg/kg) + Fractionated Laser (150 J/cm^2); vehicle control; Pc4 (2 mg/kg) + Continuous Laser (150 J/cm^2); and Pc4 only (2 mg/kg). The data reported in this Chapter encompass only 1 of 8 subjects enrolled in the study that received Pc4-mediated PDT treatment; ongoing work will apply the techniques developed in this Chapter to analysis of all subjects within the study.

Fur was removed from skin over the tumor and on the opposite flank of mice by application of Nair (Church and Dwight Co., Princeton, NJ) 24 h before dosing under anesthesia (Nembutal sodium solution, 50 mg/kg, intraperitoneal (i.p.)). Pc4 was administered to the mice at 0.01 ml/mg fasted body weight by bolus lateral tail vein injection. After Pc4 was administered, the mice were housed under Lee filter number 124 (Baltimore Stage Lighting, Baltimore, MD, USA) which transmits light almost exclusively between 450 and 600 nm. Mice were anesthetized with nembutal sodium solution (50 mg/kg, i.p.) and were gently positioned in a specially designed restrainer which allowed unobstructed access to the tumor during laser treatment. Black plastic sheets with holes of various sizes matched to tumor sizes were used to protect the areas surrounding the tumor from the laser light. Laser light at 672 nm from a Diode laser (HPD Inc., North Brunswick, NJ) was split into two beams with equal power by a bifurcated optical fiber assembly (Ocean Optics, Dunedin, FL). Two microlense fibers were connected to the two ends of the fiber assembly in order to obtain uniformly distributed light on the tumor. Laser beams from the two fiber ends were directed

on the tumor from opposite directions horizontally and encompassed the tumor areas. This method was developed to assure that the internal organs (with high level of Pc4, such as liver and kidney) below the tumor were exposed to minimal laser light. The fluence rate was kept at 132 mW/cm^2, the total fluence was 150 J/cm^2 and the exposure time was 19 min.

4.3   NUMERICAL METHODS

4.3.1   OPS Data Analysis Algorithm

This section outlines the data analysis algorithm presented by Mourant *et al.* [3]. The modified Beer-Lambert law is used to relate changes in collected light intensity measured by the OPS to changes in the absorption coefficient within the medium, as follows:

$$- \log \left(\frac{I\left(\lambda, t\right)}{I\left(\lambda, t_0\right)} \right) = \Delta \mu_a\left(\lambda, t\right) \langle L \rangle \left(\mu_a^{total}\left(\lambda, t\right) \right) + B\left(\lambda, t\right) \tag{4.1}$$

Here, λ is the wavelength, and $I\left(\lambda, t_o\right)$ and $I\left(\lambda, t\right)$ are the collected light intensities measured by the OPS at times t_o and t, $(t > t_o)$. The left-hand side term, $-\log \left(\frac{I(\lambda, t)}{I(\lambda, t_0)} \right)$, represents the change in the absorbance of the sample between t_o and t. The $\Delta \mu_a^{total}\left(\lambda, t\right)$ term represents the change in absorption coefficient between t and t_o, $\langle L \rangle \left(\mu_a^{total}\left(\lambda, t\right) \right)$ represents the mean photon path length, and $B\left(\lambda, t\right)$ represents the changes in collected light caused by changes in scattering properties between measurements at t and t_o. Each of these terms is described individually below.

This calculation treats the change in absorption coefficient as the the sum of the contribution from all chromophores within the medium, as follows:

$$\Delta \mu_a\left(\lambda, t\right) = \sum_i \epsilon_i\left(\lambda\right) \left[C_i\left(t\right) - C_i\left(t_o\right)\right] = \sum_i \epsilon_i\left(\lambda\right) \Delta C_i\left(t\right) \tag{4.2}$$

Here, $\epsilon_i\left(\lambda\right)$ represents the molar extinction coefficient. This study assumes that the tissue absorption coefficient in the wavelength range of $500 - 800$ nm is dominated by three compounds: Hb, HbO$_2$, and the PS. While other components absorb light in this wavelength

79

range, the total absorbance of other absorbers is significantly less than the dominant compounds, and they are assumed not to have an effect on this calculation [3]. Under this assumption, Equation (4.2) becomes,

$$\Delta\mu_a\left(\lambda,t\right) = \epsilon_{Hb}\left(\lambda\right)\Delta C_{Hb}\left(t\right) + \epsilon_{HbO_2}\left(\lambda\right)\Delta C_{HbO_2}\left(t\right) + \epsilon_{PS}\left(\lambda\right)\Delta C_{PS}\left(t\right) \quad (4.3)$$

The modified Beer-Lambert law, as shown in Equation (4.1), requires an estimate of the mean path length of collected photons, and it is given by $\langle L\rangle\left(\mu_a^{total}\left(\lambda,t\right)\right)$. Previously, Mourant *et al.* [3] specified an analytical relationship between $\langle L\rangle\left(\mu_a^{total}\left(\lambda,t\right)\right)$ and $\mu_a^{total}\left(\lambda,t\right)$ as follows:

$$\langle L_o\rangle\left(\mu_a^{total}\left(\lambda,t\right)\right) = x_0 + x_1 e^{\left(\mu_a^{total}(\lambda,t)x_2\right)} \quad (4.4)$$

$\langle L_o\rangle\left(\mu_a^{total}\left(\lambda,t\right)\right)$ denotes the path length function presented by Mourant *et al.* Here, x_0, x_1, and x_2 are fitted parameters (empirically determined from *in vitro* OPS measurement of blue dye in tissue-simulating phantoms [3]), and $\mu_a^{total}\left(\lambda,t\right)$ is calculated as follows:

$$\mu_a^{total}\left(\lambda,t\right) = \epsilon_{Hb}\left(\lambda\right)\left[\Delta C_{Hb}\left(t\right) + C_{Hb}\left(t_o\right)\right] + \epsilon_{HbO_2}\left(\lambda\right)\left[\Delta C_{Hb}\left(t\right) + C_{Hb}\left(t_o\right)\right]$$
$$+\epsilon_{Drug}\left(\lambda\right)C_{Drug}\left(t\right) \quad (4.5)$$

It has been shown that the OPS source-detector fiber separation in the range $1.5-1.8$ mm makes the path length insensitive to changes in the scattering properties of the medium [28]. However, changes in scattering do affect the amount of light collected, and this is represented by the $B\left(\lambda,t\right)$ term in Equation 4.1, which is given as,

$$B\left(\lambda,t\right) = z_1\left(t\right) + z_2\left(t\right)\lambda + z_3\left(t\right)\lambda^2 \quad (4.6)$$

where $z_0\left(t\right)$, $z_1\left(t\right)$, and $z_2\left(t\right)$ are fitted parameters.

The above equations were solved by minimizing the sum squared error between empirical and estimated values of $-\log\left(\frac{I(t,\lambda)}{I(t_0,\lambda)}\right)$ (in Equation (4.1)). This was achieved using the *lsqnonlin* function within the statistics toolbox in MATLAB (V.70.0.19901 R.14 ® 2008, The MathWorks, Natick, MA) [137]. This function utilized the Levenberg-Marquardt (LVM) algorithm [141] to numerically minimize the sum squared error by fitting the following parameters: $\Delta C_{Hb}\left(t\right)$, $\Delta C_{HbO}\left(t\right)$, $\Delta C_{PS}\left(t\right)$, $z_0\left(t\right)$, $z_1\left(t\right)$, and $z_2\left(t\right)$. The analysis also requires

80

estimation of initial values for $C_{Hb}(t_o)$, $C_{HbO}(t_o)$, $C_{PS}(t_o)$, which is done by solving Equation (4.1) with $I(\lambda, t_0)$ ratioed against a line with zero slope [3], as follows:

$$-\log(I(\lambda, t_o)) = \mu_a^{total}(\lambda, t_o)\langle L\rangle\left(\mu_a^{total}(\lambda, t_o)\right) + B(\lambda, t_o) \tag{4.7}$$

with all absorption assumed to be due to the presence of Hb and HbO, as follows:

$$\mu_a^{total}(\lambda, t_o) = \epsilon_{Hb}(\lambda)\,C_{Hb}(t_o) + \epsilon_{HbO}(\lambda)\,C_{HbO}(t_o) \tag{4.8}$$

4.3.1.1 Analytical Description of Photon Path Length

Equation (4.4) is unable to describe changes in $\langle L\rangle\left(\mu_a^{total}(\lambda, t)\right)$ for $\mu_a^{total}(\lambda, t) > 1.0$ cm^{-1}, instead predicting a constant $\langle L\rangle\left(\mu_a^{total}(\lambda, t)\right)$ value of 0.6 cm for absorption coefficients above that threshold. This study utilizes a MC model of the OPS measurement to investigate $\mu_a^{total}(\lambda, t)$ values between nearly zero (10^{-16}) and 30 cm^{-1}, and the resulting data are represented by the following function:

$$\langle L_n\rangle\left(\mu_a^{total}(\lambda, t)\right) = x_{n0}\left(\mu_a^{total}(\lambda, t) + x_{n1}\right)^{-x_{n2}} \tag{4.9}$$

Here, x_{n0}, x_{n1}, and x_{n2} are fitted parameters. This algorithm allows changes in $\mu_a^{total}(\lambda, t)$ when $\mu_a^{total}(\lambda, t) > 1$ cm^{-1} to affect $\langle L_n\rangle\left(\mu_a^{total}(\lambda, t)\right)$.

4.3.1.2 Vessel Correction Factor

The incorporation of a vessel correction factor is required to account for the pigment packaging effect of discrete vessels on the absorbance. Studies by Savaard *et al.* [140] and van Veen *et al.* [113] have described and implemented a functional relationship that relates the vessel correction factor to the mean vessel radius and total intra-vascular absorption coefficient (assumed to be equal to that of whole blood). This vessel correction factor, $VC(\lambda, t)$, is given as follows:

$$VC(\lambda, t) = \frac{1 - e^{-2\mu_{a,blood}(\lambda, t)r_{vessel}(t)}}{2r_{vessel}(t)\,\mu_{a,blood}(\lambda, t)} \tag{4.10}$$

Here, $\mu_{a,blood}(\lambda, t)$ is the absorption coefficient of whole blood, and $r_{vessel}(t)$ is the mean vessel radius. The $VC(\lambda, t)$ term is on the interval $[0, 1]$ and represents the fraction of

hemoglobin that contributes to the $\mu_a^{total}(\lambda, t)$ detected optically. The vessel corrected estimate of $\mu_a^{total}(\lambda, t)$, termed $\mu_a^{total,VC}(\lambda, t)$, is then given as,

$$
\begin{aligned}
\mu_a^{total,VC}(\lambda, t) &= VC(\lambda, t) f(t) \left(\epsilon_{Hb}(\lambda) C_{Hb}(t) + \epsilon_{HbO_2}(\lambda) C_{HbO_2}(t) \right) \\
&+ \sum_{i \notin \{Hb, HbO_2\}} \epsilon_i(\lambda) C_i(t)
\end{aligned}
\tag{4.11}
$$

where $f(t)$ is the blood volume fraction within the tissue, and the combined contribution of other chromophores is given by the summation term on the right-hand side of the Equation.

The $VC(\lambda, t)$ term described in Equation (4.10) is applied to the algorithm presented by Mourant *et al.* (and described in Section 4.3.1). Here, the $VC(\lambda, t)$ describes pigment packaging that results from the ratio of collected light intensities, as follows from the use of the modified Beer-Lambert law in Equation (4.1). This is an important caveat, because in this situation, the $r_{vessel}(t)$ parameter is not physiologically motivated. The value is simply the difference in vessel radius between the two intensity measurements; this topic is discussed further in Section 4.5. In order to clearly make this distinction, the 'effective' vessel radius estimated in the current work is identified by $\overline{r}_{vessel}(t)$. Incorporation of the $VC(\lambda, t)$ term into Equations (4.3) and (4.5), is given as:

$$
\begin{aligned}
\Delta\mu_a(\lambda, t) &= VC(\lambda, t) \left(\epsilon_{Hb}(\lambda) \Delta C_{Hb}(t) + \epsilon_{HbO}(\lambda) \Delta C_{HbO}(t) \right) \\
&+ \epsilon_{Drug}(\lambda) \Delta C_{Drug}(t)
\end{aligned}
\tag{4.12}
$$

$$
\begin{aligned}
\mu_a^{total}(\lambda, t) &= VC(\lambda, t) \left(\epsilon_{Hb}(\lambda) \left(\Delta C_{Hb}(t) + C_{Hb}(t) \right) + \epsilon_{HbO}(\lambda) \left(\Delta C_{HbO}(t) + C_{HbO}(t_o) \right) \right) \\
&+ \epsilon_{Drug}(\lambda) C_{Drug}(t)
\end{aligned}
\tag{4.13}
$$

It is worth noting that the inclusion of $\overline{r}_{vessel}(t)$ leads to the absence of $f(t)$ from Equations (4.12) and (4.13). This indicates that C_{Hb} and C_{Hb_2} terms in Equations (4.12) and (4.13) represent the concentration in the entire sampled tissue volume and not only the intra-vascular concentration. These equations were solved as in Section 4.3.1 (using the LVM algorithm) by fitting the parameters: $\Delta C_{Hb}(t)$, $\Delta C_{HbO}(t)$, $\Delta C_{PS}(t)$, $z_0(t)$, $z_1(t)$, $z_2(t)$, and $\overline{r}_{vessel}(t)$.

4.3.2 Monte Carlo Model

The MC model used here is an adaptation of the MCML program developed by Wang *et al.* [107], with the equations modified to describe photon movement through a medium containing either homogeneous chromophores or heterogeneous chromophores placed within discrete vessels. Figure 4.2 shows the cross-section of the MC model geometry used in simulating OPS measurement of tissue. Here, the z-coordinate specifies tissue length, the x-coordinate specifies tissue width, and the y-coordinate specifies tissue depth (which is normal to the cross-section shown in Figure 4.2). The OPS source and detector fibers are located at the air/tissue interface ($z = 0$). The source detector seperation is 1.75 mm, and the source and detector radii are 200 and 100 μM, respectively. In order to increase simulation efficiency, the detector fiber is treated as a 'ring' about the source fiber, such that all photons that exit the tissue with a radial distance from the source between 1.65 and 1.85 mm contact the detector. It is noted that this geometry does not have radial symmetry between source and detector fibers, however, this geometry may be more representative of OPS measurements on tissue because the orientation of source and detector fiber with respect to underlying vessels is never known (and is therefore never pefectly symmetric).

The tissue geometry is constructed as a semi-infinite medium, with the length of each coordinate selected such that photons propagating to these lengths would not have an impact on the detected intensity. The geometry contains discrete blood vessels that are arranged normal to the $x - z$ cross-section, and are assumed to extend uniformly in the y-coordinate. Moreover, the model specifies optical properties, such as the absorption, $\mu_{a,i}$, and scattering, $\mu_{s,i}$, coefficients as a function of position (i) in the (x, z) coordinate system. This $x - z$ cross section is uniform for the entire y-coordinate direction. This study assumed constant scattering properties throughout the geometry (including tissue and vessels), but extensions of the code to handle heterogeneous distributions of the scattering coefficient, μ_s, or anisotropy factor, g, are straightforward.

During photon propagation, the photon moves to an interaction site, where it undergoes absorption and scattering events. Photon movements are stochastically simulated [107], with
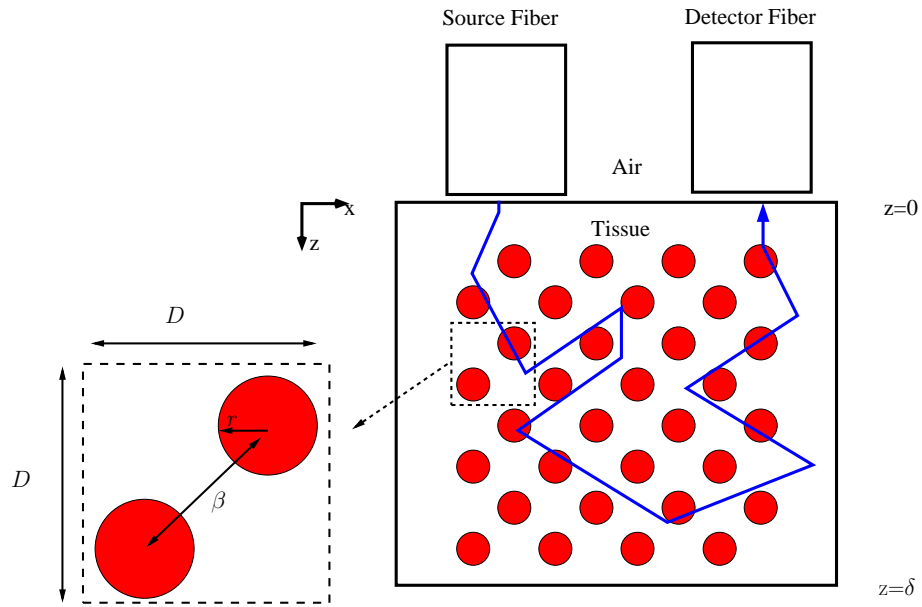
Figure 4.2: Geometry for MC model of OPS measurement of tissue, with photon packet shown propagating from source to detector fiber. The tissue includes discrete blood vessels throughout (visualized as dark circles in the diagram). Inset: tissue 'block' containing two vessels with the parameters used to define vessel position and size.

the step sizes given as:

$$l_i = \frac{-\ln(\zeta_{step})}{\mu_{s,i} + \mu_{a,i}} \tag{4.14}$$

Here, ζ_{step} is a random number uniformly distributed on the interval $(0,1]$, and $\mu_{s,i}$ and $\mu_{a,i}$ are the respective scattering and absorption coefficients specified at position (x_i, y_i, z_i).

Scattering events redirect the photon in a new direction that is specified by the scattering angle, $\theta_{scatter}$ and the azithmul angle, θ_{azim}. The azithmul angle is chosen as a uniformly distributed value on the interval $[0, 2\pi]$. The expected value of $\theta_{scatter}$ is given by the anisotropy factor of the tissue, g, which is equal to $\cos(\theta_{scatter})$. Therefore, g specifies the likelihood of the photon being forward-scattered ($g = 1$), back-scattered ($g = -1$), or isotropically scattered ($g = 0$).

The photon scattering angle, $\theta_{scatter}$, is calculating using the Henyey-Greenstein scattering phase function, which is represented by [107]:

$$\cos(\theta_{scatter}) = \frac{1}{2g}\left[1 + g^2 - \left(\frac{1 - g^2}{1 - g + 2g\zeta_{scatter}}\right)^2\right] \tag{4.15}$$

Here, $\zeta_{scatter}$ is a random number uniformly distributed on the interval $[0,1]$. For isotropic scattering, when $g = 0$, equal weight is given to all possible scattering angles, and $\theta_{scatter}$ is given by:

$$\cos(\theta_{scatter}) = 2\zeta_{scatter} - 1 \tag{4.16}$$

Photon trajectories are then given as:

$$\mu'_x = \frac{\sin(\theta_{scatter})}{\sqrt{1 - \mu_z^2}}[\mu_x\mu_z\cos(\theta_{azim}) - \mu_y\sin(\theta_{azim})] - \mu_x\cos(\theta_{scatter}) \tag{4.17}$$

$$\mu'_y = \frac{sin(\theta_{scatter})}{\sqrt{1 - \mu_z^2}}[\mu_y\mu_z cos(\theta_{azim}) + \mu_x sin(\theta_{azim})] + \mu_y cos(\theta_{scatter}) \tag{4.18}$$

$$\mu'_z = -\sin(\theta_{scatter})\cos(\theta_{azim})\sqrt{1 - \mu_z^2} + \mu_z\cos(\theta_{scatter}) \tag{4.19}$$

If $|\mu_z| > 0.999$, the photon is almost totally forward or backward scattered, and to avoid division by zero in Equations (4.17) and (4.18) the new trajectories are given as:

$$\mu'_x = \sin(\theta_{scatter})\cos(\theta_{azim}) \tag{4.20}$$

$$\mu'_y = \sin(\theta_{scatter})\sin(\theta_{azim}) \tag{4.21}$$

$$\mu'_z = -\frac{\mu_z}{|\mu_z|}\cos(\theta_{azim}) \tag{4.22}$$

As a photon propagates through the tissue, it can cross the boundaries between regions with different refractive indexes, n_i. When this occurs, the photon is propagated to the boundary, and Fresnel's equations are used to determine if it reflects back into the original region, or is refracted into the new region. The Fresnel reflection coefficient, R, is given as:

$$R = \frac{1}{2}\left[\frac{\sin^2(\theta_i - \theta_t)}{\sin^2(\theta_i + \theta_t)} + \frac{\tan^2(\theta_i - \theta_t)}{\tan^2(\theta_i + \theta_t)}\right] \tag{4.23}$$

Here, the incident angle between the photon and the boundary is given as: $\theta_i = \cos^{-1}(\mu_z)$. A random number, ζ_{ref}, uniformly distributed on the interval $[0, 1]$, is selected and compared with R, such that if $\zeta_{ref} < R$, the photon is refracted, otherwise it is reflected. For reflected photons, the z-direction vector is adjusted such that:

$$\left(\mu'_x, \mu'_y, \mu'_z\right) = (\mu_x, \mu_y, -\mu_z) \tag{4.24}$$

The photon is then moved the remainder of the original step in the new direction. For refracted photons, the direction of refraction is given by Snell's law as:

$$n_i\sin(\theta_i) = n_t\sin(\theta_t) \tag{4.25}$$

where the n_i and n_t are the refractive indexes in the original and new regions, respectively, and θ_i and θ_t are the incident and refracted angles, respectively. The directional vectors for refracted photons are then adjusted as:

$$\mu'_x = \mu_x\frac{n_i}{n_t} \tag{4.26}$$

$$\mu'_y = \mu_y\frac{n_i}{n_t} \tag{4.27}$$

$$\mu'_z = \mu_z\frac{n_i}{n_t} \tag{4.28}$$

During simulation of a medium containing discrete blood vessels, the photon path is analyzed at each step to determine if the path intersects a vessel. When this occurs, the photon is propagated to the site where the photon contacts the vessel, and the step is adjusted as:

$$\Delta l_i' = \frac{\mu_{a,i}}{\mu_{a,j}} \Delta l_i \tag{4.29}$$

Here, Δl_i is the remaining original step length, $\Delta l_i'$ is the adjusted step length, and $\mu_{a,i}$ and $\mu_{a,j}$ are the absorption coefficients at the original and new locations, respectively. The photon is then propagated to a new location and the absorption coefficient of the new location is checked and updated.

Photon absorption is modeled by simulating photon 'packet' propagation. This is a technique that allows absorption to be described by depositing portions of the photon packet at the site of each absorption event [107]. The weight for photon packet k is initialized as $W_k = 1$, and during an absorption event, the deposited photon weight is calculated as $\Delta W_{k,i} = \frac{\mu_{a,i}}{\mu_{a,i}+\mu_{s,i}}$. Here, $\Delta W_{k,i}$ is the weight of photon packet k deposited into the tissue at site i. The new weight of the photon after absorption calculated is $W_k' = W_k - \Delta W_{k,i}$, and the remainder of the photon packet is then scattered. This technique is more efficient than modeling absorption as an 'all or nothing' event, by reducing the number of photon initializations [107].

During simulation, photons that cross the air interface at the location of the detector at an angle within the fiber's cone of acceptance are detected. The model computes the collected light intensity (I) as:

$$I = \frac{\displaystyle\sum_{m=0}^{N_{collected}} W_m}{N_{collected}} \tag{4.30}$$

Here W_m is the weight of detected photon m, and $N_{collected}$ is the number of collected photons. The effective mean photon path length is given as:

$$\langle L \rangle = \frac{\displaystyle\sum_{m=0}^{N_{collected}} L_m W_m}{\displaystyle\sum_{m=0}^{N_{collected}} W_m} \tag{4.31}$$

The total path length for each collected photon is given as the sum of individual steps, as $L_m = \sum l_i$. The absorption coefficient is calculated from the modified Beer-Lambert law as:

$$\mu_a(t_2) = \left\{ -\log \left[\frac{I(t_2)}{I(t_1)} \right] + \mu_a(t_1) \left[\langle L \rangle (t_1) \right] \right\} \left[\langle L \rangle (t_2) \right]^{-1} \tag{4.32}$$

Analyzing OPS measurements in a medium with discrete vessels requires incorporation of the vessel correction factor from Equation (4.10). This is used to quantify the absolute value of the absorption coefficient (measured at t_1), as:

$$\mu_a(t_1) = VC(t_1)f(t_1)\mu_{vessel}(t_1) + (1 - f(t_1))\mu_{a,background}(t_1) \tag{4.33}$$

Here, $f(t_1)$ the blood volume fraction (as used in Equation (4.11)) and $\mu_{a,background}(t_1)$ is the background absorption of the tissue.

4.3.2.1 Model Geometry   Blood vessels were defined within the model geometry by analytical expressions using criteria similar to that reported by Verkruysse *et al.* [112]. The inset of Figure 4.2 shows the parameters that describe a tissue-capillary 'block'. Each block contains two capillaries, with the shortest distance between vessel centers given as β, the vessel radius given as r, and the block length specified as D. The blocks were repeated over the entire sample in both x- and z-directions to construct the vessel network cross-section within the tissue sample. Table 4.1 lists the parameter values for seven vessel configurations that are representative of vessel networks within skin tissue *in vivo*. For each simulated geometry, the fractional area occupied by vessels is calculated by $f = \frac{\text{vessel area}}{\text{tissue area}}$.

Table 4.1: Geometric parameters describing the blood vessel configurations. Fractional vessel area is given by f, vessel radius by r_{vessel}, and block length by D.

Geometry	$f(\%)$	$r_{vessel}(\mu m)$	$D(\mu m)$
1	33.0	32	139.6
2	22.0	32	171.0
3	16.5	32	197.5
4	11.0	32	241.9
5	5.50	32	342.0
6	2.250	32	483.7
7	1.125	32	745.2

4.3.3 Numerical Simulation

Tissue optical properties are similar to values reported by Cheong *et al.* [24], including: $\mu_{s,background} = \mu_{s,vessel} = 50$ cm^{-1}, $g = 0.95$, $n_{tissue} = 1.37$, $n_{fiber} = 1.45$, and $NA_{fiber} = 0.22$. MC simulations investigated OPS measurement of geometries with: (1) uniformly distributed chromophores; and (2) non-uniform distributions that contain discrete capillaries. For the uniform case, μ_a^{total} is specified at 11 values, as:

$\mu_a^{total} \in \{10^{-16}, 0.001, 0.003, 0.01, 0.03, 0.1, 0.3, 1, 3, 10, 30\}$ cm^{-1}. For the nonuniform case, there were 7 different model geometries constructed, with details listed in Table 4.1. The nonuniform cases specify the background (tissue) absorption fixed for all geometries at $\mu_{a,background} = 0.1$ cm^{-1}, and $\mu_{a,vessel}$ is specified at 7 discrete values:

$\mu_{a,vessel} \in \{10^{-16}, 0.1, 0.3, 1, 3, 10, 30, 100\}$ cm^{-1}. The extinction coefficients for Hb and HbO$_2$ were measured in water by Zijlstra *et al.* [2]. The concentration of total hemoglobin in whole blood was approximated by assuming 45 % hematocrit (5400 μM) [142].

MATLAB (V.70.0.19901 R.14 ® 2008, The MathWorks, Natick, MA) code was scripted to execute the MC simulations, with 10^6 photon 'packets' simulated per case. Standard deviations were calculated from the results of 3 independent simulations. The MC model was validated for the homogeneous case by comparing results with data reported by Wang *et al.* [107].

A model performance metric was utilized to determine if the extensions to the previous algorithm improved the description of the OPS data. Because the different algorithms have a different number of fitted parameters, a fair comparison of the differing models requires a metric that considers both the reduction in residual error and accounts for the additional fitted parameters. Model-estimates were evaluated using the Akaike's information criterion (AIC) as described in Equation (3.9). The model resulting in the lowest AIC value is the superior model.

4.4   RESULTS

4.4.1   MC Analysis: Photon Path Length

Figure 4.3 shows the mean photon path length calculated from simulated OPS measurement of mediums containing uniformly distributed chromophores. The data points represent the average of mean path length values from three independent simulations, and the error-bars indicate one standard deviation about the mean. Also shown on the plots are estimates of $\langle L \rangle \left(\mu_a^{total} \left(\lambda, t \right) \right)$ from both the Mourant $et\ al.$ study, $\langle L_o \rangle \left(\mu_a^{total} \left(\lambda, t \right) \right)$, and the present study, $\langle L_n \rangle \left(\mu_a^{total} \left(\lambda, t \right) \right)$. The data are shown on a linear scale on Figure 4.3 (Top) and on a $\ln - \ln$ scale on Figure 4.3 (Bottom). Note that in the range $10^{-16} < \mu_a^{total} \left(\lambda, t \right) < 0.001$ cm^{-1}, changes in $\mu_a^{total} \left(\lambda, t \right)$ are too small to have an observable effect on path length; this phenomenon is described by both $\langle L_o \rangle \left(\mu_a^{total} \left(\lambda, t \right) \right)$ and $\langle L_n \rangle \left(\mu_a^{total} \left(\lambda, t \right) \right)$. For $\mu_a^{total} \left(\lambda, t \right) <$ 1.0 cm^{-1}, Figure 4.3 (Bottom) shows that $\langle L_n \rangle \left(\mu_a^{total} \left(\lambda, t \right) \right)$ accurately represents the data, while $\langle L_o \rangle \left(\mu_a^{total} \left(\lambda, t \right) \right)$ overpredicts the path length. However, for $\mu_a^{total} \left(\lambda, t \right) > 1$ cm^{-1}, $\langle L_n \rangle \left(\mu_a^{total} \left(\lambda, t \right) \right)$ captures the relationship (and is sensitive to changes in $\mu_a^{total} \left(\lambda, t \right)$) while $\langle L_o \rangle \left(\mu_a^{total} \left(\lambda, t \right) \right)$ does not (by not being sensitive to any changes in $\mu_a^{total} \left(\lambda, t \right)$).

4.4.2   MC Analysis: Vessel Correction Factor

MC simulations investigated OPS measurement of a medium containing discrete vessels. Here, various vascular fractions are considered (range: $1.12 - 33\%$) each with the same vessel radius ($r_{vessel} = 32\ \mu m$). Figure 4.4 (Top) shows the calculated vs. the specified intra-vessel $\Delta \mu_a$. Here, the relationship between $\Delta \mu_{a,calculated}$ and $\Delta \mu_{a,vessel}$ is different for each vascular fraction, with smaller vascular fractions associated with a smaller effect on the calculated absorption coefficient. Figure 4.4 (Bottom) shows the calculated $\Delta \mu_a$ data from Figure 4.4 (Top) plotted vs. the vessel corrected $\Delta \mu_a$ (calculated from Equation (4.12)). Here, the data are shown in a $\ln - \ln$ scale in order to visualize the range of simulated absorption coefficients. This plot also contains the line of unity to show the expected relationship between the calculated and vessel corrected absorption coefficient. Here, the calculated $\Delta \mu_a$ is well-correlated with the vessel corrected $\Delta \mu_a$ ($r^2 = 0.994$) for all geometries. These data
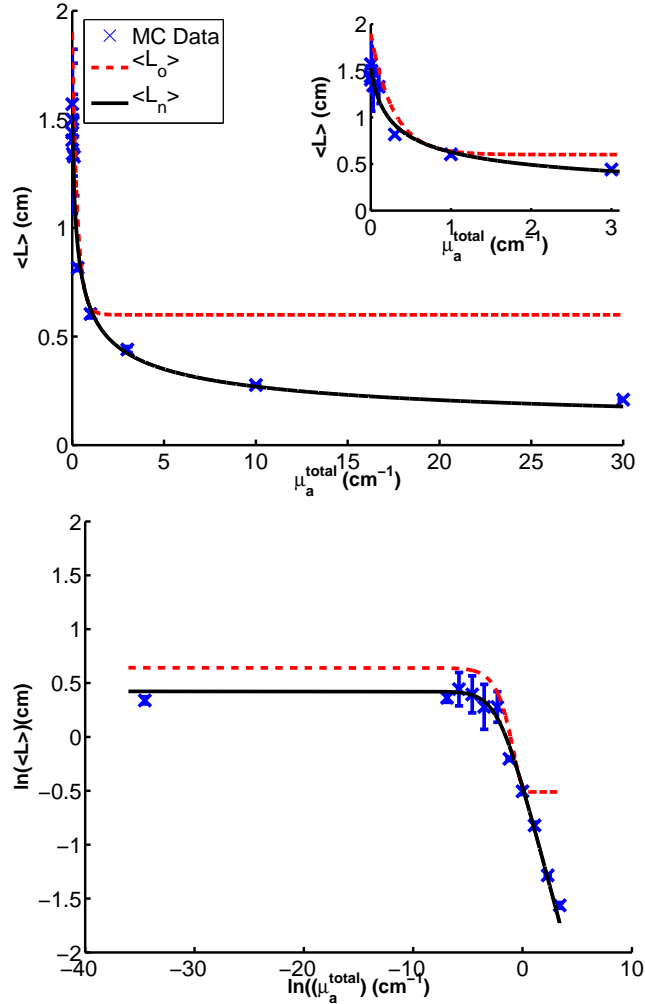
Figure 4.3: Mean photon path length calculated from MC simulation of OPS measurement of mediums containing uniformly distributed absorption coefficient. Photon path length functions presented by Mourant *et al.* [3], $\langle L_o \rangle$, and Equation (4.9), $\langle L_n \rangle$. Data shown on both linear scale (Top) and $\ln - \ln$ scale (Bottom). The inset of the Top figure expands the absorption coefficient scale over $0 - 3$ cm^{-1}.

suggest that the incorporation of a vessel correction factor into the data analysis algorithm could account for the effect of discrete vessels on the absorption coefficient estimated from OPS measurements.

4.4.3 Estimation of Pc4 Concentration in Intralipid⃝r *in vitro*

Figure 4.5 (Top) shows Pc4 concentration estimates from *in vitro* OPS measurement of an Intralipid⃝R solution containing Pc4 concentrations of 0.1, 0.3, 1, 3, 10, and 30 μM. Data points indicate Pc4 concentrations calculated from Equation (4.1), with the path length function defined as either $\langle L_o \rangle$ or $\langle L_n \rangle$. These model estimates are termed Model-o and Model-n, respectively. The line of unity (slope $= 1$) is included to show the relation between concentrations estimated by Model-o and Model-n to the expected linear relationship. The data show that for a Pc4 concentration range of $0.1 - 10$ μM, estimates from both Model-o and Model-n are near the line of unity. However, for a Pc4 concentration of 30 μM, Model-n is able to accurately predict the concentration, while the Model-o estimate contains a negative bias, with significant underprediction of the actual Pc4 concentration. The error in the Model-o estimate is due to an inability of $\langle L_o \rangle \left(\mu_a^{total} (\lambda, t) \right)$ to describe changes to path length in response to changes in $\mu_a^{total} (\lambda, t)$ caused by increases in Pc4 concentration. For the Pc4 concentration of 30 μM, the average maximum $\mu_a^{total} (\lambda, t)$ within the fitted wavelength range was 7.5 cm^{-1}. This causes the $\langle L_o \rangle \left(\mu_a^{total} (\lambda, t) \right)$ function to 'saturate' to a constant value, as shown in Figure 4.5 (Bottom), which contains the photon path length estimates vs. wavelength for one OPS measurement of Intralipid⃝R containing 30 μM Pc4. Here, the model utilizing $\langle L_o \rangle \left(\mu_a^{total} (\lambda, t) \right)$ is unable to resolve the Pc4 absorption peak. Over the same wavelength range, $\langle L_n \rangle \left(\mu_a^{total} (\lambda, t) \right)$ is able to accurately resolve the Pc4 absorption peak. These results indicate the need to incorporate $\langle L_n \rangle \left(\mu_a^{total} (\lambda, t) \right)$ for estimation of chromophore concentrations when $\mu_a^{total} (\lambda, t) > 1$ cm^{-1}.

4.4.4 Quantitation of Pc4 and Hb Concentration and Hb Saturation *in vivo*

Figure 4.6 shows an OPS measurement of a murine xenograft *in vivo* and the corresponding model-estimated parameters. The absorbance shown in Figure 4.6(A) is calculated by
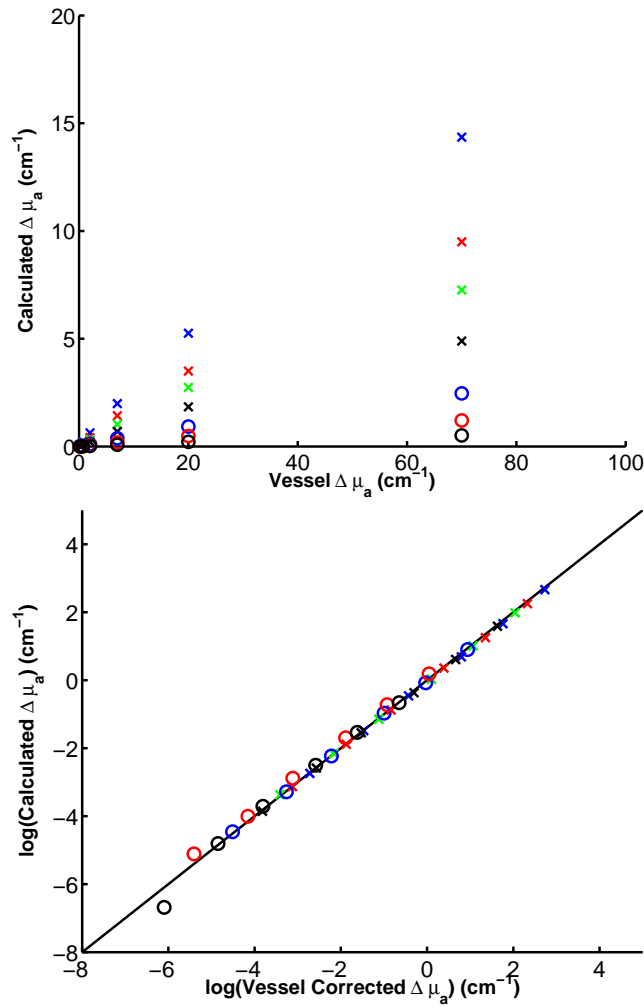
Figure 4.4: Results from MC simulation of OPS measurement of medium containing discrete vessels for various vascular fractions. Top: Change in calculated vs. specified absorption coefficient within vessels. Geometries 1-7 are included (see Table 4.1), and appear in vertical order from top (blue '×', geometry 1), to bottom (black '∘', geometry 7). Bottom: Change in calculated vs. vessel corrected absorption coefficient within medium on a $\ln - \ln$ scale.
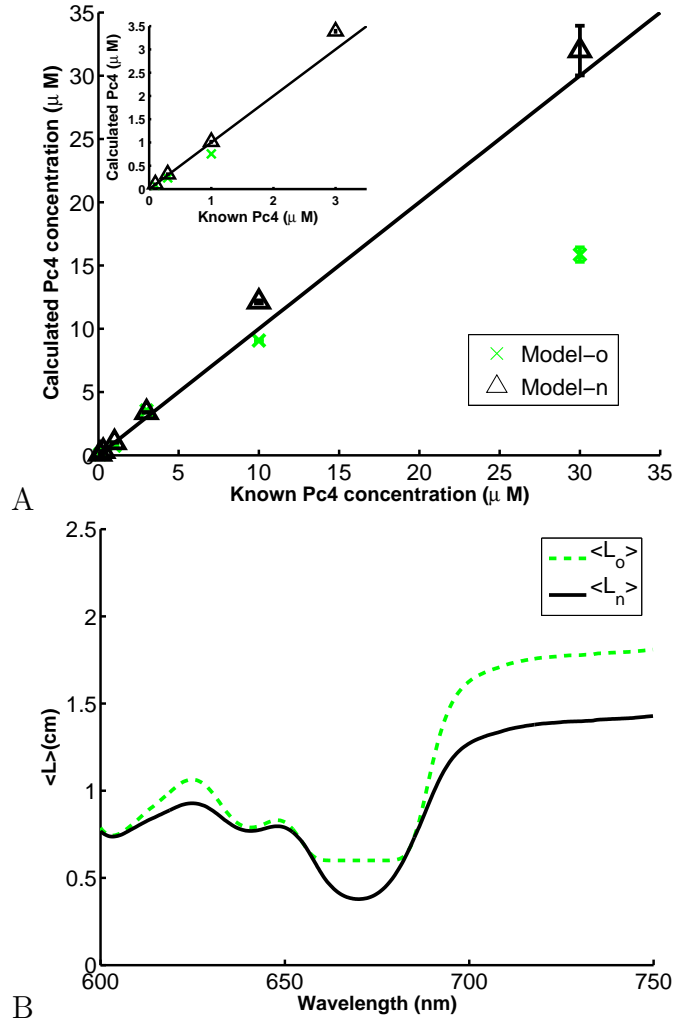
Figure 4.5: Measurement of Pc4 in Intralipid® *in vitro* by OPS. Photon path length is estimated using $\langle L_o \rangle \left(\mu_a^{total} (\lambda, t) \right)$ for Model-o and $\langle L_n \rangle \left(\mu_a^{total} (\lambda, t) \right)$ for Model-n. Top: estimated vs. known Pc4 concentration. Bottom: estimated mean photon path length vs. wavelength for both fitted models for measurement of Intralipid® containing 30 μM Pc4.

ratioing collected light intensities measured prior to Pc4 administration, and 5 min after completion of laser administration. This plot shows the model estimated absorbance from the original Mourant algorithm (termed Model-o), the algorithm with $\langle L_n \rangle \left(\mu_a^{total} (\lambda, t) \right)$ incorporated (Model-n), and the algorithm with both $\langle L_n \rangle \left(\mu_a^{total} (\lambda, t) \right)$ and the vessel correction factor incorporated (Model-nvc). The spectra shown in Figure 4.6(A) shows classic signs of 'pigment packaging'. Here, the absorption band that is clearly visible in the $740 - 760$ nm range is attributable to Hb. This should correspond with a dominant peak in the $500 - 600$ nm range; however, the absorption bands in that range are broad and flat. This effect is attributable to the shielding effect of discrete vessels on the elastically scattered light, which causes light in the $500 - 600$ nm wavelength range to only sample a subset of the blood present within the tissue. The incorporation of the vessel correction factor in Model-nvc allows the model to capture the effect of pigment packaging on $\mu_a^{total} (\lambda, t)$. Figure 4.6(B) shows the estimate of $VC (\lambda, t)$ over the fitted wavelength range, which represents the fraction of blood that is sampled by the optical measurement. Here, it is evident that light in the $500 - 600$ nm wavelength range only sampled a subset of the blood present within the tissue. Note that the absorbance spectra measured on this mouse subject at all sampling times are included in Appendix C.

As shown in Figure 4.6A, Model-nvc clearly captures all features in the empirical data. However, Model-o and Model-n are unable to describe the key absorption bands that are associated with Hb, HbO_2, and Pc4. The improvement in the quality of fit is displayed by Figure 4.6(C), which shows the residual error for each model estimate. The sum squared error (SSE) quantified over $520 - 800$ nm showed that Model-nvc reduced error by 96% compared with Model-o, and by 94% compared with Model-n. Moreover, the calculated AIC for Model-o, Model-n, and Model-nvc are -4473, -4882, and -7187, respectively, which indicates that Model-nvc is the superior model of the data.

Figures 4.6(D) and (E) show the estimates of $\mu_a^{total} (\lambda, t)$ and $\langle L \rangle \left(\mu_a^{total} (\lambda, t) \right)$ vs. wavelength for each fitted model. The strong absorption bands of Hb and HbO_2 result in estimates of $\mu_a^{total} (\lambda, t) > 1$ cm^{-1} in the $500 - 600$ nm wavelength range for all models. This causes 'saturation' of $\langle L_o \rangle \left(\mu_a^{total} (\lambda, t) \right)$ in Model-o, as shown in Figure 4.6(D), and is expected to contribute to error in predictions made using Model-o.
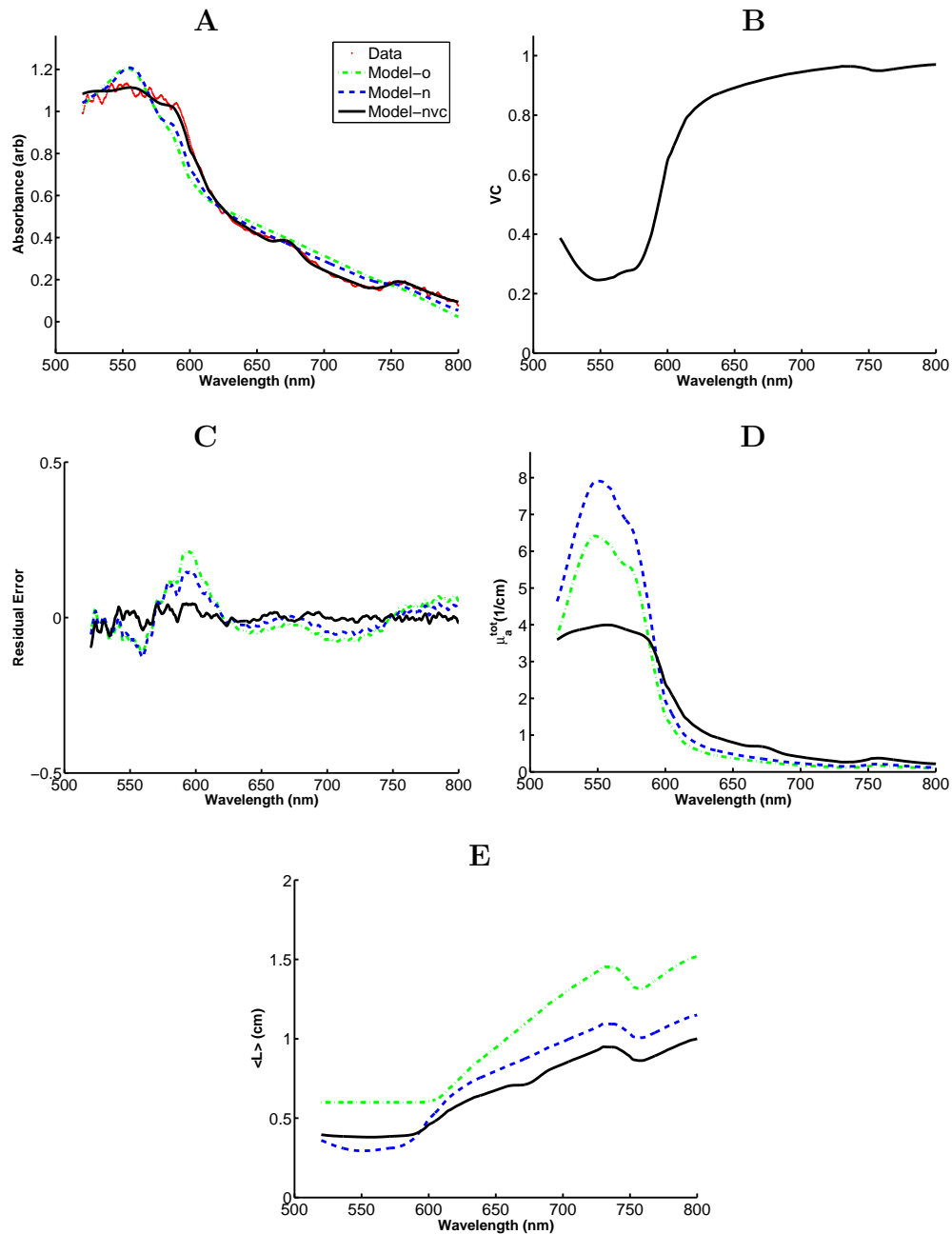
Figure 4.6: Absorbance calculated from the ratio of collected light intensities prior to Pc4 administration and 5 min after laser administration. A: empirical and model-estimated absorbance data; B: vessel correction factor over fitted wavelength range incorporated in Model-nvc; C: residual error over fitted wavelength range; D: total absorption coefficient; and E: mean photon path length.

Figure 4.7 shows total Hb concentration (A), Hb saturation (B), and Pc4 concentration (C) calculated from OPS measurements of the mouse subject at time points between 1 and 1440 min following PDT. Data points represent mean values from three OPS measurements at each time point, while error-bars indicate one standard deviation about the mean. The model estimates of total Hb concentration shown in Figure 4.7(A) are dramatically different for Model-nvc, due to the inclusion of the vessel correction factor. Here, Model-nvc estimates a 235% increase in total Hb concentration in tissue between pre-laser administration and after 5 min of laser exposure. This finding is consistent with previous studies that have reported increases in blood flow in response to PDT treatment [81]. Comparatively, over this same time interval, Model-o estimates no change in total Hb concentration, and Model-n estimates only a 20% increase.

Figure 4.7 (B) shows the estimated Hb saturation in the tumor xenograft, with no significant difference between estimates from the three models. Figure 4.7 (C) shows model estimates of Pc4 concentrations for the sampled times. After laser administration, all models estimate a reduction in Pc4 concentration, which is possibly attributable to photobleaching of the Pc4 compound. However, at 5 min after laser, Model-nvc estimates a Pc4 concentration of 0.27 μM, while Model-n estimates 0.08 μM, and the Model-o estimate is ~ 0 μM. These differences are attributed to an increased sensitivity of Model-n and Model-nvc to the presence of the Pc4 absorption bands, compared with Model-o. This is evidenced by Figure 4.6 (A), which shows that Model-nvc is able to characterize the absorbance attributable to the Pc4 absorption peak between $650 - 700$ nm, while neither Model-o nor Model-n capture these bands. These results suggest that the inclusion of the VC term allows for improved quantification of non-hemoglobin absorbers.

Figure 4.7 (D) shows the estimates of the effective mean vessel radius over the sampled time points. These values range between near zero (10^{-12}) and 0.15 mm. Estimates of vessel radius show the same temporal dynamics as the total Hb concentration shown in 4.7A, and there exists a strong correlation between the parameters ($r = 0.854$). Here, near-zero values of $\bar{r}_{vessel}(t)$ represent the situation where there is no change in pigment packaging between the ratioed intensity measurements.

The data presented thus far suggest that the incorporation of the vessel correction factor reduces the error within the model estimates of absorbance. The reduction in error is related to the magnitude of the estimated $\bar{r}_{vessel}(t)$ parameter. This is shown in Figure 4.8, which plots the percentage reduction in the residual SSE vs. the corresponding estimate of $\bar{r}_{vessel}(t)$ for each fitted spectra. The direct comparison of the SSE reduction between Model-o and Model-nvc is shown in Figure 4.8(Top). Here, the mean SSE is reduced by $52.2 \pm 35.0\%$ (range: -63.4 to 94.4). These reductions in error are attributable to the inclusion of $\langle L_n \rangle$ and the incorporation of VC. A direct comparison of the SSE resulting from Model-n and Model-nvc is shown in Figure 4.8 (Bottom). In this case, the mean SSE is reduced by $38.7 \pm 35.2\%$ (range: -0.2 to 91.2). These reductions in error are attributable solely to the effect of $VC(\lambda, t)$ on fit quality. It should be noted that negative % decreases in error shown on Figure 4.8(Top) have a negligable effect on the model estimate, and are the result of a ratio of small numbers. Negative % changes had an absolute error difference of < 0.066, a value an order of magnitude smaller than the mean error reduction in either plot (1.1, Top; 0.52, Bottom). Moreover, all fits that resulted in negative % on Figure 4.8(Top) had r^2 values > 0.98. These results indicate that incorporation of $\langle L_n \rangle \left(\mu_a^{total}(\lambda, t) \right)$ and $VC(\lambda, t)$ into Model-nvc does not introduce error into the analysis of spectra that do not contain pigment packaging. Moreover, these plots show that $\bar{r}_{vessel}(t)$ estimates are associated with reductions in SSE percentage, with larger values of $\bar{r}_{vessel}(t)$ associated with increased reduction in error.

4.5   DISCUSSION

The OPS has been suggested as a tool to monitor photosensitizer concentration, total Hb concentration, and Hb saturation in tissue *in vivo* during photodynamic therapy. This work is an extension to a previously published algorithm [3] that improves the quality of model-estimated chromophore concentrations from OPS measurements of tissue *in vivo*. An analytical relationship between effecitve photon path length and total absorption coefficient was established for $\mu_a^{total} \leq 30$ cm^{-1}. This novel functionality improved the estimates of Pc4 concentrations in Intralipid® solutions *in vitro*. The results show the need to incorpo-
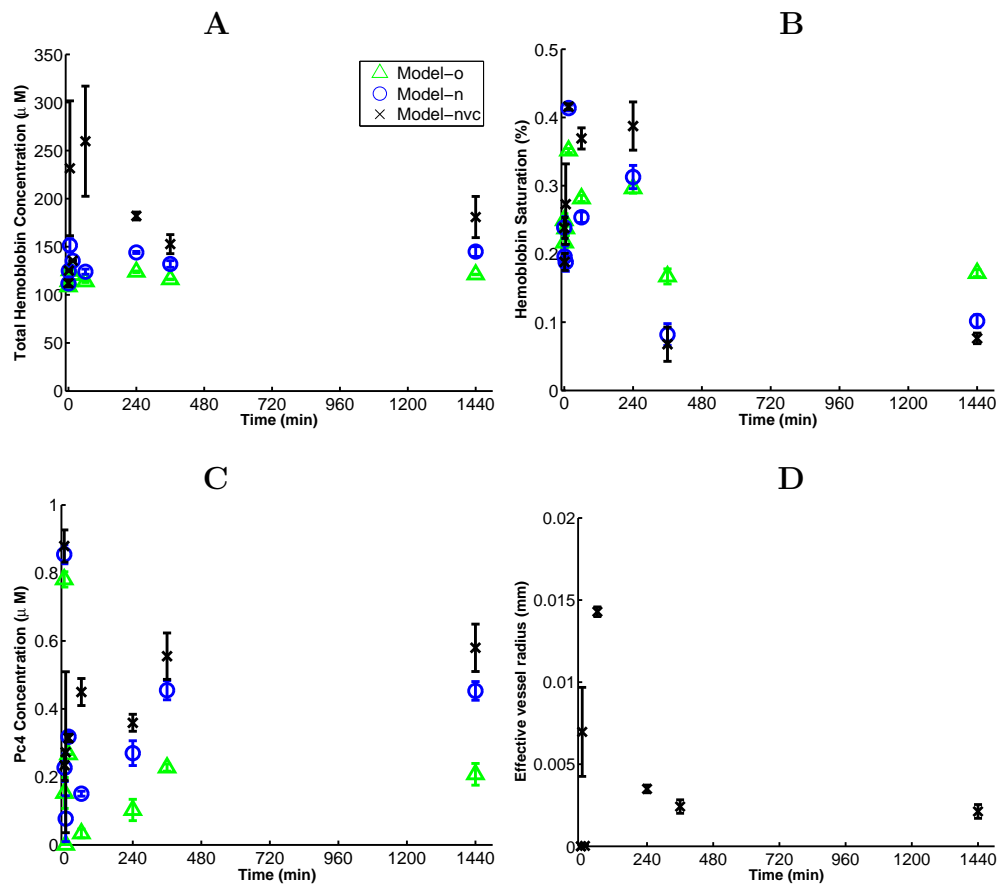
Figure 4.7: Model-estimated system parameters from measurements of murine xenograft by the OPS at sampling time prior to- and following laser administration. Estimates are given for all three fitted models. A: total Hb concentration; B: Hb saturation; C: Pc4 concentration; and D: effective vessel radius.
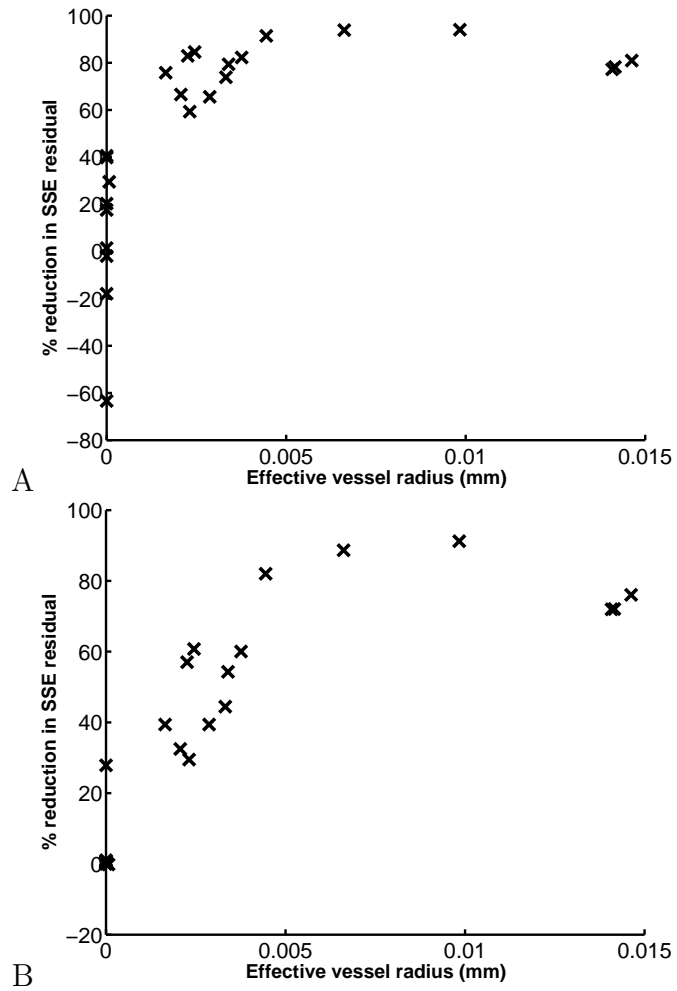
Figure 4.8: Percentage reduction in SSE residual vs. the estimated vessel radius. A: SSE reduction between model Model-o and Model-nvc. B: SSE reduction between Model-n and Model-nvc.

rate a novel functional relationship between mean photon path length and total absorption coefficient that captures the relationship for $\mu_a^{total} > 1$ cm^{-1}.

The results also motivate the incorporation of a vessel correction factor for analysis of OPS measurements of tissue *in vivo*. The vessel correction factor accounts for the pigment packaging effect of discrete blood vessels on the absorption coefficient estimated from OPS measurements. The pigment packaging effect has been described thoroughly [29], and is related to the mean vessel size and absorption coefficient of the blood [112]. The factor was incorporated into analysis of measurements of tissue during PDT, resulting in large reductions in the SSE residual and significant changes to model estimates of total Hb concentration and Pc4 concentration. Incorporation of the $VC(\lambda, t)$ term allows accurate estimation of changes to the total blood content sampled within tissue, the importance of which is shown by the marked reduction in SSE attributable to the $VC(\lambda, t)$ term. Total blood content is an important factor for analysis of tissue after PDT treatment. PDT damage to the tissue can cause increased blood flow via either vessel dilation or vascular spasm [81]. Moreover, damage to the vasculature may cause blood to enter the tissue interstitial space [81]. The results in Figure 4.7A show a 2.5-fold increase in the total Hb concentration after the administration of laser. In order for the OPS to accurately estimate these changes following PDT treatment, incorporation of the vessel correction factor is required.

The $\overline{r}_{vessel}(t)$ parameter incorporated into the $VC(\lambda, t)$ term in this study is an 'effective' value, and is not representative of actual vessel size. This is because instead of applying the vessel correction factor to absolute values of measured spectra (as done previously [113]), this study uses the vessel correction factor to correct for differences in 'pigment packaging' between two intensity measurements. The maximum estimated values of $\overline{r}_{vessel}(t)$ in this study were below 200 μm, which is a physiologically realistic value for tissue [113]. However, the algorithm allows the the $\overline{r}_{vessel}(t)$ term to approach zero, which occurred for spectra that did not show 'pigment packaging' features. In situations where $\overline{r}_{vessel}(t)$ is near zero, the $VC(\lambda, t)$ term will be equal to unity over the entire wavelength range, and the absorbance estimate of algorithm Model-nvc collapses to Model-n.

4.5.1 Summary

This study presented OPS measurement data from *in vivo* measurement of one mouse subject bearing a xenograft undergoing PDT. This was included to express the utility of the extended algorithm. The results show that incorporation of $\langle L_n \rangle$ and VC reduced the SSE and resulted in different model estimates for total Hb concentration and Pc4 concentration. Moreover, algorithms without the VC factor were unable to capture key features that were representative of pigment packaging. However, the current study does not include an independent measurement of total Hb concentration, Hb saturation, or Pc4 concentration within the tissue *in vivo*. So, while the results of the current study describe the theoretical justification for the extensions and application of the extended algorithm to *in vivo* data, and suggest the utility of such extensions, there still exists the need for future work to validate these claims *in vivo*. Moreover, while the current study presents *in vivo* data exclusively from one murine subject, ongoing work will present analysis of multiple subjects, including an analysis of intra- vs. inter-subject variability.

5.0 *IN SILICO* DETECTION OF TUMOR HYPOXIA BY OPS

5.1 BACKGROUND

Optical spectroscopy is a technique capable of measuring noninvasively the absorption caused by changes in chromophore concentrations in tissue *in vivo* [15]. Hemoglobin is an endogenous absorber that has an oxygenation-state dependent absorption coefficient. This makes it possible to optically quantitate changes in hemoglobin saturation (HbSat) noninvasively in tissue. This measurement is important to the field of PDT because it may be possible to use knowledge of tissue oxygen concentrations to 'potentiate' treatment effect [45]. However, the clinical relevance of HbSat measured by the OPS is not well-understood. The OPS measures a 'bulk' signal that is representative of the tissue volume sampled optically. The volume interrogated by the OPS is approximately 1 mm^3 [3], a volume that can be much larger than hypoxic regions existing in the tissue microenvironment [103, 105, 143]. The optical signal lacks information about the spatial distribution of chromophores, and therefore, may lack sensitivity to the existence of small hypoxic regions. A previous study by Conover *et al.* [1] investigated the sensitivity of a near-infrared reflectance spectroscopy (NIRS) device to subpopulations of hypoxic vessels that were present in a murine tumor model. That study compared HbSat measured *in vivo* by NIRS with a spatially-resolved measurement made by cryospectrophotometry (Cryo). The results showed that a NIRS measurement of $\geq 70\%$ hemoglobin saturation was a statistical indicator that $< 6\%$ of vessels were hypoxic (with hypoxia defined as $< 10\%$ HbSat). These findings suggest that an optical device with limited spatial resolution may still provide clinically relevant information.

Measurement of hemoglobin saturation during PDT treatment presents further complications. During PDT treatment, rapid consumption of oxygen, damage to local vasculature,

and variation in blood supply may place the tissue microenvironment into a state of acute hypoxia [76, 81, 143]. It is not known if the 'bulk' optical measurement of a device such as the OPS is sensitive to areas of severe hypoxia at a time when the tissue may contain significant heterogeneity in oxygen concentration and hemoglobin saturation. Moreover, it is not known if such a measurement would provide any information of the potential ROS yield during PDT treatment.

This Chapter describes the development of mathematical models used to investigate the sensitivity of the OPS to physiologically realistic levels of hypoxia within tumor tissue. Simulations test the ability of the OPS to detect both chronic hypoxia, which is persistently present in tumor tissue, and acute hypoxia, which is induced during the photochemical reaction of PDT. The underlying goal of this study is to evaluate the clinical relevance of an OPS measurement of HbSat in tumor tissue *in vivo*.

5.2 NUMERICAL METHODS

This section outlines the set of mathematical models utilized in this study. First, microvascular maps are constructed that mimic the vessel arrangement within the tumor microenvironment. Second, a finite-element reaction/diffusion model is presented that describes spatial and temporal changes in oxygen, ROS, and hemoglobin saturation within the model geometry. Third, a Monte Carlo model of light propagation in tissue is applied to the model geometry to simulate measurement by the OPS.

5.2.1 Tumor Vascular Map

This model treats the tumor tissue environment as a two-dimensional space that contains discrete vessels interspersed throughout. It is well known that blood vessels within tumor tissue are not arranged in the repeating grid-like patterns that are observed in normal tissue [104]. Instead, tumor vessels may occur at irregular intervals, and this may contribute to the existence of chronic hypoxic regions within the tissue [104, 143]. Kelly *et al.* [105]

reported a mathematical technique that reproduced the irregular arrangement of vessels in two-dimensional cross-sections. In this method, the percentage of the tissue space that is occupied by vasculature is calculated as follows:

$$p_{\text{voxel}} = \frac{\text{MVD} \times \pi r_{vessel}^2}{\text{TA}} \qquad (5.1)$$

Here, r_{vessel} is the vessel radius, and TA is the area of the tissue cross-section. MVD is a clinical measurement of vessel density, given as the average number of vessels observed in 1 mm^2 tissue. The tissue space is discretized into a grid (grid size: 50×50 μm), and each grid was assigned a vessel from a binomial distribution using the *binornd* function in the MATLAB® statistics toolbox [137]. This function was assigned values of either 0 or 1 in each grid element based on the number of grid elements and the percentage of the grid elements that are expected to contain vessels (given as p_{voxel}). Grid elements assigned a 1 were populated with vessels. The resultant map represents vessels that are assumed to be normal to the plane of the tissue cross-section. To estimate the presence of non-normal vessels, the map is convoluted using a 3×3 convolution kernel that approximates the portion of the cos function between $-\frac{\pi}{2}$ and $\frac{\pi}{2}$, as done previously by Kelly *et al.* [105]. The resultant map was validated by comparing the sizes and distributions of the hypoxic areas within tumor cross-sections between experimental observations and model predictions [105].

5.2.2   Reaction/Diffusion Model

To describe the relationship among ground state oxygen (O_2) concentration, ROS concentration, and HbSat in the tumor tissue, a finite element reaction/diffusion model was applied to the model geometry. The geometry is a two-dimensional representation of a tissue cross-section, with discrete capillaries interspersed throughout. Oxygen supply to the tissue is modeled by diffusion from the capillaries. The intra-vascular area is assumed to be a homogeneous hemoglobin solution, with blood flow normal to the tissue cross-section with velocity, V_{blood}. A balance on dissolved oxygen within a vessel is given as follows:

$$\frac{\partial C_{O2}^v}{\partial t} \quad = \quad D_{O2}\nabla^2 C_{O2}^v + V_{blood}\left(C_{O2supply}^v - C_{O2}^v\right) - \kappa_{tiss} \qquad (5.2)$$

Here, C_{O2}^v represents the intra-vascular concentration of ground state oxygen (with units mol/cm^3), and D_{O2} is the diffusivity of oxygen in blood. The ground state oxygen carried by blood flowing into the vessel is given by $C_{O2supply}^v$, and oxygen exchanged with the surrounding tissue is given by κ_{tiss}. HbSat within each vessel is calculated from the oxygen partial pressure (given by Henry's law: $P_{O2}^v = H_{O2}C_{O2}^v$, with H_{O2} representing Henry's constant) within the vessel as follows:

$$HbSat = \frac{\left(\frac{P_{O2}^v}{P_{50}}\right)^{n_{Hill}}}{1 + \left(\frac{P_{O2}^v}{P_{50}}\right)^{n_{Hill}}} \tag{5.3}$$

Here n_{Hill} is the Hill constant, and P_{50} is the partial pressure of oxygen at which hemoglobin is 50% of its saturated value.

Oxygen transport and reaction within the tissue is governed by:

$$\frac{\partial C_{O2}}{\partial t} = D_{O2}\nabla^2 C_{O2} + \kappa_{vessels} - \kappa_{met} - \kappa_{PDT} \tag{5.4}$$

Here, C_{O2} represents the tissue concentration of ground state oxygen (with units mol/cm^3). The diffusivity of oxygen in tissue, D_{O2}, is assumed to be the same as in intra-vascular space [142]. Oxygen transport between tissue and intra-vascular space is continuous across the vessel wall, making the common assumption that the capillary wall offers negligible mass transfer resistance [142]. The rate of oxygen transport across the vessel wall is given as:

$$\kappa_{vessels} = \kappa_{tiss} \tag{5.5}$$

The depletion rate of oxygen in the tissue space due to normal metabolic activity is represented by κ_{met}, and is assumed to follow Michaelis-Menten kinetics, as follows:

$$\kappa_{met} = \bar{\kappa}_{met}\frac{C_{O2}}{k_{50} + C_{O2}} \tag{5.6}$$

Here, $\bar{\kappa}_{met}$ is the maximum metabolic rate and k_{50} is the oxygen concentration at which $\kappa_{met} = \frac{\hat{\kappa}_{met}}{2}$.

The photodynamic reaction is modeled using an expression published by Nichols and Foster [99], where the ground state oxygen consumption term is given as follows:

$$\kappa_{PDT} = \phi\beta_{PDT}\left(\frac{C_{O2}}{\frac{k_p}{k_{ot}} + C_{O2}}\right) \tag{5.7}$$

Here, ϕ is the delivered fluence rate, β_{PDT} is the proportionality constant between fluence and photochemical reaction rate (κ_{PDT}), k_p is the rate of monomolecular decay of the excited photosensitizer, and k_{ot} is the biomolecular rate of quenching for the excited photosensitizer. The values for β_{PDT} used in this study correspond to Foscan, a commonly used PS compound [74], a uniform concentration in the tissue of 0.6 μg/ml, which is similar to concentrations in murine tumors 3 hr after i.v. administration of 0.3 mg/kg [74]. The rate of production of ROS is assumed to be equal and opposite to the PDT oxygen consumption rate.

$$\frac{dC_{ROS}}{dt} \;=\; \kappa_{PDT} \tag{5.8}$$

This model does not account for ROS diffusion after generation, which is consistent with previous reports that singlet oxygen diffuses very short distances *in vivo*. On average, singlet oxygen only diffuses 0.1 μm and generally reacts with components within the immediate cellular environment [144].

The values of photosensitizer concentration and delivered fluence rate are assumed to be uniform throughout the tissue geometry; in this way photobleaching of the photosensitizer is neglected. In examination of macroscopic tissue over the course of treatment, ϕ and PS concentration variations are known to have significant effect on the photochemical reaction [74]. However, this investigation focuses on the dynamics associated with one short laser illumination period. For the simulated reaction, the oxygen consumption rate is assumed to be faster than the photobleaching rate [145], making it reasonable to neglect the effect of photobleaching as a first approximation.

5.2.3   MC Model

The Monte Carlo (MC) model developed in Chapter 4 is utilized to simulate OPS measurement of the tissue undergoing the photochemical reaction. All equations governing the propagation of photons through the heterogeneous medium are unchanged. The unique extension to the MC model in this Chapter is that $\mu_{a,vessel}$ is calculated from the outputs of the reaction/diffusion model described in Section 5.2.2. Here, the absorption coefficient for each vessel is calculated from the mean HbSat within the intravascular space. The tissue

geometry utilized in the reaction/diffusion simulation has dimensions of 1 mm × 1 mm. This cross-sectional area may be smaller than the cross section of the tissue volume sampled by the OPS during measurement. This was addressed by simply repeating the 1 mm × 1 mm cross section, in a 'tiling' manner, 16 times into a 4 × 4 grid, resulting in a 4 mm × 4 mm geometry, which was adequate to simulate the OPS measurement of tissue.

5.2.4 Numerical Simulation

MATLAB® code was scripted to execute all simulations. For simulations evaluating the detection of chronic hypoxia by the OPS, individual vessel hemoglobin saturations were selected from frequency distributions as reported by Conover *et al.* [1]. The present study evaluates all nine of the frequency distributions reported by Conover *et al.* (Figure 2(a − i), page 2692 [1]). These distributions are reprinted in this dissertation in Appendix D. After vessel arrangement within the vascular map, the vessels were populated with HbSat values from each distribution 10 independent times. The MC model was used to simulate OPS measurement of each of these 10 maps 3 times *in silico*. This results in 30 simulated OPS measurements (10 randomizations, 3 measurements of each) of each map.

A finite element method (FEM) analysis was used to numerically solve the reaction/diffusion model. MATLAB® code utilized the partial differential equation toolbox [146] to sequentially import the vascular map geometry, generate and refine the mesh surface, specify boundary and initial conditions, and iteratively solve the set of equations. The oxygen supply term ($C_{O2supply}^{v}$) for each individual vessel is selected from a range of values that represent the mean oxygen content in a vascular bed. Note that this supply term does not refer to the arterial influx of blood into a vessel (which would be appropriate in a model that considers axial length of vessels). Instead, the $C_{O2supply}^{v}$ term represents the oxygen content within a vessel at a section between the arteriolar and venular ends. This study investigates two cases of this oxygen supply term: Case 1 — 'venous' supply, $C_{O2supply}^{v}$ is selected from a uniform distribution over the range $40 - 70$ μM, values that are similar to the volume averaged standard oxygen concentrations in normally functioning tissue [142]; and Case 2 — 'hypoxic' supply, $C_{O2supply}^{v}$ is selected from a uniform distribution over the range $10 - 40$ μM,

109

values that represent a diminished, or hypoxic, oxygen supply compared with the standard conditions.

MC simulations initialized 10^6 photon packets per measurement, with standard deviations calculated from the results of 3 independent simulations. Values for tissue optical properties were the same as those reported in Chapter 4. The scattering coefficient was assumed to be constant throughout the tissue, with $\mu_s = 100$ cm^{-1}, and an anisotropic scattering condition of $g = 0.9$ was used. The refractive indices of the tissue and fibers were given as $n_{tissue} = 1.37$ (equal to that of water) and $n_{fiber} = 1.46$, and the fiber numerical aperture was given as 0.22 [3]. The MC model simulates OPS measurement at a single wavelength of 620 nm. Assuming total hemoglobin concentration in the blood as 2.5 mM, the absorption coefficients of oxygenated and deoxygenated hemoglobin within vessels are $\mu_{a,HbO_2} = 8.096$ cm^{-1}, and $\mu_{a,Hb} = 82.502$ cm^{-1}, respectively, at 620 nm. Background tissue absorption is given as $\mu_{a,background} = 0.1$ cm^{-1}.

5.3   RESULTS

Figure 5.1 (Top) shows the spatial probability map for vessel locations within the model tissue geometry with a cross-sectional area of 16 mm^2. Figure 5.1 (Bottom) shows the arrangement of vessels after stochastic assignment using the probabilities in 5.1 (Top). This probability map is generated using methods in Section 5.2.1

5.3.1   OPS Detection of Chronic Hypoxia

Prior to OPS measurement of the vascular map in Figure 5.1 (Bottom), the intravascular Hb-Sat values were specified by either (1) populating vessels uniformly throughout the map with known HbSat values of 0, 25, 50, 75, or 100%; or (2) populating vessels stochastically using tumor HbSat frequency distributions reported by Conover *et al.* [1]. The OPS-estimated $\mu_a (t_2)$ vs. the known HbSat values for the uniform distribution case is shown in the top plot of Figure 5.2. Here, each data point represents the mean of three independent MC simula-

Table 5.1: Parameter values used in simulations.

Model	Parameter	Value	Units	Reference
Vascular	r_{vessel}	20	μ m	[113]
Map	MVD	85	vessels/mm^2	[105]
	D_{O2}	2000	μM^2/sec	[142]
	H_{O2}	0.74	mmHG/μM	[142]
	$\bar{\kappa}_{met}$	5.77	μM/sec	[74]
	k_{50}	0.5	μM	[74]
Reaction /	n_{Hill}	2.46		[142, 74]
Diffusion	P_{50}	26	mmHG	[142, 74]
	V_{blood}	100	μm/sec	[74]
	ϕ	250	mW/(cm^2 sec)	
	β_{PDT}	0.1415	(μM cm^2 sec)/mW	[74]
	$\frac{k_p}{k_{ot}}$	8.7	μM	[74]
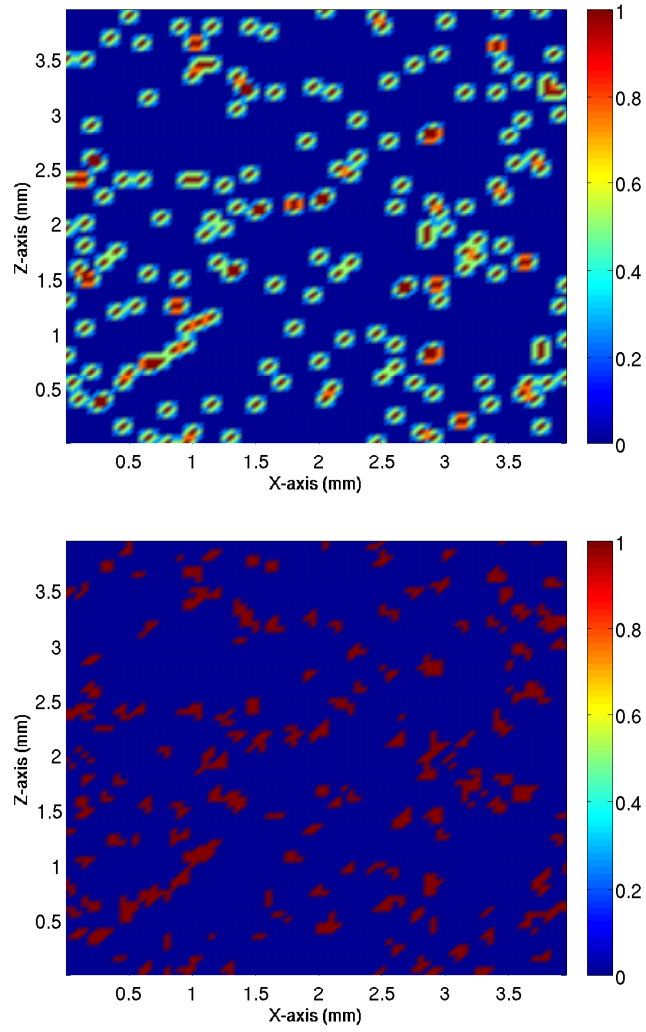
Figure 5.1: (Top) Probability map for vessel area location after sequential vessel placement and convolution, and (Bottom) vessel locations after assignment.

tions and error-bars indicate one standard deviation about the mean. A linear relationship exists between $\mu_a(t_2)$ and HbSat ($r = 0.995$). This function is used to relate HbSat with the $\mu_a(t_2)$ measured from the stochastically populated vascular maps. The bottom plot in Figure 5.2 shows the mean $\mu_a(t_2)$ calculated from simulated measurement of vascular maps populated with each of the 9 frequency distributions from Conover *et al.* [1] and the corresponding HbSat. Here, each data point represents the mean of 30 MC simulations (10 HbSat randomizations from a given distribution, 3 measurements of each), and error-bars indicate one standard deviation about the mean. The mean HbSat data are included in Table 5.2 for comparison with measurements made by Cryo and NIRS for each distribution reported by Conover *et al.* [1]. HbSat measured by OPS and Cryo were well-correlated ($r = 0.986$); the discrepency between Cryo and OPS for case i is discussed in Seection 5.4. The Cryo and OPS measurements agree with the NIRS values for distributions $a - d$, but not for $e - i$; this is discussed further in Section 5.4.

Figure 5.3 shows the relationship between the percentage of hypoxic vessels (HbSat < 10%) and the OPS-measured HbSat. Here symbols indicate measurement of different distributions (convention is listed in Table 5.2), with points representing the mean OPS measurement for each of the 10 assignments of each distribution (resulting in 10 points per distribution). Plotting the data in this configuration shows the relationship between the 'bulk' HbSat detected optically and subpopulations of hypoxic vessels present within each map. The OPS-estimated HbSat values are consistent the threshold suggested for NIRS [1], with an HbSat of $\geq 70\%$ indicating < 6% of vessels in a hypoxic state. Inspection of the data presented in Figure 5.3 shows that no distributions that contained $\geq 6\%$ hypoxic vessels resulted in an OPS-detected HbSat $\geq 57\%$. Therefore, for the distributions investigated in this series of simulations, the threshold may be lower for the OPS than for NIRS; the reasons for this are discussed in Section 5.4.

5.3.2 Tumor Tissue Before and After PDT Reaction

5.3.2.1 Tumor: Venous O_2 Supply A 1 mm^2 subset of the vascular map shown in Figure 5.1 (Bottom) was selected as the geometry for the finite element reaction/diffusion

Table 5.2: Hemoglobin saturations measured by Cryo and NIRS reported by Conover *et al.* [1], and from simulated measurement by the OPS.

Distribution	Cryo	NIRS	OPS	Symbol
a	73	73	72 ± 3	△
b	99	100	92 ± 2	◯
c	32	32	36 ± 7	□
d	43	45	46 ± 6	×
e	54	62	52 ± 5	*
f	76	100	74 ± 3	.
g	65	92	64 ± 5	+
h	44	59	45 ± 5	◁
i	21	48	37 ± 6	▷
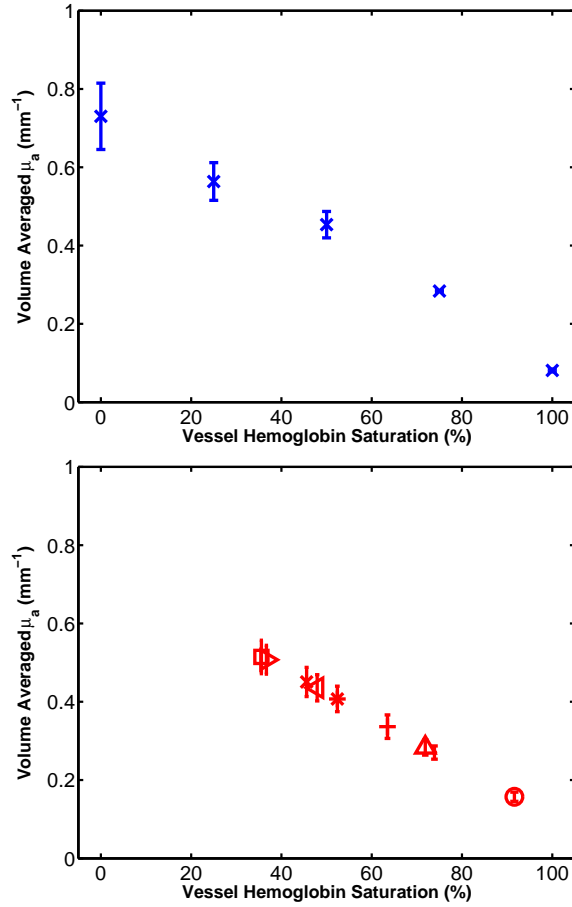
Figure 5.2: 'Bulk' μ_a measured by OPS vs. volume-averaged HbSat. (Top) Uniformly specified HbSat with values of 0, 25, 50, 75, and 100%, and (Bottom) Stochastically specified HbSat from 9 frequency distributions reported by Conover *et al.* [1]
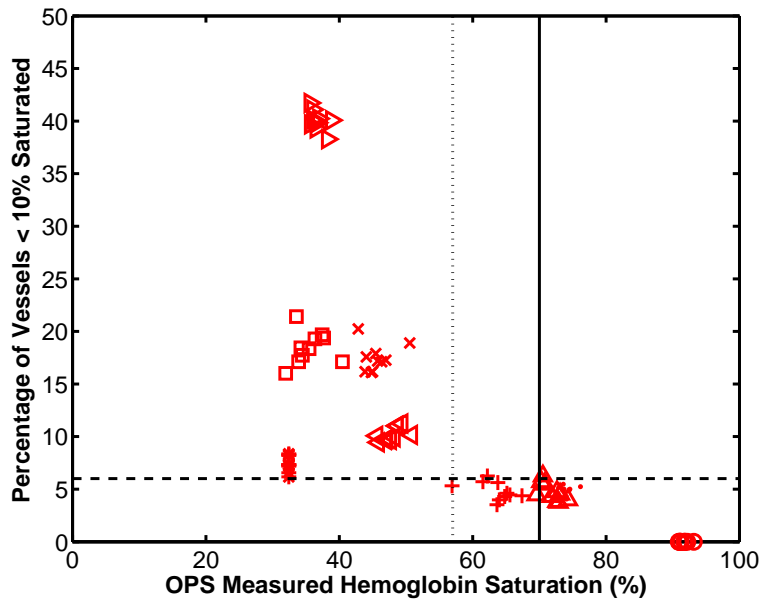
Figure 5.3: Comparison of OPS-estimated HbSat with the percentage of vessels that contain an HbSat < 10%. The horizontal black line indicates 6% hypoxic vessels. Vertical lines indicate 'threshold' HbSat values at 70% (suggested for NIRS by Conover [1]) and 57% (representative of simulated OPS data).

model. Figure 5.4 (Top) shows the spatial profile of oxygen concentration in tumor tissue at steady-state with the the oxygen supply similar to normal venous values. Predicted oxygen concentrations range from approximately zero to ≈ 80 μM. The irregular nature of the vessel location within the tumor tissue cross-section causes some areas of the tissue to have a steady state oxygen concentration near zero, a phenomenon which has been reported *in vivo* [76]. Figure 5.4 (Bottom) shows the predicted HbSat distribution within vessels for this simulated geometry, which is comparatively similar to normal venous values (range from 55 to 85%) [142].

The photochemical reaction of PDT is conducted by administration of a short (30 sec), intense (250 mW/cm^2) laser illumination to the tissue. Figure 5.5 (Top) shows the oxygen concentration throughout the tissue following the reaction. The rapid consumption of oxygen during the reaction has caused an increase in tissue area exposed to near-zero oxygen concentrations. Figure 5.5 (Middle) shows the spatial profile of ROS throughout the tissue, with high yield associated with tissue in close proximity to vessels. Here, intra-vascular ROS has been removed from the plot (dark circles) in order to better visualize the gradient throughout the tissue space. Because oxygen is the limiting factor for this reaction, areas with low (near zero) oxygen concentrations at steady state are exposed to low (near zero) ROS yield during treatment. While the photochemical reaction rapidly decreased the amount of oxygen in the tissue, the HbSat values were relatively unchanged, as shown in Figure 5.5 (Bottom). The HbSat distribution spans the same range of values as pre-PDT. The possible explanations for this predicted phenomenon are described in Section 5.4.

5.3.2.2   Tumor: Hypoxic O_2 Supply   This Section utilizes the same vascular map as in the previous Section, but the oxygen supply to each vessel is selected from a range of lower values (10-50 μM) inducing more pronounced hypoxia within the tissue. The steady state oxygen concentration profile and vessel HbSat distribution are shown in the top and bottom of Figure 5.6. As expected, the tissue oxygen concentrations are lower than the 'venous supply' case, and the HbSat distribution is shifted toward zero, with a range between ~ 0 and 55%. This situation represents tumors that contain areas of persistently low oxygen concentration (< 10 μM) [76, 103, 143, 105].
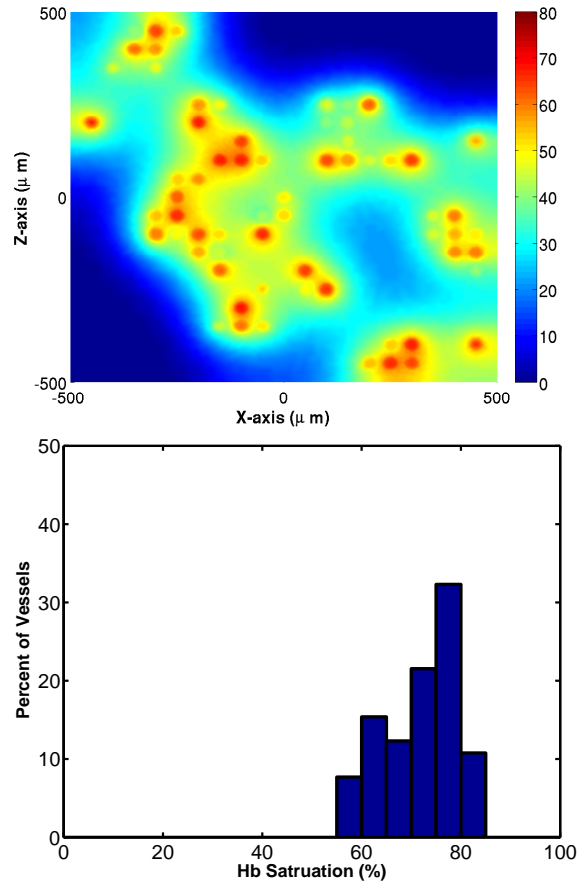
Figure 5.4: Model predictions for tumor tissue with venous oxygen supply at steady state. (Top) Spatial profile of oxygen concentration; and (Bottom) vessel HbSat frequency distribution.

Figure 5.5: Model predictions for tumor tissue with venous oxygen supply following 30 sec of laser illumination during PDT treatment. (Top) Spatial profiles of oxygen concentration; (Middle) tissue ROS yield; and (Bottom) vessel HbSat frequency distribution.

Figure 5.7 shows model predicted outputs for the 'hypoxic supply' case following the PDT reaction. Comparison of Figure 5.7 with Figure 5.5 shows decreased oxygen concentrations (Top), tissue ROS yield (Middle), and vessel HbSat distribution (Bottom) following PDT for the 'hypoxic supply' case. These results are expected to result from diminished oxygen supply within the vasculature. As observed for the 'venous supply', there is little shift in the vessel HbSat distribution between pre- and post laser; this is evidenced by comparing the bottom plots of Figures 5.5 and Figure 5.7.

5.3.3 Acutely Damaged Tumor Tissue Before and After PDT Reaction

This model uses total ROS yield as a surrogate marker of tissue damage. Based on this marker, the 25% of vessels that experienced the highest ROS yield in Sections 5.3.2.1 and 5.3.2.2 were assumed to be damaged, and enter vascular stasis. This was modeled by setting the blood flow velocity to zero in these vessels.

5.3.3.1 Acutely Damaged Tumor: Venous O_2 Supply Figure 5.8 (Top) shows the spatial profile of oxygen concentration in the acutely damaged tumor tissue at steady state. A decrease in tissue oxygen concentration is evident between the undamaged (Figure 5.4 (Top)) and acute cases (Figure 5.8 (Top)). The vessel HbSat distribution in Figure 5.8 (Bottom) is shifted toward zero from the undamaged tumor tissue case, which is shown in Figure 5.4 (Bottom).

Figure 5.9 shows that, following the PDT reaction, tissue oxygen concentrations (Top), tissue ROS (Middle), and HbSat values (Bottom) are all lower than in the undamaged case (see Figure 5.7). The ROS yield shown in Figure 5.9 (Middle) shows some mircoregional decreases in yield around static vessels. In this case, the static vessels are unable to replenish oxygen lost during the photodynamic reaction. These are distinguishable on Figure 5.9 (Bottom) as the subpopulation located between 0 and 20% HbSat.

5.3.3.2 Acutely Damaged Tumor: Hypoxic O_2 Supply Figure 5.10 shows the steady state oxygen concentration profile (Top) and vessel HbSat distribution (Bottom) for
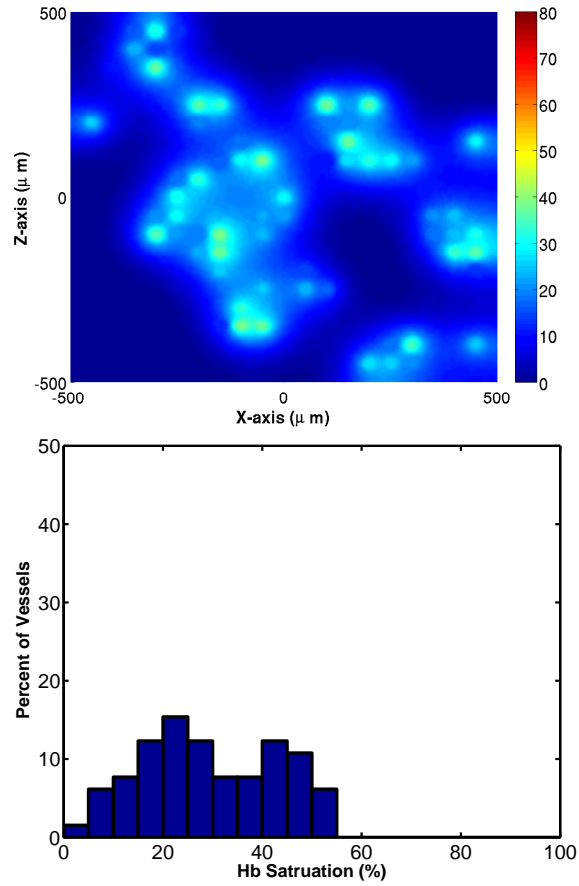
Figure 5.6: Model predictions for tumor tissue with hypoxic oxygen supply at steady state. (Top) Spatial profile of oxygen concentrations and (Bottom) vessel HbSat frequency distribution.
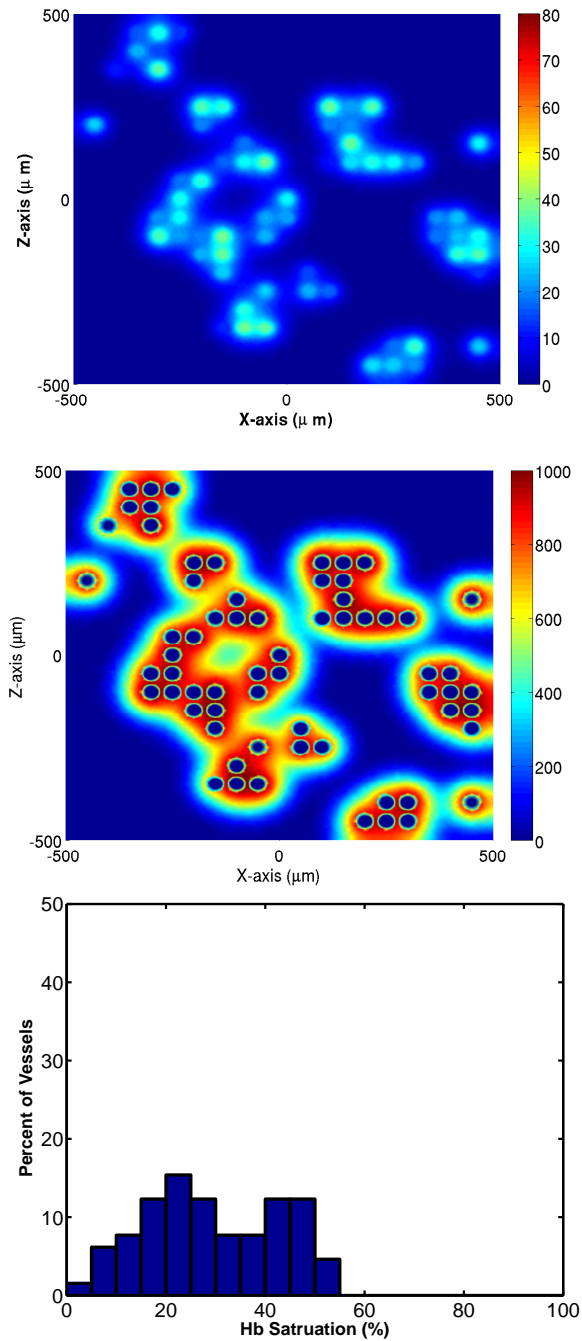
Figure 5.7: Model predictions for tumor tissue with hypoxic oxygen supply following 30 sec of laser illumination during PDT treatment. (Top) Oxygen concentration; (Middle) tissue ROS yield; and (Bottom) frequency distribution of vessel HbSat.
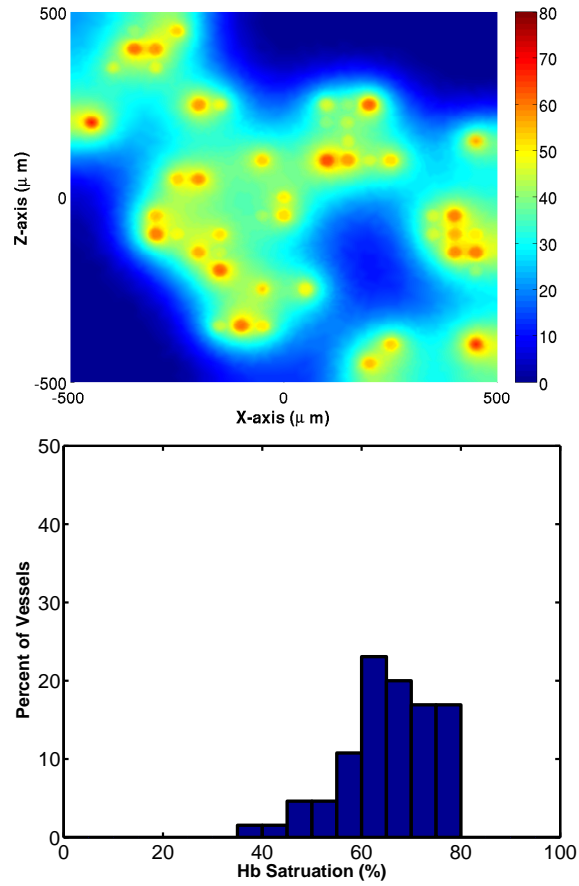
Figure 5.8: Model predictions for acutely damaged tumor tissue with venous oxygen supply at steady state. (Top) Oxygen concentrations and (Bottom) vessel HbSat frequency distribution.
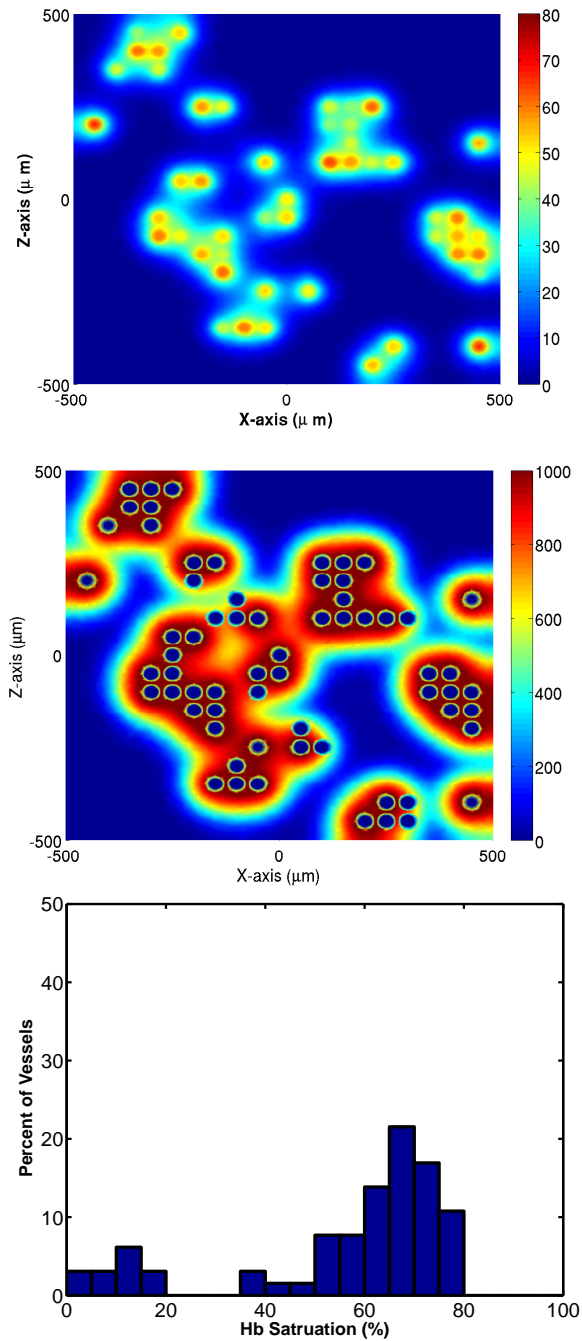
Figure 5.9: Model predictions for acutely damaged tumor tissue with venous oxygen supply after 30 sec of laser illumination during PDT treatment. (Top) Oxygen concentration; (Middle) tissue ROS yield; and (Bottom) vessel HbSat frequency distribution.

the acutely damaged tumor tissue with hypoxic oxygen supply. As expected, both oxygen concentrations and HbSat values are lower than in all previous cases both at steady state (Figure 5.10) and following PDT (Figure 5.11). The volume-averaged ROS yield is 17% lower for this case than for undamaged tumor tissue with venous oxygen supply.

5.3.4 OPS Detection of PDT-Induced Hypoxia

The MC model simulated *in silico* OPS measurement of tumor tissue prior to and following a short PDT reaction. The HbSat data for each case is shown in Table 5.3. Here, the OPS-estimated HbSat is well-correlated with the volume-average value ($r = 0.983$). Figure 5.12 shows the percentage of hypoxic vessels within the simulated tumor tissue vs. OPS-estimated 'bulk' HbSat for each case. These data suggest that while the 'bulk' measurement of HbSat by the OPS may be able to indicate the development of subpopulations of hypoxic vessels, this measurement may not indicate the presence or absence of hypoxic regions within the tissue.

5.4 DISCUSSION

This study investigates the sensitivity of OPS measurement of HbSat measured by OPS to both chronic and acute hypoxia within tumor tissue. This problem is important because regions of hypoxia within tumor tissue may be much smaller than the volume of tissue optically sampled by the OPS during measurement. A previous study by Conover *et al.* reported that a 'bulk' HbSat measured by a NIRS device could indicate the presence of a significant population of hypoxic vessels within the tissue [1]. The study identified a threshold value of $\geq 70\%$ HbSat measured by NIRS that was indicative of a hypoxic vessel fraction below 6%. The threshold was identified by comparing the NIRS measurement with a spatially-resolved measurement of vessel HbSat by Cryo. The NIRS measurement was not always representative of the Cryo value, as evidenced by distributions (e-i) in Table 5.2. Error between the two measurement techniques could potentially be caused by at least three
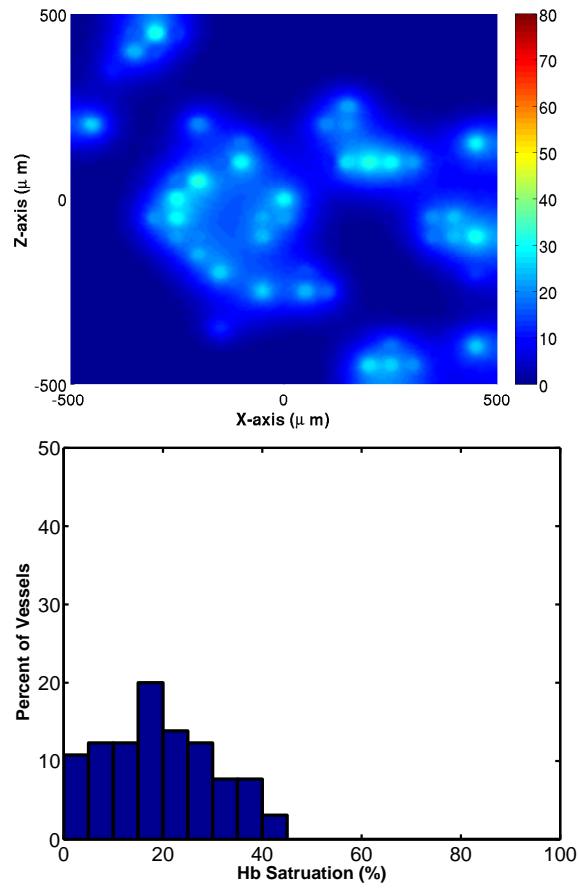
Figure 5.10: Model predictions for acutely damaged tumor tissue with hypoxic oxygen supply at steady state. (Top) Oxygen concentrations and (Bottom) vessel HbSat frequency distribution.
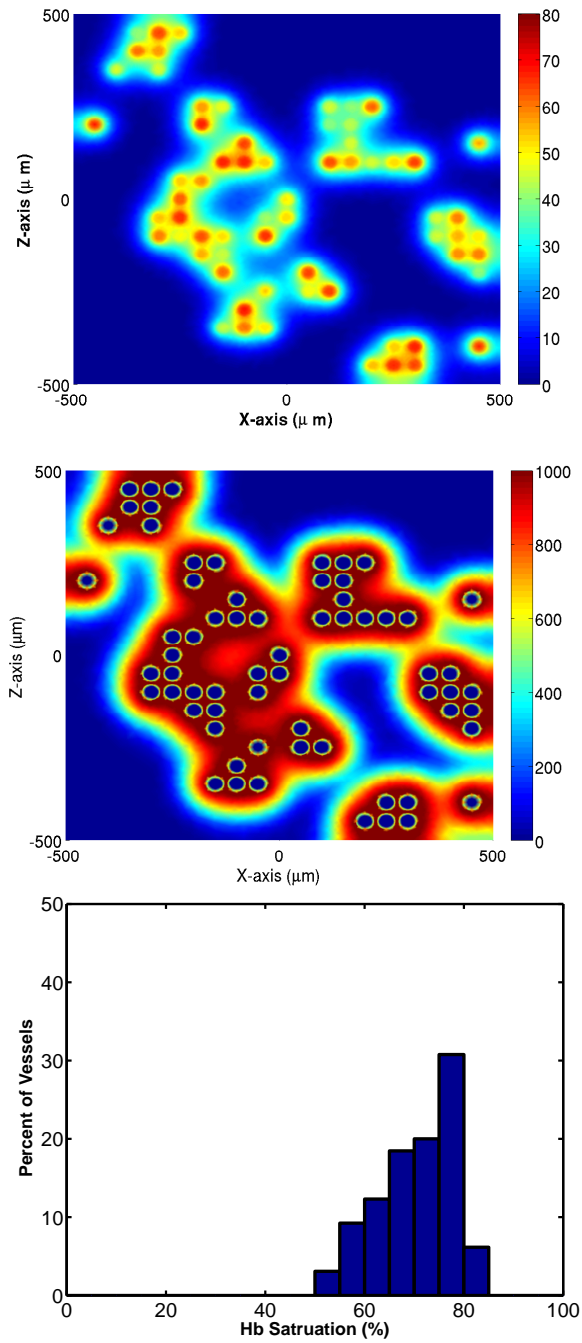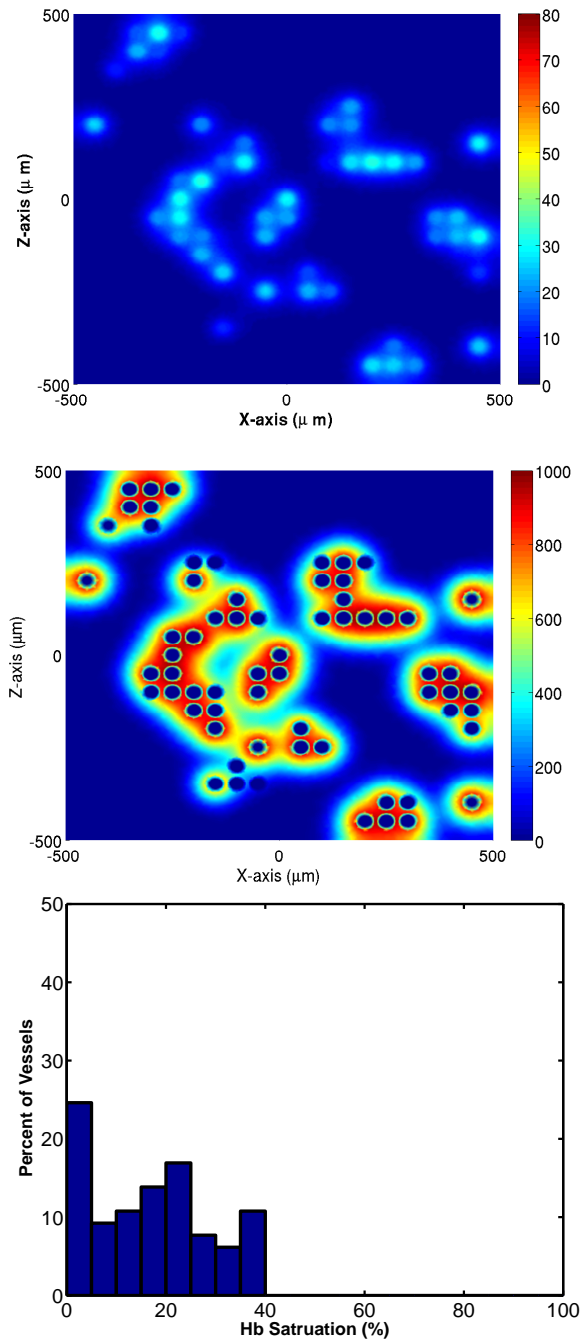
Figure 5.11: Model predictions for acutely damaged tumor tissue with hypoxic oxygen supply after 30 sec of laser illumination during PDT treatment. (Top) Oxygen concentration; (Middle) tissue ROS yield; and (Bottom) vessel HbSat frequency distribution.
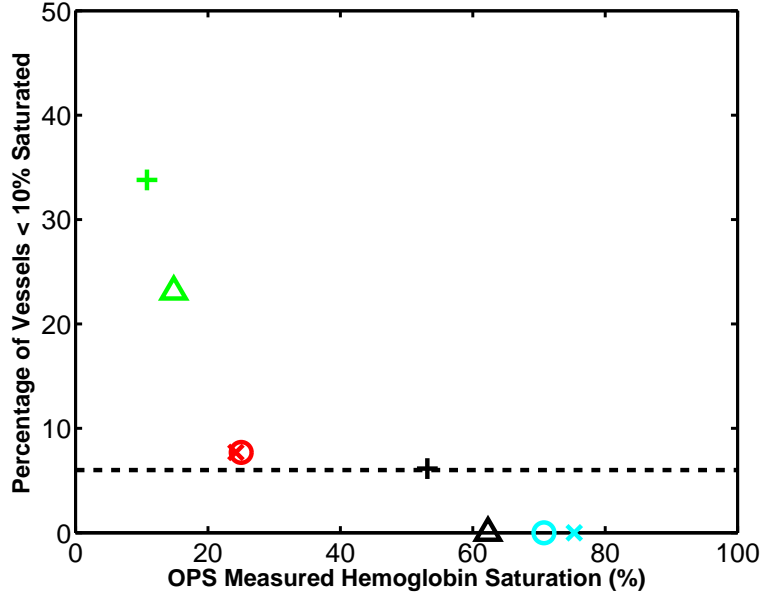
Figure 5.12: Percentage of hypoxic vessels vs. OPS-estimated HbSat in simulated tumors. Symbol convention given in Table 5.3.

Table 5.3: Tumor tissue hemoglobin saturations calculated from the reaction/diffusion model. Hemoglobin saturations calculated from OPS measurement of tissue *in silico* and volume-averaged value. Symbols correspond with data in Figure 5.12

Oxygen Supply	Tissue Case	OPS-HbSat (%)	VolAvg-HbSat (%)	Symbol
Venous	steady state	75 ± 2	72	cyan $\times$
	after PDT	71 ± 4	71	cyan $\bigcirc$
	acutely damaged at steady state	62 ± 5	65	black $\triangle$
	acutely damaged after PDT	53 ± 5	56	black $+$
Hypoxic	steady state	24 ± 8	29	green $\times$
	after PDT	25 ± 7	29	green $\bigcirc$
	acutely damaged at steady state	15 ± 8	19	red $\triangle$
	acutely damaged after PDT	11 ± 8	17	red $+$

factors, as identified previously by Conover *et al.* [1]. First, the NIRS measurement was made *in vivo*, while the Cryo measurement was made after the mouse was euthanized, and the tissue extracted and frozen. Oxygen metabolism in the tumor during the time between euthanization and freezing could cause HbSat measured by Cryo to be systemically lower. Because this phenomenon was not observed in all cases, this source of error was not expected to contribute significantly. Second, some tumor sections contained depth-dependent oxygen gradients, which can cause the optically detected signal to no longer represent the volume-averaged value. Third, the NIRS device interrogated a larger section of tissue than the Cryo method, with the NIRS sampling depths up to 10 mm into the tumor, while the Cryo measured an extracted tissue section that was 4 mm in depth. The present study simulates OPS measurement of tissue sections similar to those reported [1]. This was interesting because the OPS samples a volume of tissue that closely matches the volume sampled by Cryo. OPS-estimated HbSat values were well-correlated with the Cryo measurements ($r = 0.986$) for all distributions reported by Conover *et al.* [1]. Moreover, the OPS-estimated HbSat values were consistent with the 'threshold' HbSat value of $\geq 70\%$ suggested for NIRS. The data presented in Figure 5.3 show that no distributions that contained $\geq 6\%$ hypoxic vessels resulted in an OPS-detected HbSat $\geq 57\%$. These results suggest that the OPS may have clinical utility in determining the possible presence of chronically hypoxic vessels; the statistical strength of this threshold is yet to be quantified. It should be noted that the threshold described here relates to a specific type of tumor line, and variations in both the size and orientation of hypoxic regions exist among tumor lines [104]. It is possible that such a threshold established in one tumor line would not be valid in another tumor line, or in the same tumor line during acute conditions [76].

This study also investigates the sensitivity of OPS measured HbSat to acute PDT-induced hypoxia within tumor tissue. The data in Figure 5.12 suggest that the OPS measurement of HbSat may follow a threshold value, similar to that defined for detection of a subpopulation of chronically hypoxic vessels in Figure 5.3. However, the results of this study question if such a threshold is useful in estimating either tissue oxygen concentrations or ROS yield in the tissue during PDT. Only 1 of the 4 post-PDT cases results in a percentage of hypoxic vessels $\geq 10\%$, however, all 4 spatial oxygen profiles show significant regions of

hypoxia within the tissue. In order to compare ROS yields for each of the 4 PDT cases, the volume-averaged ROS concentration was calculated for the entire tissue area and then normalized by the maximum value. The data are shown in Table 5.4. The conclusions drawn from these data are intuitive, with ROS yield increasing with increasing oxygen available for reaction. It is worth noting that these values are strongly-correlated with the HbSat measured by OPS prior to PDT treatment ($r = 0.983$). This suggests that for a short, intense PDT reaction, the 'bulk' HbSat measured by the OPS prior to treatment may be an indicator of the amount of ROS generated during laser administration. Conversely, the mean value of ROS generation in tissue may not be a useful indicator of treatment, because if the ROS dose is not uniform (which it clearly appears to be from results shown in Figures 5.5, 5.7, 5.9, 5.11), then regions that are exposed to low amounts of ROS are more likely to survive treatment.

It is worth noting that the model presented here simulated only one wavelength of light to quantify changes in HbSat. This experimental design allows the estimation of one parameter (hemoglobin saturation) from changes at the one wavelength, which was selected to provide distinguishable differences in absorption from oxygenated and deoxygenated hemoglobin. In practice, the OPS simultaneously measures wavelengths over a range between 450 and 900 nm. This range of values would allow the estimation of multiple parameters that define the system (initial total hemoglobin concentration, vascular fraction, mean vessel radius, etc.). Furthermore, the large data set would also reduce the effect of measurement noise on the estimated parameters. Simulation of multiple wavelengths was not conducted in this dissertation due to computational intensity, but the models presented here are readily extendable to such investigations. It is also worth noting that the discrepency in Table 5.2 between OPS and Cryo for case i is attributable to relatively low numbers of collected photons due to the increased total absorption coefficient for this case. This error could be avoided by selecting the number of photon packets initialized for each simulation based on the fraction that are collected.

The mathematical models presented in this Chapter are unique due to the link between the photochemical reaction of PDT within tissue and the measurement of the tissue by an optical device. This model structure has the potential to provide information about

Table 5.4: Normalized ROS yields for each of the post-PDT cases

Oxygen Supply	Tissue Case	Normalized ROS
Venous	undamaged after PDT	1
	acutely damaged after PDT	0.91
Hypoxic	undamaged after PDT	0.73
	acutely damaged after PDT	0.61

not only what system parameters are important to the optimization of PDT treatment, but also considers what parameters are observable optically. However, the current model structure may be limited in its ability to describe realistic temporal changes in HbSat. This is because the two-dimensional geometry specifies an oxygen supply term that accounts for flow 'in' and 'out' of the vessel. This formulation numerically prevents intravascular oxygen concentrations from approaching values near zero during the simulation because the supply term is always added during each time step. This calculation also assumes that blood flow does not change during PDT, an assumption that is known to be false [81]. Moreover, in real tissue, axial gradients develop along the length of the capillary, and these are known to affect spatially-resolved values of oxygen and ROS within tissue during PDT [74]. The outcome of this study suggests that there may be a disconnect between intra-vascular HbSat and oxygen concentrations throughout the tumor tissue that requires further resolution. A recent model published by Wang [74] described spatial and temporal changes in HbSat along the axial length of a blood vessel during PDT. The axial component of vascular transport could be incorporated into the present model by making the geometry three-dimensional (which presents obvious computational challenges). Another option to incorporate non-uniform oxygen supply would be the specification of a time-varying oxygen supply term, which accounts for oxygen diffusion into tissue 'upstream' within the axial length of a vessel. Incorporation of either extension could overcome the limitations experienced here; these potential extensions are discussed in Chapter 6.

5.5   SUMMARY

This study utilizes mathematical models to simulate OPS measurement of hemoglobin saturation in tissue *in silico*. The model geometry mimics the tumor microvascular environment, with irregular vessel patterns and hemoglobin saturations estimated from empirically reported frequency distributions. The model structure also links the photodynamic reaction of PDT, which predicts spatial and temporal changes in oxygen, reactive oxygen species, and hemoglobin saturation, with a Monte Carlo model that emulates the OPS measurement of

tissue. Moreover, PDT-induced damage is estimated and used to approximate the effect of vascular stasis on the photodynamic reaction and the optically detected signal. Simulation results indicate that the OPS is sensitive to the presence of hypoxic vessels, with a threshold hemoglobin saturation value of $\geq 57\%$ indicating $< 6\%$ of vessels are in a hypoxic state. However, simulated optical measurements also suggest that the hemoglobin saturation measured by the OPS immediately following a short, intense PDT reaction may not reflect acute hypoxia within the tissue.

6.0 SUMMARY AND FUTURE WORK

6.1 SUMMARY

The work presented in this dissertation focuses on the use of the OPS to measure noninvasively PS concentrations and hemoglobin concentration and saturation in tissues *in vivo*. The following sections summarize the findings from each of the investigations outlined in this document.

6.1.1 Quantitation of MGd Noninvasively by OPS

The OPS was utilized to measure concentrations of the anti-cancer agent MGd in mouse tissues noninvasively and nondestructively using elastic-scattering spectroscopy. The magnitude of MGd absorbance was quantitated by integration of the MGd peak absorbance area, and MGd concentrations were estimated by comparison with standard curves that were validated by high performance liquid chromatography (HPLC) *ex vivo*. In tissue-simulating phantoms *in vitro*, MGd peak absorbance area correlated with MGd concentration. In a mouse PK study, OPS measurements of tissues *in vivo* detected MGd present in both tissue and blood perfusing the tissue. Both the OPS and the HPLC detected selective localization of MGd in malignant tissues compared with surrounding non-malignant tissues, and neither technique detected MGd in brain tissue. Tumor-specific MGd concentrations measured by HPLC correlated with those measured by OPS *in vivo* and *in situ*. Best fit lines to the concentration estimates (forced through zero) had slopes of 0.900 and 1.185, respectively; however, the variability was significant ($r^2 = 0.477$ and 0.269). Overall, comparison of MGd concentrations measured by HPLC and OPS is complicated by mismatch between measured

tissue volumes, heterogeneous spatial distribution of MGd in tissues, and blood-localized MGd at early time points.

The mathematical method developed here is applicable to other optically-active compounds that have detectable absorption in the long visible wavelength spectrum. This method is advantageous for compounds that experience a matrix-induced wavelength shift in the extinction coefficient. In such a situation, specification of the extinction coefficient *a priori* can be problematic, and may potentially be a source of error when estimating concentrations.

It is worth noting that this technique stands to benefit significantly from the development of *in vitro* tissue-simulating phantoms having optical properties that closely match tissues. The availability of such a phantom would remove the need to estimate initial concentrations of deoxygenated and oxygenated hemoglobin within the tissue at time t_o. Currently, this is a source of error in concentration estimates because the relationship between absorbance area and concentration is nonlinear, and it depends upon the initial value of the total absorption coefficient. Hypothetically, the standardization of the optical properties in the measurement of $I(\lambda, t_o)$ could improve concentration estimates.

6.1.2   PK Analysis of MGd *in vivo*

Tissue-localized MGd concentrations measured by OPS and HPLC were utilized to develop PK models of MGd disposition in plasma, tumor, and skin. The models predicted both the rapid initial distribution and slow elimination phases of MGd in plasma, the fast transport of MGd out of the skin (with no MGd detectable after 120 min), and MGd retention at long times in the tumor (with detectable MGd at 24 hr). The same compartmental structure was used to model MGd concentrations measured by OPS *in situ* and HPLC *ex vivo*. *In vivo* tumor MGd concentrations measured using the OPS can be estimated by a linear combination of the plasma, tumor, and skin PK profiles. These results support the use of PK models to estimate tumor localized MGd from OPS measurements *in vivo*. The PK modeling techniques developed here are extendable to other radiation- and photodynamic-

sensitizing agents that are optically detectable by the OPS. The potential application of PK modeling to determine patient specific treatment scheduling is addressed in Section 6.2.1.

6.1.3 OPS Monitoring of PDT

The OPS was utilized to monitor chromophore changes in a mouse xenograft model *in vivo* following silicon phthalocyanine (Pc4) mediated PDT. OPS measurements were made on the xenograft prior to and following laser administration. A previously published algorithm [3] was utilized to estimate PS and Hb concentration and Hb saturation from the light intensity measurements collected by the OPS. However, the previous algorithm predicted unrealistic behavior for the photon path length for absorption coefficients above $1\ cm^{-1}$. Also, the previous algorithm was not capable of characterizing key features in the absorbance data that are normally associated with the 'pigment packaging' effect of discrete vessels in tissue. This study utilizes a MC model to emulate the OPS measurement of tissue containing either homogeneously distributed chromophores or heterogeneously distributed chromophores in discrete vessels. Simulation results were used to motivate: (1) a novel functionality between photon path length and tissue absorption coefficient; and (2) the incorporation of a vessel correction factor. Incorporating these extensions into the structure of the previous algorithm resulted in marked reduction in residual error between measured and model-estimated absorbance, with mean reduction in sum squared error of $52.2 \pm 35.0\%$. For measurements following PDT treatment, the extended algorithm was able to capture key features in the data that were classically associated with pigment packaging. These features were potentially caused by increased blood volume within the tissue resulting from PDT-induced damage during treatment. The algorithm that incorporated both the new path length function and vessel correction factor estimated a 2.4 fold increase in total hemoglobin concentration in the targeted tissue following PDT, while the previous algorithm estimated no change. Moreover, the extended algorithm showed an increased sensitivity to Pc4 absorption bands following treatment. These results indicate that the extended algorithm is more sensitive to both hemoglobin and non-hemoglobin absorbers in tissue *in vivo*.

6.1.4 OPS Measurement of HbSat *in silico*

Mathematical models were utilized to investigate *in silico* the sensitivity of the OPS measurement of HbSat to chronic and acute hypoxia in tumor tissue. The model geometry was constructed to mimic the tumor microvascular environment, with irregular vessel patterns and hemoglobin saturations estimated from empirically reported frequency distributions. The model structure also linked the photodynamic reaction of PDT, which predicts spatial and temporal changes in oxygen, reactive oxygen species, and hemoglobin saturation, with a Monte Carlo model that emulates the OPS measurement of tissue *in silico*. Moreover, PDT-induced damage was estimated from ROS yield and used to approximate the effect of vascular stasis on the photodynamic reaction and the optically detected signal. Simulation results indicate that the OPS is sensitive to the presence of hypoxic vessels, with a threshold hemoglobin saturation value of ≥ 57 % indicating < 6 % of vessels are in a hypoxic state. Simulation results also suggest that OPS measurement of hemoglobin saturation immediately following a short, intense PDT reaction may not detect the acute changes in tissue oxygen concentrations. The *in silico* measurements may be limited due to the model formulation utilized in this investigation; this complication is the basis for future work outlined in Section 6.2.2.

6.2 FUTURE WORK

The following Sections outline work that would apply the principles presented in this dissertation to further the understanding and application of the OPS as a PDT dosimetric tool.

6.2.1 *in vivo* PK Model PDT Dosimetry

Recent studies [93,92] have investigated PS dosing regimens that are designed to target both the tissue cellular components and the vasculature during PDT. These treatments incorporate two sequential PS doses, followed by laser administration of the targeted area. This dose

sequence is illustrated in Figure 6.1. Administration of the first bolus PS dose is followed by adequate time to allow distribution of the compound into the tumor tissue interstitial space, usually a time period of hours to days. The second bolus PS dose is then usually administered a few minutes to a few hours prior to laser administration. Theoretically, this dose schedule allows the PS that was administered in the initial dose to have localized in tissue, such that during laser administration, the ROS attacks the cellular components of the malignant tissue. The PS delivered in the second administration is thought to be in close proximity to blood vessels when the laser is administered. Therefore, the ROS generated from the PS provided by the second bolus dose is thought to damage the blood vessels. Targeting the vasculature is effective because by reducing blood supply, the supply of oxygen and nutrients is also reduced. The drug-light interval between each PS dose and laser administration is selected based on studies that have shown that efficacy 'peaks' in treatment are often bi-modal, with the early peak associated with vascular damage, and the later peak associated with cellular damage [97].

This drug-laser administration schedule may correlate well with mean outcome from study groups, however, the treatment method does not take into account inter-patient variability in the distribution rate of the PS following administration. Knowledge of the PS distribution rates for individual patients could potentially allow clinicians to administer the second PS dose at a time that would potentate the PDT-induced damage delivered during laser administration.

Logistically, this drug-laser administration schedule may lend itself to the on-line incorporation of a PK model. Hypothetically, after the initial PS dose, it is possible to make OPS measurements of the PS concentration in the tumor *in vivo*. These measurements could be used to inform a patient-specific PK model, which could be used to estimate the drug-light interval between the second PS dose and the laser administration. This mathematical structure is shown in block-diagram form in Figure 6.2. This treatment regimen provides adequate time to make the noninvasive measurements of PS concentration and ample time for the PK parameters to be identified. Furthermore, dosing recommendations can be made and then evaluated by clinical experts. This treatment structure could potentially reduce variability

in treatment response that is attributable to patient-specific variability in PS concentrations in the target tissue(s) during laser administration.

6.2.2 Extended *in silico* Model of PDT Monitoring by OPS

Chapter 5 outlines a set of mathematical models that link the photochemical reaction of PDT with a simulated optical measurement of the tissue by the OPS. This model structure utilizes a two-dimensional description of the model geometry when solving the photochemical reaction. In this formulation, there is no axial component to intra-capillary transport, and therefore, the model cannot account for axial concentration gradients that either exist within tissue at steady state or are induced during PDT. It has been hypothesized that these gradients may be important to the delivery of PDT dose [74]. During laser illumination, micro-regional oxygen gradients can develop and may limit the generation of ROS. The model presented by Wang *et al.* [74] suggests that volume average measurements of hemoglobin saturation may not be sensitive to the presence of these gradients, and therefore, such measurements may have limited application to on-line treatment design.

The model developed by Wang *et al.* accounts for both radial and axial species transport within a tissue section during the photochemical reaction [74]. The model utilizes a Krogh tissue cylinder to define transport between blood vessels and surrounding tissue [147]. Moreover, hemoglobin saturation is linked to intra-capillary oxygen transport using the Hill equation. The allows reasonable estimation of spatial and temporal changes to species within the representative capillary-tissue section during the PDT reaction.

It is possible to extend the mathematical formulation developed in Chapter 5 to consider axial gradients within vessels. A logical extension of the current method would involve the incorporation of time-varying oxygen supply terms within vessels. Here, the axial oxygen gradients that occur during PDT could be estimated in the model by Wang, and then used to approximate temporal changes to the oxygen supply term utilized in the two-dimensional model formulation. This model implementation would have the advantage of estimating axial changes in intra-capillary oxygen concentrations while still accounting for irregular vessel arrangement within the tumor.
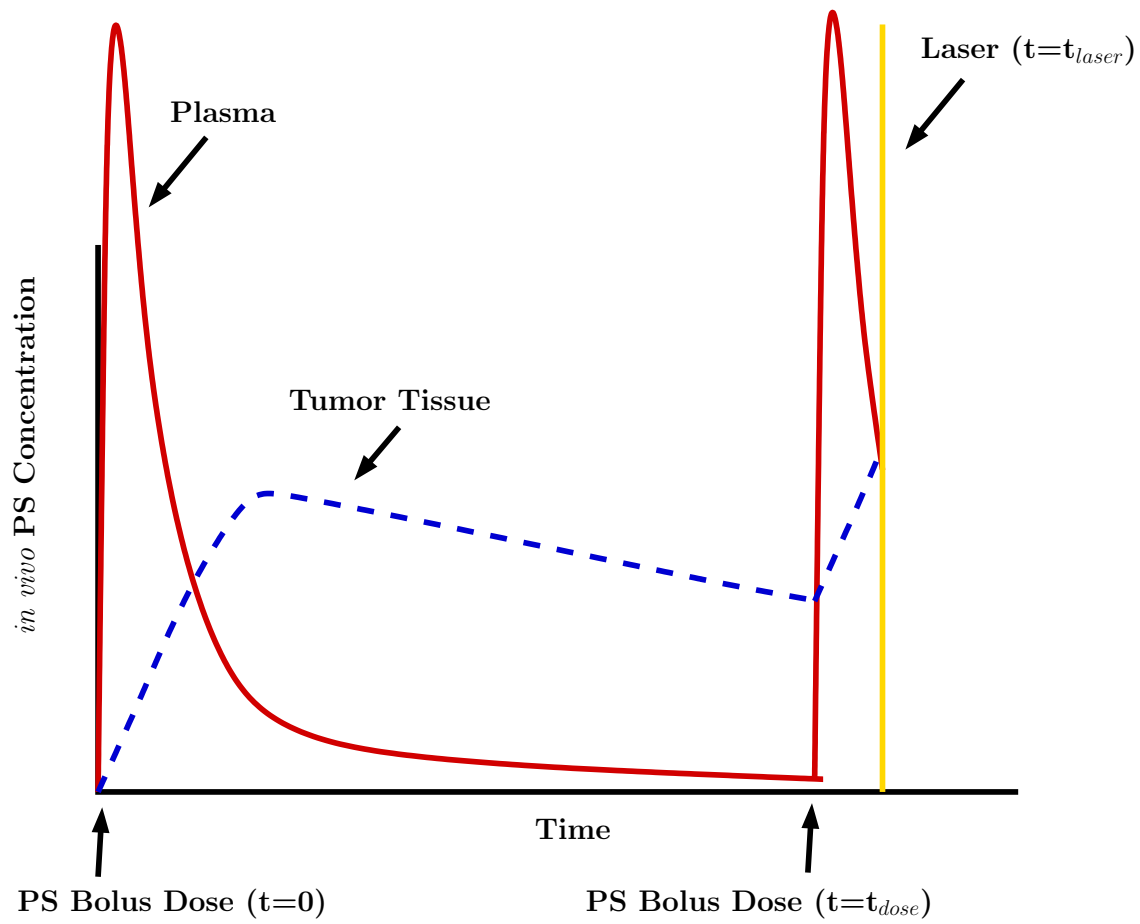
Figure 6.1: Illustration of tumor PS concentration during combined dose regimen.
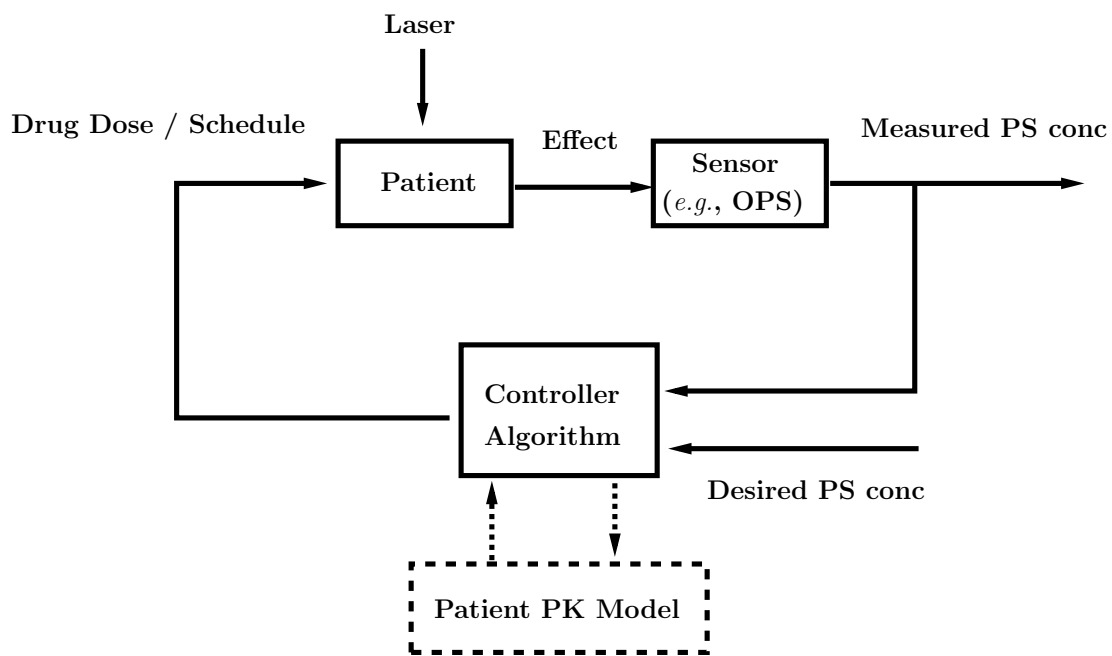
Figure 6.2: Control loop structure for patient-specific estimation of PS dose during dual-dose PDT treatment.

Another potential extension of this previous model would involve the incorporation of three-dimensional distribution of vessels throughout a tissue section. In this case, the vessels would be arranged stochastically, with variable distances between neighboring vessels. Additional complexities that could be incorporated include variable vessel sizes, orientations, and oxygen supplies. This more complicated model structure would further investigate the utility of optical devices to measure noninvasively changes in hemoglobin saturation during PDT treatment. It should be noted that such a model would be computationally intensive, and may require highly specialized numerical solution techniques in order to efficiently solve the set of partial differential equations for the three-dimensional geometry.

6.2.3 *In silico* Analysis of On-line Laser Scheduling during PDT

Efficient anti-cancer PDT treatment can be defined as adequate generation of ROS that results in uniform tumor cell kill. To date, there has been little development in determining how to utilize measurements of PS concentration and HbSat made during treatment to make clinical decisions that could improve the potency of the delivered dose for individual patients. It has been reported that the ideal length of light and dark cycles during fractionated PDT treatment would be asymmetrical, with longer time periods given to the dark periods because diffusive oxygen resupply is slower than oxygen consumption during treatment. Moreover, as treatment progresses the resupply may become slower (due to vascular occlusion or stasis), and may require progressively longer dark periods in order to allow adequate oxygen concentrations to be reached prior to laser administration. This is illustrated in Figure 6.3, which shows a representation of increased dark cycle length required to allow consistent initial oxygen concentration within the tissue for laser administration. Hypothetically, it may be possible to increase the ROS yield delivered to individual patients based on tailoring of the light/dark fractionation schemes during treatment.

The models developed in Chapter 5 and the potential extensions described in Section 6.2.2 represent a tool to theoretically investigate the utility of the hemoglobin saturation measurements made during PDT treatment. This model structure could be placed into a control system, as shown in Figure 6.4. This mathematical structure could simulate treat-

ment *in silico*, including measurements of the physiological system. A model-based control algorithm could be constructed to accept the measurements of oxygen concentrations within the tissue during treatment, and make decisions about the temporal sequence of laser administration.

This theoretical study would involve the evaluation of treatment 'case studies' *in silico*. The initial case would evaluate the ability of the proposed control structure to achieve target tissue damage with a perfect knowledge of all physiological quantities (*e.g.*: PS concentration, Hb concentration and saturation, ROS yield, blood flow rates, etc.). These quantities would be known both temporally and spatially during treatment. The relationships between the laser administration and ROS generation would be quantitated, with the focus of the treatment being the delivery of adequate uniform ROS yield to all regions of tumor tissue. Simulations of this case will establish an 'upper bound' on the level of control achievable if all states were known during treatment.

The next, more-complicated case would evaluate the feasibility of control with sensor limitations. Here, the OPS could be incorporated into the sensor block. The system block will output spatial and temporal changes to the chromophores within the tissue, and the MC model would simulate OPS measurement of the tissue *in silico*. OPS estimates of 'bulk' changes in hemoglobin saturation would be sent to the controller. Simulations of treatment in this case will evaluate the role of the OPS in PDT dosimetry and treatment scheduling.

The current light fractionation schemes used clinically were suggested by ideal theoretical cases [69, 70], with constant blood flow and oxygen supply during treatment. In these circumstances, it is possible to achieve adequate (uniform) ROS generation because the oxygen resupply during dark periods is constant. However, in real treatment, there are changes to blood flow (due to vasodilation, vasoconstriction, and capillary damage) [81]. These complications could be incorporated into the system as 'Disturbances'. The control loop should still achieve the desired treatment outcome if the sensor is capable of detecting these disturbances. Therefore, simulations that consider these complications would evaluate if the treatments adjusted using on-line dosimetry could improve efficacy compared with pre-determined light fractionation schemes.

The proposed series of *in silico* case studies have multiple applications to the field of PDT. The studies would evaluate the potential of patient-specific dosimetry to improve PDT treatment efficacy, specifically investigating the use of the OPS to monitor PDT treatment in real-time. In the future, this modeling and control scheme could be used to suggest appropriate PDT laser light dosage protocols for novel PS compounds, prior to clinical testing. Additionally, the model could be used to re-evaluate PDT treatments using PS compounds that previously did not achieve desired treatment outcome in the clinic using the standard protocols, and estimate if the PS could successfully be employed if dosimetry design techniques would have been incorporated into the trial.
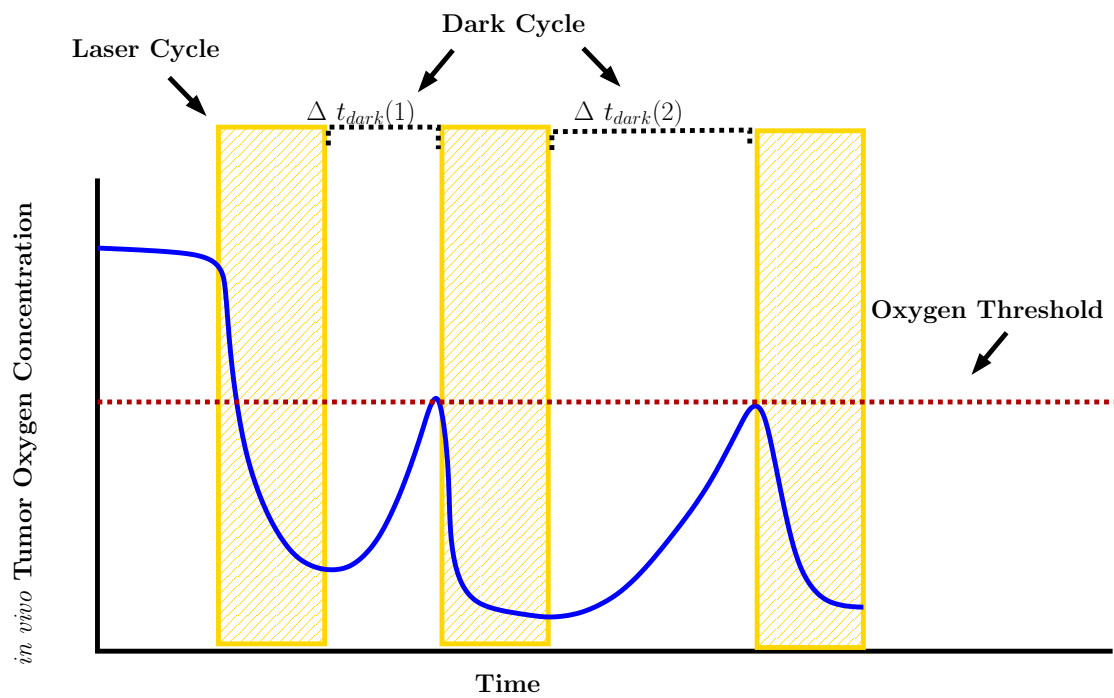
Figure 6.3: Illustration of tumor oxygen concentration during fractionated PDT treatment.
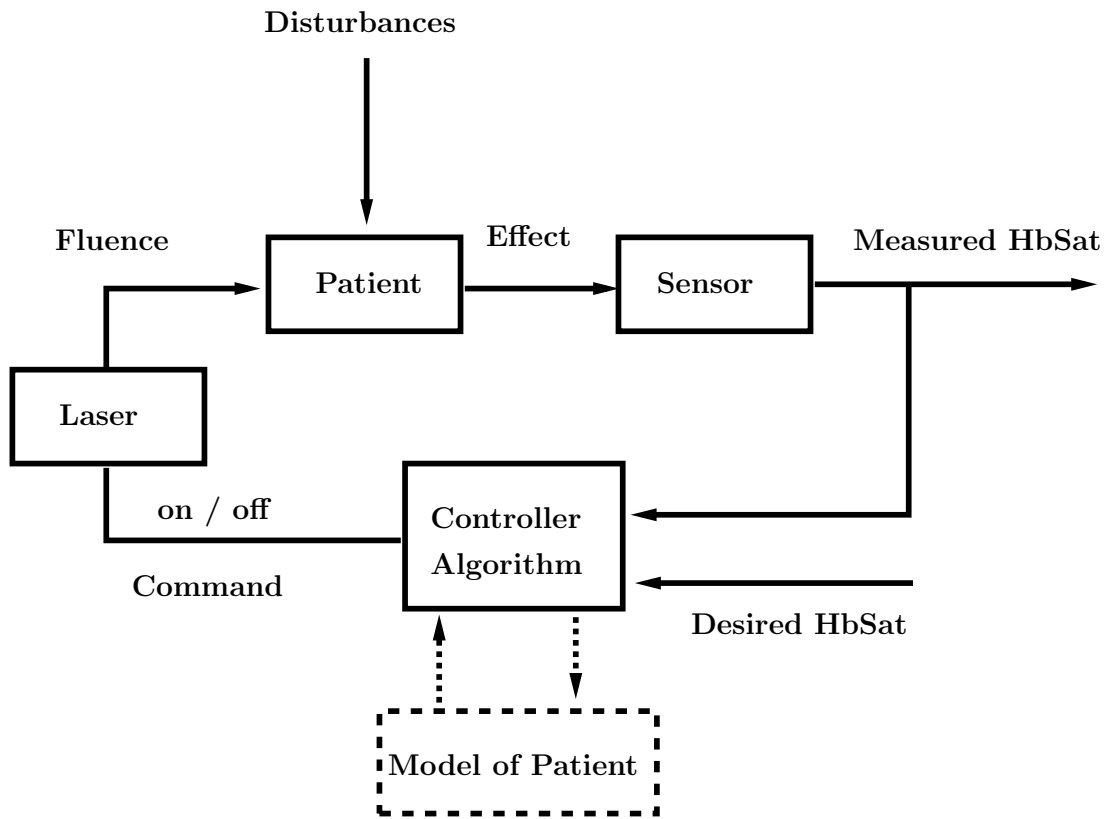
Figure 6.4: Control loop structure for patient-specific estimation of laser light fractionation periods during PDT.

APPENDIX A

NOMENCLATURE

Abbreviations	
AIC	Akaike information criterion
ALA	5-aminolevulinic acid
AlPcS	aluminum phthalocyanine
Cryo	cryospectrophotometry
HPLC	high preformance liquid chromatography
i.v.	intravenous
i.p.	intraperitoneal
LLD	lower limit of detection
LLQ	lower limit of quantitation
LVM	Levenberg-Marquardt algorithm
m-THPC	meta-tetrahydroxyphenyl chlorin
MC	Monte Carlo
MCML	Monte Carlo model of light transport through multi-layered tissue from Wang *et al.* [107]
MGd	motexafin gadolinium
MLu	motexafin lutetium
TA	area of tissue cross-section
MVD	vessel density

NIR	near infrared
NIRS	near infrared reflectance spectroscopy
OPS	Optical Pharmacokinetic System
PDT	photodynamic therapy
PK	pharmacokinetics
PS	photosensitizer
ROS	reactive oxygen species
SCID	severe combined immunodeficiency
SSE	sum squared error
TA	area of tissue cross-section
vis	visible

General Notation

A	total absorbance
A_i	absorbance attributable to compound i
$\mathcal{A}$	absorbance area
$\mathcal{A}_{noise}$	absorbance area attributable to noise
B	changes in collected light caused by changes in scattering properties between different measurements
C_i	concentration of compound i
C_{O2}^v	intra-vascular concentration of ground state oxygen
$C_{O2supply}^v$	ground state oxygen concentration of blood flowing into a vessel
D_{O2}	diffusivity of oxygen in both tissue and intra-vascular space
f	fractional vessel area
G	geometry-dependent factor accounting for light lost due to scattering
H_{O2}	Henry's constant
Hb	deoxygenated hemoglobin
HbO_2	oxygenated hemoglobin

I	collected light intensity
I_{atten}	intensity of attenuated light collected by detector fiber
$I_{incident}$	intensity of light incident on sample
k_p	rate of monomolecular decay of excited PS
k_{ot}	biomolecular rate of quenching for the excited PS
L	geometrical distance from source to detector
$\langle L \rangle$	effective photon path length
$\langle L_o \rangle$	effective photon path length function presented by Mourant *et al.* [3]
$\langle L_n \rangle$	effective photon path length function presented in Chapter 3
l	longest diameter of tumor
M	number of estimated parameters
N	number of data points
n_{Hill}	Hill constant
O_2	ground state oxygen
P_{50}	partial pressure of oxygen at which hemoglobin is 50% of its saturated value
P_{O2}^v	intra-vascular partial pressure of oxygen
r	Pearson correlation coefficient
r_{vessel}	mean vessel radius
$\overline{r}_{vessel}$	'effective' vessel radius
t	time
V_{blood}	velocity of blood flow within blood vessel
V_{Tumor}	measured tumor volume
VC	vessel correction factor
w	length of tumor diameter perpendicular to l
x, y	power law coefficients
z_i	fitted parameters within description of B

Greek Letters

β_{PDT}	proportionality constant between fluence and photochemical reaction rate
δ_L	factor relating difference between effective photon path length between multiple measurements
ϵ_i	extinction coefficient of compound i
κ_{PDT}	photochemical reaction oxygen consumption rate
κ_{tiss}	intra-vascular oxygen exchanged with the surrounding tissue
$\kappa_{vessels}$	intra-tissue oxygen exchanged with the discrete vessels
λ	wavelength
μ_a	absorption coefficient
μ_s	scattering coefficient
σ	standard deviation
ϕ	delivered fluence rate

Pharmacokinetic modeling parameters (Chapter 3)

$\hat{C}_i^{HPLC}$	model estimated MGd concentration in compartment i fitted to HPLC tissue data
$\hat{C}_i^{OPS}$	model estimated MGd concentration in compartment i fitted to OPS tissue data
$\hat{C}_{invivo}^{OPS/HPLC}$	*in vivo* concentration estimated by HPLC tissue measurements
$\hat{C}_{invivo}^{OPS/OPS}$	*in vivo* concentration estimated by OPS tissue measurements
D	bolus dose of MGd
f_{plasma}	estimated fractional plasma concentration contributing to *in vivo* tumor MGd concentration
f_{skin}	estimated fractional skin concentration contributing to *in vivo* tumor MGd concentration

f_{tumor}	estimated fractional tumor concentration contributing to *in vivo* tumor MGd concentration
k_{10}	mass elimination rate of MGd from plasma
k_{mn}	mass transport rate from compartment m to n
N_t	number of time points
N_c	number of compartments with corresponding measured concentration
V_i	volume of distribution of compartment i
x_q	mass of MGd in compartment q (where $q \in \{1, 2, 3, 4, 5\}$)
J_i	output of objective function
p	parameter set

Monte Carlo Model parameters (Chapter 4)

β	shortest distance between two vessel centers
θ_{azim}	photon azithmul angle
θ_i	incident angle for photon crossing an interface
θ_t	transmitted angle for photon crossing an interface
$\theta_{scatter}$	photon scattering angle
μ_a^{total}	total absorption coefficient
$\mu_{a,background}$	absorption coefficient of tissue background
$\mu_{a,vessel}$	absorption coefficient of discrete vessels
$\mu_{s,background}$	scattering coefficient of tissue background
$\mu_{s,vessel}$	scattering coefficient of discrete vessels
μ_x, μ_y, μ_z	photon trajectory in x,y,z direction
$\zeta_{scatter}, \zeta_{step}, \zeta_{ref}$	random numbers uniformly distributed on the interval $(0, 1]$
D	discrete vessel block length
g	anisotropy factor
l_i	stocastic step size for photon i
$N_{collected}$	number of photons collected by detector

NA_{fiber}	numerical aperature of fiber
n_i	refractive index of medium i
p_{voxel}	percentage of tissue space occupied by vasculature
R	Fresnel reflection coefficient
W_k	weight of photon k
x, y, z	coordinate direction

APPENDIX B

ABSORBANCE AREA SPECTRA: MGD
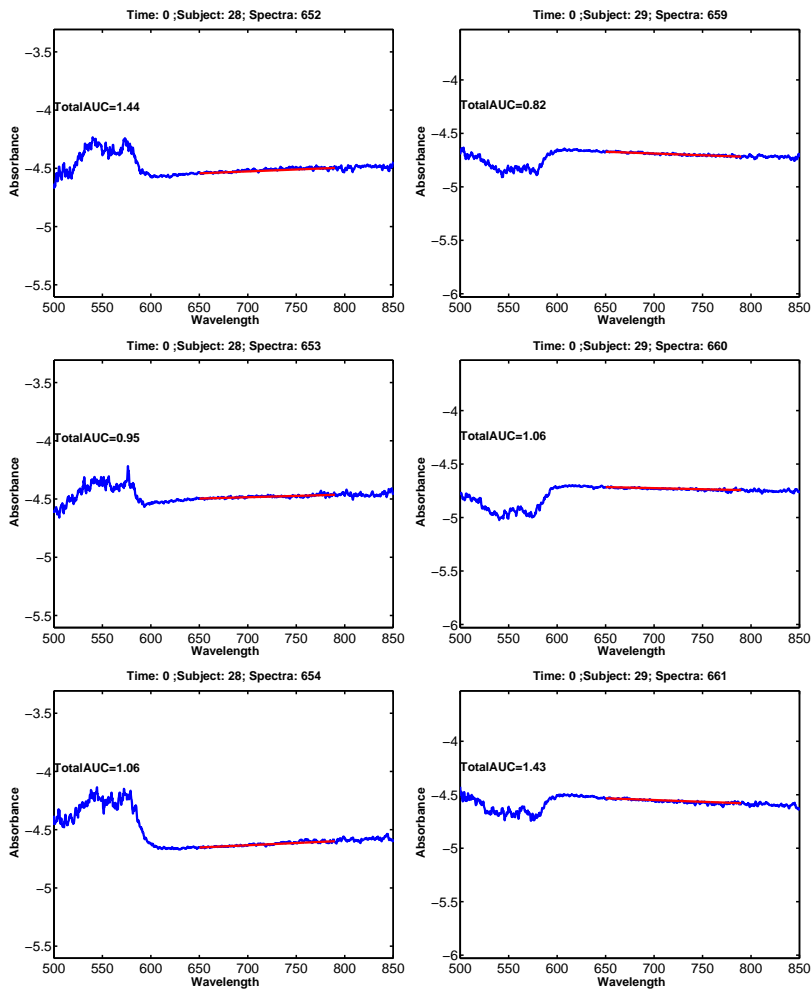
Figure B1: Model estimates of absorbance from OPS measurement of murine xenograft. Measurements made prior to MGd administration.
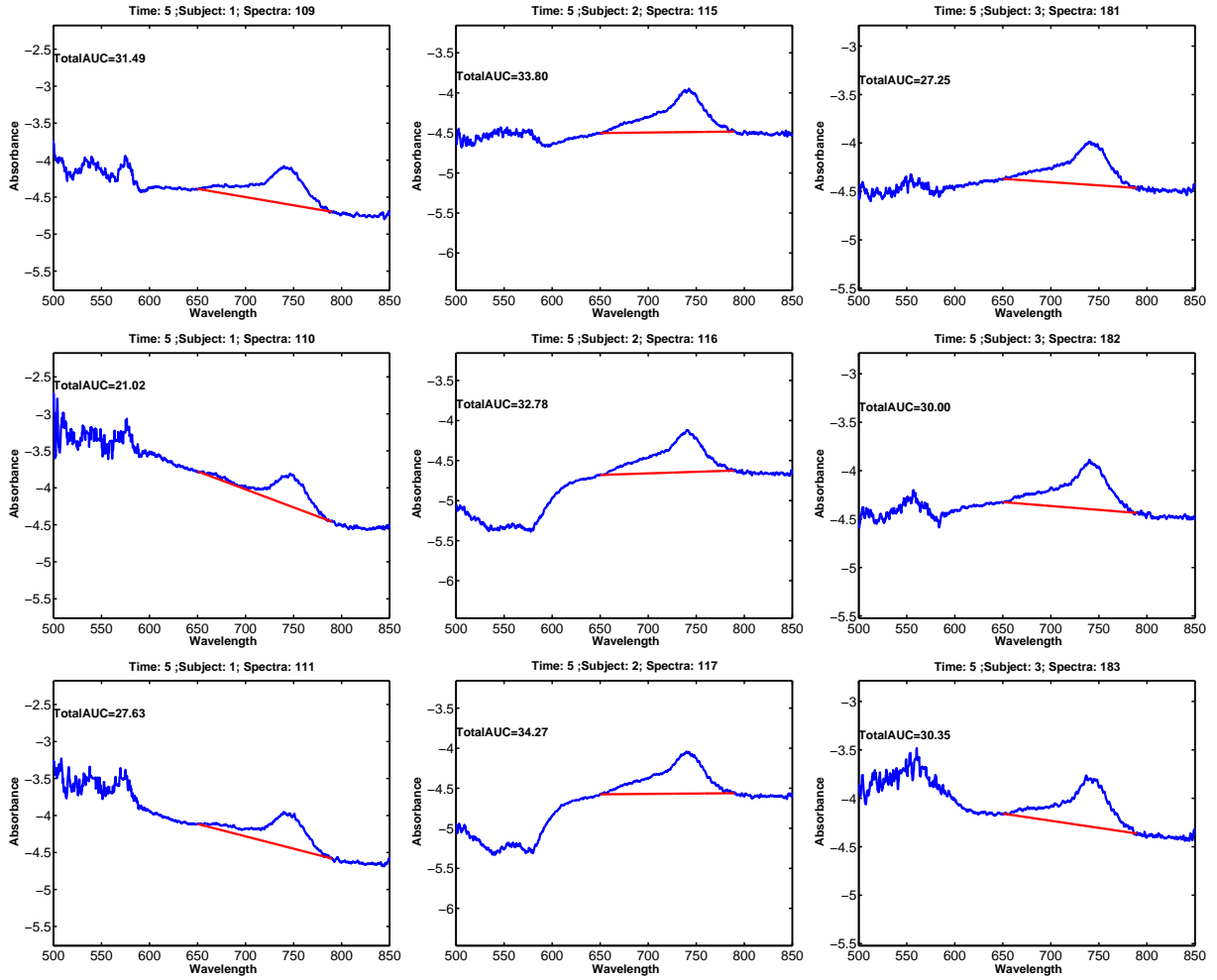
Figure B2: Model estimates of absorbance from OPS measurement of murine xenograft. Measurements made 5 min after MGd administration.
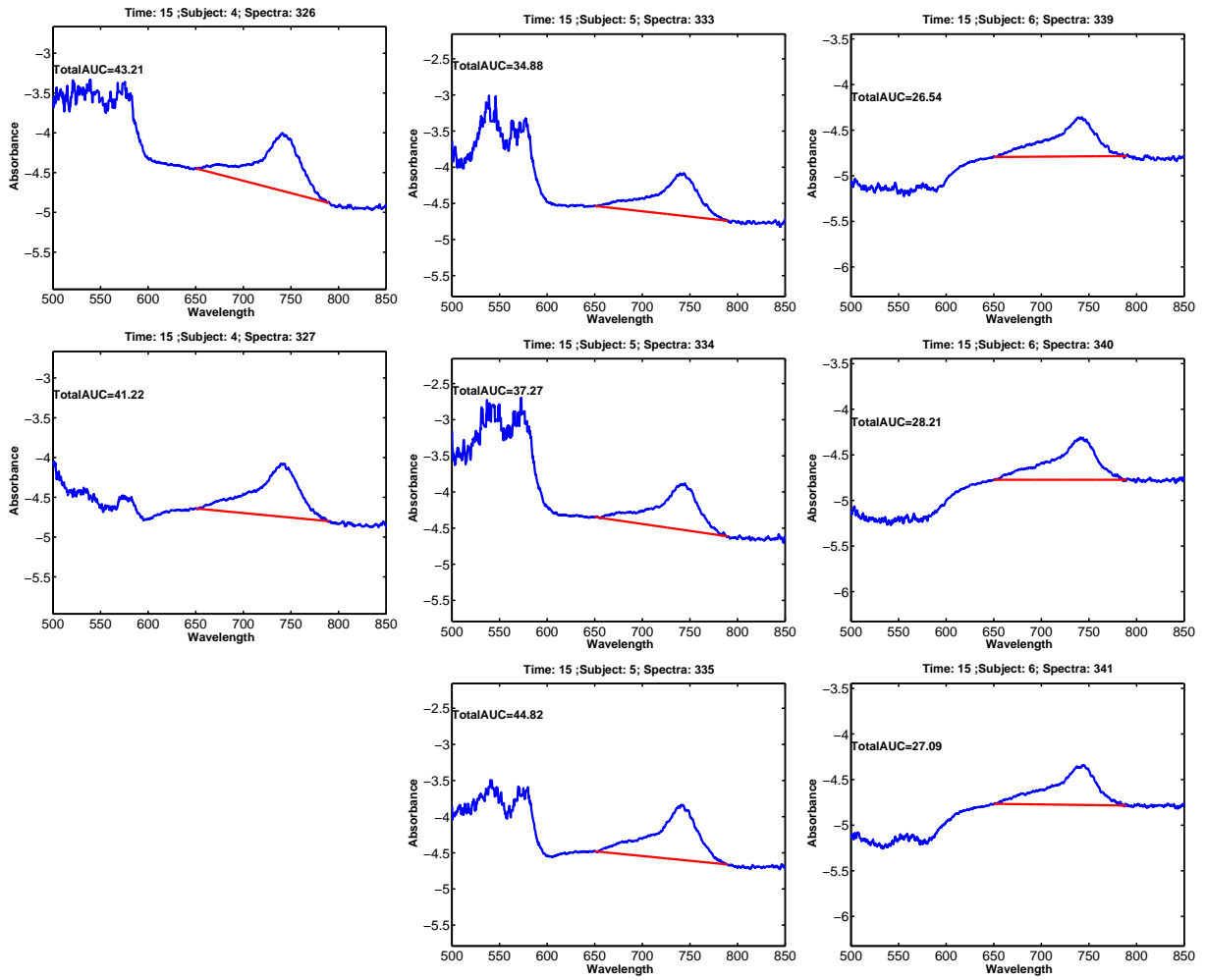
Figure B3: Model estimates of absorbance from OPS measurement of murine xenograft. Measurements made 15 min after MGd administration.
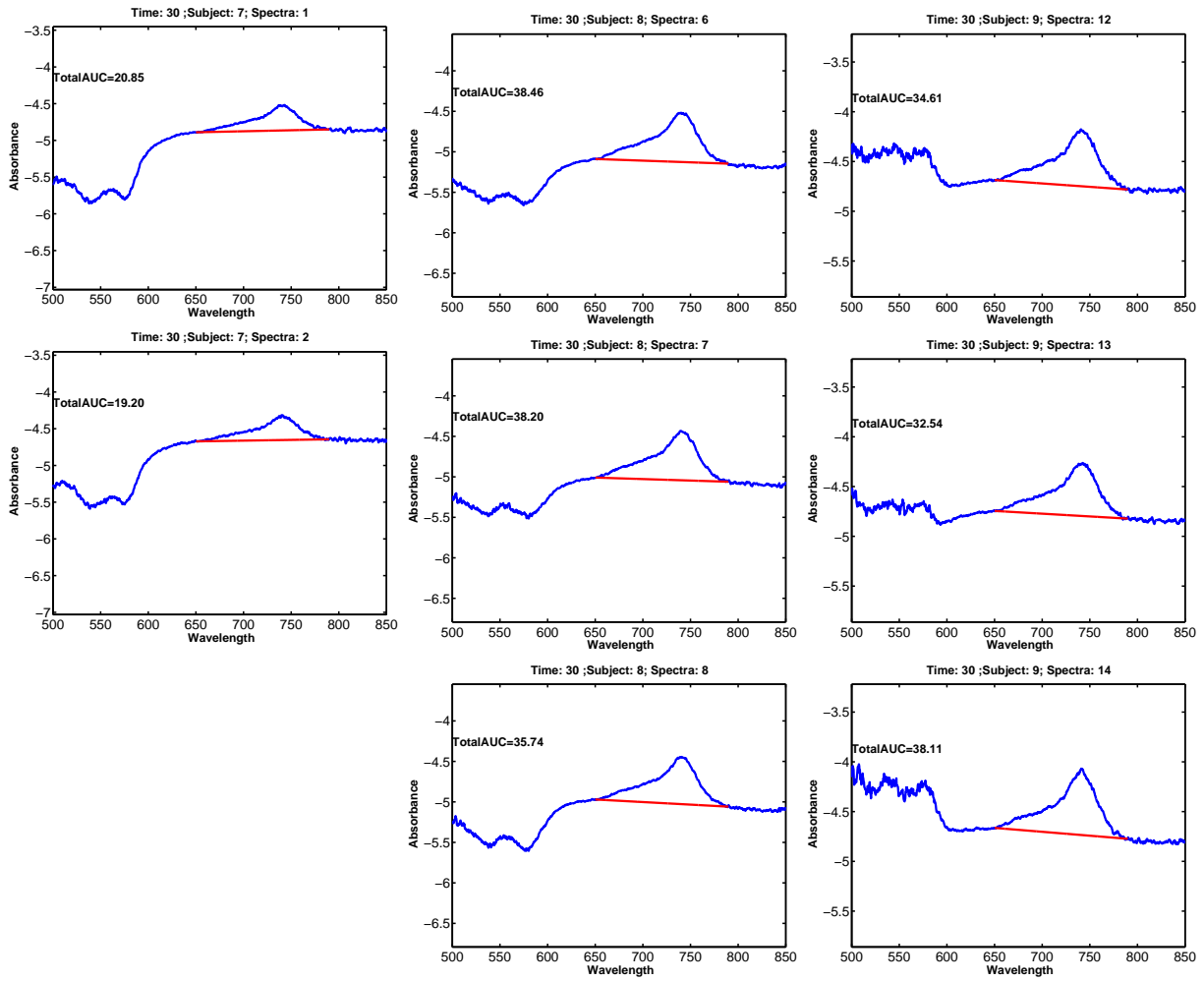
Figure B4: Model estimates of absorbance from OPS measurement of murine xenograft. Measurements made 30 min after MGd administration.
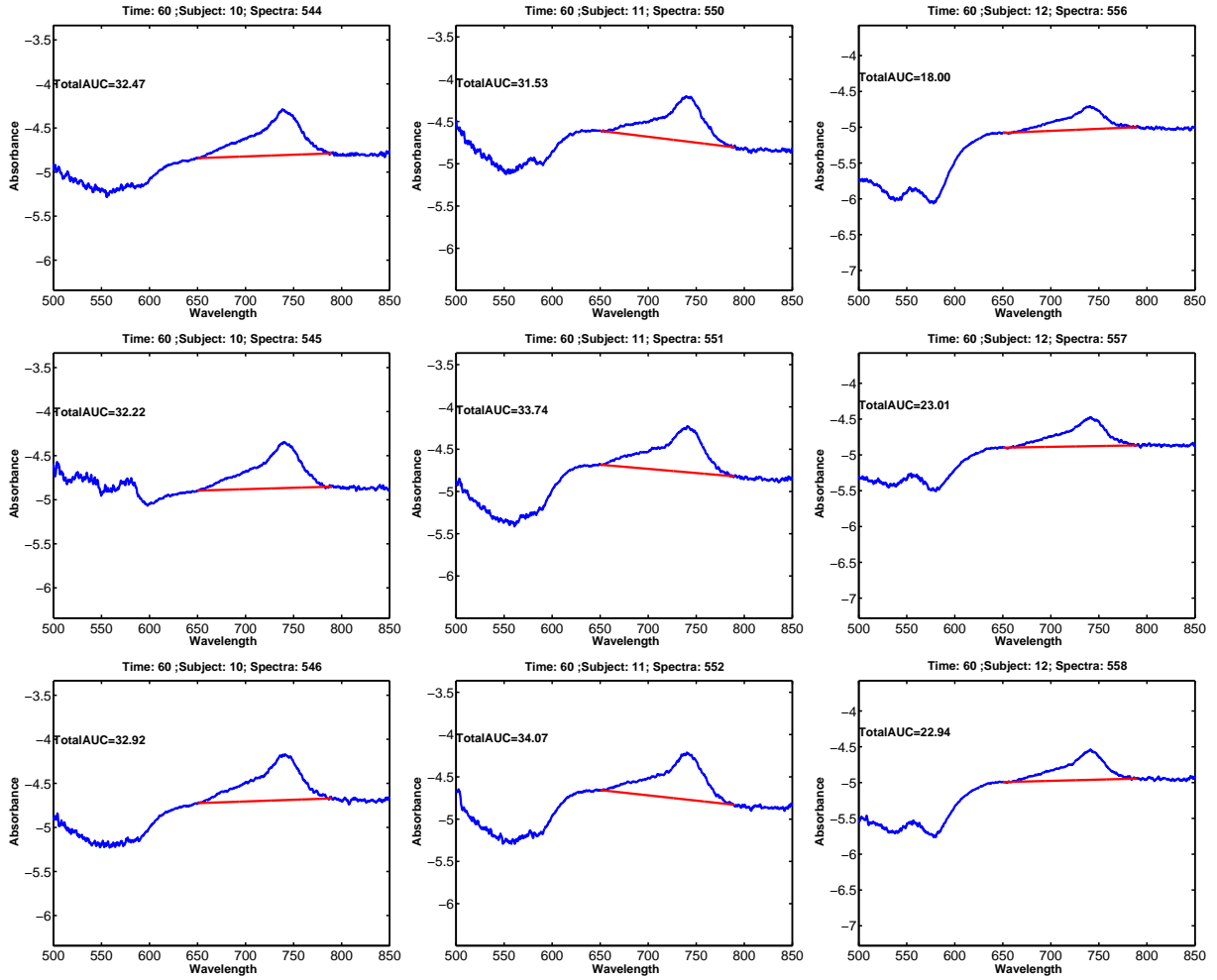
Figure B5: Model estimates of absorbance from OPS measurement of murine xenograft. Measurements made 60 min after MGd administration.
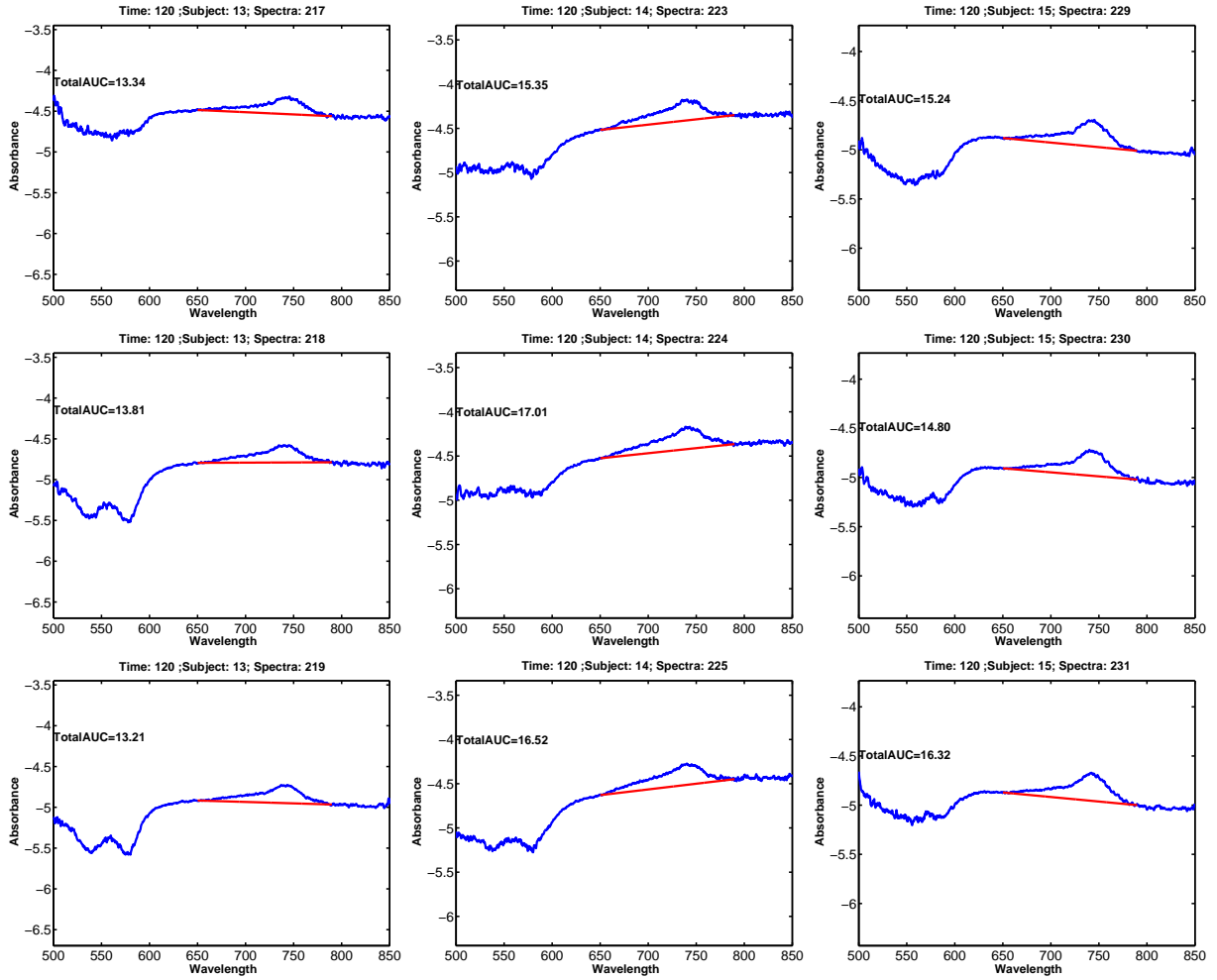
Figure B6: Model estimates of absorbance from OPS measurement of murine xenograft. Measurements made 120 min after MGd administration.
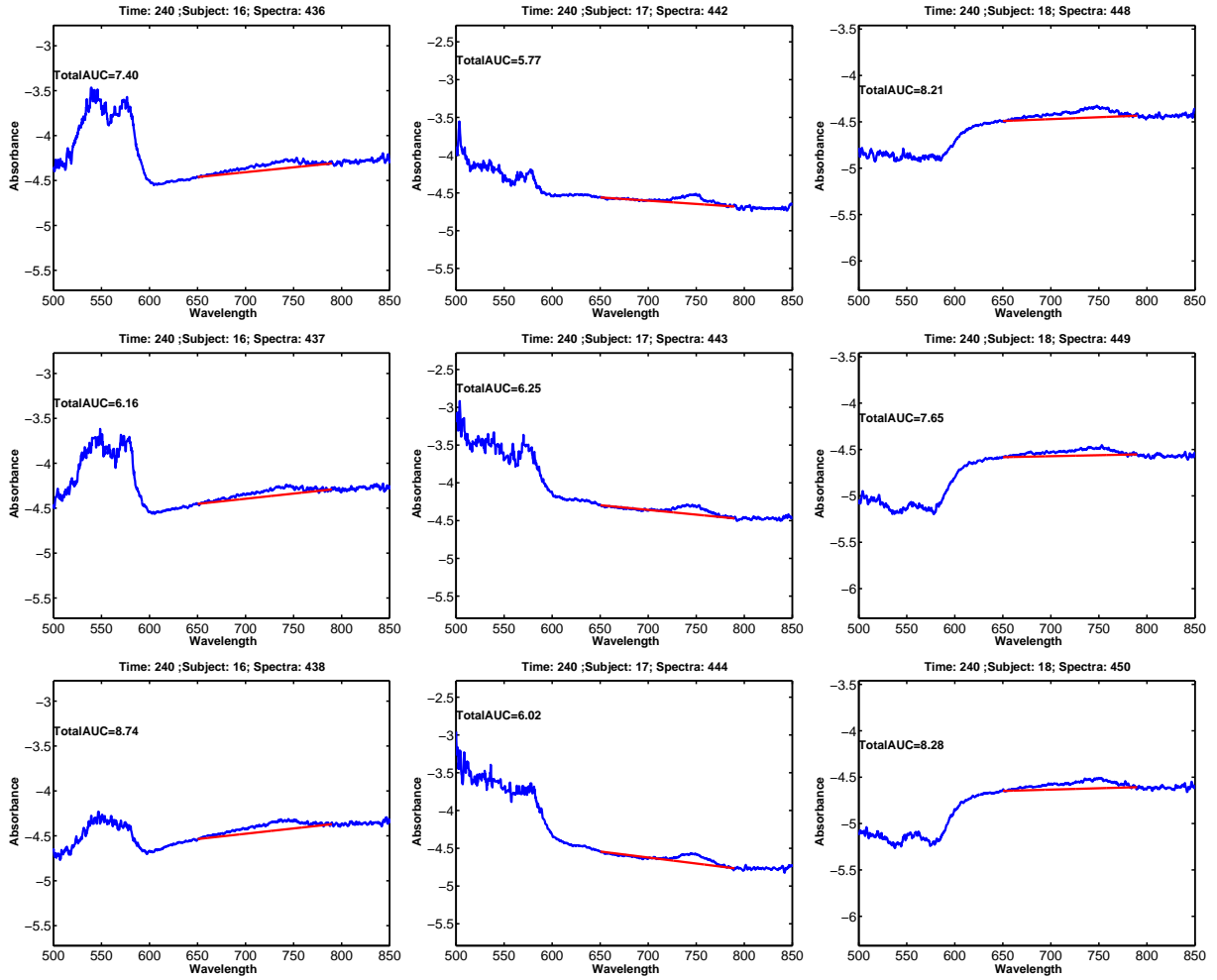
Figure B7: Model estimates of absorbance from OPS measurement of murine xenograft. Measurements made 240 min after MGd administration.
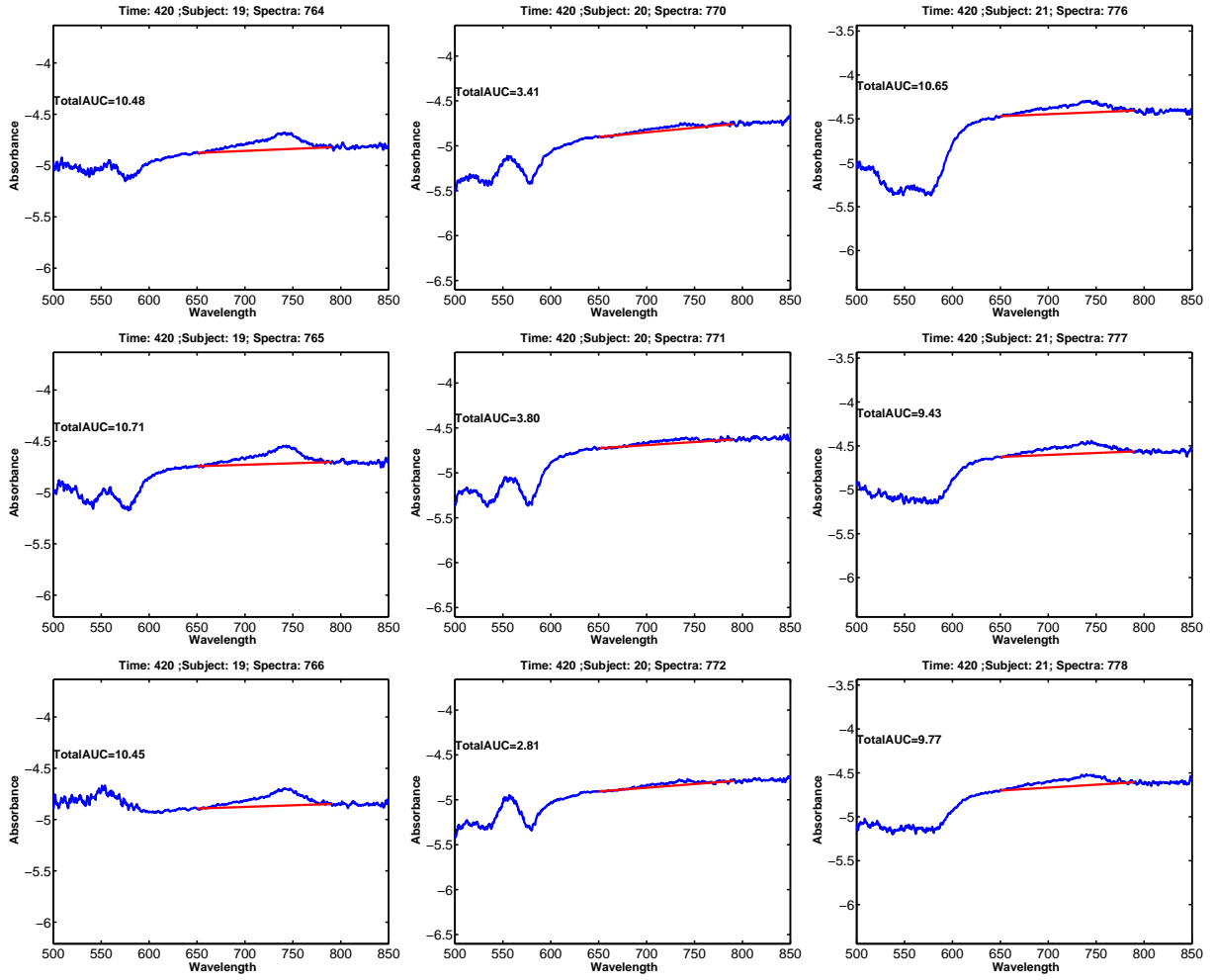
Figure B8: Model estimates of absorbance from OPS measurement of murine xenograft. Measurements made 420 min after MGd administration.
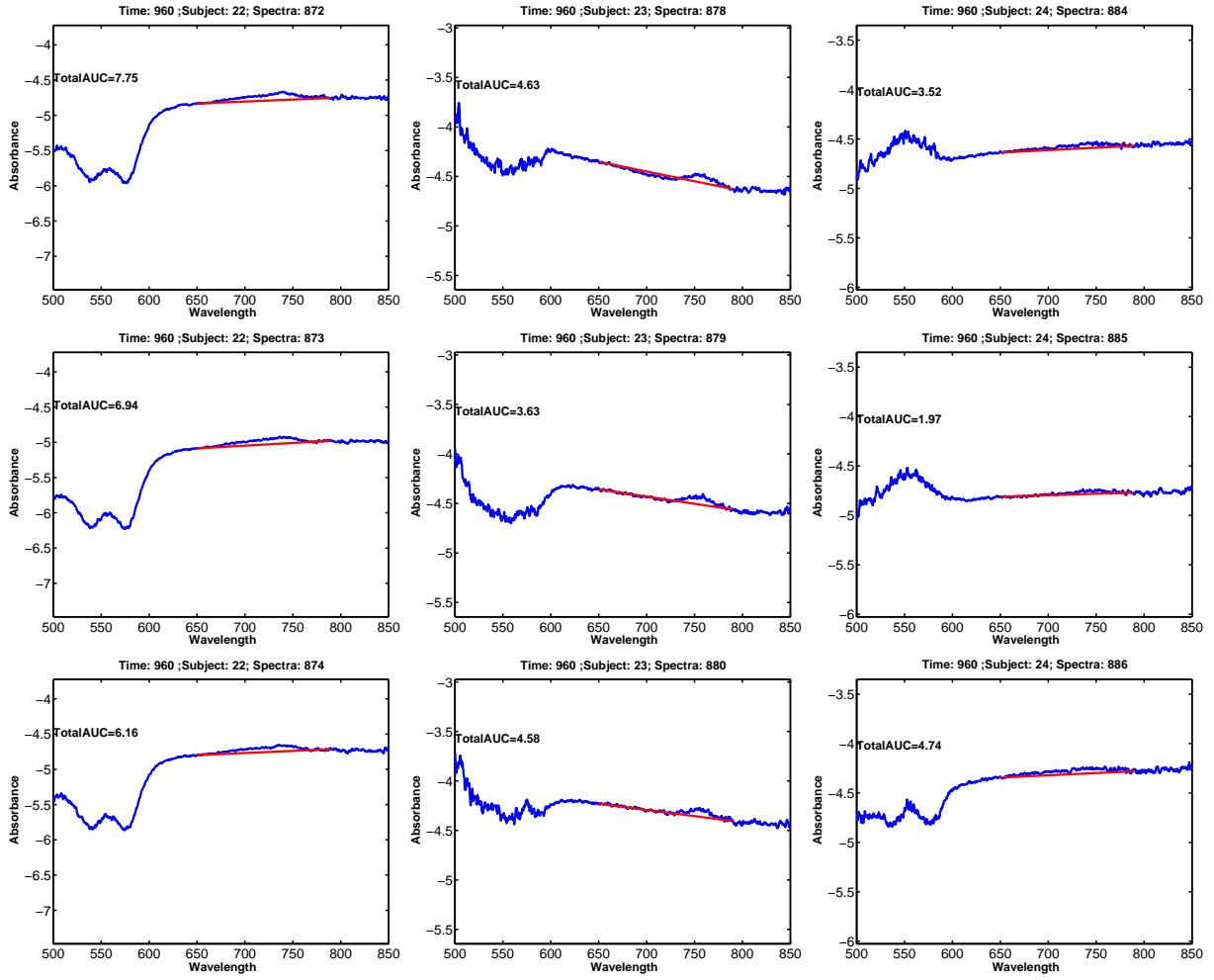
Figure B9: Model estimates of absorbance from OPS measurement of murine xenograft. Measurements made 960 min after MGd administration.
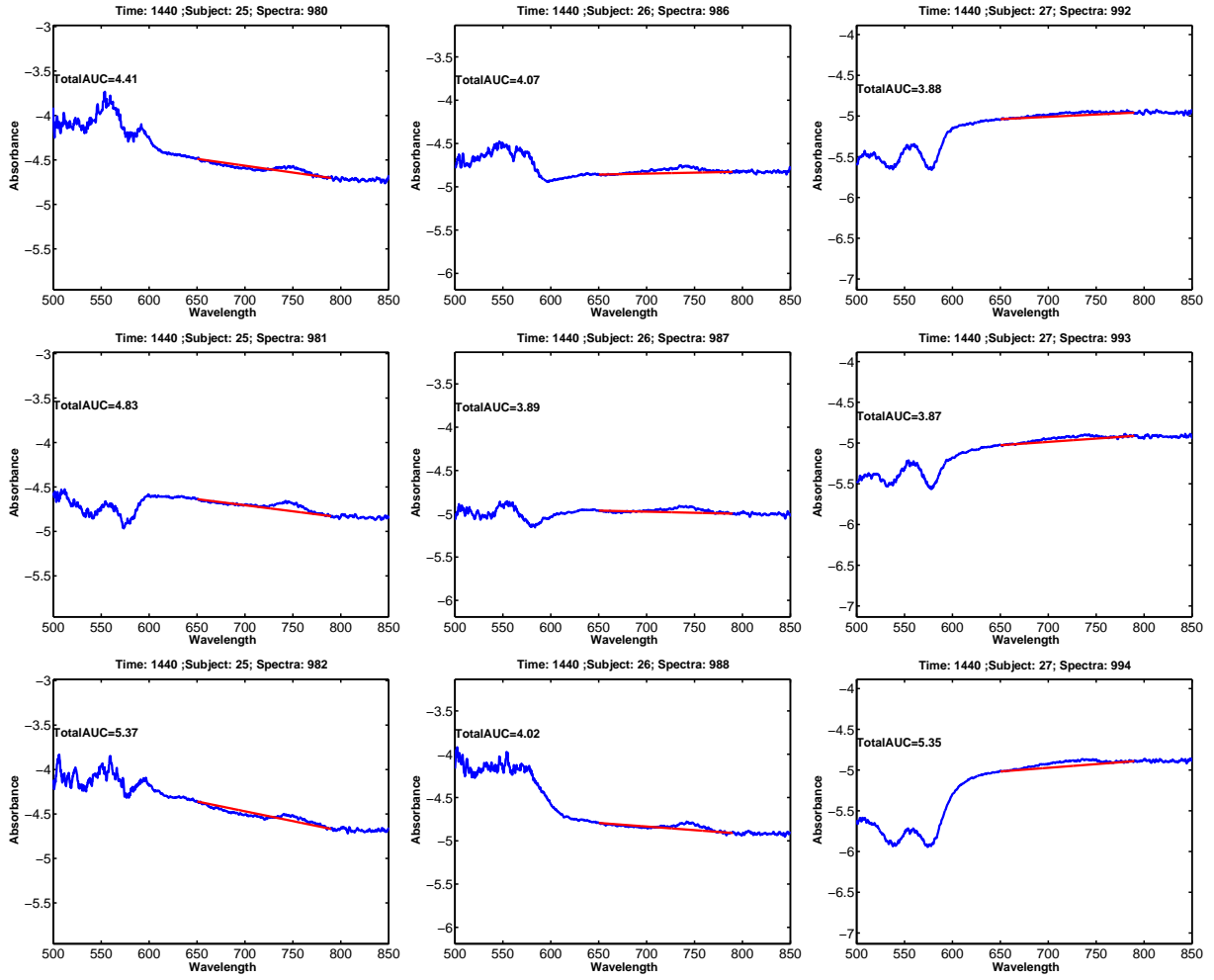
Figure B10: Model estimates of absorbance from OPS measurement of murine xenograft. Measurements made 1440 min after MGd administration.

APPENDIX C

FITTED SPECTRA: PC4, HB, AND HBO$_2$
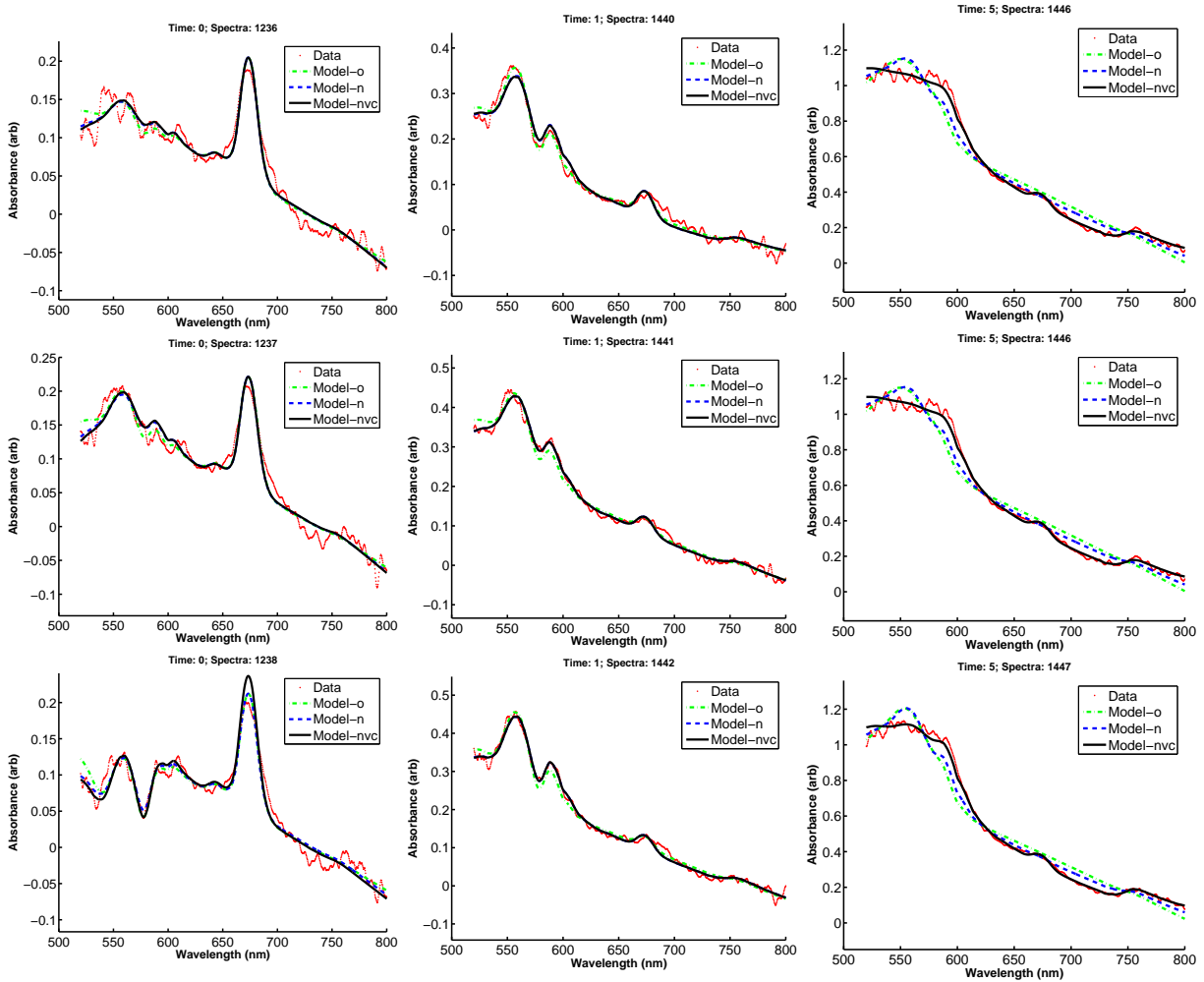
Figure C1: Model estimates of absorbance from OPS measurement of murine xenograft. Measurements made prior to- (time= 0min), and 1 min, and 5 min following Pc4-mediated PDT.
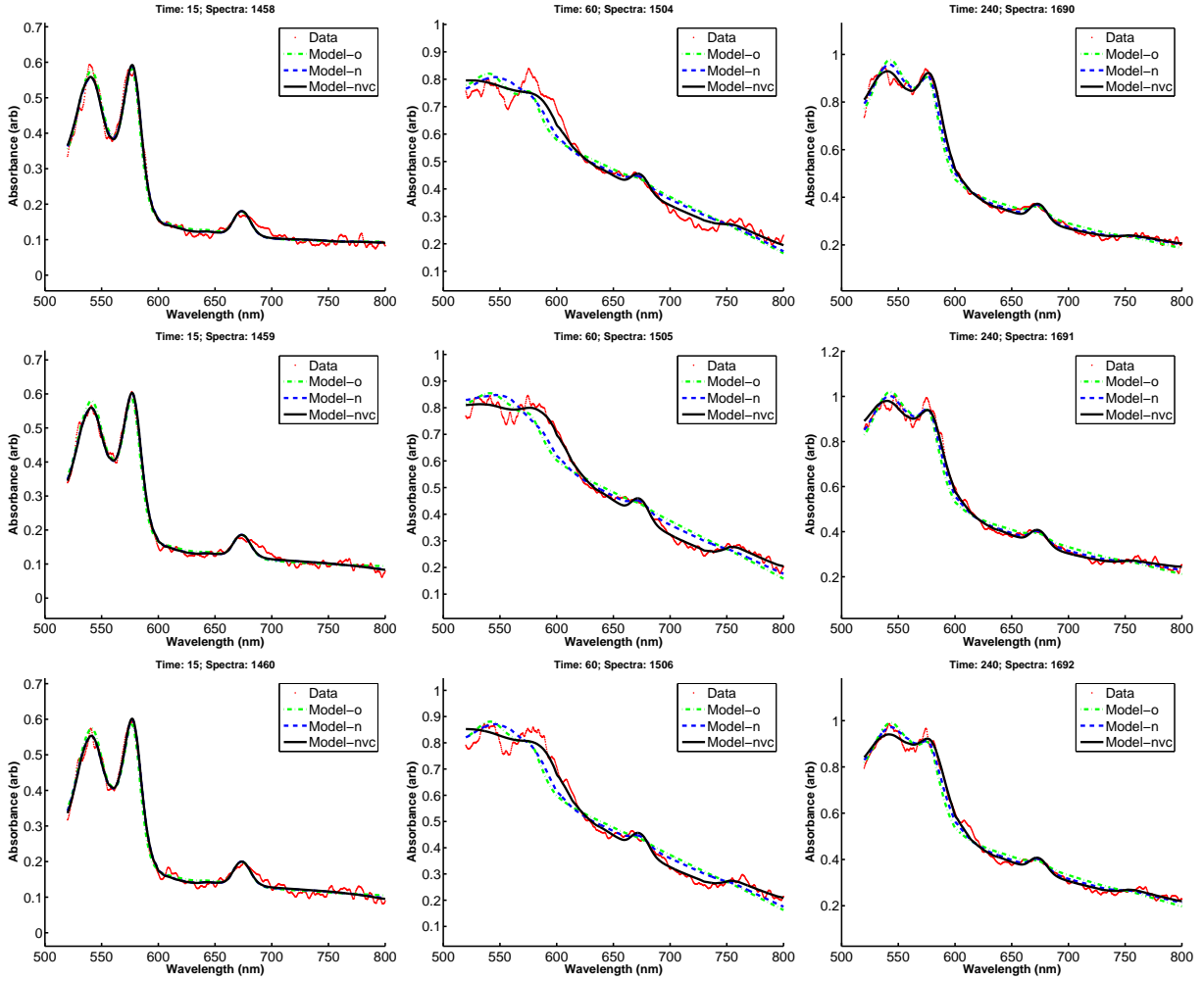
Figure C2: Model estimates of absorbance from OPS measurement of murine xenograft. Measurements 15 min, 60 min, and 240 min following Pc4-mediated PDT.
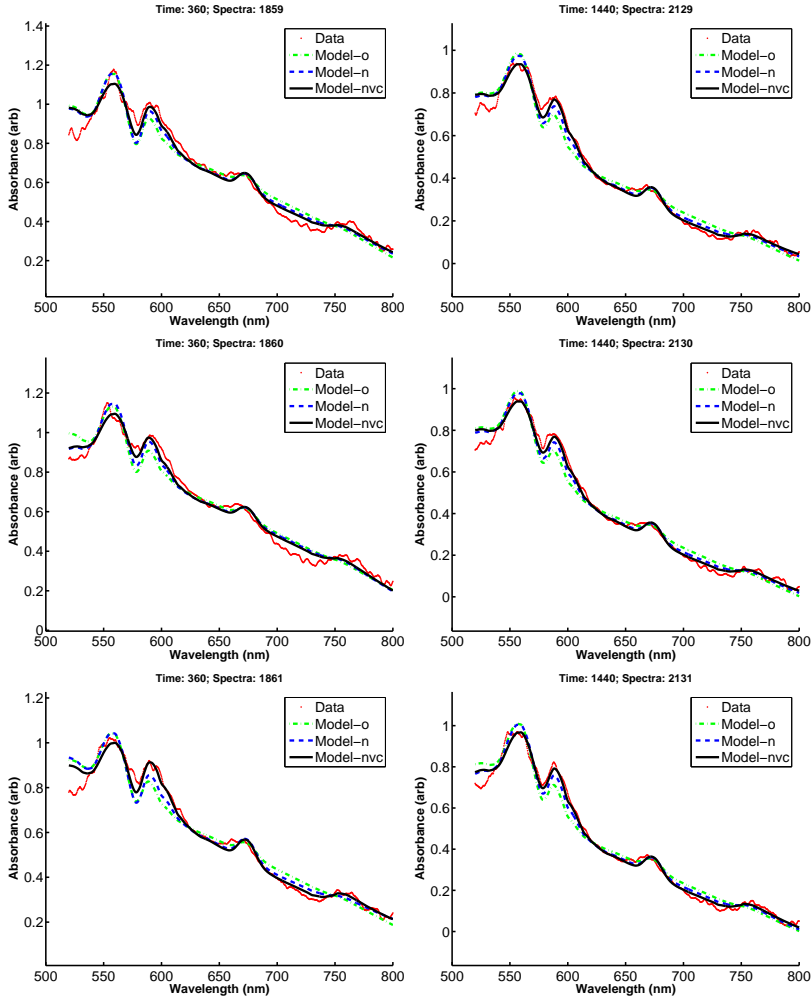
Figure C3: Model estimates of absorbance from OPS measurement of murine xenograft. Measurements 360 min and 1440 min following Pc4-mediated PDT.

APPENDIX D

HBSAT FREQUENCY DISTRIBTIONS
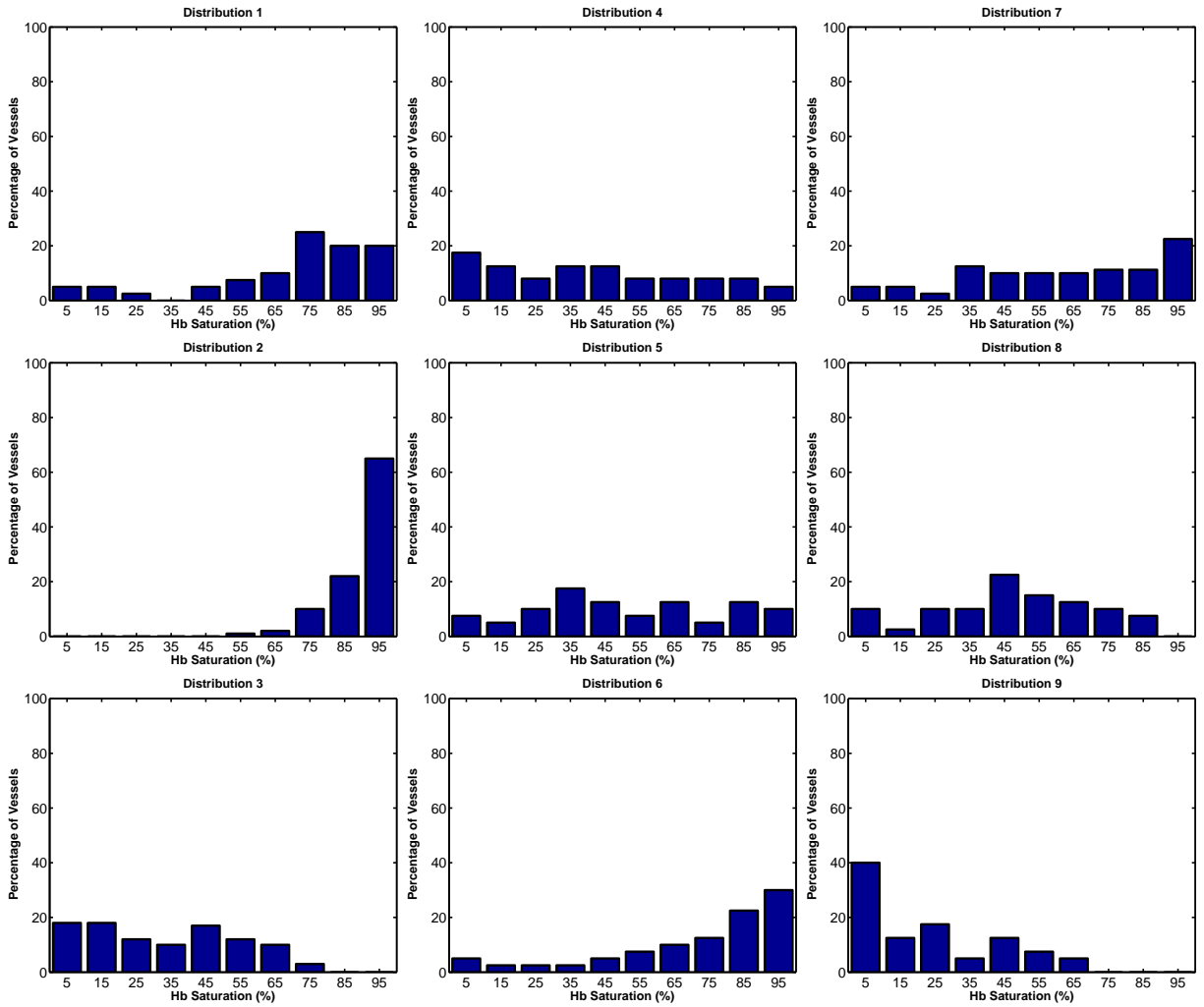
Figure D1: Hemoglobin saturation frequency distributions (1-9) in tumor cross sections measured by cryospectrophotometry and reported by Conover *et al.* [1].

APPENDIX E

MATLAB CODE

E.1 ABSORBANCE AREA CALCULATION

The code contained here can be run using MATLAB or an open-source alternative which accepts "m" files. This code contains multiple M-files, of which, the first in the sequence (AbsorbanceAreaInputs.m) is designed to edited to by users to define details of the required analysis.

E.1.1 AbsorbanceAreaInputs.m

```
%%%%%%%%%%%%%%%%%%%%%%%%%%%%%%%%%%%%%%%%
% OPS metric evaluation software
% Code evaluates Absorbance Area over a user specified wavelength range
%
% To execute first load data in the following formats:
% wavelength (1 column, all measured wavelength values)
% datavector (n columns, with intensity measured at each wavelength)
%
% In order to deconvolute hemoglobin absorbance from data,
% extinction coefficient of Hb and HbO2 must be loaded
% current code calls this as a file 'Hb_ext_coeff.txt'
% column 1: wavelength
% column 2: oxygenated hemoglobin extinction coefficient
% column 3: deoxygenated hemoglobin extinction coefficient
%
% M-file Calls --
% AreaCall.m: call algorithms used to preform calculations
```

```
%
% Code generated by Chad Kanick and Robert Parker
% University of Pittsburgh
% Department of Chemical Engineering
%%%%%%%%%%%%%%%%%%%%%%%%%%%%%%%%%%%%%%%

%Enter column identification information -------------------------
% BID contains columns within datavector that identify
% location of baseline (no drug) measurements
BID=[1:10]; %

% TID contains columns within datavector that identify
% location of measurements with drug
TID=[1:100]; %

% Integration Area Options -------------------------
% intbounds.sw - initial wavelength to start area comparison;
% intbounds.fw - wavelength at which to end area comparison;
intbounds.sw=650;
intbounds.fw=790;

% npavg: Location of linear baseline endpoints is calcualted
% at an average of data points on the absorbance curve
% about start / end wavelength bounds
% [See Chapter 2 for Details]
npavg=15; %npavg - number of data points

%Data Filter Options -------------------------
% Boxcar filter used to smooth absorbance data
% Applies nsmooth-pt boxcar filter at each datapoint
% (with endpoints accounted for) ; NOTE: n MUST BE an ODD number
applysmooth=0; %toggle boxcar smoothing on/off (0=off, 1=on)
nsmooth=15;

%Fit Absorbtion spectra for HB and HBO2 over the bounds (sw to fw)
applyfit=0; %toggle hemoglobin deconvolution on/off (0=off, 1=on)
hbbounds.sw=520;    %hbbounds.sw: starting wavelength for hb fitting
hbbounds.fw=620;    %hbbounds.fw: ending wavelength for hb fitting

%%%%%%%%%%%%%%%%%%%%%%%%%%%%%%%%%%%%%%%
%%% DO NOT MAKE CHANGES WITHIN THIS SECTION %%%%%%%%
%if applyfit == 1
    load Hb_ext_coeff.txt
    Hb_ext_coeff(:,[2,3])=Hb_ext_coeff(:,[2,3]).*.001;
    inputs.Hb_ext_coeff=Hb_ext_coeff;
```

```
%end

inputs.wavelength=wavelength;
inputs.datavector=datavector;
inputs.BID=BID;
inputs.TID=TID;
inputs.intbounds=intbounds;
inputs.npavg=npavg;
inputs.SCParams=SCParams;
inputs.plotbounds=plotbounds;
inputs.nsmooth=nsmooth;
inputs.hbbounds=hbbounds;
inputs.applysmooth=applysmooth;
inputs.applyfit=applyfit;
inputs.applyLLD=applyLLD;
inputs.LLDfactor=LLDfactor;

%%%%%%%%%%%%%%%%%%%%%%%%%%%%%%%%%%%%
[outputs]=AreaCall(inputs);

% variables outputted to workspace:_____
% outputs.wavelength - vector of all wavelength values
% outputs.baseline - vector of all baseline spectra intensity values
% outputs.measure -vector of all target spectra intensity values
% outputs.logratio -vector of the negative logratio values
% outputs.Acurve - vector of calculated area under the curve
% outputs.AdjAreas - vector of areas reduced by noise area
% outputs.LLDarea -  equal to integrated area of curve
% 'without drug' attributed to noise
```

E.1.2 AreaCall.m

```
function [outputs]=AreaCall(inputs);
%%%%%%%%%%%%%%%%%%%%%%%%%%%%%%%%%%%%%%%%%%%%%
% This file accepts user-defined inputs,
% used to call 'downstream' m-files
% Calulates logratio of intensity data
% M-file Calls --
% boxsmooth.m: boxcar smoothing function
% HBfitplugin.m: hemoglobin fitting/deconvolution
% AreaCalculator.m: numerically integrates absorbance area
% AdjAreas.m: calculates and adjusts area
%     attributable to 'noise'
%%%%%%%%%%%%%%%%%%%%%%%%%%%%%%%%%%%%%%%%%%%%%
```

```
%------------------------------------------------------------
% Initialize counting variables
outputs.tc=size(inputs.TID,2);
% calculates length of data set to be analyzed
outputs.baseline=inputs.datavector(:,inputs.BID);
% pulls 'no drug' intensity measures
outputs.measure=inputs.datavector(:,inputs.TID);
% pulls 'with drug' intensity measures
outputs.meanbaseline(:,1)=mean(outputs.baseline,2);
% averages 'no drug' intensities


%------------------------------------------------------------
% Calculate ratio of each measure 'with drug'
% to mean baseline 'without drug'
for i =1:size(inputs.TID,2),
outputs.ratio(:,i)=(outputs.measure(:,i)+.0000001)
./(outputs.meanbaseline+.0000001);
%ratio value with (small) correction to
%avoid division by zero log of zero
end
% Absorbance is related to log of the ratio
%[See text in Chapter 2 for details]
outputs.logratio(:,:)=log(outputs.ratio(:,:).*100);


%------------------------------------------------------------
% Boxcar Smoothing
if inputs.applysmooth == 1
[outputs.logratio]=boxsmooth(outputs.logratio,inputs.nsmooth);
% Calculation returns variable the same size as outputs.logratio
% with values averaged over boxcar width
end


%------------------------------------------------------------
% HB fitting and absorbance removal
if inputs.applyfit == 1
[Hbcalc.Yreduced,Hbcalc.X]=HBfitplugin(inputs,outputs);
outputs.logratio=Hbcalc.Yreduced;
outputs.Hbrat=Hbcalc.X;
end


%------------------------------------------------------------
% Calculate absorbance areas
[outputs.Acurve,outputs.line,outputs.pline]=
AreaCalculator(inputs,outputs);
```

```
%---------------------------------------------------------------
% Calculate and remove 'noise' area
[outputs]=AdjAreas(outputs,inputs)
```

E.1.3   boxsmooth.m

```
function [datavectoroutput]=boxsmooth(datavector,nsmooth)
%%%%%%%%%%%%%%%%%%%%%%%%%%%%%%%%%%%%
% This file returns a 'smoothed' absorbance data
% Employs a simple boxcar filter, with each data point
% equated to the average of all points located within
% 'window' that is 'nsmooth' in width.
%%%%%%%%%%%%%%%%%%%%%%%%%%%%%%%%%%%%
Y=datavector(:,:);
L=size(Y,1);
w=size(Y,2);
n=(nsmooth-1)/2;

for j=1:w,
    smoothmeasure(1:n,j)=Y(1:n,j);
    smoothmeasure(L-n:L,j)=Y(L-n:L,j);
for k=n+1:(L-n-1)
smoothmeasure(k,j)=sum(Y(k-n:k+n,j))/(2*n+1);
end
end

datavectoroutput=smoothmeasure;
```

E.1.4   Hbfitplugin.m

```
function [YreducedA,X]=Hbfitplugin(inputs,ocalc)

%%%%%%%%%%%%%%%%%%%%%%%%%%%%%%%%%%%%%%%%%
% M-file coded to regress contribution of Hb and HbO2 to
% OPS collected -log(I/Io) spectra%
%
% Inputs:
% Load the following files into the matlab workspace:
% (can be loaded as .mat or .txt format)
% Hb_ext_coeff.txt:
%(matrix col1: wavelength, col2: extcoeff_HbO2, col3: extcoeff_Hb)
% wavelength.txt (vector)
% datavector.txt (matrix):
```

```matlab
% containing all -log(I/Io) values
%
% Define the following variables:
% hbbounds.sw:  wavelength to begin Hb/HbO2 fitting
% hbbounds.fw:  wavelength to end Hb/HbO2 fitting
%
%%%%%%%%%%%%%%%%%%%%%%%%%%%%%%%%%%%%%%%%%%

%-----------------------------------------------------------
% Tenames logratio vector and gets number of columns
% (to calculate the number of measured spectra)
L=ocalc.logratio;
l=size(ocalc.logratio,2);

%-----------------------------------------------------------
% interpolates the Hb extinction coefficients
% allows better estimation of
% Hb ext coeff at OPS-measured wavelengths
Ex(:,1)=interp(inputs.Hb_ext_coeff(:,1),10);
Ex(:,2)=interp(inputs.Hb_ext_coeff(:,2),10);
Ex(:,3)=interp(inputs.Hb_ext_coeff(:,3),10);

%-----------------------------------------------------------
%loop set up to analyze each measured spectra
for n=1:l;

% searches for 'closest' input.wavelength
% at bounds between measured spectra
% and wavelength range of interest
[isv,j]=min((inputs.wavelength(:,1)-inputs.hbbounds.sw).^2);
[ifv,f]=min((inputs.wavelength(:,1)-inputs.hbbounds.fw).^2);

% truncate wavelength and logratio values
% to the wavelength range of interest
W=input.wavelength(j:f);
Y=ocalc.logratio([j:f],n);

% searches for 'closest' wavelength at bounds
% between extinction coefficients
% and wavelength range of interest
[isv,j]=min((Ex(:,1)-inputs.hbbounds.sw).^2);
[ifv,f]=min((Ex(:,1)-inputs.hbbounds.fw).^2);

% truncate extinction coefficients to the
% wavelength range of interest
```

```
KF=(Ex([j:f],1));
% wavelengths for extinction coefficients
FF1=(Ex([j:f],2));
% pull extinction coefficient values for Hb
FF2=(Ex([j:f],3));
% pull extinction coefficient values for HbO2

% expand (via interpolation) ext coeff
% to match collected light spectra
for p=1:length(Y)
     Fnew(p,1)=W(p,1);
      [z1,z2]=min((KF(:,1)-W(p,1)).^2);
      Fnew(p,2)=FF1(z2,1);
      Fnew(p,3)=FF2(z2,1);
end

% treats the 'fitting' of the extinction
% coefficients as a generalized least squares
% problem and computes an analytical solution
Fones=ones(length(Fnew),1);
% create a vector of 1's
A=[Fnew(:,2),Fnew(:,3),Fones];
% compse the A matrix
AT=A';
% transpose of the A matrix
xA=((AT*A)^-1)*AT*Y(:,1);
% calculate the value of xA
% xA(:,1) is the contribution of Hb
% xA(:,2) is the contribution of HbO2
% xA(:,3) is the correction factor for the verticle shift mismatch
%       between the logratio values and the extinction coefficients

Yplot=xA(1).*Fnew(:,2)+xA(2).*Fnew(:,3)+xA(3);
% Note: Yplot can be used to plot data for
% visualization of hemoglobin absorbance

%establish range of wavelengths collected by OPS
inputs.hbbounds.rsw=inputs.wavelength(1);
inputs.hbbounds.rfw=inputs.wavelength(length(inputs.wavelength));
[isv,j]=min((inputs.wavelength(:,1)-inputs.hbbounds.rsw).^2);
[ifv,f]=min((inputs.wavelength(:,1)-inputs.hbbounds.rfw).^2);
%selects correct logratio column
YE=ocalc.logratio([j:f],n);

%selects the extinction coefficient values
```

```
% of the range of OPS-measured values
[isv,j]=min((Ex(:,1)-inputs.hbbounds.rsw).^2);
[ifv,f]=min((Ex(:,1)-inputs.hbbounds.rfw).^2);


KFE=(Ex([j:f],1));% wavelengths for extinction coefficients
FF1E=(Ex([j:f],2));
FF2E=(Ex([j:f],3));


for p=1:length(inputs.wavelength)
FEnew(p,1)=inputs.wavelength(p,1);
[z1,z2]=min((KFE(:,1)-inputs.wavelength(p,1)).^2);
FEnew(p,2)=FF1E(z2,1);
FEnew(p,3)=FF2E(z2,1);
end


% Code subtracts the weighted values of
% both extinction coefficints from the
% logratio vector over 'all' wavelengths measured by OPS
% YreducedA: -logratio with Hb and HbO2 contribution removed
YreducedA(:,n)=YE(:,1)-(xA(1).*FEnew(:,2)+xA(2).*FEnew(:,3));
% X: relative estimates of Hb and HbO2 contribution to -logratio
X(n,:)=[xA(1),xA(2)];
end
```

E.1.5   AreaCalculator.m

```
function [Acurve,line,pline]=AreaCalculator(inputs,ocalc)
%%%%%%%%%%%%%%%%%%%%%%%%%%%%%%%%%%%%%%%%%%%%
% This calculation numerically integrates the area between the
% data in an the ocalc.logratio matrix, and a linear baseline,
% that is constructed individually for each spectra between
% the specified wavelength endpoints. Modified Simpsons rule
% used for numerical integration, given by Equation 2.16.
%%%%%%%%%%%%%%%%%%%%%%%%%%%%%%%%%%%%%%%%%%%

%Begin Calculation of peak absorbance area
%-----------------------------------------------------------
[rsize,csize]=size(inputs.wavelength);
% gets size of wavelength vector
[rsize2,csize2]=size(ocalc.logratio);
% gets size of logratio matrix

% Variables (j and f) describe the position in the
% wavelength vector which most
```

```
% closely match the selected bounds (sw,fw)
[isv,j]=min((inputs.wavelength(:,1)-inputs.intbounds.sw).^2);
[ifv,f]=min((inputs.wavelength(:,1)-inputs.intbounds.fw).^2);
stepsize=abs(inputs.wavelength(2,1)-inputs.wavelength(1,1));

%-------------------------------------------------------------
% Loops for each meausure contained in TID.
% Code treats endpoints of line as 'pointA' and 'pointB'.
% 'pointA' is located at starting wavelength (sw)
% 'pointB' is located at ending wavelength (fw)
% Note: atrimstudy is a dummy variable
% Note: pline can be used to plot linear baseline on same scale
%            as absorbance area curve
for i=1:ocalc.tc,
pointA(1,i)=mean(-ocalc.logratio((j-inputs.npavg):(j),i));
pointB(1,i)=mean(-ocalc.logratio((f):(f+inputs.npavg),i));
trimstudy(:,i)=-ocalc.logratio(j:f,i);
    %generates 'dummy' data set for manipulations
    [rt,ct]=size(trimstudy);
    [im,jm]=min(abs([pointA(1,i);pointB(1,i)]));
    %this finds the min of abs value @ either end

Va=pointA(1,i);
Vb=pointB(1,i);
        Sa=sign(pointA(1,i));
        Sb=sign(pointB(1,i));
        if Vb == 0,
            pointB(1,i)=0.0001;
            Vb=pointB(1,i);
        end;
        if Va == 0,
            pointA(1,i)=0.0001;
            Va=pointA(1,i);
        end;

% if PointA is greater than PointB, then subtract
% the value of PointB across all points
if Va > Vb,
line(:,i)=((Vb-Va)/(inputs.wavelength(f,1)-inputs.wavelength(j,1)))
*(inputs.wavelength(j:f,1)-inputs.wavelength(j,1))+Va;
pline(:,i)=line(:,i)+pointB(1,i);
atrimstudy(:,i)=abs(trimstudy(:,i)-line(:,i));
Atotal(1,i)=stepsize*(sum(atrimstudy(3:rt-2,i))+(13/12)*(atrimstudy(2,i)
+atrimstudy(rt-1,i))+(5/12)*(atrimstudy(1,i)+atrimstudy(rt,i)));
Acurve(1,i)=Atotal(1,i);
```

```
% if PointB is greater than PointA, then subtract
% the value of PointA across all points
elseif Vb > Va,
line(:,i)=((Vb-Va)/(inputs.wavelength(f,1)-inputs.wavelength(j,1)))
*(inputs.wavelength(j:f,1)-inputs.wavelength(j,1))+Va;
pline(:,i)=line(:,i)+pointA(1,i);
atrimstudy(:,i)=abs(trimstudy(:,i)-line(:,i));
Atotal(1,i)=stepsize*(sum(atrimstudy(3:rt-2,i))+(13/12)*(atrimstudy(2,i)
+atrimstudy(rt-1,i))+(5/12)*(atrimstudy(1,i)+atrimstudy(rt,i)));
Acurve(1,i)=Atotal(1,i);
end;

end;

%-----------------------------------
```

E.1.6   AdjAreas.m

```
function [outputs]=AdjAreas(outputs,inputs)
%%%%%%%%%%%%%%%%%%%%%%%%%%%%%%%%%%%%%%%%
% Code calculates area attributable to 'noise' in spectra
% Areas can be reduced by this amount, effectively removing the
% contribution of 'noise' to absorbanced area.
% [See Chapter 2 for details]
%%%%%%%%%%%%%%%%%%%%%%%%%%%%%%%%%%%%%%%
NAreas=outputs.Acurve;  %initialize manipulated variable

%LLD set (a priori) as mean + standard deviation
% of integrated areas with no drug on board
outputs.LLDarea=std(ocalc.Acurve(1:length(inputs.BID)))
+mean(ocalc.Acurve(1:length(inputs.BID))),
k=1;
for t=1:length(outputs.Acurve),
if outputs.Acurve(t) > outputs.LLDarea,
%if Area is above LLD, 'adjusted area' is reduced by LLD value
NAreas(k)=outputs.Acurve(t)-outputs.LLDarea;
k=k+1;
else
%if Area is below LLD, 'adjusted area' is set to LLD value
NAreas(k)=outputs.LLDarea;
end
end
```

```
outputs.AdjAreas=NAreas;
```

E.2   MONTE CARLO CODE: PROPAGATION WITH DISCRETE VESSELS

The code contained here is written in C-script, and is intended to be 'mex-ed' prior to use in the MATLAB environment. The code file contained here is intended to work in sequence with the MCML code published by Lihong Wang (Texas A&M) and Steven L. Jacques (Oregon). Specifically, the enclosed file determines if photons propagating through a medium with discrete vessels intersect any vessel/tissue interface during propagation. This code would be called after a new photon location has been selected, but prior to the movement of the photon.

The MATLAB call for this function can be given as:

```
[hit,Distmoved,Xh,Zh,muah,mush]=PhotonStepCheck(XPosition(MT,1),
XPosition1(MT,1),Xc,ZPosition(MT,1),
ZPosition1(MT,1),Zc,r,muap(MT,1),
musp(MT,1),muatiss,mustiss,muacap,muscap);
```

Where the function inputs are:

```
% MT:  vector (length # of photons simulated) providing
% providing binary yes/no if photons are being propagated
% (No would indicates photon had exited tissue or absorbed)
%XPosition: vector (length # of photons simulated) providing
% x-coordinate prior to current step
%XPosition1: vector (length # of photons simulated) providing
% x-coordinate expected at end of current step
%Xc: vector (length # of vessels) providing x-coordinate of
% each vessel center
%ZPosition: vector (length # of photons simulated) providing
% z-coordinate prior to current step
%ZPosition1: vector (length # of photons simulated) providing
% z-coordinate expected at end of current step
%Zc: vector (length # of vessels) providing z-coordinate of each
% vessel center
%r: vector (length # of vessels) providing radius of each vessel
%muap(MT,1): vector (length # of photons simulated) providing
% absorption coefficient for each photon at (XPosition,ZPosition)
```

```
%musp(MT,1): vector (length # of photons simulated) providing
% scattering coefficient for each photon at (XPosition,ZPosition)
%muatiss: scalar indicating tissue absorption coefficient
%mustiss: scalar indicating tissue scattering coefficient
%muacap: vector (length # of vessels) providing
% absorption coefficient within each vessel
%muscap: vector (length # of vessels) providing
% scattering coefficient within each vessel
```

And the function returns:

```
% hit: vector (length # of photons): providing binary yes/no
% (1/0) if photons hit vessel during propagation step
% Distmoved: vector (length # of photons): total distance between
% staring point and interaction point with vessel
% Xh: vector (length # of photons):
%     x-coordinate of photon/vessel interaction
% Zh: vector (length # of photons):
%      z-coordinate of photon/vessel interaction
% muah: vector (length # of photons): new absorption coefficient
% for photon crossing vessel
% mush: vector (length # of photons): new scattering coefficient
% for photon crossing vessel
```

E.2.1   PhotonStepCheck.c

```c
#include "mex.h"
#include <stdio.h>
#include <stdlib.h>
#include <math.h>
#include "io64.h"

void PhotonStepCheck(double *data0x, double *data1x,
double *data2x, double *data0z, double *data1z,
double *data2z, double *datar, int nphoton, int ncap,
double *hit, double *distmoved, double *xhit,
double *zhit, double *datamua, double *datamus,
double *muahit, double *mushit, double *datamuaback,
double *datamusback, double *datamuacap,
double *datamuscap)
{

 double disthit1, disthit2, d, newX, newZ;
 double tempa, tempb, tempc, dataxmax, dataxmin;
 double datazmax, datazmin, intpt1, intpt2, temprint;
```

```
 double tempc1, tempc2, tempc3, tempc4, p1, p2;
 double dataq, step, distregion, checknewpoint, push;
 int  i, j;
 double dx, dz, dr, D, check, intx1, intx2, intz1, intz2;

/* Loop through each photon*/
for (i = 0; i < nphoton; i++)
 {

/* Find min and max X and Z values.
 * Used later to determine if intersection point
 * falls between inital and final points. */

    if (data1x[i] > data0x[i])
    {
dataxmax = data1x[i];
dataxmin = data0x[i];
    }
    else
    {
dataxmax = data0x[i];
dataxmin = data1x[i];
    }
    if (data1z[i] > data0z[i])
    {
     datazmax = data1z[i];
datazmin = data0z[i];
    }
    else
    {
datazmax = data0z[i];
datazmin = data1z[i];
    }
/* Calculate photon step in x-z direction */
step= sqrt((data0x[i]-data1x[i]) * (data0x[i]-data1x[i])
+ (data0z[i]-data1z[i]) * (data0z[i]-data1z[i]));
/* Initalize these for each photon */
distmoved[i]=0.0;
xhit[i]=data1x[i];
zhit[i]=data1z[i];
hit[i]=0.0;
muahit[i]=datamua[i];
mushit[i]=datamus[i];

/* Loop through each capillary (n=j) within geometry*/
```

```
    for (j = 0; j < ncap; j++)
{
/* if distregion>=0, Photon is outside of capillary(j) at (x0,z0)*/
/* Calculate minimum distance to hit capillary(j) */
distregion= sqrt((data0x[i]-data2x[j]) * (data0x[i]-data2x[j])
+ (data0z[i]-data2z[j]) * (data0z[i]-data2z[j]))-datar[j];
/* mexPrintf("step: %g, dist: %g\n", step, distregion);  */
/* Determine if photon is currently within capillary(j) */
if (distregion >= 0.0)
{
/* Determine if capillary(j) is within stepping region */
if (step >= distregion)
{
/* Formula used to analytically determine possible intersection
 * points between line (photon path) and circle (vessel) */
dx = (data1x[i]-data2x[j])-(data0x[i]-data2x[j]);
dz = (data1z[i]-data2z[j])-(data0z[i]-data2z[j]);
dr = sqrt(dx*dx + dz*dz);
D = (data0x[i]-data2x[j])*(data1z[i]-data2z[j])
   - (data1x[i]-data2x[j])*(data0z[i]-data2z[j]);
check = datar[j]*datar[j]*dr*dr - D * D;

if (check == 0.0)
/* Photon contacts capillary at one point
 * (tangent intersection) */
{
intx1 = ((D * dz ) / (dr * dr)) + data2x[j];
intz1 = ((-D * dx) / (dr * dr)) + data2z[j];
disthit1= sqrt((data0x[i]-intx1) * (data0x[i]-intx1)
+ (data0z[i]-intz1) * (data0z[i]-intz1));
}
if (check > 0.0)
{
if (dz >= 0.0)
{
intx1 = ((D * dz + dx * sqrt(check)) / (dr * dr)) + data2x[j];
intx2 = ((D * dz - dx * sqrt(check)) / (dr * dr)) + data2x[j];
intz1 = ((-D * dx + dz * sqrt(check)) / (dr * dr)) + data2z[j];
  intz2 = ((-D * dx - dz * sqrt(check)) / (dr * dr)) + data2z[j];
}
else
{
intx1 = ((D * dz - dx * sqrt(check)) / (dr * dr)) + data2x[j];
intx2 = ((D * dz + dx * sqrt(check)) / (dr * dr)) + data2x[j];
intz1 = ((-D * dx - dz * sqrt(check)) / (dr * dr)) + data2z[j];
```

```
    intz2 = ((-D * dx + dz * sqrt(check)) / (dr * dr)) + data2z[j];
}
disthit1= sqrt((data0x[i]-intx1)
* (data0x[i]-intx1) + (data0z[i]-intz1)
* (data0z[i]-intz1));
disthit2= sqrt((data0x[i]-intx2)
* (data0x[i]-intx2) + (data0z[i]-intz2)
* (data0z[i]-intz2));
}
if (check >= 0.0 && intx1 >= dataxmin && intx1 <= dataxmax)
{
if (distmoved[i] > 0.0)
{
if (distmoved[i] > disthit1)
{
/* If yes: log distance,
 * X and Z coordinates */
hit[i]=1.0;
distmoved[i]=disthit1;
xhit[i]=intx1;
zhit[i]=intz1;
muahit[i]=datamuacap[j];
mushit[i]=datamuscap[j];
}
}
else
{
/* If yes: log distance,
 * X and Z coordinates */
hit[i]=1.0;
distmoved[i]=disthit1;
xhit[i]=intx1;
zhit[i]=intz1;
muahit[i]=datamuacap[j];
mushit[i]=datamuscap[j];
}
}
if (check > 0.0 && intx2 >= dataxmin && intx2 <= dataxmax)
/* if (intx2 >= dataxmin && intx2 <= dataxmax)*/
{
if (distmoved[i] > 0.0)
{
if (distmoved[i] > disthit2)
{
/* If yes: log distance,
```

```
 * X and Z coordinates */
distmoved[i]=disthit2;
xhit[i]=intx2;
zhit[i]=intz2;
hit[i]=1.0;
muahit[i]=datamuacap[j];
mushit[i]=datamuscap[j];
}
}
else
{
/* If yes: log distance,
 * X and Z coordinates */
distmoved[i]=disthit2;
xhit[i]=intx2;
zhit[i]=intz2;
hit[i]=1.0;
muahit[i]=datamuacap[j];
mushit[i]=datamuscap[j];
}
}
}
}
else
{
checknewpoint=sqrt((data1x[i]-data2x[j])*(data1x[i]-data2x[j])
+ (data1z[i]-data2z[j])*(data1z[i]-data2z[j]))-datar[j];
if (checknewpoint <= 0.0)
{
/* New point inside of vessel*/
hit[i]=0.0;
muahit[i]=datamuacap[j];
mushit[i]=datamuscap[j];
distmoved[i]=step;
xhit[i]=data1x[i];
zhit[i]=data1z[i];
    }
else
{
/* Photon exits vessel*/
/*  mexPrintf("photon exits capillary. \n"); */
dx = (data1x[i]-data2x[j])-(data0x[i]-data2x[j]);
dz = (data1z[i]-data2z[j])-(data0z[i]-data2z[j]);
dr = sqrt(dx*dx + dz*dz);
D = (data0x[i]-data2x[j])*(data1z[i]-data2z[j])
```

```
- (data1x[i]-data2x[j])*(data0z[i]-data2z[j]);
check = datar[j]*datar[j]*dr*dr - D * D;
if (check > 0.0)
{
if (dz >= 0.0)
{
intx1 = ((D * dz + dx * sqrt(check))
/ (dr * dr)) + data2x[j];
intx2 = ((D * dz - dx * sqrt(check))
/ (dr * dr)) + data2x[j];
intz1 = ((-D * dx + dz * sqrt(check))
/ (dr * dr)) + data2z[j];
  intz2 = ((-D * dx - dz * sqrt(check))
/ (dr * dr)) + data2z[j];
}
else
{
intx1 = ((D * dz - dx * sqrt(check)) / (dr * dr)) + data2x[j];
intx2 = ((D * dz + dx * sqrt(check)) / (dr * dr)) + data2x[j];
intz1 = ((-D * dx - dz * sqrt(check)) / (dr * dr)) + data2z[j];
  intz2 = ((-D * dx + dz * sqrt(check)) / (dr * dr)) + data2z[j];
}
disthit1= sqrt((data0x[i]-intx1) * (data0x[i]-intx1)
+ (data0z[i]-intz1) * (data0z[i]-intz1));
disthit2= sqrt((data0x[i]-intx2) * (data0x[i]-intx2)
+ (data0z[i]-intz2) * (data0z[i]-intz2));
}
/*if (intx1 >= dataxmin && intx1 <= dataxmax)*/
if (check >= 0.0 && intx1 >= dataxmin && intx1 <= dataxmax)
{
if (distmoved[i] > 0.0)
{
if (distmoved[i] > disthit1)
{
/* If yes: log distance, X and Z coordinates */
hit[i]=1.0;
distmoved[i]=disthit1;
xhit[i]=intx1;
zhit[i]=intz1;
muahit[i]=datamuaback[0];
mushit[i]=datamusback[0];
}

}
else
```

```c
{
/* If yes: log distance, X and Z coordinates */
hit[i]=1.0;
distmoved[i]=disthit1;
xhit[i]=intx1;
zhit[i]=intz1;
muahit[i]=datamuaback[0];
mushit[i]=datamusback[0];
}
}
/*  if (intx2 >= dataxmin && intx2 <= dataxmax) */
if (check > 0.0 && intx2 >= dataxmin && intx2 <= dataxmax)

{
if (distmoved[i] > 0.0)
{
if (distmoved[i] > disthit2)
{
/* If yes: log distance, X and Z coordinates */
distmoved[i]=disthit2;
xhit[i]=intx2;
zhit[i]=intz2;
hit[i]=1.0;
muahit[i]=datamuaback[0];
mushit[i]=datamusback[0];
}
}
else
{
/* If yes: log distance, X and Z coordinates */
hit[i]=1.0;
distmoved[i]=disthit2;
xhit[i]=intx2;
zhit[i]=intz2;
muahit[i]=datamuaback[0];
mushit[i]=datamusback[0];
}
}
}
    }
}
}
}

void mexFunction(int nlhs, mxArray *plhs[], int nrhs, const mxArray *prhs[])
```

```
{
 int nphoton, ncap;
 double *data0x, *data1x, *data2x, *data0z, *data1z, *data2z;
 double *datar, *datamua, *datamus, *datamuaback;
 double *datamusback, *datamuacap, *datamuscap;
 double *hit, *distmoved, *xhit, *zhit, *muahit, *mushit;

    /* Find the dimensions of the data */
    nphoton = mxGetM(prhs[0]);
    ncap = mxGetM(prhs[2]);

    /* Retrieve the input data */
    data0x = mxGetPr(prhs[0]);
/* data0x:  x coordinates for initial photon positions */
     data1x = mxGetPr(prhs[1]);
/* data1x:  x coordinates for final photon positions */
     data2x = mxGetPr(prhs[2]);
/* data2x:  x coordinates for centers of each vessel */
     data0z = mxGetPr(prhs[3]);
/* data0z:  x coordinates for initial photon positions */
    data1z = mxGetPr(prhs[4]);
/* data2z:  x coordinates for final photon positions*/
     data2z = mxGetPr(prhs[5]);
/* data2z:  z coordinates for centers of each vessel */
   datar  = mxGetPr(prhs[6]);
/* datar:  radius of each capillaries within geometry  */
datamua  = mxGetPr(prhs[7]);
/* datamua: absorption coefficient at (x0,y0,z0)  */
datamus  = mxGetPr(prhs[8]);
/* datamua: absorption coefficient at (x0,y0,z0)  */
datamuaback = mxGetPr(prhs[9]);
/* datamuaback: background absorption of tissue  */
datamusback = mxGetPr(prhs[10]);
/* datamuaback: background absorption of tissue  */
datamuacap = mxGetPr(prhs[11]);
/* datamuacap: absorption within 'capillary' regions  */
datamuscap = mxGetPr(prhs[12]);
/* datamuacap: absorption within 'capillary' regions  */
    /* Create a pointer to the output data */
    plhs[0]=mxCreateDoubleMatrix(nphoton,1,mxREAL);
    hit  = mxGetPr(plhs[0]);
    /* hit:  Binary indicator if photon intersects vessel (1=yes/0=no) */
    plhs[1]=mxCreateDoubleMatrix(nphoton,1,mxREAL);
    distmoved = mxGetPr(plhs[1]);
    /* distmoved:  distance moved from inital point to
```

```
 * intersection point capillary (0 for no intersection photons) */
plhs[2]=mxCreateDoubleMatrix(nphoton,1,mxREAL);
xhit = mxGetPr(plhs[2]);
/* xhit:  x coordinate for intersection point */
/*(0 for no intersection photons) */

plhs[3]=mxCreateDoubleMatrix(nphoton,1,mxREAL);
zhit = mxGetPr(plhs[3]);
/* zhit:  z coordinate for intersection point */
/*(0 for no intersection photons) */

plhs[4]=mxCreateDoubleMatrix(nphoton,1,mxREAL);
muahit = mxGetPr(plhs[4]);
/* muahit:  mua at intersection point */

plhs[5]=mxCreateDoubleMatrix(nphoton,1,mxREAL);
mushit = mxGetPr(plhs[5]);
/* mushit:  mus at intersection point */

PhotonStepCheck(data0x,data1x,data2x,data0z,data1z,data2z,
datar,nphoton,ncap,hit,distmoved,xhit,zhit,
datamua,datamus,muahit,mushit,datamuaback,
datamusback,datamuacap,datamuscap);
```

BIBLIOGRAPHY

[1] D. L. Conover, B. M. Fenton, T. H. Foster, and E. L. Hull. An evaluation of near infrared spectroscopy and cryospectrophotometry estimates of haemoglobin oxygen saturation in a rodent mammary tumour model. *Phys. Med. Biol.*, 45(9):2685–700, 2000.

[2] W. G. Zijlstra, A. Buursma, and O. W. van Assendelft. *Visible and Near Infrared Absorption Spectra of Human and Animal Haemoglobin.* Utrecht, Boston, MA, 2000.

[3] J. R. Mourant, T. M. Johnson, G. Los, and I. J. Bigio. Non-invasive measurement of chemotherapy drug concentrations in tissue: preliminary demonstrations of *in vivo* measurements. *Phys. Med. Biol.*, 44:1397–1417, 1999.

[4] T. J. Dougherty, C. J. Gomer, B. W. Henderson, G. Jori, D. Kessel, M. Korbelik, J. Moan, and Q. Peng. Photodynamic therapy. *J. Natl. Cancer Inst.*, 90:889–905, 1998.

[5] I. J. MacDonald and T. J. Dougherty. Basic principles of photodynamic therapy. *J. Porphyrins Phthalocyanines*, 5:105–129, 2001.

[6] J. Moan. Properties of optimal PDT sensitizers. *J. Photochem. Photobiol., B*, 5:521–524, 1990.

[7] D. Phillips. The photochemistry of sensitizers for photodynamic therapy. *Pure Appl. Chem.*, 67:117–126, 1995.

[8] T. M. Busch, S. M. Hahn, E. P. Wileyto, C. J. Koch, D. L. Fraker, P. Zhang, M. Putt, K. Gleason, D. B. Shin, M. J. Emanuele, K. Jenkins, E. Glatstein, and S. M. Evans. Hypoxia and photofrin uptake in the intraperitoneal carcinomatosis and sarcomatosis of photodynamic therapy patients. *Clin. Cancer Res.*, 10:4630–4638, 2004.

[9] B. W. Pogue, B. Chen, X. Zhou, and T. Hasan. Analysis of sampling volume and tissue heterogeneity on the *in vivo* detection of fluorescence. *J. Biomed. Opt.*, 10:041206, 2005.

[10] H. Eichler and M. Muller. Drug distribution the forgotten relative in clinical pharmacokinetics. *Clin. Pharmacokinet.*, 34:95–99, 1998.

[11] E. Vermeire, H. Hearnshaw, P. Van Royen, and J. Denekens. Three decades of research. A comprehensive review. *J. Clin. Pharm. Ther.*, 26:331–342, 2001.

[12] M. Canpolat and J. R. Mourant. Monitoring photosensitizer concentration by use of a fiber-optic probe with small source-detector separation. *Appl. Opt.*, 39:6508–6514, 2000.

[13] I. J. Bigio and S. G. Bown. Spectroscopic sensing of cancer and cancer therapy. *Cancer Biol. Ther.*, 3:259–267, 2004.

[14] F. F. Jobsis. Noninvasive, infrared monitoring of cerebral and myocardial oxygen sufficiency and circulatory parameters. *Science*, 198:1264–1267, 1977.

[15] B. W. Wilson and S. L. Jacques. Optical reflectance and transmittance of tissues: Principles and applications. *IEEE Journal of Quantum Elect.*, 26:2186–2199, 1990.

[16] D. T. Delpy and M. Cope. Quantification in tissue near-infrared spectroscopy. *Phil. Trans. R. Soc. Lond. B Biol. Sci.*, 352:649–659, 1997.

[17] J. A. Wahr, K. T. Tremper, S. Samra, and D. T. Delpy. Near infraread spectroscopy: theory and applications. *J. Cardiothorac. Vasc. Anesth.*, 10:406–418, 1996.

[18] E. L. Hull, M. G. Nichols, and T. H. Foster. Quantitative broadband near-infrared spectroscopy of tissue-simulating phantoms containing erythrocytes. *Phys. Med. Biol.*, 43:3381–3404, 1998.

[19] T. O. McBride, B. W. Pogue, E. D. Gerety, S. B. Poplack, U. L. Osterberg, and K. D. Paulsen. Spectroscopic diffuse optical tomography for the quantitative assessment of hemoglobin concentration and oxygen saturation in breast tissue. *Appl. Opt.*, 38:5480–5490, 2000.

[20] J. C. Finlay and T. H. Foster. Hemoglobin oxygen saturations in phantoms an *in vivo* from measurements of steady-state diffuse reflectance at a single, short source-detector separation. *Med. Phys.*, 31:1949–1959, 2004.

[21] J. A. Parrish. New concepts in therapeutic photomedicine: photochemistry, optical targeting and the therapeutic window. *J. Invest. Dermatol.*, 77:45–50, 1981.

[22] P. Rolfe. *In vivo* near-infrared spectroscopy. *Annu. Rev. Biomed. Eng.*, 2:715–754, 2000.

[23] I. J. Bigio and J. R. Mourant. Ultraviolet and visible spectroscopies for tissue diagnostics: fluorescence spectroscopy and elastic-scattering spectroscopy. *Phys. Med. Biol.*, 42:803–814, 1997.

[24] W. Cheong, S. A. Prahl, and A. J. Welch. A review of the optical properties of biological tissues. *IEEE J. Quantum Electron.*, 26:2166–2185, 1990.

[25] M. G. Nichols, E. L. Hull, and T. H. Foster. Design and testing of a white-light, steady-state diffuse reflectance spectrometer for determination of optical properties of highly scattering systems. *Appl. Opt.*, 36:93–104, 1997.

[26] A. Amelink and H. J. C. M. Sterenborg. Measurement of the local optical properties of turbid media by differential path-length spectroscopy. *Appl. Opt.*, 43:3048–3054, 2004.

[27] T. J. Farrell and M. S. Patterson. A diffusion theory model of spatially resolved, steady-state diffuse reflectance for the nonivasive determination of tissue optical properties. *Med. Phys.*, 19:879–888, 1992.

[28] J. R. Mourant, I. J. Bigio, D. A. Jack, T. M. Johnson, and H. D. Miller. Measuring absorption coefficients in small volumes of highly scattering media: Source-detector separations for which path lengths do not depend on scattering properties. *Appl. Opt.*, 36:5655–5661, 1997.

[29] J. C. Finlay and T. H. Foster. Effect of pigment packaging on diffuse reflectance spectroscopy of samples containing red blood cells. *Opt. Lett.*, 29:965–968, 2004.

[30] E. L. Hull and T. H. Foster. Steady-state reflectance spectroscopy in the P_3 approximation. *J. Opt. Soc. Am. A*, 18:584–599, 2001.

[31] A. van Veen, R. L. P. Amelink, M. Menke-Pluymers, C. van der Pol, and H. J. C. M. Sterenborg. Optical biopsy of breast tissue using differential path-length spectroscopy. *Phys. Med. Biol.*, 50:2573–2581, 2005.

[32] M. S. Patterson, S. Andersson-Engels, B. C. Wilson, and E. K. Osei. Absorption spectroscopy in tissue simulating materials: A theoretical and experimental study of photon paths. *Appl. Opt.*, 34, 1995.

[33] M. S. Patterson, B. Chance, and B. C. Wilson. Time resolved reflectance and transmittance for the noninvasive measurement of tissue optical properties. *Appl. Opt.*, 28:2331–2336, 1989.

[34] D. T. Delpy, M. Cope, P. van der Zee, S. R. Arridge, S. Wray, and J. S. Watt. Estimation of optical pathlength through tissue from direct time of flight measurements. *Phys. Med. Biol.*, 33:1433–1442, 1988.

[35] M. Hiraoka, M. Firbank, M. Essenpreis, M. Cope, S. R. Arridge, P. van der Zee, and D. T. Delpy. A Monte Carlo investigation of optical pathlength in inhomogeneous tissue and its application to near-infrared spectroscopy. *Phys. Med. Biol.*, 38:1859–1876, 1993.

[36] G. A. Wagnieres, W. M. Star, and B. C. Wilson. *In vivo* fluorescence spectroscopy and imaging for oncological applications. *Photochem. Photobiol.*, 68:603–632, 1998.

[37] R. Reif, M. Wang, S. Joshi, O. A'Amar, and I. J. Bigio. Optical method for real-time monitoring of drug concentrations facilitates the development of novel methods for drug delivery to brain tissue. *J. Biomed. Opt.*, 12:034036, 2007.

[38] N. L. Oleinick, R. L. Morris, and I. Belichenko. The role of apoptosis in response to photodynamic therapy: what, where, why, and how. *Photochem. Photobiol. Sci.*, 1:1–21, 2002.

[39] O. Raab. Uber die wirkung fluoreszierender stoffe auf infusorien. *Z. Biol.*, 39:524–546, 1900.

[40] T. J. Dougherty, G. B. Grinday, R. Fiel, and K. R. Weishaupt. Photoradiation therapy II: cure of animal tumors with haematoporphrin and light. *J. Natl. Cancer. Inst.*, 55:115–121, 1975.

[41] T. J. Dougherty. Photoradiation therapy for the treatment of malignant tumors. *Cancer Res.*, 36:2628–2635, 1978.

[42] K. R. Weishaupt, C. J. Gomer, and T. J. Dougherty. Identification of singlet oxygen as cytotoxic agent in photo-inactivation of a murine tumor. *Cancer Res.*, 36:2326–2329, 1976.

[43] M. A. Henson and D. E. Seborg. Nonlinear control strategies for continuous fermentors. *Chem. Eng. Sci.*, 47:821–835, 1992.

[44] N. Solban, I. Rizvi, and T. Hasan. Properties of optimal PDT sensitizers. *Lasers. Surg. Med.*, 38:522–531, 2006.

[45] C. Hopper. Photodynamic therapy: A clinical reality in the treatment of cancer. *Lancet. Oncol.*, 1:212–219, 2000.

[46] H. Pass. Photodynamic therapy in oncology: Mechanisms and clinical use. *J. Natl. Cancer. Inst.*, 85:443–456, 1993.

[47] U. Schmidt-Erfurth, J. Miller, M. Sickenberg, H. Laqua, I. Barbazetto, E. Gragoudas, L. Zografos, B. Piguet, C. Pournaras, G. Donati, A. Lane, R. Birngruber, H. van den Berg, A. Strong, U. Manjuris, T. Gray, M. Fsadni, and N. Bressler. Photodynamic therapy with verteporfin for choroidal neovascularization caused by age-related macular degeneration. Results of retreatments in a phase 1 and 2 study. *Arch. Ophthalmol.*, 117:1177–1187, 1999.

[48] R. Ackroyd, C. Kelty, N. Brown, and M. Reed. The history of photodetection and photodynamic therapy. *Photochem. Photobiol.*, 74:656–669, 2001.

[49] H. Lui, L. Hobbs, W. D. Tope, P. K. Lee, C. Elmets, N. Provost, A. Chan, H. Neyndorff, X. Y. Su, H. Jain, I. Hamzavi, D. McLean, and R. Bissonnette. Photodynamic therapy of multiple nonmelanoma skin cancers with verteporfin and red lightemitting diodes. *Arch. Dermatol.*, 140:26–32, 2004.

[50] M. Dilkes, M. DeJode, A. Rowntree-Taylor, J. McGilligan, G. Kenyon, and P. McKelvie. m-THPC photodynamic therapy for head and neck cancer. *Lasers Surg. Med.*, 11:23–29, 2005.

[51] M. Biel. Photodynamic therapy treatment of early oral and laryngeal cancers. *Photochem. Photobiol.*, 83:1063–1068, 2007.

[52] F. Cairnduff, M. Stringer, E. Hudson, D. Ash, and S. Brown. Superficial photodynamic therapy with topical 5-aminolaevulinic acid for superficial primary and secondary skin cancer. *Br. J. Cancer*, 69:605–608, 1994.

[53] O. Akilov, S. Kosaka, K. ORiordan, and T. Hasan. Parasiticidal effect of δ-aminolevulinic acid-based photodynamic therapy for cutaneous leishmaniasis is indirect and mediated through the killing of the host cells. *Experimental Dermatology*, 16:651–660, 2007.

[54] A. Dimofte, T. Zhu, S. Hahn, and R. Lustig. In vivo light dosimetry for motexafin lutetium-mediated PDT of recurrent breast cancer. *Lasers Surg. Med.*, 31:305–312, 2002.

[55] K. L. Du, R. Mick, T. M. Busch, T. C. Zhu, J. C. Finlay, G. Yu, A. G. Yodth, S. B. Malkowicz, D. Smith, R. Wittington, D. Stripp, and S. M. Hahn. Preliminary results of interstitial motexafin lutetium-mediated PDT for prostate cancer. *Lasers Surg. Med.*, 38:427–434, 2006.

[56] R. A. Miller, K. Woodburn, Q. Fan, M. F. Renschler, J. L. Sessler, and J. A. Koutcher. *In vivo* animal studies with gadolinium (III) texaphyrin as a radiation enhancer. *Int. J. Radiat. Oncol., Biol., Phys.*, 45:981–989, 1999.

[57] A. E. Evens. Motexafin gadolinium: A redox-active tumor selective agent for the treatment of cancer. *Curr. Opin. Oncol.*, 16:576–580, 2004.

[58] C. M. Whitacre, D. K. Feyes, T. Satoh, J. Grossman, J. W. Mulvihill, H. Mukhtar, and N. L. Oleinick. Photodynamic therapy with phthalocyanine photosensitizer Pc 4 of SW480 human colon cancer xenografts in athymic mice. *Clin. Cancer. Res.*, 6:2021–2027, 2000.

[59] J. Miller, E. Baron, H. Scull, A. Hsia, J. Berlin, T. McCormick, V. Colussi, M. Kenney, K. Cooper, and N. Oleinick. Photodynamic therapy with the phthalocyanine photosensitizer Pc 4. the case experience with preclinical mechanistic and early clinical-translational studies. *Toxicol. Appl. Pharmacol.*, 224:290299, 2007.

[60] X. Zhou, B. W. Pogue, B. Chen, E. Demidenko, R. Joshi, J. Hoopes, and T. Hasan. Pretreatment photosensitizer dosimetry reduces the variation in tumor response. *Int. J. Radiattion Oncologuy Biol. Phys.*, 64:1211–1220, 2006.

[61] A. E. Profio and E. R. Doiron. Dosimetry considerations in phototherapy. *Am. Assoc. Phys. Med.*, 8:190–196, 1981.

[62] B. W. Henderson, T. M. Busch, L. A. Vaughan, N. P. Frawley, D. Babich, T. A. Sosa, J. D. Zollo, A. S. Dee, M. T. Cooper, D. A. Bellnier, W. R. Greco, and A. R. Oseroff. Photofrin photodynamic therapy can significantly deplete or preserve oxygenation in human basal cell carcinomas during treatment, depending on fluence rate. *Cancer Res.*, 60:525–529, 2000.

[63] W. R. Potter, T. S. Mang, and T. J. Dougherty. The theory of photodynamic therapy dosimetry: Consequences of photo-destruction of sensitizer. *Photochem. Photobiol.*, 46:97101, 1987.

[64] L. I. Grossweiner. Light dosimetry model for photodynamic therapy treatment planning. *Lasers Surg. Med.*, 11:165–173, 1991.

[65] B. C. Wilson, M. S. Patterson, and L. Lilge. Implicit and explicit dosimetry in photodynamic therapy: a new paradigm. *Lasers Sci. Med.*, 12:182–199, 1997.

[66] M. J. Niedre, M. S. Patterson, and B. C. Wilson. Singlet oxygen luminescence as an *in vivo* photodynamic therapy dose metric: Validation in normal mouse skin with optical amino-levulinic acid. *Br. J. Cancer.*, 92:298–304, 2005.

[67] B. A. Standish, X. Jin, J. Smolen, A. Mariampillai, N. R. Munce, B. C. Wilson, I. A. Vitkin, and V. X. D. Yang. Interstitial doppler optical coherence tomography monitors microvascular changes during photodynamic therapy in a Dunning prostate model under varying treatment conditions. *J. Biomed. Opt.*, 12:034022–1–7, 2007.

[68] V. H. Fingar, W. R. Potter, and B. W. Henderson. Drug and light dose dependence of photodynamic therapy: a study of tumor cell clonogenicity and histologic changes. *Photochem. Photobiol.*, 45:643–650, 1987.

[69] T. H. Foster, R. S. Murant, R. G. Bryant, R. S. Knox, S. L. Gibson, and R. Hilf. Oxygen consumption and diffusion effects in photodynamic therapy. *Rad. Res.*, 126:296–303, 1991.

[70] T. H. Foster and L. Gao. Dosimetry in photodynamic thearpy: Oxygen and the critical importance of capillary density. *Rad. Res.*, 130:379–383, 1992.

[71] J. S. Dysart and M. S. Patterson. Photobleaching kinetics, photoproduct formation, and dose estimation during AlA induced PpIX PDT of MLL cells under well oxygenated and hypoxic conditions. *Photochem. Photobiol.*, 5:73–81, 2006.

[72] M. T. Jarvi, M.J. Niedre, M.S. Patterson, and B. C. Wilson. Singlet oxygen luminescence dosimetry (SOLD) for photodynamic therapy: Current status, challenges and future prospects. *Photochem. Photobiol.*, 82:11981210, 2006.

[73] J. S. Dysart, G. Singh, and M. S. Patterson. Calculation of singlet oxygen dose from photosensitizer fluorescence and photobleaching during mTHPC photodynamic therapy of MLL cells. *Photochem. Photobiol.*, 81:196–205, 2005.

[74] K. K. Wang, S. Mitra, and T. H. Foster. A comprehensive mathematical model of microscopic dose deposition in photodynamic therapy. *Med. Phys.*, 34:282–293, 2007.

[75] T. J. Farrell, B. C. Wilson, M. S. Patterson, and M. C. Olivo. Comparison of the *in vivo* photodynamic threshold dose for photofrin, mono- and tetrasulfonated aluminum phthalocyanine using a rat liver model. *Photochem. Photobiol.*, 68:394–399, 1998.

[76] B. W. Pogue, R. D. Braun, J. L. Lanzen, C. Erickson, and M. W. Dewhirst. Analysis of the heterogeneity of P_{O2} dynamics during photodynamic therapy with verteporfin. *Photochem. Photobiol.*, 74:700–706, 2001.

[77] C. C. Lee, B. W. Pogue, J. A. O'Hara, C. M. Wilmot, R. R. Strawbridge, G. C. Burke, and P. J. Hoopes. Spatial heterogeneity and temporal kinetics of photosensitizer $(AlPcS_2)$ concentration in murine tumors RIF-1 and MTG-B. *Photochem. Photobiol.*, 2:145–150, 2003.

[78] T. C. Zhu, J. C. Finlay, and S. M. Hahn. Determination of the distribution of light, optical properties, drug doncentration, and tissue oxygenation *in vivo* in human prostate during motexafin lutetium mediated photodynamic therapy. *J. Photochem. Photobiol., B*, 79:231–241, 2005.

[79] T. C. Zhu, A. Dimofte, J. C. Finlay, D. Stripp, T. Busch, J. Miles, R. Whittington, S. Malkowicz, Z. Tochner, E. Glatstein, and S. M. Hahn. Optical properties of human prostate at 732nm measured in vivo during motexafin lutetium-mediated photodynamic therapy. *Photochem. Photobiol.*, 81:96–105, 2005.

[80] H. Schouwink, H. Oppelaar, M. Ruevekamp, M. van der Valk, G. Hart, P. Rijken, P. Baas, and F. A. Stewart. Oxygen depletion during and after mTHPC-mediated photodynamic therapy in RIF1 and H-MESO1 tumors. *Rad. Res.*, 159, 2003.

[81] T.M. Busch. Local physiological changes during photodynamic therapy. *Lasers Surg. Med.*, 38:494–499, 2006.

[82] B. W. Henderson, T. M. Busch, and J. W. Snyder. Fluence rate as a modulator of PDT mechanisms. *Lasers Surg. Med.*, 38:489–493, 2006.

[83] S. Iinuma, K. T. Schomacker, G. Wagnieres, M. Rajadhyaksha, M. Bamberg, T. Momma, and T. Hasan. *In vivo* fluence rate and fractionation effects on tumor response and photobleaching. *Cancer Res.*, 59:6164–6170, 1999.

[84] J. H. Woodhams, L. Kunz, S. G. Bown, and A. J. MacRobert. Correlation of real-time haemoglobin oxygen saturation monitoring during photodynamic therapy with

microvascular effects and tissue necrosis in normal rat liver. *Br. J. Cancer.*, 91:788–794, 2004.

[85] A. Curnow, J. C. Haller, and S. G. Bown. Oxygen monitoring during 5-aminolaevulinic acid induces photodynamic therapy in normal rat colon. Comparison of continuous and fractionated light regimes. *J. Photochem. Photobiol., B*, 58:149–155, 2000.

[86] A. Major, S. Kimel, S. Mee, T. E. Milner, S. M. Smithies, D. J. Srinivas, Z. Chen, and J. S. Nelson. Microvascular photodynamic effects determined *in vivo* using optical doppler tomography. *IEEE J. Selected Topics in Quantum Electronics*, 5:1168–1175, 1999.

[87] H. Wang, M. E. Putt, M. J. Emanuele, D. B. Shin, E. Glatstein, A. G. Yodh, and T. M. Busch. Treatment-induced changes in tumor oxygenation predict photodynamic therapy outcome. *Cancer Res.*, 64:7553–7561, 2004.

[88] G. Yu, T. Durduran, C. Zhou, H. Wang, M. E. Putt, H. M. Saunders, C. M. Sehgal, E. Glatstein, A. G. Yodh, and T. M. Busch. Noninvasive monitoring of murine tumor blood flow during and after photodynamic therapy provides early assessment of therapeutic efficacy. *Clin. Cancer Res.*, 11:3543–3552, 2005.

[89] B. W. Pogue, J. A. O'Hara, I. A. Goodwin, C. J. Wilmot, G. P. Fournier, A. R. Akay, and H. Swartz. Tumor po_2 changes during photodynamic therapy depend upon photosensitizer type and time after injection. *Comp. Biochem. and Physiol. A: Physiol.*, 132:177–184, 2002.

[90] B. Chen, B. W. Pogue, I. A. Goodwin, J. A. O'Hara, C. M. Wilmot, J. E. Hutchins, P. J. Hoopes, and T. Hasan. Blood flow dynamics after photodynamic therapy with verteporfin in the RIF-1 tumor. *Rad. Res.*, 160:452–459, 2003.

[91] B. Chen, B. W. Pogue, J. M. Luna, R. L. Hardman, P. J. Hoopes, and T. Hasan. Tumor vascular permeabilization by vascular-targeting photosensitization: effects, mechanisms, and therapeutic implications. *Clin. Cancer Res.*, 12:917–923, 2006.

[92] B. Chen, B. W. Pogue, P. J. Hoopes, and T. Hasan. Combining vascular and cellular targeting regimes enhances the efficacy of photodynamic therapy. *Int. J. Radiattion Oncology Biol. Phys.*, 61:1216–1226, 2005.

[93] D.E. Dolmans, A. Kadambi, J. S. Hill, K. R. Flores, J. N. Gerber, J. P. Walker, I. H. Borel Rinkes, R. Jain, and D. Fukumura. Targeting tumor vasculature and cancer cells in orthotopic breast tumor by fractionated photosensitizer dosing photodynamic therapy. *Cancer Res.*, 62:4289–4294, 2002.

[94] M. Triesscheijn, M. Ruevekamp, M. Aalders, P. Baas, and F. A. Stewart. Outcome of mTHPC mediated photodynamic therapy is primarily determined by vascular response. *Photochem. Photobiol.*, 81:1161–1167, 2005.

[95] T. Teorell. Kinetics of distribution of substances administered to the body I. *Arch. Int. Pharma. Ther.*, 57:202–225, 1937.

[96] T. Teorell. Kinetics of distribution of substances administered to the body II. *Arch. Int. Pharma. Ther.*, 57:226–240, 1937.

[97] H. J. Jones, D. I. Vernon, and S. B. Brown. Photodynamic therapy effect of m-THPC (Foscan ®) *in vivo*: Correlation with pharmacokinetics. *Br. J. Cancer*, 89:398–404, 2003.

[98] C. C. Lee, B. W. Pogue, R. R. Strawbridge, K. L. Moodie, L. R. Bartholomew, G. C. Burke, and P. J. Hoopes. Comparison of photosensitizer (AlPcS$_2$) quantification techniques: *In situ* fluorescence microsampling vs. tissue chemical extraction. *Photochem. Photobiol.*, 71:453–460, 2001.

[99] M. G. Nichols and T. H. Foster. Oxygen diffusion and reaction kinetics in the photodynamic therapy of multicell tumour spheroids. *Phys. Med. Biol.*, 39:2161–2181, 1994.

[100] M.A. Henson and D.E. Seborg, editors. *Nonlinear Process Control*. Prentice Hall, Englewood Cliffs, NJ, 1997.

[101] J. Yuan, P. A. Mahama-Relue, R. L. Fournier, and J. A. Hampton. Predictions of mathematical models of tissue oxygenation and generation of singlet oxygen during photodynamic therapy. *Rad. Res.*, 148:386–394, 1997.

[102] B. W. Pogue and T. Hasan. A theoretical study of light fractionation and dose-rate effects in photodynamic therapy. *Rad. Res.*, 147:551–559, 1997.

[103] B. W. Pogue, K. D. Paulsen, J. A. O'Hara, C.M. Wilmot, and H. M. Swartz. Estimation of oxygen distribution in RIF-1 tumors by diffusion model-based interpretation of pimonidazole hypoxia and eppendorf measurements. *Rad. Res.*, 155:15–25, 2001.

[104] P. Vaupel, F. Kallinowski, and P. Okunieff. Blood flow, oxygen and nutrient supply, and metabolic microenvironment of human tumors: A review. *Cancer Res.*, 49:6449–6465, 1989.

[105] C. J. Kelly and M. Brady. A model to simulate tumour oxygenation and dynamic [18F]-Fmiso PET data. *Phys. Med. Biol.*, 51:5859–5873, 2006.

[106] S. T. Flock, M. S. Patterson, B. C. Wilson, and D. R. Wyman. Monte Carlo modeling of light propagation in highly scattering tissues-I: Model predictions and comparison with diffusion theory. *IEEE T. Bio.-Med. Eng.*, 36:1162–1168, 1989.

[107] L. Wang, S. L. Jacques, and L. Zheng. MCML–Monte Carlo modeling of light transport in multi-layered tissues. *Comput. Meth. Programs Biomed.*, 47:131–146, 1995.

[108] I. V. Meglinski and S. J. Matcher. Computer simulation of skin reflectance spectra. *Comput. Meth. Programs Biomed.*, 70:170–186, 2003.

[109] S. V. Patwardhan, A. P. Dhawan, and P. A. Relue. Monte Carlo simulation of light-tissue interaction: Three-dimensional simulation for trans-illumination-based imaging of skin. *IEEE T. Bio.-Med. Eng.*, 52:1227–1236, 2005.

[110] H. Liu, B. Chance, A. H. Hielscher, S. J. Jacques, and F. K. Tittel. Influence of blood vessels on the measurement of hemoglobin oxygenation as determined by time-resolved reflectance spectroscopy. *Med. Phys.*, 22:1209–1217, 1995.

[111] M. Firbank, E. Okada, and D. T. Delpy. Investigation of the effect of discrete absorbers upon the measurement of blood volume with near-infrared spectroscopy. *Phys. Med. Biol.*, 42:465–477, 1997.

[112] W. Verkruysse, G. W. Lucassen, J. F. de Boer, D. J. Smithies, J. S. Nelson, and M. J. C. van Gemert. Modelling light distributions of homogeneous versus discrete absorbers in light irradiated turbid media. *Phys. Med. Biol.*, 42:51–65, 1997.

[113] R. L. P. van Veen, W. Verkruysse, and H. J. C. M. Sterenborg. Diffuse-reflectance spectroscopy from 500 to 1060 nm by correction for inhomogeneously distributed absorbers. *Opt. Lett.*, 27:246–248, 2002.

[114] T. D. Mody and J. L. Sessler. Texaphyrins: A new approach to drug development. *J. Porphyrins Phthalocyanines*, 5:134–142, 2001.

[115] A. M. Evens, P. Lecane, D. Magda, S. Prachand, S. Singhal, J. Nelson, R. A. Miller, R. B. Gartenhaus, and L. I. Gordon. Motexafin gadolinium generates reactive oxygen species and induces apoptosis in sensitive and highly resistant multiple myeloma cells. *Neoplasia*, 105:1265–1273, 2005.

[116] S.W. Young, F. Qing, A. Harriman, J. L. Sessler, W. C. Dow, T. D. Mody, G. W. Hemmi, Y. Hao, and R. A. Miller. Gadolinium(III) texaphyrin: A tumor selective radiation sensitizer that is detectable by MRI. *Proc. Natl. Acad. Sci.*, 93:6610–6615, 1996.

[117] J. Viala, D. Vanel, P. Meingan, E. Lartigau, P. Carde, and M. Renschler. Phases IB and II multidose trial of gadolinium texaphyrin, a radiation sensitizer detectable by MR imaging: Preliminary results in brain metastases. *Radiology*, 212:755–759, 1999.

[118] D. I. Rosenthal, P. Nurenberg, C. R. Becerra, E. P. Frenkel, D. P. Carbone, B. L. Lum, R. Miller, J. Engel, S. Young, D. Miles, and M. F. Renschler. A phase I single-dose trial of gadolinium texaphyrin (Gd-Tex), a tumor selective radiation sensitizer detectable by magnetic resonance imaging. *Clin Cancer Res*, 5(4):739–45, 1999.

[119] P. Carde, R. Timmerman, M. P. Mehta, C. D. Koprowski, J. Ford, R. B. Tishler, D. Miles, R. A. Miller, and M. F. Renschler. Multicenter phase Ib/II rrial of the

radiation enhancer motexafin gadolinium in patients with brain metastases. *J. Clin. Oncol.*, 19:2072–2083, 2001.

[120] S. Xu, K. Zakian, H. Thaler, C. Matei, A. Alfieri, Y. Chen, and J. A. Koutcher. Effects of motexafin gadolinium on tumor metabolism and radiation sensitivity. *Int. J. Radiat. Oncol. Biol. Phys.*, 49:1381–1390, 2001.

[121] H. Jaffae. *Theory and Applications of Ultraviolet Spectroscopy.* Wiley, New York, NY, 1962.

[122] S. C. Kanick, J. L. Eiseman, E. Joseph, J. Guo, and R. S. Parker. Noninvasive and nondestructive optical spectroscopic measurement of motexafin gadolinium in mouse tissues: Comparison to high-performance liquid chromatography. *J. Photochem. Photobiol., B*, 88:90–104, 2007.

[123] R. A. Parise, D. R. Miles, and M. J. Egorin. Sensitive high-performance liquid chromatographic assay for motexafin gadolinium and motexafin lutetium in human plasma. *J. Chromatogr. B. Biomed. Sci. Appl.*, 749(2):145–52, 2000.

[124] National Research Council, editor. *Guide for the Care and Use of Laboratory Animals.* Institute of Laboratory Animal Resources Commission on Life Sciences. National Academy Press, Washington, D.C., 1996.

[125] M. Shimada, Y. Yamada, M. Itoh, and T. Yatagai. Melanin and blood concentration in a human skin model studied by multiple regression analysis: Assessment by Monte Carlo simulation. *Phys. Med. Biol.*, 46:2397–2406, 2001.

[126] R. Richards-Kortum and E. Sevick-Muraca. Quantitative optical spectroscopy for tissue diagnosis. *Annu. Rev. Phys. Chem.*, 47:555–606, 1996.

[127] J.C. Finlay. Reflectance and fluorescence spectroscopies in photodynamic therapy. Phd thesis, University of Rochester, Rochester, NY, 2003.

[128] E. Carson and C. Cobelli, editors. *Modelling Methodology for Physiology and Medicine.* Academic Press, San Diego, CA, 2001.

[129] M. R. Spiegel. *Theory and Problems of Probability and Statistics, 2nd ed.* McGraw-Hill, New York, 1992.

[130] C. Sheng, B. W. Pogue, E. Wang, J. E. Hutchins, and P. J. Hoopes. Assessment of photosensitizer dosimetry and tissue damage assay for photodynamic therapy in advanced-stage tumors. *Photochem. and Photobiol.*, 79:520–525, 2004.

[131] W. C. Zamboni, A. C. Gervais, M. J. Egorin, J. H. Schellens, D. R. Hamburer, B. J. Delauter, A. Grim, E. G. Zuhowski, E. Joseph, D. Pluim, D. M. Potter, and J. L. Eiseman. Inter- and intratumoral disposition of platinum in solid tumors after administration of cisplatin. *Clin. Cancer Res.*, 8:2992–2999, 2002.

[132] R. J. Gilles, P. A. Schornack, T. W. Secomb, and N. Raghundand. Causes and effects of heterogeneous perfusion in tumors. *Neoplasia*, 1:197–207, 1999.

[133] H. Boxenbaum. Interspecies scaling, allometry, physiological time, and the ground plan of pharmacokinetics. *J. Pharmacokinet. Pharmacodyn.*, 10:201–227, 1982.

[134] C. H. Sibata, V. C. Colussi, N. L. Oleinick, and T. J. Kinsella. Photodynamic therapy in oncology. *Expert. Opin. Pharmacother.*, 2:917–927, 2001.

[135] US EPA Office of Health and Environmental Assessment by the International Life Sciences Institute. Physiological parameter values for PBPK models, 1984.

[136] H. Akaike. A new look at the statistical model identification. *IEEE Trans. Aut. Control*, AC-19(6):716–723, 1974.

[137] MathWorks Inc. Matlab statistics toolbox 6 user's guide. Natick, MA, 2007.

[138] G. W. Boswell, D. R. Miles, P. A. Thiemann, and M. Mesfin. Population pharmacokinetics and bioavailability of motexafin gadolinium (Xcytrin ®) in CD1 mice following intravenous and intraperitoneal injection. *Invest. New Drugs*, 24:281–289, 2006.

[139] T. J. Pfefer, L. S. Matchette, C. L. Bennett, J. A. Gall, J. N. Wilke, A. J. Durkin, and M. N. Ediger. Reflectance-based determination of optical properties in highly attenuating tissue. *J. Biomed. Opt.*, 8:206–215, 2003.

[140] L. O. Svaasand, E. J. Fiskerstrand, G. Kopstad, L. T. Norvang, E. K. Svaasand, J. S. Nelson, and M. W. Berns. Theraputic response during pulsed laser treatment of portwine stains: Dependence on vessel diameter and depth in dermis. *Lasers Med. Sci.*, 10:235–243, 1995.

[141] D. Marquardt. An algorithm for least-squares estimation of nonlinear parameters. *SIAM J. App. Math.*, 15:431–444, 1963.

[142] R. L. Fournier. *Basic Transport Phenomena in Biomedical Engineering*. Edwards Brothers Printing, Lillington, NC, 1998.

[143] A. Dasu, I. Toma-Dasu, and M. Karlsson. Theoretical simulation of tumour oxygenation and results from acute and chronic hypoxia. *Phys. Med. Biol.*, 48:2829–2842, 2003.

[144] H. Sies and C. F. Menck. Singlet oxygen induced DNA damage. *Mutat. Res.*, 275:367–375, 1992.

[145] J. C. Finlay, S. Mitra, and T. H. Foster. *In vivo* mTHPC photobleaching in normal rat skin exhibits unique irradiance-dependent features. *Photochem. Photobiol.*, 75:282–288, 2002.

[146] MathWorks Inc. Matlab partial differential equation toolbox user's guide. Natick, MA, 2007.

[147] A. Krogh. The supply of oxygen to the tissues and the regulation of the capillary circulation. *J. Physiol.*, 20:457–474, 1919.